Centrifugal Fans: Similarity, Scaling Laws, and Fan Performance

by

Asad M. Sardar

A thesis submitted to the
Department of Mechanical and Aerospace Engineering
and the Faculty of the Graduate School of the
State University of New York at Buffalo
in partial fulfillment of the requirements for the degree of

Doctor of Philosophy

February 2001

Abstract

Centrifugal fans are rotodynamic machines used for moving air continuously against moderate pressures through ventilation and air conditioning systems. There are five major topics presented in this thesis:

- fan installation effects on overall fan performance and evaluation of fan testing methods;
- analysis of the fan scaling laws and consequences of dynamic similarity on modelling;
- mean velocity and turbulence intensity measurements (flow field studies) at the inlet and outlet of large scale blower;
- detailed flow visualization studies (in water) covering the flow path starting at the fan blade exit to the evaporator core of an actual HVAC fan scroll-diffuser module;
- two point coherence and spectral measurements conducted on an actual HVAC fan module for flow structure identification of possible aeroacoustic noise sources.

A major objective of the study was to identify flow structures within the HVAC module that are responsible for noise and in particular "rumble noise" generation. Possible mechanisms for the generation of flow induced noise in the automotive HVAC fan module are also investigated. It is demonstrated that different modes of HVAC operation represent very different internal flow characteristics. This has implications on both fan HVAC airflow performance and noise characteristics.

It is demonstrated from principles of complete dynamic similarity that fan scaling laws require that Reynolds number matching is a necessary condition for developing scale model fans or fan test facilities. The physical basis for the fan scaling laws derived was established from both pure dimensional analysis and also from the fundamental equations of fluid motion.

Fan performance was measured in a three times scale model (large scale blower)in air of an actual forward curved automotive HVAC blower. Different fan testing methods (based on AMCA fan test codes) were compared on the basis of static pressure measurements. Also, the flow through an actual HVAC fan-impeller/diffuser section in water was observed with a flow visualization technique using a shear-thickening dye (in addition to a conventional dye). Full dynamic similarity was maintained between HVAC operation in water as when operated in air. Recommendations are provided both for further investigation of critical flow regions with more sophisticated measurement methods and for improved fan-scroll design to reduce possible aeroacoustic noise with improved aerodynamic performance.

Contents

List of Figures

List of Tables

Acknowledgments

I would like acknowledge all those...

Chapter 1

Background

1.1 Foreword

Centrifugal fans are rotodynamic machines used for moving air continuously against moderate pressures through ventilation and air conditioning systems. The flow through a centrifugal fan is fairly complex with a highly convoluted flow path due to the complicated geometry and especially due to the rotating blades. The shape of the fan blades, scroll casing, inlet and outlet geometry all affect the fan performance and fan efficiency as well as the noise characteristics. The high specific speed [1] blowers used in the HVAC application have a typical squirrel-cage rotor[2], which is housed in a scroll casing, with a nonstandard inlet and outlet geometry, see Fig. 1.1.

[1] The equation for specific speed (dimensionless) is:

$$\sigma_s = [2\pi^2(\frac{\rho}{\Delta p})^3 Q^2]^{\frac{1}{4}}\Omega \tag{1.1}$$

Where Ω is rotational speed, Q is the flow rate, ρ is density and Δp is the pressure rise.

[2] Squirrel-cage rotors have 35 or more forward curved blades and rotor exit to inlet area ratios range typically between 1.5 to 3.0, resulting in much higher blade span to chord ratios compared to other centrifugal fan rotors.

The high manufacturing costs that arise due to complex design with high tolerances often result in major design compromises in commercial fan design. The design of a centrifugal fan for a specific application stems from the experience of the designer based on established results from previous tests (mostly concerning the overall performance of the fan), rather than from a thorough understanding of the internal fluid mechanics.

The applied research and development efforts on centrifugal fans over the past fifty years have lead to higher fan efficiencies with improved noise characteristics. This development, however, has largely been of a trial and error nature. Fans generally do not operate in an isolated environment, since they can have downstream and/or upstream flow resistance elements such as evaporators, grids, diffusers, complex ducting, flow conditioners, various throttling devices, etc. All these type of flow resistance elements affect the systems resistance (or back-pressures), and thus affect the fan operating characteristics. As a consequence, the primary objective has been to obtain an improvement of overall performance for fans working in specific environments.

As automobile cabin noise standards have become stricter in recent years, small automobile HVAC squirrel-cage fans have received considerable attention. HVAC fans have been observed to generate noise that is both tonal (due to blade passage noise) and broadband (so-called "rumble noise", mostly at low frequencies). It has been suggested that this "rumble noise" is primarily due to a flow induced phenomena rather than structural.

It is well known from fan noise studies [47] that fans with high aerodynamic efficiencies produce less noise. In general the noise characteristics of a fan are coupled to both the fans aerodynamic performance characteristics and duct acoustics. A better understanding of the relationship between the fan's overall performance characteristics and the fan's flow field characteristics and their correlation would give the fan designer a better understanding of the possible flow mechanisms responsible for the

decrease in fan performance and efficiency, and the increase in the noise levels found in typical HVAC fans (with forward curved impeller geometries).

Another problem lies in the so-called fan laws which are used for design and for scaling given designs to different sizes and applications. These classical fan laws were originally derived for hydro-power applications where the Reynolds numbers (ratio of inertia to viscous forces) is so large it can be assumed infinite. This is certainly not true of typical HVAC squirrel-cage type fans which operate at Reynolds numbers less than 3×10^5. As a result they show a Reynolds number dependence which affects both the selection of the best efficiency fan operating point and fan motor selection.

There are two areas targeted for blower improvement in the automobile HVAC system. First, the blower efficiency is lower than the efficiencies stated for some of the existing commercial designs, typically 65 percent. Second, the blower system produces a particular 'rumbling' noise that is not purely tonal but mixed with broadband noise. It is observed that the blower "rumble" is most critical at high fan speeds when in heater mode (high system resistance setting). Also evident, is the significantly lower airflow under the heater mode compared to the AC mode (low system resistance setting), indicating an increase in system resistance. This suggests that "rumble" results from the changing flow pattern within the blower, the changing flow pattern elsewhere in the HVAC module (due to a geometry change resulting from a change in the mode of operation), and the complex interaction of both these effects.

A computational (CFD) approach to a squirrel-cage blower operating in a scroll casing ideally should allow rapid, low cost studies on the effects of the variation of individual geometric parameters on blower performance and aerodynamic efficiency. The CFD approach however, requires boundary conditions which must be representative of the actual flow across the blower at the inlet and outlet. Assumed boundary conditions may give a totally inaccurate picture about the flow field through the

blower system as well as the effects of the critical parameters affecting its performance. Also unlike hydropower turbines that are often meticulously constructed and highly polished, automotive fans are usually poorly manufactured and rough. For this reason an experimental approach is required to provide the real boundary conditions and realistic test results for validation purposes of the CFD code. Experimentation can also indicate relevant changes in turbulence length scales, thus serving as a guide in selection of model parameters and the appropriate mesh sizes. Experimental studies (such as those presented later) also highlight the fact that global flow pattern information for complex turbomachinery flows is a prerequisite for any kind of sophisticated CFD code. Thus, a balanced approach combining CFD, acoustical and flow measurement techniques is required to achieve aerodynamic/aeroacoustic performance improvements.

This thesis derives generalized fan scaling laws and compares them (perhaps for the first time) to the classical fan scaling laws. Then it shows examples of how these generalized fan scaling laws can be used to design different experimental approaches to improve understanding of the aerodynamic flow characteristics and fan performance of centrifugal blowers operating at low blade tip-speed Mach numbers (i.e., Ma < 0.1). Finally, some improvements are suggested for the fan/scroll/diffuser aerodynamic design and in fan performance testing.

1.2 Previous Work

A detailed literature survey on centrifugal blowers (fans) is included as Appendix A that covers both the aerodynamics and flow field studies. Included in this survey is a discussion of the relevant acoustical measurements connected to the flow field through the blower. In contrast to the numerous reviews concerning noise production of blowers (for example, [47], [48] and [39]), one of the striking outcomes of the

survey was that there is not a single review paper on the aerodynamics of centrifugal blowers. The work concerning the flow field through blowers up until 1967 is listed in Gardow's thesis [25], which clearly shows the lack of detailed experimental studies as well as theoretical analysis. Much of the earlier research originated from Germany, and is referenced mainly in the standard textbooks by Eck [20] and Traupel [66], and the book by Osborne [52].

In the last thirty years there has been considerable progress in centrifugal fan development, both from fundamental research (mostly gained from other types of turbomachinery and cascade experiments) and from industrial interest mainly aimed at noise reduction. Papers on noise reduction evidenced little interest in understanding centrifugal fan aerodynamics for purposes of improving fan efficiency. This can be contrasted with the numerous industrial publications on both centrifugal pumps, and compressors, and axial fans and compressors. For example, the book on fan engineering by Jorgensen [35] and the industrial research sponsored by Westinghouse ([71], [73], [74] and [41]) describing the experimental investigation on the flow field through blowers clearly show the industrial interest in improving the aerodynamic and noise characteristics of centrifugal blowers. There has also been significant interest in this area by the Japanese automotive industry ([61], [67] and [2]), along with the areas of sound and vibration ([62], [51], [50] and [1]). The British publications in this area are mostly associated with industrial applications [10] in building ventilation systems, and concentrate on the areas of noise and power consumption. However there has been some progress in the area of centrifugal fan aerodynamics by a few British researchers [15]. Early Canadian research in this field was of a pioneering nature, which came about due to studies on low speed centrifugal compressors in the late sixties and early seventies initiated by Fowler ([21], [22], [23], and [24]), Howard and Lenneman ([40] and [33]) and [42]. Fowler used hot wire anemometry to conduct detailed flow field studies on centrifugal fans including the blade passage area.

In summary, it appears that most of the experimental research conducted on centrifugal blowers in the last twenty years was in industry, and very little basic research was pursued. The situation is rapidly changing however. With the advent of LDA instrumentation, PIV analysis and powerful CFD packages with high speed computers, research is now being directed towards understanding the complex flow patterns and the interaction of the aerodynamics with the acoustical field (i.e., flow induced noise). Examples include the recent PTV study of Denger and McBride [17], the PIV study of Shepard et al. [59], and LDA studies of Goulas and Mealing [32].

1.3 An Outline of this Study

1.3.1 New (Generalized) Fan Scaling Laws

A standard dimensional/physical analysis is performed in Chapter 2 on centrifugal fans in order to develop and evaluate fan-scaling laws. On the basis of fundamental fluid flow theory, dynamic flow similarity between the model and the prototype fan requires that the pressure coefficient (type of an Euler number) and the volume flow coefficient (inverse of the Strouhal number) be matched. In addition, the Reynolds number must also be matched for complete dynamic similarity. The fundamental theory also indicates that geometric similarity is a prerequisite for dynamic similarity; thus all boundary conditions must be similar between model and prototype.

The dimensional/physical analysis highlights the differences between the classical fan scaling laws and the more generalized fan scaling laws derived herein which include the effect of Reynolds number. Note that the classical fan (affinity) laws preclude Reynolds number similarity. Chapter 3 discusses the differences and similarities between the classical and the generalized fan scaling laws with application to

model fan design and fan performance prediction. Chapter 3 also includes the theoretical establishment of fan design criteria and fan test conditions for fan operation in a fluid medium with different viscosity and density properties; for example, water under dynamically similar conditions to those in air using the generalized fan scaling laws.

1.3.2 Dynamically Similar Models

Chapter 4 describes the flow visualization experiment and results of an actual HVAC fan module operated in water under dynamically similar conditions as those in air. The experimental testing identified both qualitatively and quantitatively flow structures possibly responsible for noise augmentation and loss of aerodynamic efficiency. For this purpose conventional and special (shear thickening) dye injection flow visualization techniques were used to study the complex 3-dimensional vortical and unsteady flow patterns that occur in typical HVAC fans. Using water as the medium for model testing, the scaling laws indicated that a 1 to 1 scale model was sufficient for the proper application of low speed (less than $1m/s$) flow visualization techniques. Maintaining constancy of Reynolds number implied that the model fan speed and the flow rate can both be reduced by a factor of fifteen because the kinematic viscosity of water is 1/15 that of air. This reduction in the flow velocity was essential in order to use the dye injection technique. Fan scroll diffuser interaction was also studied as function of fan speed. Flow visualization was able to indicate the large-scale flow patterns through the blower and clearly showed areas of flow separation (which is the major cause of aerodynamic inefficiency and noise production) and recirculation zones within the blower housing.

Another objective of this study was to design and empirically test a large scale centrifugal blower model in order to reveal the details of the flow field and to obtain a deeper understanding of the physics of the flow processes. The design of the large

scale blower test facility is described in detail in Chapter 5. This LSB model was a three-times scale model of an actual HVAC centrifugal fan (the prototype), and designed to maintain complete dynamic similarity. The model and prototype fan impeller and scroll volute geometries were also similar. Geometric similarity was not exactly maintained, however, since the model inlet and outlet geometries were of much simpler geometry than the prototype fan inlet and outlet geometries. In order to understand the differences between the actual HVAC prototype and the LSB fan, an exact one third model of the LSB fan, the Mini-LSB fan was designed and tested like the LSB. The Mini-LSB fan test facility is also described in Chapter 5.

Details of the measurement techniques used and instrumentation for the LSB and Mini-LSB are discussed in Chapter 6. Chapter 7 presents the results of both the LSB fan performance testing (pressure measurements) and detailed hot-wire flow field surveys, conducted at the inlet and the outlet of the fan. The pressure measurements were obtained using piezometric static pressure taps. Hot-wire surveys were used to determine the volume flow rate. These detailed flow field surveys consisted of mean velocity and turbulence measurements (or variance) at the fan inlet and fan exit. In addition, the LSB fans performance characteristic test results were compared to the Mini-LSB (a 1/3 exact scale model of the LSB fan) fan performance in order to verify conformance with the generalized fan scaling laws, and in turn the experiments themselves.

Hot-wire anemometry and Pitot tubes were used for obtaining multidimensional velocity profiles and pressure distribution within the blower facility. This information demonstrated the relationship between the various aerodynamic parameters, performance characteristics (such as flow coefficient and pressure coefficient), and design variables unique to the blower facility. The flow characteristics were studied at the inlet and outlet regions using a single sensor hot-wire probe. The hot-wire technique was used to obtain the mean velocity and the variance (i.e. normal stress) in the

streamwise flow direction. Tuft flow visualization was also done at fan inlet and outlet sections.

1.3.3 Prototype Testing

An automotive HVAC system is comprised of many components. Each of them can produce a strong flow coupling between the component itself and the HVAC fan impeller, which in turn affects the performance of the fan and the efficiency of the module. This inter-component flow coupling phenomena can also affect the flow-induced noise characteristics of the whole HVAC system. These characteristics could be either low frequency noise (e.g., blower rumble, rotating stall, noise due to recirculating flow and noise due to low frequency vortex shedding) or high frequency noise (e.g., the interaction between the blade passage and the scroll cut-off or the high speed shear layers which can occur in diffusers). As a case in point, all the experimental evidence suggests that the rumble noise is present only when the fan and scroll assembly are combined with the module as a complete system.

In Chapter 8, the unsteady and instantaneous flow field inside an actual HVAC fan module is mapped using frequency domain and coherence function analysis (based on velocity-velocity cross correlation technique) with two hot-wires spatially separated. The finding of strong coherence between the two velocity signals indicates the presence of an organized flow structure. Power spectral measurements provide information about the frequency content of these structures. The presence of shear layers, regions of fan blade stalling, and flow coupling between the diffuser and fan blade exit were identified and studied as function of HVAC system resistance.

1.3.4 Evaluation of Industry Standard Tests and Methodologies

There are a number of "standard testing procedures" used by industry to evaluate fan performance. Because of their importance to the overall fan characterization, a discussion of them is included as Appendix C, even though it is somewhat tangential to the general thrust of this dissertation. The most popular of these are referred as the AMCA test methods. Appendix C describes these fan testing methodologies and verification procedures. Various fan testing facilities were evaluated in order to improve the characterization of fan performance and highlight the effect of boundary conditions (including fan installation effects) on fan performance. AMCA/ASHRAE Standard fan testing facilities were also evaluated and compared to each other under various inlet source flow conditions. The AMCA/ASHRAE fan test facility was verified using a uniform laminar inlet source flow that was generated by an axisymmetric jet. The evaluation of the different fan testing methodologies revealed the significance of the flow damping effects due to system resistance elements attached to the isolated fan. These system elements appear to be essential for proper characterization of fan performance.

1.3.5 Summary

Generalized fan scaling laws (GFSL) were derived to conform with strict dynamic similarity. These were used to conduct fan performance studies (in air) on an automotive centrifugal fan, a large scale model of it (the LSB), a smaller model of the model (the Mini-LSB), and conduct flow visualization studies on an actual automotive HVAC module (in water). These were evaluated and tested using the AMCA/ASHRAE procedures, which were themselves evaluated. Flow characteristics were studied using a variety of hot-wire and flow visualization techniques.

Flow characterization of both mean flow and the unsteady instantaneous flow fields on both the models and an actual HVAC centrifugal fan gave a better understanding of the flow through the fan and significantly improved the understanding of the relationship between the flow field and fan performance. It also was able to demonstrate the effects of system resistance on the flow field through the fan. The resulting knowledge can be used to suggest design improvements, with the objectives of reducing flow induced noise levels and improving the aerodynamic performance of the centrifugal fan/scroll combination for HVAC applications.

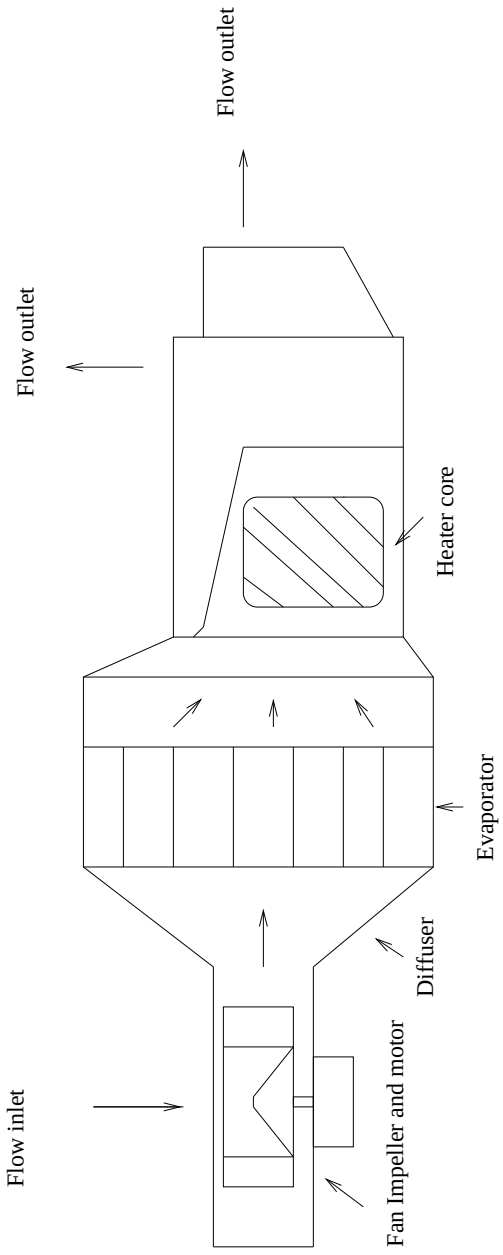

Figure 1.1: A Typical Automotive HVAC Module

Chapter 2

Generalized Fan Similarity (Scaling) Laws

2.1 Introduction

The prediction of the aerodynamic performance of a fan is critical for the proper selection and application of a fan within a given system. These applications vary widely from simple house blowers to more complicated ventilation and HVAC systems. Different applications require different fan performance characteristics. The overall performance of turbomachines can in theory be obtained from dimensional analysis. This is a formal procedure wherein the group of all the possible variables representing some physical phenomena is reduced into a smaller number of dimensionless groups.

In general fan engineering practice and according to the classical fan scaling laws (which are discussed in detail in Section 2.7), the dependent dimensionless fan performance variables are considered to be functions of only one independent dimensionless fan performance variable (in the case of low Mach number fans), usually the volume flow coefficient. The classical fan laws neglect the effects of surface roughness and

Reynolds number on fan performance. It is argued that this is justified since surface roughness and Reynolds number effects frequently lie outside the usual range of fan operation. Actual testing of centrifugal fans, however, over a wide range of fan operation speeds (including low fan test speeds) and for small fan sizes, has found discrepancies in fan performance prediction based on the classical fan laws ([12], [13] and [68]). Also, how to account for the influence of Reynolds number and surface roughness has been the subject of some controversy for many years (see [60], [3] and [72]). Phellan, Russell, and Zeluff [54] studied the influence of Reynolds number (based on fan blade tip and fan diameter) on fan performance for five different types of centrifugal fans. They found that there exists a threshold Reynolds number above which the fan performance is independent of Reynolds number; below this threshold value fan performance varies with Reynolds number. Their study also included the testing of several geometrically similar fans of different sizes.

In fact, the AMCA fan modeling and testing rules state that the effects due to the size, scale effect, and Reynolds number need not be included when a minimum model test size and speed ensures a Reynolds number of $R_e = ND^2/\nu > 3 \times 10^6$ (Schetz and Fuchs [57]). Typical HVAC centrifugal fans, however, operate at Reynolds numbers within the range of $Re = 1 \times 10^5$ to 4×10^5, *well below the design limit set by the AMCA Standards!*. Hence it is not surprising that these environments present serious problems for the designer. In today's globally competitive market where *every design uncertainty may be a competitor's opportunity*, these challenges can no longer be ignored.

Many authors have proposed various methods of adjusting fan performance for Reynolds number and surface roughness variations (especially for small machines) [13]. It is probably understating the situation to say that the proposed methods of adjusting fan performance and efficiency are not fully agreed upon in the international turbomachinery community. In order to avoid the discrepancy between model

and prototype fan performance due to scale effects, especially for modelling small automotive HVAC fans, a more general treatment of the fan laws is required. This more general approach developed below includes Reynolds number similarity as a necessary requirement for fan scaling from the outset.

It is well known that the solutions to real physical problems (especially in fluid mechanics) involve a combination of mathematical modelling and experimental verification. Experiments unfortunately are usually expensive and time-consuming. Numerical solutions can sometimes assist in experimental design, but because of uncertainties about boundary conditions, limitations of the codes, and the limitations of the turbulence models used, experiments are almost always an essential step to obtain the final solution. By contrast, a proper dimensional and physical analysis *guarantees* that the least number of experiments (or numerical runs) is required for a given physical problem. In addition, the dimensionless parameters can also be used to correlate experimental (or numerical) data for concise presentation using the minimum possible number of graphical plots and tables.

Dimensional analysis applied to turbomachines has two further important uses [18]: (a) prediction of a prototype's performance from tests conducted on a scale model (similitude): (b) determination of the most suitable type of turbomachine, on the basis of maximum efficiency, for a specified range of head (pressure rise), impeller speed and flow rate.

This chapter reconsiders the entire question of how fans should be scaled. The results are valid for *all* fans (under incompressible flow conditions), but are especially relevant to small ones. These scaling laws are also valid for hydraulic pumps operating under non-cavitating conditions. The remainder of the chapter is organized as follows:

- First, a physical basis is provided for the pertinent dimensionless fan performance variables in terms of scaling laws necessary for dynamic similarity. These

arise naturally from the equations of fluid motion applied to rotating turbomachinery; in fact, so naturally it is somewhat surprising that they are not already in widespread use.

- Second, generalized fan scaling laws (GFSL) which include Reynolds number effects are derived, and these are compared to the classical fan scaling laws (CFSL). Incorporating Reynolds number similarity into the fan scaling laws gives rise to multidimensional functional relationships among the dimensionless variables associated with fan performance.

- Third, the GFSL scaling is used to design a one to one scale model (Zfan) of an automotive HVAC fan module (prototype) operated in water for the purpose of flow visualization studies.

- Fourth, the GFSL are applied to the design of a large (three times scale) model fan (LSB) of an actual automotive HVAC forward curved centrifugal fan (the prototype) operated in air. The application of both GFSL and CFSL scaling laws to the LSB fan highlight the differences between the two types of scaling laws on model fan testing.

- Fifth, the GFSL scaling is applied to design and to test an exactly 1/3 scale model of the LSB fan, the Mini-LSB fan, in order to verify the generalized fan similarity laws. These two exact, but scaled models, the LSB and the Mini-LSB, allow the effect of the slight geometrical differences between the LSB and the prototype to be examined in detail.

It is important to note that all these applications of the GFSL maintain strict dynamic similarity.

2.2 The Generalized Fan Similarity Laws (GFSL) from Dynamic similarity

The advantage of physical analysis using the governing differential equations over purely dimensional analysis is that it simplifies the problem. Instead of arbitrary (and often numerous) combinations of variables which can arise with only dimensional analysis, the relevant variables arise naturally from the equations ([38], [46]). Moreover, no important variable is omitted, provided the governing equations are correctly specified.

Basic Equations

Consider the flow across the fan in the non-inertial (or accelerating) frame of reference (not the blade fixed reference frame)[1]. The differential equations describing the flow through the blades are just Newton's laws; i.e., $\vec{f} = m\vec{a}$! These are most conveniently expressed in terms of the Navier-Stokes equations. Under the assumptions of incompressible flow (or constant density flow) and Newtonian fluid (linear relation between stress and strain rate), these are given by the following differential form [6]

$$\frac{\partial \vec{u}}{\partial t} + \vec{u} \cdot \nabla \vec{u} = -\frac{\vec{\nabla} p}{\rho} + \nu \nabla^2 \vec{u} + \vec{B}_f - 2\Omega \times \vec{u} - \Omega \times (\Omega \times \vec{r}) \tag{2.1}$$

The last two terms are the Coriolis and centripetal forces, respectively.

In addition to the equation of motion, the continuity equation (based on mass conservation) must also be satisfied. The second governing equation for incompressible flow is:

$$\nabla \cdot \vec{u} = 0 \tag{2.2}$$

[1] The description of the fluid dynamical equations in the frame of reference of the rotating blades translates into a periodically steady flow system without the extra pressure gradients imposed by the Coriolis and centrifugal forces.

Non-dimensionalization

If U is a characteristic flow velocity across the centrifugal fan, L is a characteristic length (such as fan diameter), and Ω is the fan rotation rate, then Eq. 2.1 can be non-dimensionalized using standard normalization using a set of starred variables. The geometric and flow parameters are normalized using the following ratios:

$$\begin{array}{rclrclrclrcl} x^* & = & x/L; & y^* & = & y/L; & z^* & = & z/L; & r^* & = & r/L; \\ U^* & = & U/U_\infty; & V^* & = & V/U_\infty; & W^* & = & W/U_\infty; & & & \\ p^* & = & p/p_\infty; & t^* & = & t/\tau; & B_k^* & = & B_k/g; & \tau & = & 1/\Omega \end{array} \tag{2.3}$$

Note that, the fan rotation speed (Ω), fluid density (ρ) and viscosity (μ) are all assumed constant in the problem considered. Substituting for each of the terms in Eq. 2.1 and dividing both sides by U^2/L results in the following non-dimensional form of the equation 2.1:

$$\begin{aligned} (\frac{\Omega L}{U_\infty})\frac{\partial u^*}{\partial t^*} + u^* \cdot \nabla u^* &= -(\frac{P - P_\infty}{\frac{1}{2}\rho U_\infty^2})\nabla p^* + (\frac{\nu}{U_\infty L})\nabla^2 u^* + (\frac{gL}{U_\infty^2})B_f^* \\ &\quad -(\frac{\Omega L}{U_\infty})\Omega^* \times u^* - (\frac{\Omega L}{U_\infty})^2 \Omega^* \times \Omega^* \times r^* \end{aligned} \tag{2.4}$$

In terms of the new variables Eq. 2.2 transforms to:

$$\nabla \cdot \vec{u}^* = 0 \tag{2.5}$$

All the bracketed terms in Eq. 2.4 represent key dimensionless groups in fluid mechanics. After inserting the dimensionless groups into Eq. 2.4, the resulting equation is:

$$[Str]\,\frac{\partial u^*}{\partial t^*} + u^* \cdot \nabla u^* = -\,[Eu]\,\nabla p^* + \frac{\nabla^2 u^*}{[Re]} + \frac{B_f^*}{[Fr^2]} - [Str]\,(\Omega^* \times u^*) - \left[Str^2\right](\Omega^* \times \Omega^* \times r^*) \tag{2.6}$$

where :

$$Str = \frac{\Omega L}{U_\infty} \qquad \text{Strouhal number} \tag{2.7}$$

$$Eu = \frac{P - P_\infty}{\frac{1}{2}\rho U_\infty^2} \qquad \text{Euler number} \tag{2.8}$$

$$Re = \frac{U_\infty L}{\nu} \qquad \text{Reynolds number} \tag{2.9}$$

$$Fr = \frac{U_\infty}{\sqrt{Lg}} \qquad \text{Froude number} \tag{2.10}$$

The dimensionless forms of Eqs. 2.1 and 2.2, Eqs. 2.5 and 2.6, can be used to establish similarity requirements. From these equations it follows that if two different flow systems are governed by these equations, then the solutions (in terms of $u^*, v^*, w^*, p^*, x^*, y^*, z^*, t^*$ and r^*) will be the same if the four parameters Str, Re, Fr and Eu are equal. When this is true, the two systems are said to be *dynamically similar*, since it is impossible to tell from the dimensionless governing equations any difference between them. It is also essential that the boundary conditions and initial conditions expressed in dimensionless form be equal for the two systems. This is called complete geometric similarity, and is a requisite condition for dynamic similarity.

The dimensionless parameters obtained from the differential equations of fluid motion can be used to obtain relevant information about an unknown flow field from experiments conducted under more convenient and practical conditions than those of the unknown flow field. Consider the application of the method of similitude based on the governing equations to a flow through a centrifugal fan under conditions of incompressible flow with no free surfaces[2]. Using Eq. 2.6, the resulting non-dimensional

[2]In equation 2.6, it must be recognized that the Froude number is important, as a similarity parameter, only when a free surface or density variations are present (N.B., the free surface boundary condition is influenced by gravity). If there are no free surfaces nor density variations, the only effect of gravity is to superimpose a hydrostatic pressure distribution on the pressure distribution created by the fluid motion [46]. The hydrostatic pressure distribution can be eliminated from the governing equation (Eq. 2.6) by defining a new pressure, $\tilde{p} = p - \rho g z$, and with this change the Froude number

governing equation in the non-inertial frame of reference for flow through a centrifugal fan is:

$$Str\frac{\partial u^*}{\partial t^*} + u^* \cdot \nabla u^* = -Eu\nabla p^* + \frac{\nabla^2 u^*}{Re} - Str(\Omega^* \times u^*) - Str^2(\Omega^* \times \Omega^* \times r^*) \quad (2.11)$$

From Eq. 2.11 it is clear that the main dimensionless parameters for the fan are the Strouhal, Euler and Reynolds numbers. Therefore, in order to achieve full dynamic similarity (that includes geometric similarity) between the flow through the model and prototype, they must not only be geometrically scale models of each other, but the Strouhal, Euler and Reynolds numbers along with the boundary conditions must be also completely matched between model and prototype. Therefore the similarity requirements or modeling laws (fan scaling laws) can be specified from equation 2.11 between model (m) and prototype (p), as follows:

$$Str = \frac{\Omega_m L_m}{U_m} = \frac{\Omega_p L_p}{U_p} \quad (2.12)$$

$$Re = \frac{\rho_m U_m L_m}{\mu_m} = \frac{\rho_p U_p L_p}{\mu_p} \quad (2.13)$$

and

$$Eu = \frac{\Delta p_m}{\frac{1}{2}\rho_m U_m^2} = \frac{\Delta p_p}{\frac{1}{2}\rho_p U_p^2} \quad (2.14)$$

Equations 2.12 to 2.14 dictate both the model fan geometric dimensions and also the relevant model fan (aerodynamic) performance parameters. They both govern the design of the model fan experimental tests and provide the main fluid dynamic dimensionless parameters for correlating the experimental data.

is eliminated from the dimensionless governing equation. Therefore a reduction in the number of similarity requirements is achieved by removing the free surface condition.

2.3 Some Simple Scaling Consequences of the GSFL

This section illustrates some of the consequences of the Generalized Fan Scaling Laws (GSFL) for a simple size change if dynamic similarity is to be maintained. Note that these results represent fundamental scaling laws based on the equations of fluid motion for rotating turbomachinery for constant viscosity and density (and non-cavitating flows) flow conditions. Hence, in some sense at least, the conclusions are not debatable, however *unusual* they may appear!

Suppose the geometric length scale ratio between model and prototype is given by

$$\frac{L_m}{L_p} = \Lambda \tag{2.15}$$

so Λ is the size ratio of model to prototype.

The application of the fan scaling laws (based on N-S equations as derived above) to a scaled fan indicates that on the basis of Reynolds number similarity the fluid velocity scaling ratio is related to the fan geometric scale ratio (assuming constant viscosity) by:

$$\frac{U_m}{U_p} = \frac{1}{\Lambda} \tag{2.16}$$

In words, the velocity at every point in the model will be $1/\Lambda$ times the velocity at the corresponding point in the prototype.

Similarly, the relationship (based on Reynolds and Strouhal number similarity) between fan size (e.g., fan diameter) and fan rotation rate, Ω, is given by:

$$\frac{\Omega_m}{\Omega_p} = \frac{1}{\Lambda^2} \tag{2.17}$$

Interestingly, to maintain strict dynamic similarity, *the fan speed must be reduced by a factor of* $1/\Lambda^2$*, even though the flow speed only drops by a factor of* $1/\Lambda$. This is a major difference from the classical fan laws described later which would require the fan speed ratio be reduced by only $1/\Lambda$. This is why the implementation of

the classical fan laws usually requires corrections for Reynolds number, which is not maintained constant. This will be discussed in detail below.

In like manner, the model fan pressure scaling ratio is:

$$\frac{\Delta p_m}{\Delta p_p} = \frac{1}{\Lambda^2} \tag{2.18}$$

The fan power (K) scaling can be derived from the use of the simplified energy equation for a rotating fan blade at constant rotation rate (see Appendix B.3). Since:

$$K \propto \Delta p Q \qquad , \tag{2.19}$$

then using the Euler number and definition of volume flow rate, it follows that:

$$K \propto \rho U^3 L^2 \tag{2.20}$$

Also, the fan power can be expressed in the form of a coefficient; that is,

$$\tilde{\lambda} = \frac{K}{\rho U^3 L^2} \tag{2.21}$$

From the perspective of matching fan behavior between the model and prototype, the fan power coefficient must also be matched in addition to the Str, Eu and Re numbers. The additional fundamental scaling law for matching fan power can be expressed as:

$$\frac{K_m}{K_p} = \frac{{U_m}^3}{{U_p}^3}\frac{{L_m}^2}{{L_p}^2} \tag{2.22}$$

or

$$\frac{K_m}{K_p} = \frac{1}{\Lambda} \tag{2.23}$$

The fan torque (T_{shaft}) can be expressed in fundamental flow variables as:

$$T_{shaft} \propto \rho U^2 L^3 \tag{2.24}$$

Similarly a fan torque coefficient, $\tilde{\gamma}$, can be expressed as:

$$\tilde{\gamma} = \frac{T_{shaft}}{\rho U^2 L^3} \tag{2.25}$$

Under dynamic similarity conditions the fan torque coefficient between model and prototype will also be similar. Thus the fundamental torque scaling law is given by:

$$\frac{T_{shaft_m}}{T_{shaft_p}} = \frac{{U_m}^2}{{U_p}^2}\frac{{L_m}^3}{{L_p}^3} \tag{2.26}$$

or

$$\frac{T_{shaft_m}}{T_{shaft_p}} = \Lambda \tag{2.27}$$

These results can be applied to the three times scale model which will be considered later. Application of the fundamental fan scaling laws shows that for a three times scale model, the flow velocity decreases by a factor of three, whereas both the model fan rotation rate and fan pressure rise *decrease by a factor of* 9*!* Moreover, the power decreases by a factor of three, but the torque *increases* by a factor of three! As will be seen later, these differ substantially from application of the classical fan laws.

2.4 The Generalized Fan Similarity Laws from Dimensional Analysis

Under incompressible flow conditions, the performance of low Mach number centrifugal fans can also be predicted using simple dimensional analysis. Unlike the derivation in the previous section where the relevant dimensionless ratios fell naturally out of the governing equations, here it must be decided which of the possible dimensionless groups are useful. In the following paragraphs, the approach of Dixon [18] will be applied to a centrifugal fan in order to establish the relevant dimensionless groups and the fan scaling laws. The results are exactly equivalent, although the dimensionless ratios have been chosen to coincide with the classical approach.

From the general theory of dimensional analysis (Bridgeman [11]), the relevant dimensionless parameters can be derived for a given physical process. According to

the Buckingham π theorem, if a physical process satisfies the principle of dimensional homogeneity (i.e., all the additive terms of the governing equation have the same dimensions) and involves n dimensional variables, then it can be reduced to a state that involves only m dimensionless groups (or π numbers). The reduction, $k = n - m$, equals the maximum number of dimensionless groups which do not form a π number among themselves. And k is always less than or equal to the number of dimensions describing the dimensionless groups. Finally all the independent π groups can be obtained once the k scaling variables are selected. These can be formed into power products in combination with one additional variable with a non-zero exponent [69]. This dimensional analysis approach is illustrated by application to fans below.

For the centrifugal fan, the net pressure rise, ΔP, the efficiency, η, and the power supplied, K, can be regarded as dependent variables; whereas the flow rate, Q, fan speed, Ω, fan diameter, D, fluid density, ρ, fluid absolute viscosity, μ, and geometric length scale ratios, ϵ/D, l_1/D, etc., can be considered as independent variables. Thus three functional relationships can be written as:

$$\begin{aligned} \Delta p &= f_1(Q, \Omega, D, \rho, \mu, \varepsilon/D, l_1/D, ...) \\ \eta &= f_2(Q, \Omega, D, \rho, \mu, \varepsilon/D, l_1/D, ...) \\ K &= f_3(Q, \Omega, D, \rho, \mu, \varepsilon/D, l_1/D, ...) \end{aligned} \tag{2.28}$$

where $K = \Omega T_{shaft}$.

The flow through fan involves the following variables: $\Delta p, K, Q, \Omega, D, \rho, \mu, \varepsilon/D$. The dimensions of all the relevant fan aerodynamic and geometric variables, and physical fluid properties are given as follows:

$[\Delta p] \sim ML^{-1}T^{-2}, [Q] \sim L^3T^{-1}, [K] \sim ML^2T^{-3}, [\Omega] \sim T^{-1}$

$[D] \sim L, [\rho] \sim ML^{-3}, [\mu] \sim ML^{-1}T^{-1}, [\epsilon/D] \sim 1, [\eta] \sim 1, [l_1/D] \sim 1$ where $\sim$ means 'has the dimensions of'.

Standard dimensional analysis can be conducted on the system of equations 2.28 selecting , Ω , D and ρ as the independent scaling variables. Notice that the chosen independent variables themselves do not form a dimensionless group. From inspection of the list of major variables, there are only three basic dimensions: mass, length and time. Thus according to the Buckingham Π theorem, there can only be $8 - 3$, or 5 independent dimensionless groups relevant to this problem. These 5 independent groups can be chosen in a number of ways. For both physical reasons and to conform with historical precedent, the following five independent dimensionless groups are selected:

1. *The pressure coefficient:* The pressure coefficient, ψ (or C_p), is defined as:

$$\psi = \frac{8\Delta p}{\rho \Omega^2 D^2} \tag{2.29}$$

   Note that ψ is the counterpart of Eu, except in the former Δp is made non-dimensional using the fan rotation speed and length (i.e., fan diameter), while the latter uses the flow velocity U and length. Obviously these need not be the same unless the fan is operating in a precisely dynamically similar manner (meaning all other dimensionless ratios are fixed). ψ is also called the head or energy transfer coefficient in hydraulic turbomachinery literature.

2. *Volume flow coefficient:* The volume flow coefficient for centrifugal fans, ϕ, involves the ratio of the fluid velocity at the blade tip to the blade tip speed and is defined as:

$$\phi = \frac{Q}{\Omega D^3} \tag{2.30}$$

   For centrifugal fans it represents in some form the ratio of centrifugal forces to the inertial force across the fan blades, and is similar to the blade velocity coefficient defined for axial turbomachinery. Note that ϕ is the counterpart to the Str number defined earlier, but again it has been made non-dimensional by

Ω and D instead of U and L. *These are equivalent only if dynamic similarity is maintained.*

3. *Reynolds number:* A Reynolds number for fans (also called the rotational Reynolds number by some authors) can be defined in terms of the blade rotation rate, Ω, and the blade tip diameter, D, and can be expressed as:

$$R = \frac{\rho \Omega D^2}{\mu} \tag{2.31}$$

Obviously R and Re differ in like manner to the above parameters.

4. *Power coefficient:* The power coefficient is the ratio of power input to the fan and the power delivered to the fluid by the fan impeller. It is defined as:

$$\lambda = \frac{K}{\rho \Omega^3 D^5} \tag{2.32}$$

λ is obviously the counterpart to $\tilde{\lambda}$ defined earlier.

5. *Surface relative roughness:* Surface roughness is usually defined in terms of a characteristic solid surface roughness length, often as relative to a typical fan characteristic length, such as, fan outer diameter, D. It is defined as:

$$\epsilon^* = \frac{\epsilon}{D} \tag{2.33}$$

The fan efficiency is an important fan performance parameter, but it does not form an independent dimensionless group, since it is defined in terms of the Δp, Q and K; i.e.,

$$\eta = \frac{\Delta p Q}{K} = \frac{\Delta p Q}{\Omega T_{shaft}} \tag{2.34}$$

The functional relation between the pressure coefficient (or the energy transfer coefficient) and the other variables (ratios) can now be expressed as:

$$\psi = \frac{8 \Delta p}{\rho \Omega^2 D^2} = f_4(\frac{Q}{\Omega D^3}, \frac{\rho \Omega D^2}{\mu}, \frac{\epsilon}{D}, \frac{l_1}{D}, ...) \tag{2.35}$$

Note the pressure coefficient, ψ, can be expressed in terms of the blade tip characteristic velocity U where $U = \Omega D/2$; i.e.,

$$\psi = \frac{2\Delta p}{\rho U^2} \tag{2.36}$$

Similarly, the functional relation between the fan efficiency and the other variables (ratios) can be expressed as:

$$\eta = \frac{\Delta p Q}{\Omega T_{shaft}} = f_5(\frac{Q}{\Omega D^3}, \frac{\rho \Omega D^2}{\mu}, \frac{\epsilon}{D}, \frac{l_1}{D}, ...) \tag{2.37}$$

Finally, the functional relation between the power coefficient and the other variables (ratios) can be expressed as:

$$\lambda = \frac{K}{\rho \Omega^3 D^5} = f_6(\frac{Q}{\Omega D^3}, \frac{\rho \Omega D^2}{\mu}, \frac{\epsilon}{D}, \frac{l_1}{D}, ...) \tag{2.38}$$

From Eq. 2.38, a relation for the torque coefficient can be obtained as:

$$\gamma = \frac{T_{shaft}}{\rho \Omega^2 D^5} = f_7(\frac{Q}{\Omega D^3}, \frac{\rho \Omega D^2}{\mu}, \frac{\epsilon}{D}, \frac{l_1}{D}, ...) \tag{2.39}$$

From equations 2.35-2.39, it can be concluded that for geometrically similar fans (including surface roughness), the functional relationships are:

$$\psi = f_4(\frac{Q}{\Omega D^3}, \frac{\rho \Omega D^2}{\mu}) = f_4(\phi, \mathrm{R}) \tag{2.40}$$

$$\eta = f_5(\frac{Q}{\Omega D^3}, \frac{\rho \Omega D^2}{\mu}) = f_5(\phi, \mathrm{R}) \tag{2.41}$$

$$\lambda = f_6(\frac{Q}{\Omega D^3}, \frac{\rho \Omega D^2}{\mu}) = f_6(\phi, \mathrm{R}) \tag{2.42}$$

$$\gamma = f_7(\frac{Q}{\Omega D^3}, \frac{\rho \Omega D^2}{\mu}) = f_7(\phi, \mathrm{R}) \tag{2.43}$$

Dimensional analysis cannot progress further in search of the solution for the given physical system, so the actual form of the functions f_4, f_5, f_6 and f_7 can only be established by experiment.

Using Eqs. 2.40 and 2.41, it can be shown that the Reynolds number dependence can be eliminated from Eqs. 2.40 and 2.41. The new functional relationship can be written in the following form, relating η, ψ and ϕ:

$$\eta = f_7(\phi, \psi) \tag{2.44}$$

Now, Eqs. 2.40 and 2.41 can be rewritten in the following functional forms:

$$\mathrm{R} = f_8(\phi, \psi) \tag{2.45}$$

$$\mathrm{R} = f_9(\phi, \eta) \tag{2.46}$$

from which Eq. 2.44 follows.

It can also be shown that a relationship exists for fans (under the conditions of Reynolds number and geometric similarity, i.e., dynamic similarity) among fan efficiency, fan power coefficient, pressure coefficient and volume flow coefficient. From a combination of the basic definitions of the fan's power, volume and pressure coefficients and, fan efficiency, the fan power coefficient can be expressed as:

$$\lambda = \frac{K}{\rho \Omega^3 D^5} = \frac{Q}{\Omega D^3} \frac{8\Delta p}{\rho \Omega^2 D^2} \frac{1}{\eta} \tag{2.47}$$

It follows that:

$$\lambda = \frac{\phi \psi}{\eta} \tag{2.48}$$

Thus the function f_6 can be derived from the functions f_4 and f_5.

2.5 The Formulation of Additional Dimensionless Variables for Fans

In the dimensional analysis conducted above, if a different set of independent scaling variables are chosen (e.g., Q, ρ and D), then two additional forms of dimensionless groups can be formed. These are, however, not independent π groups, but are related to the first set that was derived previously. These additional π groups are:

$$Eu_Q = \frac{\Delta p D^4}{\rho Q^2} \tag{2.49}$$

$$Re_Q = \frac{Q}{\nu D} \tag{2.50}$$

$$\zeta = \frac{K D^4}{\rho Q^3} \tag{2.51}$$

$$\xi = \frac{T_{shaft} D}{\rho Q^2} \tag{2.52}$$

$$\eta = \frac{\Delta p Q}{\Omega T_{shaft}} \tag{2.53}$$

The relationship between the first and second set of π groups are given below:

$$Eu_Q = \frac{\psi}{\phi^2} \tag{2.54}$$

$$Re_Q = \phi R \tag{2.55}$$

$$\zeta = \frac{\lambda}{\phi^3} \tag{2.56}$$

and,

$$\xi = \frac{\gamma}{\phi^2} \tag{2.57}$$

The plot of systems Euler number, Eu_Q, versus the systems Reynolds number, Re_Q, characterizes the system behavior (or system resistance). Note that this relationship is independent of the fan rotation rate, Ω, and thus does not characterize the fan's aerodynamic performance. The other additional dimensionless groups can be considered as directly coupled to the first set. From the set of equations given above, it is observed for example, the pressure coefficient, ψ, is functionally related to both the flow coefficient (or Strouhal number) and the Euler (systems) number. Also, both the power coefficient, λ, and the torque coefficient, γ, are functionally related to the flow coefficient (or Strouhal number) and the power and torque coefficients (expressed in characteristic flow variables used in the Navier-Stokes equation) respectively.

2.6 Implications of GFSL Scaling for Fan Design and Testing

The prediction of fan performance for geometrically (or homologous series) similar machines is of importance for both fan manufacturing and fan selection. The GFSL can be applied to predict the performance of a fan, and they can also be used to design model fans for studying both their aerodynamic and aeroacoustic characteristics. These can be investigated by using both experimental and computational (CFD) approaches, to obtain model fan test conditions based on the prototype fan test conditions. In order to be useful, model test results must duplicate both the overall prototype fan characteristics and the prototype flow field characteristics (in particular, the ratios of flow velocities, accelerations and forces), in addition to having matched system resistances (or load). Thus, the main question is: what are the conditions necessary to ensure complete similarity between the model and the prototype fans?

The answer to this question can be obtained on the basis of the fundamental equations of fluid motion (physical analysis) and the proper application of dimensional analysis to the fan. The design of a homologous series of fans of different sizes that have similar aerodynamic characteristics requires that the flows be dynamically similar in both scaled fan and its prototype. The application of the GFSL between a scaled fan (model) and its prototype *ensures* that the flow in the two fans will be dynamically similar if both the volume flow coefficient and the Reynolds numbers are matched between model and prototype. Alternatively, both model and prototype will have exactly the same behavior, from the perspective of the Navier-Stokes equations (and in fact!), if in addition to the requirement of the Strouhal and Euler number similarity (or matching), the Reynolds numbers are identical between the model and prototype. Thus both sets of constraints are equivalent; in particular, both require that the Reynolds number be the same between model and prototype.

The functional relations given by Eqs. 2.40 to 2.43 indicate that for full dynamic similarity (including strict geometric similarity), the volume flow coefficient, ϕ, and Reynolds number, Re, must be fully matched between scale model and prototype. If so, then from equations 2.40 to 2.43, the pressure coefficient, ψ, the fan efficiency, η, the power coefficient, λ, and the torque coefficient, γ, will also be matched.

The set of equations above, Eqs. 2.40 to 2.43, establish the most general scaling (or modeling) laws. They can be used to predict the complete fan performance characteristics for homologous[3] series of fans, and also to predict the performance of the same fan at different test conditions. The implications of the general fan scaling laws (GFSL) are summarized by the expressions below (based on Eqs. 2.40 to 2.42). Note that m = model and p = prototype.

[3]Machines which are geometrically similar (i.e., the only variable is machine size (diameter) not shape [18])

Reynolds number similarity requires simply that:

$$Re_m = Re_p \tag{2.58}$$

or

$$\frac{U_m D_m}{\nu_m} = \frac{U_p D_p}{\nu_p} \tag{2.59}$$

Since dynamic similarity is maintained, the velocity, U, is related to the rotation rate, Ω, and size, D, by

$$U \propto \Omega D \tag{2.60}$$

Thus, it follows that Eq. 2.59 becomes

$$\frac{\Omega_m D_m^2}{\nu_m} = \frac{\Omega_p D_p^2}{\nu_p} \tag{2.61}$$

The volume flow coefficient (or inverse Strouhal number) similarity implies:

$$\phi_m = \phi_p \tag{2.62}$$

or

$$\frac{Q_m}{\Omega_m D_m^3} = \frac{Q_p}{\Omega_p D_p^3} \tag{2.63}$$

Since

$$Q \propto U D^2 \tag{2.64}$$

then the flow coefficient (ϕ) can be rewritten as:

$$\frac{U_m}{\Omega_m D_m} = \frac{U_p}{\Omega_p D_p} \tag{2.65}$$

The GFSL imply that if ϕ and Re similarity (matching) are maintained, then ψ, λ, η and γ will also be matched between model and prototype. Thus,

The pressure coefficient similarity implies

$$\psi_m = \psi_p \tag{2.66}$$

or

$$\frac{\Delta p_m}{\rho_m \Omega_m^2 D_m^2} = \frac{\Delta p_p}{\rho_p \Omega_p^2 D_p^2} \tag{2.67}$$

The power coefficient similarity implies

$$\lambda_m = \lambda_p \tag{2.68}$$

or

$$\frac{K_m}{\rho_m \Omega_m^3 D_m^5} = \frac{K_p}{\rho_p \Omega_p^3 D_p^5} \tag{2.69}$$

Finally, the fan efficiency similarity implies

$$\eta_m = \eta_p \tag{2.70}$$

or

$$\frac{\Delta p_m Q_m}{\Omega_m T_{shaft_m}} = \frac{\Delta p_p Q_p}{\Omega_p T_{shaft_p}} \tag{2.71}$$

In summary, when the generalized fan scaling laws, given by Eqs. 2.58 to 2.71, are applied to a homologous series of fans that undergo only a change in the fan diameter, the scaling laws predict that the fan speed must change by a factor of D_m^2/D_p^2 in order to maintain Reynolds number similarity. This is contrary to the classical laws discussed below which require a change of only D_m/D_p. As noted earlier, use of the classical laws instead of the generalized ones developed above to develop specifications for a series of fans is the primary reason for scale effects, and the source of considerable frustration to engineers and customers as well.

2.7 The Classical Fan Scaling Laws (CFSL)

Although many authors have derived the classical fan laws (or the so-called *Affinity Laws*) in the past, they are reproduced here for the sake of completeness.These classical fan laws, CFSL, ([58], [70]) have largely been applied to large-scale hydraulic

pumps and similar turbomachinery. Traditional dimensional analysis of turbomachinery based on incompressible fluid analysis was conducted ([58] and [18]) with the major assumption of neglecting viscous losses. Thus these CFSL differ from the GFSL derived in section 2.3 in that the effect of Reynolds number has been neglected. The direct consequence of this neglect is the so-called "Scale Effect". These famous "inviscid" fan laws have been (and still are) applied to hydraulic turbomachinery under non-cavitating conditions and to general fluid turbomachinery under incompressible flow conditions. One of the major points of this dissertation is that *they should not be* applied to small fans.

The classical fan laws can be derived using the dimensional analysis procedure outlined in section 2.3, with the major assumptions of complete geometric similarity while neglecting the influence of the Reynolds number and surface roughness. Mach number effects are insignificant for turbomachines operating under incompressible flow conditions.

The neglect of Reynolds number effects (according to classical fan law theory) results in a major simplification of the functional relationships between the pressure coefficient (ψ), volume flow coefficient (ϕ), fan efficiency (η) and power coefficient (λ) and torque coefficient (γ). The resulting fan laws for geometrically similar fans according to classical theory are:

$$\psi = g_1(\frac{Q}{\Omega D^3}) = g_1(\phi) \tag{2.72}$$

$$\eta = g_2(\frac{Q}{\Omega D^3}) = g_2(\phi) \tag{2.73}$$

$$\lambda = g_3(\frac{Q}{\Omega D^3}) = g_3(\phi) \tag{2.74}$$

$$\gamma = g_4(\frac{Q}{\Omega D^3}) = g_4(\phi) \tag{2.75}$$

From Eqs. 2.72 to 2.75 it can be shown that g_3 can be derived from g_1 and g_2 since Eq.2.48 holds; i.e.,

$$\lambda = \frac{\phi\psi}{\eta} = \frac{\phi g_1(\phi)}{g_2(\phi)} = g_3(\phi) \tag{2.76}$$

The classical fan laws imply that the fan efficiency (η), pressure coefficient (ψ), power coefficient (λ), and the torque coefficient (γ) for a fan of given geometry are unique functions of the volume flow coefficient (ϕ) since Reynolds number effects are neglected. Therefore the application of the classical fan laws between the scale model and the prototype fans can be written in the following manner:

$$\phi_m = \phi_p \Rightarrow \frac{Q_m}{\Omega_m D_m^3} = \frac{Q_p}{\Omega_p D_p^3} \tag{2.77}$$

$$\psi_m = \psi_p \Rightarrow \frac{\Delta p_m}{\rho_m \Omega_m^2 D_m^2} = \frac{\Delta p_p}{\rho_p \Omega_p^2 D_p^2} \tag{2.78}$$

$$\lambda_m = \lambda_p \Rightarrow \frac{K_m}{\rho_m \Omega_m^3 D_m^5} = \frac{K_p}{\rho_p \Omega_p^3 D_p^5} \tag{2.79}$$

Since the fan power input, K, is related to fan torque, T, similarity of the torque coefficient is given as:

$$\gamma_m = \gamma_p \Rightarrow \frac{T_{shaft_m}}{\rho_m \Omega_m^2 D_m^5} = \frac{T_{shaft_p}}{\rho_p \Omega_p^2 D_p^5} \tag{2.80}$$

It can be concluded from the combination of Eqs. 2.77 to 2.79 and Eq. 2.48 that the fan efficiency of the model fan and the prototype fan will also be equal; i.e.,

$$\eta_m = \eta_p \Rightarrow \frac{\Delta p_m Q_m}{\Omega_m T_m} = \frac{\Delta p_m Q_m}{\Omega_m T_m} \tag{2.81}$$

Therefore, using Eqs. 2.77 to 2.81, the complete fan pressure, power, torque and efficiency characteristics can be determined for homologous series of fans and for the same fan operating at under different operating conditions.

Comparing the fan scaling laws established from generalized similarity requirements, Eqs. 2.58 to 2.71 to the classical fan laws, Eqs. 2.77 to 2.81, the main difference arises due to Reynolds number similarity, which puts an additional constraint on scaling fan speed and fan diameter (i.e., the size of the machine). That is, fan diameter changes must accompany fan speed changes according to Eq. 2.17. Thus according to the GFSL, the scaling of fan speed and fan diameter are dependent on each other. The classical fan scaling laws (CFSL), on the other hand, suggest *erroneously* (at least from the viewpoint of the laws of nature) that the fan diameter ratio can be altered independently of the fan speed ratio when scaling geometrically similar fans.

Thus, the classical fan laws completely neglect viscous effects and use the fact that the aerodynamic performance of *large* turbomachines handling mostly incompressible fluids (under non-cavitating conditions) usually do not show any Reynolds number effects. Strict similarity is often *not* adhered to in scale model testing in hydraulics because cost and size constraints prohibit adherence to strict similarity, so reduced similarity models are sometimes used. As long as the Reynolds numbers are very high ($> 10^6$) AND boundary layer effects play little role in overall performance, these reduced models work reasonably well. As noted in the Introduction, these conditions generally do *not* apply to the small fans typical of automotive applications, and probably do not apply in many other situations as well.

2.8 The Importance of Geometric Similarity Between Model and Prototype

Geometric similarity implies that the model and prototype have length dimensions in a constant ratio throughout and that equivalent angles are preserved (i.e., angles

are equal). This implies that both the shape and all the scaled length ratios remain constant between model and prototype.

When applied to centrifugal fans, true geometric similarity between the model and prototype fan implies that the inlet and outlet fan/duct geometries should be similar, in addition to the fan impeller and fan scroll. Maintaining geometric similarity is a necessary condition for the obtaining true kinematic similarity between the model and prototype, and this implies simulating exactly the (kinematic) inlet boundary and outlet boundary conditions between the model and prototype. The accuracy of the scaled fan performance is dependent upon the proper achievement of both geometric/kinematic and dynamic similarity between model and prototype. A lack of geometric similarity at the inlet or exit of the fan can in theory change the dynamics of the flow, thereby affecting the prediction of fan performance based on fan scaling laws. Thus it is essential to maintain geometric similarity (within practical constraints) between model and prototype fans in order to obtain truly similar fan performance characteristics.

2.9 Summary of Parameters and their Inter-relation

A flow time scale can be deduced as $\tau_f = L/U$ (an inertial flow time scale) . The rotating blades give rise to second time scale in the flow in addition to the mean flow time scale; namely, $\tau_b = 1/\Omega$. The ratio of the inertial flow time scale, τ_f, to the unsteady time scale, τ_b, is defined as the Strouhal number, Str, given by: ($Str = \frac{\Omega L}{U}$).

On rearranging the basic form of the Strouhal number, Str, as given by Eq. 2.17, a relationship with flow coefficient, ϕ, is evident. Since the flow rate, Q, is proportional to the flow velocity, U, and a characteristic area, L^2, the Strouhal number can be written as:

$$Str = \frac{\Omega L}{U}(\frac{L^2}{L^2}) = \frac{\Omega L^3}{UL^2} \equiv \frac{\Omega L^3}{Q} \tag{2.82}$$

Thus the Strouhal number is inversely proportional to the flow coefficient

$$Str = \frac{1}{\phi} \tag{2.83}$$

Equation 2.83 confirms that the requirement of flow coefficient similarity derived from the classical fan law theory is indeed directly related to one of the fundamental similarity constraints derived from the the Navier-Stokes equations, which requires Strouhal number similarity for dynamically similar flow systems.

Euler number similarity establishes the ratio of pressure differences between the model and prototype fans. The Euler number can be expressed in two ways:

- First in the form of a pressure coefficient (ψ) using the fact that $U = \Omega D/2$; i.e.,

$$Eu = \frac{\Delta p}{\frac{1}{2}\rho U^2} = \frac{8\Delta p}{\rho \Omega^2 D^2} \tag{2.84}$$

- Second, in the form of a fan system resistance coefficient, using the fact that:

$$Eu_{sys} = \frac{\Delta p}{\frac{1}{2}\rho U^2} = \frac{\pi^2 \Delta p D^4}{8\rho Q^2} \tag{2.85}$$

In fan engineering practice it is common to use the symbol ψ for the fan pressure rise coefficient and to use the diameter coefficient, δ, to represent the system resistance characteristics. The diameter coefficient, δ, is an additional dimensionless parameter that can be formed in terms of the volume and pressure coefficients, by eliminating the fan rotation rate, Ω; i.e.,

$$\delta = \frac{\psi^{\frac{1}{4}}}{\phi^{\frac{1}{2}}} = \frac{D(\Delta p/8\rho)^{\frac{1}{4}}}{(Q/\pi)^{\frac{1}{2}}} \tag{2.86}$$

Note that the Euler number, Eu_{sys}, is equivalent to δ^4.

Another dimensionless parameter that is independent of fan size (i.e., fan diameter) is the speed coefficient, σ, which can be formed using the flow coefficient and pressure coefficient. It was defined in chapter 1 as:

$$\sigma_s = \frac{\phi^{\frac{1}{2}}}{\psi^{\frac{3}{4}}} = [2\pi^2(\frac{\rho}{\Delta p})^3 Q^2]^{\frac{1}{4}}\Omega \tag{2.87}$$

These specific fan performance variables serve to characterize the performance and geometric parameters of a fan in a unique way. The application of these variables usually arises in the area of low-pressure axial fan selection, as was first demonstrated by Cordier [14], and then by Balje [4] and Csanady [16]. They all showed that the most optimal turbomachine (or fan) of a given type can be selected on the basis of the specific speed, specific diameter and fan efficiency. From the range of the combination of σ versus δ and η versus δ for a given series of fan design, the best or the most efficient fan can be determined. This concept is referred to as a Cordier line. This method of fan selection is also applicable to low Mach number centrifugal fans.

Chapter 3

Application and Comparison of the GFSL and the CFSL Approaches to Fan Design

3.1 Introduction

In this section both the generalized fan scaling laws, GFSL (based on complete dynamic similarity), and the classical fan scaling laws, CFSL (based on the assumption of an infinite Reynolds number), are applied to a forward curved centrifugal fan, and a comparison is made between the different fan-scaling approaches. The GFSL scaling relationships between the prototype fan and the model fan are given by Eqs. 2.29 to 2.34 On the other hand, the CFSL scaling relationships between the prototype fan and the model fan are given by Eqs. 2.77 to 2.73.

This chapter is organized as follows: First, the GFSL and CFSL approaches are applied to design a 3 times scale model of an automotive HVAC fan. Second, the different scaling laws are applied to the same fan at a scale ratio of one for the

purpose of performance prediction. Third, the GFSL approach is used to design both a 3 times scale large scale blower model test facility, the LSB, and a Mini-LSB (an exact 1/3 scale model of the LSB). Fourth, the GFSL approach is used to design an experiment to test an actual HVAC fan module *in water* under dynamically similar conditions to those in air.

3.2 Comparison of the GFSL and the CFSL Approaches to Fan Design

The GFSL approach is based on three independent and fundamental similarity conditions: Strouhal number, Euler number and Reynolds number similarity. The CFSL approach, however, is based on only one independent and fundamental similarity condition, the volume flow coefficient (inverse of the Strouhal number). The major consequences on fan scaling due to these differences between the application of the CFSL and the GFSL approaches to fan design are summarized in Tables 3.1 and 3.2 which describe the basic GFSL and CFSL approaches while assuming constant viscosity and density between model and prototype.

The major differences between CFSL and GFSL approaches occur due to the additional requirement of Reynolds number similarity between model and prototype for the GFSL approach. This additional similarity condition, given in Eq. 2.59, introduces a constraint on the model and prototype fan size and flow velocity ratios. In addition, when this constraint is applied to the fan together with the constraint established due to the Strouhal number similarity, Eq. 2.11, then a new constraint is obtained; namely, $\Omega_m L_m^2 = \Omega_p L_p^2$. This constraint is unique to the GFSL approach.

It can be observed from the CFSL approach in Table 3.2 that the fan speed

Similarity parameters	Scaling laws	Scaling laws in terms of Λ
$Re_m = Re_p$	$\frac{U_m}{U_p} = \frac{L_p}{L_m}$	$\frac{U_m}{U_p} = \frac{1}{\Lambda}$
$Str_m = Str_p$	$\frac{\Omega_m}{\Omega_p} = (\frac{U_m}{U_p})(\frac{L_p}{L_m})$	$\frac{\Omega_m}{\Omega_p} = \frac{1}{\Lambda^2}$
$Eu_m = Eu_p$	$\frac{\Delta p_m}{\Delta p_p} = (\frac{\Omega_m}{\Omega_p})^2(\frac{L_m}{L_p})^2$	$\frac{\Delta p_m}{\Delta p_p} = \frac{1}{\Lambda^2}$
$\tilde{\lambda}_m = \tilde{\lambda}_p$	$\frac{K_m}{K_p} = (\frac{\Omega_m}{\Omega_p})^3(\frac{L_m}{L_p})^5$	$\frac{K_m}{K_p} = \frac{1}{\Lambda}$
$\tilde{\gamma}_m = \tilde{\gamma}_p$	$\frac{T_m}{T_p} = (\frac{\Omega_m}{\Omega_p})^2(\frac{L_m}{L_p})^5$	$\frac{T_m}{T_p} = \Lambda$
$\frac{Q_m}{Q_p}$	$\frac{Q_m}{Q_p} = (\frac{U_m}{U_p})(\frac{L_m}{L_p})^2$	$\frac{Q_m}{Q_p} = \Lambda$

Table 3.1: GFSL Approach

ratio and fan size ratio scale independently of each other. In fact, both are free scaling parameters in the CFSL approach. By contrast, in the GFSL approach (under constant fluid viscosity and density), as observed from Table 3.1, *either* the fan size ratio or the fan speed ratio may be used as the independent scaling parameter, *but not both*! This is because of the requirement of satisfying Reynolds number similarity.

Reynolds number similarity also introduces another fundamental relation (assuming constant viscosity between model and prototype) between the fluid velocity and fan size, Eq. 2.16, which states that fluid velocity ratio is inversely proportional to fan size ratio. In the CFSL approach, however, there is no direct fundamental constraint on the fluid velocity ratio. There is however an indirect constraint on flow velocity through the requirement of the volume flow coefficient similarity since the volume flow rate is proportional to the fan blade tip velocity, ΩL. In fact, it can be observed from

Similarity parameters	Scaling laws	Scaling laws in terms of Λ
$\phi_m = \phi_p$	$\frac{Q_m}{Q_p} = (\frac{\Omega_m}{\Omega_p})(\frac{L_m}{L_p})^3$	$\frac{Q_m}{Q_p} = (\frac{\Omega_m}{\Omega_p})(\Lambda)^3$
$\psi_m = \psi_p$	$\frac{\Delta p_m}{\Delta p_p} = (\frac{\Omega_m}{\Omega_p})^2(\frac{L_m}{L_p})^2$	$\frac{\Delta p_m}{\Delta p_p} = (\frac{\Omega_m}{\Omega_p})^2(\Lambda)^2$
$\lambda_m = \lambda_p$	$\frac{K_m}{K_p} = (\frac{\Omega_m}{\Omega_p})^3(\frac{L_m}{L_p})^5$	$\frac{K_m}{K_p} = (\frac{\Omega_m}{\Omega_p})^3(\Lambda)^5$
$\gamma_m = \gamma_p$	$\frac{T_m}{T_p} = (\frac{\Omega_m}{\Omega_p})^2(\frac{L_m}{L_p})^5$	$\frac{T_m}{T_p} = (\frac{\Omega_m}{\Omega_p})^2(\Lambda)^5$
$\frac{U_m}{U_p}$	$\frac{U_m}{U_p} = \frac{\Omega_m L_m}{\Omega_p L_p}$	$\frac{U_m}{U_p} = \frac{\Omega_m}{\Omega_p}\Lambda$

Table 3.2: CFSL Approach

Table 3.2 that in the application of the CFSL approach to the fan model/prototype system, the fan blade tip velocity ratio U_m/U_p, is dependent on both the fan size and the fan speed ratios, and these are arbitrary scaling parameters. On the other hand, in the GFSL approach the flow velocity ratio is constrained by only the fan size ratio.

Another important observation can be made from Tables 3.1 and 3.2. From Table 3.1(GFSL approach) it is clearly evident that all the pertinent fan performance parameters are strictly a function of only the fan geometric scale ratio, Λ. On the other hand, according to the CFSL approach shown in Table 3.2, all the pertinent fan performance parameters are dependent on both the fan geometric scale ratio (fan size), Λ, and the fan speed ratio, Ω_m/Ω_p.

As a result of these fundamental difference between the GFSL and CFSL approaches, the fan scaling laws obtained from each of these approaches are quite different. Moreover, they lead to different model fan design criteria and different model fan test conditions. There is however one exception to the above statement: if the fan

speed ratio in the CFSL approach is chosen in such a way that makes the model to prototype Reynolds number the same (i.e., satisfying the constraint given by Eq. 2.17), then and only then can these two different types of fan scaling approaches concur with each other.

3.3 A critical analysis of the CFSL approach to fan design

In the CFSL approach, the fan size ratio and the fan speed ratio can be selected arbitrarily. The arbitrary choice of the fan size and fan speed ratios results in different scaling criteria for the dependent model fan performance parameters such as fan pressure rise, volume flow rate, fan input power, and required fan torque. The arbitrary choice of the fan size and fan speed ratios also affects the Reynolds number matching between the model and prototype. Table 3.3 shows the effect of the different fan speed ratios for a given fan size ratio on the scaling of the major fan performance parameters. Table 3.3 is not an exhaustive list of all the possible variation of fan speed ratio, but rather those fan speed ratios are selected that correspond to the following criteria for a homologous fan series:

1. *Fans designed for constant speed;* $\Omega_m/\Omega_p = 1$
2. *Fans designed for constant pressure rise;* $\Delta p_m/\Delta p_p = 1$
3. *Fans designed for constant input power;* $K_m/K_p = 1$
4. *Fans designed for constant torque;* $T_m/T_p = 1$
5. *Fans designed for constant volume flow rate;* $Q_m/Q_p = 1$
6. *Fans designed for constant Reynolds number;* $Re_m/Re_p = 1$

A close study of Table 3.3 indicates that the application of the CFSL approach to fan design using an additional criterion that maintains Reynolds number similarity

$\frac{\Omega_m}{\Omega_p}$	**1**	1/3	4/25	1/9	5/78	1/27
$\frac{Q_m}{Q_p} = (\frac{\Omega_m}{\Omega_p})(\Lambda)^3$	27	9	4 17/52	3	1 41/56	**1**
$\frac{\Delta p_m}{\Delta p_p} = (\frac{\Omega_m}{\Omega_p})^2(\Lambda)^2$	9	**1**	3/13	1/9	1/27	1/81
$\frac{K_m}{K_p} = (\frac{\Omega_m}{\Omega_p})^3(\Lambda)^5$	243	9	**1**	1/3	5/27	1/81
$\frac{T_m}{T_p} = (\frac{\Omega_m}{\Omega_p})^2(\Lambda)^5$	243	27	6 6/25	3	**1**	1/3
$\frac{Re_m}{Re_p} = (\frac{\Omega_m}{\Omega_p})(\Lambda)^2$	9	3	1 23/25	**1**	56/97	1/3

Table 3.3: CFSL approach; Parametric analysis to study the effect of fan speed ratio on the fan scaling laws for a geometric scale ratio of $\Lambda = 3$

for the same fan size ratio gives identical results to those obtained using the GFSL approach. Table 3.3 also shows clearly that most of the choices of fan speed ratio can satisfy all fan design criteria *except* Reynolds number similarity. These choices, however, violate the requirement of full dynamic similarity.

Obviously the different fan design criteria based on the CFSL approach show varying degrees of deviation from the condition of full dynamic similarity, depending on their sensitivity to the Reynolds number. Deviation from the conditions required for full dynamic similarity (i.e., Reynolds number, Strouhal number and Euler number similarity) can, however, result in major differences in the way pertinent fan performance parameters scale between model and prototype. For example using Table 3.3, compare the fan scaling laws resulting from fan design based on constant pressure to the fan scaling laws obtained while keeping the Reynolds number constant. Under the same fan size ratio, the power input requirement for constant pressure fan design is *twelve* times higher than that required for a constant Reynolds number fan design, while the comparison of the pressure indicates a 9:1 ratio, the comparison of fan speed and Reynolds number show 1:3 and 3:1 ratios respectively. Also note that the relative difference between the Reynolds number obtained from a model fan designed with constant fan speed and a fan designed with constant Reynolds number is *nine* times, an order of magnitude difference!

For the design and evaluation of small low Mach number fans, application of the CFSL approach can lead to large discrepancies in Reynolds number between the model and prototype fans. These can result in large differences in the viscous losses and thus cause differences in the performance characteristics of the model and prototype. They can also cause a significant loss of accuracy in model fan performance prediction. Thus it is highly recommended that the GFSL approach be used to avoid such situations.

3.4 Application of the GFSL approach to fan design

The GFSL approach was used to design a three times scale model, the LSB fan, of an automotive HVAC fan, the prototype. The fundamental parameters and ratios for the GFSL approaches are shown in Table 3.4. Since the model LSB fan and the prototype HVAC fan both operate in air at approximately the same temperature, the kinematic viscosity and density ratios are assumed to be equal to one.

The geometric scale of the model (LSB) fan was chosen to be three times to that of the prototype. A three times scale model size was chosen since it served as a best compromise between the size of the test facility and the ability to accurately measure very low pressures at the exit of the fan. The model fan torque and motor power values were derived using the additional similarity scaling law based on the fact that input fan power is related to the fan shaft speed and characteristic fan diameter (see Eq. 2.86).

Table 3.4 highlights the CFSL and GFSL scaling relations for a three-to-one model fan. The table shows clearly that once the fan size ratio is fixed, the GFSL approach indicates that *all* the fan performance parameters are also fixed (since they all scale with only the geometric scale ratio). By contrast, in the CFSL approach, all fan scaling parameters depend also on the choice of the fan speed ratio.

Table 3.4 shows that for a three-to-one scale model, the power required at the model fan shaft is much lower than for the prototype. It can also be observed from above scaling laws (Eqs. 2.29 to 2.34), that a model fan operating in air, under full dynamic similarity conditions, with a geometric scale ratio of 3, requires a *reduction of the fan speed by nine times.* Flow velocities, on the other hand, are only reduced by 3 times compared to those in the prototype HVAC fan. This is nonetheless a considerable reduction in flow velocity, and together with the increased spatial scales, allows

GFSL	CFSL
$\frac{U_m}{U_p} = \frac{1}{3}$	$\frac{U_m}{U_p} = 3\frac{\Omega_m}{\Omega_p}$
$\frac{\Delta p_m}{\Delta p_p} = \frac{1}{9}$	$\frac{\Delta p_m}{\Delta p_p} = 9(\frac{\Omega_m}{\Omega_p})^2$
$\frac{K_m}{K_p} = \frac{1}{3}$	$\frac{K_m}{K_p} = 243(\frac{\Omega_m}{\Omega_p})^3$
$\frac{T_m}{T_p} = 3$	$\frac{T_m}{T_p} = 243(\frac{\Omega_m}{\Omega_p})^2$
$\frac{Q_m}{Q_p} = 3$	$\frac{Q_m}{Q_p} = 27(\frac{\Omega_m}{\Omega_p})$

Table 3.4: Comparison of GFSL and CFSL for $\Lambda = 3$

proper flow measurement to be conducted. Pressure coefficient similarity indicates that the model to prototype ratio is nine times smaller for the large scale model fan. Also, notice that the torque ratio scales as a function of the geometric scale ratio: the larger fan requires a larger torque input under the conditions of dynamic similarity. Similarly, the fan capacity ratio scales as a function of the geometric scale ratio (or fan size ratio); in particular, the larger fan produces a larger volume flow rate under conditions of dynamic similarity.

A small scale version (1/3 scale model) of the LSB fan, the Mini-LSB fan, was designed using the GFSL approach. The reasons for designing the Mini-LSB are provided later in chapter 5. Table 3.5 shows the scaling for the Mini-LSB fan based on $\Lambda = 1/3$.

Similarity parameter	Scaling law
$Re_m = Re_p$	$\frac{U_m}{U_p} = 3$
$Str_m = Str_p$	$\frac{\Omega_m}{\Omega_p} = 9$
$Eu_m = Eu_p$	$\frac{\Delta p_m}{\Delta p_p} = 9$
$\lambda_m = \lambda_p$	$\frac{K_m}{K_p} = 3$
$\gamma_m = \gamma_p$	$\frac{T_m}{T_p} = \frac{1}{3}$
$\frac{Q_m}{Q_p}$	$\frac{Q_m}{Q_p} = \frac{1}{3}$

Table 3.5: Mini-LSB fan design; GFSL for $\Lambda = 1/3$

3.5 Application of GFSL and CFSL approaches to fan performance prediction under variable fan speed conditions

The preceding applications of both the GFSL and the CFSL approaches consider only a change in fan size. The two fan scaling approaches can also be contrasted when the fan size is fixed but the fan speed is varied. Table 3.6 illustrates the application of both CFSL and GFSL approaches to the fan for which $\Lambda = 1$ and where fan speed ratio is variable.

From Table 3.6, it is clearly evident that in the case of the GFSL the constraints on the fluid velocity ratio due to the Reynolds number and Strouhal number similarity

GFSL ($Re \neq$ constant)	CFSL
$\frac{U_1}{U_2} = (\frac{L_2}{L_1}) = 1$	
$\frac{U_1}{U_2} = (\frac{\Omega_1}{\Omega_2})$	$\frac{U_1}{U_2} = (\frac{\Omega_1}{\Omega_2})$
$\frac{\Delta p_1}{\Delta p_2} = (\frac{\Omega_1}{\Omega_2})^2$	$\frac{\Delta p_1}{\Delta p_2} = (\frac{\Omega_1}{\Omega_2})^2$
$\frac{K_1}{K_2} = (\frac{\Omega_1}{\Omega_2})^3$	$\frac{K_1}{K_2} = (\frac{\Omega_1}{\Omega_2})^3$
$\frac{T_1}{T_2} = (\frac{\Omega_1}{\Omega_2})^2$	$\frac{T_1}{T_2} = (\frac{\Omega_1}{\Omega_2})^2$
$\frac{Q_1}{Q_2} = (\frac{\Omega_1}{\Omega_2})$	$\frac{Q_1}{Q_2} = (\frac{\Omega_1}{\Omega_2})$

Table 3.6: Comparison of GFSL and CFSL for the same fan ($\Lambda = 1$) with variable speed, Ω.

cannot be simultaneously satisfied. For $\Lambda = 1$, Reynolds number similarity requires:

$$\frac{U_1}{U_2} = \frac{1}{\Lambda} = 1 \tag{3.1}$$

But Strouhal number similarity requires (for $\Lambda = 1$):

$$\frac{U_1}{U_2} = \frac{\Omega_1}{\Omega_2} \tag{3.2}$$

From these two constraints on the fluid velocity ratio, it is obvious that the Reynolds number similarity constraint cannot be satisfied under the given set of test conditions; i.e., $\Lambda = 1$ and $\Omega =$ variable.

Since the Strouhal number similarity constraint can be satisfied if the Reynolds number constraint is ignored, it has become the leading constraint for the fan scaling laws in the CFSL approach. Thus full dynamic similarity cannot be maintained between different fan operating points for the same fan in the CFSL approach. If extreme speed ranges are encountered during fan operation; this can lead to large variations in Reynolds number which may require corrections to be made to the classical fan laws. Typical methods of corrections to fan laws due to Reynolds number effects have been proposed by many authors, ([12], [68], [43], and [60]). These are, of course, unnecessary when the GFSL approach is used.

3.6 Application of fan laws to test an automotive HVAC prototype fan module in water

The GFSL approach to fan design as given in Table 3.1 assumed constant viscosity and density ratios between model and prototype. These restrictions can be relaxed, however, and the scaling relations can be re-derived to incorporate viscosity and density effects for application to model fans operated under different flow mediums.

Viscosity	$\frac{\nu_m}{\nu_p} = \tilde{\nu}$
Density	$\frac{\rho_m}{\rho_p} = \tilde{\rho}$
Length	$\frac{L_m}{L_p} = \Lambda$
$Re_m = Re_p$	$\frac{U_m}{U_p} = \frac{\tilde{\nu}}{\Lambda}$
$Str_m = Str_p$	$\frac{\Omega_m}{\Omega_p} = \frac{\tilde{\nu}}{\Lambda^2}$
$Eu_m = Eu_p$	$\frac{\Delta p_m}{\Delta p_p} = \tilde{\rho}\frac{\tilde{\nu}^2}{\Lambda^2}$
$\lambda_m = \lambda_p$	$\frac{K_m}{K_p} = \tilde{\rho}\frac{\tilde{\nu}^3}{\Lambda^2}$
$\gamma_m = \gamma_p$	$\frac{T_m}{T_p} = \tilde{\rho}\frac{\tilde{\nu}^2}{\Lambda}$
$\frac{Q_m}{Q_p}$	$\frac{Q_m}{Q_p} = \tilde{\nu}\Lambda$

Table 3.7: GFSL approach to fan design; that includes the effect of variable viscosity and density ratios between model and prototype

The application of GFSL to fan design that includes the effect of variable viscosity ratios, $\tilde{\nu}$, and variable density ratios, $\tilde{\rho}$, are given in Table 3.7.

Equation 2.11 demonstrates that there are three fundamental non-dimensional parameters which are relevant to ensure full dynamic similarity (which includes geometric similarity and kinematic similarity): the Strouhal, Reynolds and Euler numbers. In HVAC systems the pressure rise across the fan impeller under external load (i.e., back pressure due to system resistance) is one of the most important aerodynamic fan performance parameters, since it characterizes the resulting back pressure in a flow system in comparison to the dynamic pressure (mean kinetic energy of the flow) produced by the turbomachine. The Euler number is also indicative of the system resistance (i.e., losses in the system for turbulent flow). Subsequently the interaction of the system resistance with the fan performance curve sets the operating point of the fan. Thus in addition to Reynolds and Strouhal number similarity, Euler number similarity also becomes a significant parameter, in establishing HVAC fan performance.

Consider an automotive HVAC module that is to be operated in air, the prototype, and the exact same HVAC prototype fan running in water, called the model. Reynolds number similarity requires:

$$\frac{U_m L_m}{\nu_m} = \frac{U_p L_p}{\nu_p} \tag{3.3}$$

So the characteristic velocity ratio derived from Eq. 3.3 is:

$$\frac{U_m}{U_p} = (\frac{\nu_m}{\nu_p})(\frac{L_p}{L_m}) \tag{3.4}$$

Strouhal number similarity requires:

$$\Rightarrow \frac{\Omega_m L_m}{U_m} = \frac{\Omega_p L_p}{U_p} \tag{3.5}$$

It follows from Eqs. 3.3 and 3.4 that the ratio of model to prototype fan speed ratio is:

$$\frac{\Omega_m}{\Omega_p} = (\frac{U_m}{U_p})(\frac{L_p}{L_m}) \tag{3.6}$$

Combining Eqs. 3.4 and 3.6, equation 3.6 can be expressed as:

$$\frac{\Omega_m}{\Omega_p} = (\frac{\nu_m}{\nu_p})(\frac{L_p}{L_m})^2 \tag{3.7}$$

Finally Euler number similarity establishes the ratio of pressure differences between the model and prototype HVAC fan modules. Thus,

$$\frac{\Delta p_m}{\rho_m U_m^2} = \frac{\Delta p_p}{\rho_p U_p^2} \tag{3.8}$$

Using Eq. 3.4, Eq. 3.8 can be expressed as follows

$$\frac{\Delta p_m}{\Delta p_p} = (\frac{\rho_m}{\rho_p})(\frac{\nu_m}{\nu_p})^2(\frac{L_p}{L_m})^2 \tag{3.9}$$

The fan power and torque ratios can similarly be derived in terms of the geometric scale and density ratios between model and prototype. The power ratio is given by:

$$\frac{K_m}{K_p} = (\frac{\rho_m}{\rho_p})(\frac{\nu_m}{\nu_p})^3(\frac{L_p}{L_m}) \tag{3.10}$$

and, the torque ratio by:

$$\frac{T_m}{T_p} = (\frac{\rho_m}{\rho_p})(\frac{\nu_m}{\nu_p})^2(\frac{L_p}{L_m}) \tag{3.11}$$

Using water as the medium for model testing, the scaling laws indicate that a 1-to-1 scale model will be sufficient to achieve the proper low speed (less than 1 m/s) for flow visualization techniques. This reduction in the flow velocity is essential in order to use dye injection technique in the experiments described later in chapter 4.

Further, a fifteen times reduction in the flow velocity in the model fan implies that the model fan speed and the flow rate both are reduced by a factor of fifteen. In addition, Reynolds number similarity implies Euler number similarity. Euler number similarity indicates a pressure ratio between scale model fan and prototype fan of approximately 3.7. The system resistance for the model fan scales with the Euler number based on the resistance component; i.e, the evaporator core. Hence, an added

advantage of selecting a 1-to-1 scale model fan system is that the original evaporator core can itself be used as the system resistance for the model fan tests.

The application of the fluid dynamic scaling laws to the model fan *insures* that the actual flow is realized at the prototype operating conditions using the actual fan module. Therefore, in this case *the actual fan can be used as the model fan, but operating in water at dynamically similar conditions so it exactly simulates the actual prototype fan operating conditions.*

The model (and in this case the prototype as well) HVAC fan operating conditions for complete dynamic similarity in water (using Eqs. 2.29 to 2.34) are given as follows:

For

$$\frac{L_m}{L_p} = \frac{L_{water}}{L_{air}} = 1 \tag{3.12}$$

the velocity, fan speed and pressure ratio, respectively become:

$$\frac{U_m}{U_p} = (\frac{\nu_m}{\nu_p})(\frac{L_p}{L_m}) = (\frac{\nu_{water}}{\nu_{air}}) \approx \frac{1}{15} \tag{3.13}$$

$$\frac{\Omega_m}{\Omega_p} = (\frac{\nu_m}{\nu_p})(\frac{L_p}{L_m})^2 = (\frac{\nu_{water}}{\nu_{air}}) \approx \frac{1}{15} \tag{3.14}$$

$$\frac{\Delta p_m}{\Delta p_p} = (\frac{\rho_m}{\rho_p})(\frac{\nu_m}{\nu_p})^2(\frac{L_p}{L_m})^2 = (\frac{\rho_{water}}{\rho_{air}})(\frac{\nu_{water}}{\nu_{air}})^2 \approx 3.7 \tag{3.15}$$

The HVAC model, fan torque and motor power values are derived using the additional similarity scaling law based on the fact that input fan power are related to the fan shaft speed and characteristic fan diameter. Under full dynamic similarity conditions between the model and the prototype, the fan power coefficient, λ, (Eq. 2.32) must also be constant.

Under the given experimental constraints of a geometric scale ratio of unity and, a model fan that operates in water and a prototype fan that runs in air, the torque

ratio (i.e., Eq. 3.11) becomes:

$$\frac{T_{water}}{T_{air}} = (\frac{\rho_{water}}{\rho_{air}})(\frac{\nu_{water}}{\nu_{air}})^2 \approx 3.7 \tag{3.16}$$

Notice that the torque required to the turn the fan in water compared to that in air is much higher.

From Eq. 3.10 the estimate for the fan input power ratio between the model and prototype HVAC fans can be obtained as:

$$\frac{K_{water}}{K_{air}} = (\frac{\rho_{water}}{\rho_{air}})(\frac{\nu_{water}}{\nu_{air}})^3 \approx 0.25 \tag{3.17}$$

Notice that for a one to one scale model, the power required at the fan shaft when operating in water is much lower than for that in air, even though the required fan torque is much higher.

Table 3.8 summarizes the application of fully viscous GFSL approach to an HVAC fan for the 3 : 1 model considered earlier, but operated instead in water. Note that although the scale change is only 3, the reduction in velocity is 45, and in fan speed 135! Obviously these can create considerable opportunities for the experimentalist to visualize and measure the flow, and perhaps even be the difference between success and failure of a measurement program. Moreover, if the above scaling relations are adhered to, even accurate predictions of the air values for torque, power, etc. can be made from measurements taken in water. This can be used to great advantage in testing, since the order of magnitude differences make some measurements easier and more accurate in water, while others are better made in air.

$\Lambda = 1$	$\Lambda = 3$
$\frac{U_m}{U_p} = \frac{1}{15}$	$\frac{U_m}{U_p} = \frac{1}{45}$
$\frac{\Omega_m}{\Omega_p} = \frac{1}{15}$	$\frac{\Omega_m}{\Omega_p} = \frac{1}{135}$
$\frac{\Delta p_1}{\Delta p_2} = 3.7$	$\frac{\Delta p_1}{\Delta p_2} = 0.41$
$\frac{K_1}{K_2} = 0.25$	$\frac{K_1}{K_2} = 0.028$
$\frac{T_1}{T_2} = 3.7$	$\frac{T_1}{T_2} = 1.23$
$\frac{Q_1}{Q_2} = \frac{1}{15}$	$\frac{Q_1}{Q_2} = \frac{3}{15}$

Table 3.8: Application of GFSL to establish fan test conditions for a 1:1 and a 1:3 scale model fan operated in water

Chapter 4

Flow visualization study of an HVAC fan module

4.1 Introduction

An automotive HVAC system (see Fig. 4.1) is comprised of many components each of which may produce a strong flow coupling between the component itself and the HVAC fan impeller affecting the performance of the fan and the efficiency of the module. This inter-component flow coupling phenomena can also affect the flow induced noise characteristics of the whole HVAC system. These characteristics could be either linked to low frequency noise, (for example, blower rumble, rotating stall, noise due to recirculating flow and noise due to low frequency vortex shedding), or high frequency noise (for example, the interaction between the blade passage and the scroll cut-off or high speed shear layers, perhaps in a diffuser with very small length to inlet width ratio. The flow field studies described later using both the hot-wire and LDA measurement techniques conducted on both actual HVAC modules and on the Large Scale Blower facility (LSB) have indicated that the flow is highly complex at the exit of the fan. Also significant changes occur in the flow field both in terms of the

Figure 4.1: HVAC fan module used for flow visualization study in water

mean velocity and the turbulence levels with changes in the system resistance. The hot-wire velocity measurements conducted at the fan throat of an HVAC fan module (**??**) have shown the existence of a strong jet of flow entering the diffuser. Further, measurements conducted just upstream of the evaporator core clearly show that the flow impinges on the evaporator as a confined jet. However the measurements seem to also indicate that the flow diffuses significantly across the evaporator giving a more uniform flow pattern downstream of the evaporator. Two-point velocity coherence measurements (see Chapter 8) conducted inside the actual automotive HVAC fan module using hot-wires, both across the fan blades and at the fan throat exit region, have clearly indicated both a frequency shift in the low frequency end of the energy spectrum and a change in the magnitude (level) of the energy spectrum with the changes in system resistance.

Considering all the available experimental evidence on typical automotive HVAC and model test facilities, it can be concluded that significant changes occur in the flow

field through the HVAC module when the system resistance changes (for example, from AC full cold mode to heater full hot mode of fan operation). How these changes occur, however, what are their causes and what are the flow coupling mechanisms still remain unanswered.

Even with the available experimental data it is still not clear what is the main source of blower rumble. Certain theories have been presented for what is thought to be the main flow induced mechanism responsible for blower rumble, namely the flow coupling between the fan inlet flow and the fan impeller, the fan impeller and the fan cut-off[1], and the flow coupling between the fan cut-off and the diffuser. In order to obtain a better understanding of what the actual flow is doing under these different fan-operating modes and fan speeds, detailed flow visualization studies were conducted on the HVAC module.

4.2 Previous experimental results on centrifugal fan and HVAC fan modules

Actual HVAC fan inlet and exit flow patterns are highly complex. Previous studies using tufts (see Chapter 7), smoke visualization [**?**] and [36], LDA [32] and [**?**] and hot-wire data [**?**], [**?**] and (see Chapter 7) at the fan exit (near the fan cut-off) indicate a very high turbulence intensity ($\sim$50%) and a large degree of swirl (indicative of complex vortical flow patterns). It is also known qualitatively that a flow recirculation occurs at the fan inlet. The literature on centrifugal fans also indicates that a large recirculation occurs at fan exit and near the cut-off region. Hot-wire data from actual HVAC modules indicate that a jet flow type of flow pattern occurs in the diffuser section (see Fig. 4.2). This is contrary to the conventional wisdom that the diffuser

[1](n.b. the literature survey on centrifugal fans (see Appendix A) indicates that this mechanism is mainly responsible for blade passage noise)

Figure 4.2: Jet flow pattern at the exit of a fan upstream of evaporator

does not separate due to high pressure drops across the evaporator. This conventional view is clearly wrong! Worse this separation and resulting jet-like flow in the diffuser causes a deterioration of other components. Moreover, all of this unsteady complex flow is related to the aerodynamic noise generated by the fan.

As shown below, a flow visualization study of the flow pattern in the diffuser/fan region reveals important information about what the flow actually does and what types of flow structures exist. The flow visualization study uses water instead of air as the flow medium, but also uses an actual scale HVAC module. The application of the fluid dynamic scaling laws (that is, Reynolds and Strouhal number similarity) between the prototype fan and the scale model fan allows the characteristic flow velocity in the model fan to be reduced by 15 times of that of the prototype fan, since the kinematic viscosity of water is 15 times lower than that of air. it is this reduction in the flow speed alone which makes the visualization possible.

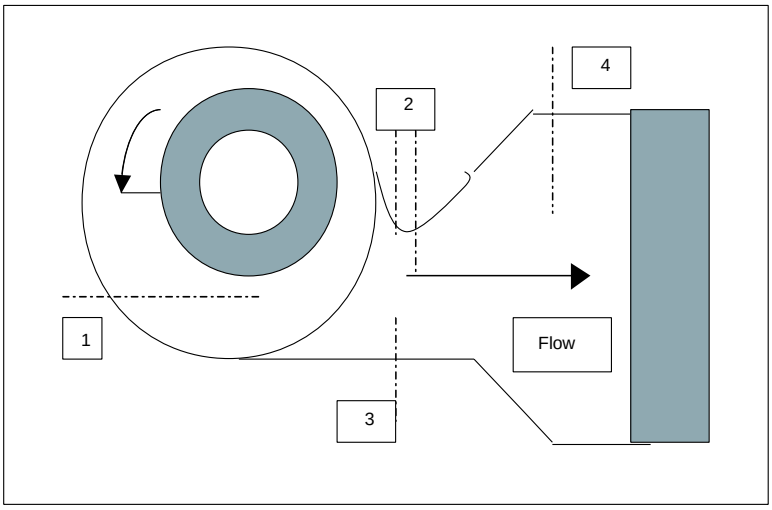

Figure 4.3: Locations used for Dye injection inside the HVAC

4.3 Aims and objectives

The main objective is to obtain global flow pattern information both around the fan throat and in the diffuser sections and detail information about localized and specific flow structures and their dynamics under various modes of fan operation. The flow visualization through the model fan was photographed and video taped enabling the study of the steady and unsteady flow phenomena. The new dye injection method used [**?**] (for turbulent flow visualization) reveals the flow streaklines, and reveals how the flow structures behave, and how their structure changes under different fan operating conditions.

Areas where dye injection have been applied are as follows: fan impeller exit, fan scroll wall boundary layer region, fan scroll cut-off, fan throat, diffuser and upstream of evaporator. These areas of dye injection inside the HVAC are shown in Fig. 4.3.

The study of flow patterns through the fan will be seen to reveal many different types of information; for example, regions of reversing flow, separated flow, shifts in the position of the separation bubbles at the fan throat, shear layers at the exit of

fan and along diffuser walls, and any unsteady flow phenomena (i.e., oscillatory and periodic vortex shedding, etc.). The jet "splash effect" (i.e., the separated jet flow from the fan throat impinging on the evaporator face) was also investigated, and may lead to possible improvements in HVAC component design.

4.4 Scaling Laws and Similarity Considerations

The scaling laws indicate that a 1 to 1 scale model will be sufficient for the proper application of low speed (less than 1m/s) flow visualization techniques when using water as the medium for model testing. This reduction in the flow velocity is essential in order to use the proposed flow visualization techniques of virtually any type. The reduction in flow speed arises from the constancy of the Reynolds number, UL/ν, since L is the same and the kinematic viscosity of water, ν, is one fifteenth that of water. The application of the generalized fan scaling laws (GFSL) to HVAC fans for the purpose of comparing model and prototype testing between and air/water systems was established in Section 3.6. Further, a fifteen times reduction in the flow velocity in the model fan implies that the model fan speed and the flow rate are reduced by a factor of fifteen.

In addition, Reynolds number similarity (for fixed Strouhal number) implies Euler number similarity. The fan scaling results derived in Section 3.6 show that Euler number similarity indicates a pressure ratio between scale model fan and prototype fan of approximately 3.7. The system resistance for the model fan scales with the Euler number based on the resistance component, in this case, the evaporator core. Thus, another advantage of selecting a 1 to 1 scale model fan system is that *the original evaporator core can itself be used as the system resistance for the model fan tests.* The application of the fluid dynamic scaling laws to the model fan has insured that the actual flow is realized at the prototype operating conditions using the actual fan

module, even though it is operating in water instead of air. *Therefore, the actual fan can be used as the model fan in water at dynamically similar conditions,* thus insuring that the model exactly simulates the actual prototype fan operating conditions.

4.5 Design and fabrication of the water tank experimental test facility

An experimental test facility was designed and fabricated to allow proper flow visualization and house the HVAC module. The model fan (the actual fan module in this case), and in fact the entire HVAC assembly, was placed in a large lexan tank (volume of about 400 gallons). That motor was coupled via a gear reduction of 15 times to achieve the correct model fan speed (see Fig. 4.4). The geometric dimensions of the 400 gallon tank were $6ft \times 3ft \times 3ft$. The test HVAC model had maximum dimensions of $1.3ft \times 1ft \times 1ft$. The tank size selected was sufficiently large to avoid any flow coupling between the inlet flow and exit flow from the model fan. This was confirmed using conventional dye and tufts inside the tank to study the pattern in the external flow (outside of the model fan along the return flow). The actual quantity of water used in the tank was approximately 360 gallons.

It was shown from the fan scaling laws (from Eqs. 3.12 to 3.10), that full dynamic similarity is achieved for a one-to-one scale ratio between the model (operating in water) and prototype (operating in air) the fan, if the model fan speed is reduced by 15 times to that of the prototype. The model fan speed reduction was achieved through a reduction gear (worm type) acting with a horizontal input and vertical output. The speed reduction gear was coupled to a dc. motor (1/4 hp. and 3600 Rpm max.) which ran of a variable dc. power supply (30 V and 20 amp max.). The speed of the fan was determined by using a stroboscope on the motor output shaft

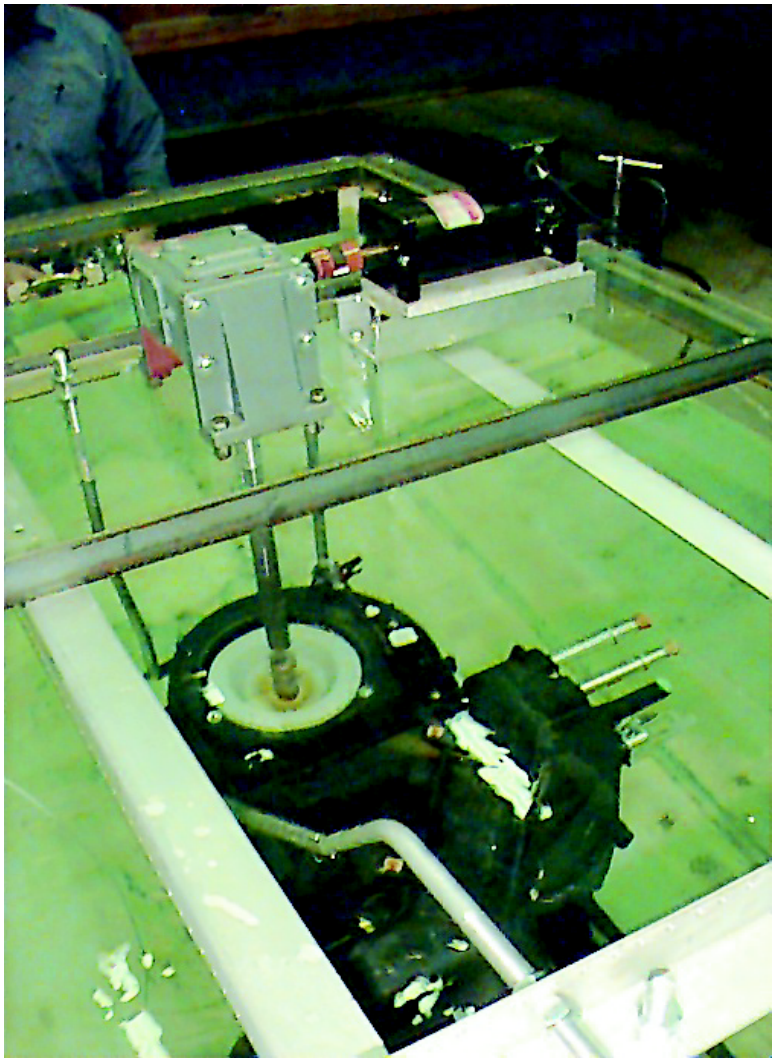

Figure 4.4: The actual test facility used for flow visualization experiments

(i.e., input to the reduction gear).

The fan speed was altered by varying the input voltage and letting the current draw be set by the fan /system coupling itself, which served as an indicator for system resistance. The fan speed was monitored by a stroboscope. Notice that the fan speed can be reduced independent of the system resistance (back-pressure) using this method of fan testing.

The water tank was fabricated using clear lexan sheet material, with tank walls of $\frac{1}{2}$ inch thickness and a tank floor of 1-in. thick clear lexan. The tank wall was fastened with screws and was made water-tight using silicon sealant at all the wall junctions to prevent leakage. The tank walls were braced (supported) using steel plates in order to distribute the load along the walls due to the water pressure. A steel frame was made for the tank in order to provide extra support at the corners and sides. This also allowed for ease of transportation of the tank.

The model fan was submerged under water, such that the inlet of the fan was at a depth of 18 inches under the water surface. In addition, the model fan was placed in the center of the tank width-wise; but lengthwise the fan was positioned at 26 in. from one of the end walls, so that there is sufficient space available for the exit flow to diffuse before returning to the fan inlet side. The size of the tank was large enough to ensure that the exit flow from the evaporator is decoupled from the flow at the fan inlet. This was verified by using both tufts and conventional dye to observe the return flow pattern along the exterior of the HVAC model fan. Both the flow visualization techniques confirmed that the flow entering the fan inlet orifice was similar to a potential flow pattern that is analogous to the flow pattern at the inlet of a suction duct from an infinite environment (for example the flow into the Borda's mouthpiece Batchelor [6]).

The actual HVAC module was modified to allow for the application of the visualization techniques by replacement of key sections of the module casing with clear

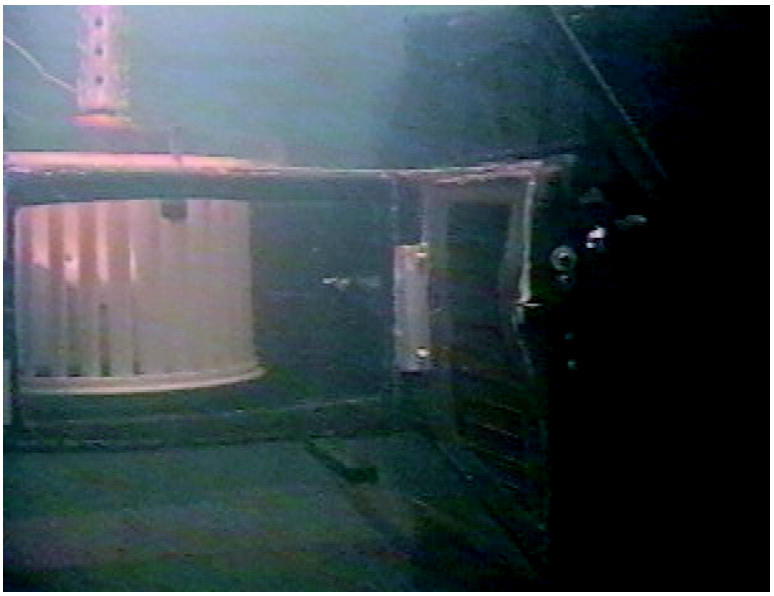

Figure 4.5: Location for the flow visualization windows on the HVAC module: Side view

lexan panels (with a thickness of 1/16 inch). Regions of the fan scroll, and the diffuser walls were cut out and the lexan put in its place, as shown in Figs. 4.5 and 4.6 .

The HVAC model was completely submerged inside the water tank and was held in place by four aluminum threaded rods connected to the top plate which was placed on top of the steel frame around the tank, (Fig. 4.7). The dc. motor and reduction gear was rigidly connected to the top Plexiglass plates. The fan shaft was properly aligned and connected to the output of the reduction gear via two concentric aluminum shafts. The fan shaft was press fitted to the fan impeller and secured by an additional set-screw.

It is important that the model fan be rigidly supported inside the tank since the fan experiences angular torques and rectilinear motion in both the horizontal directions. This was achieved by proper fastening and supporting the fan model to the top Plexiglass plate via four struts. Fan casing vibration and oscillations can

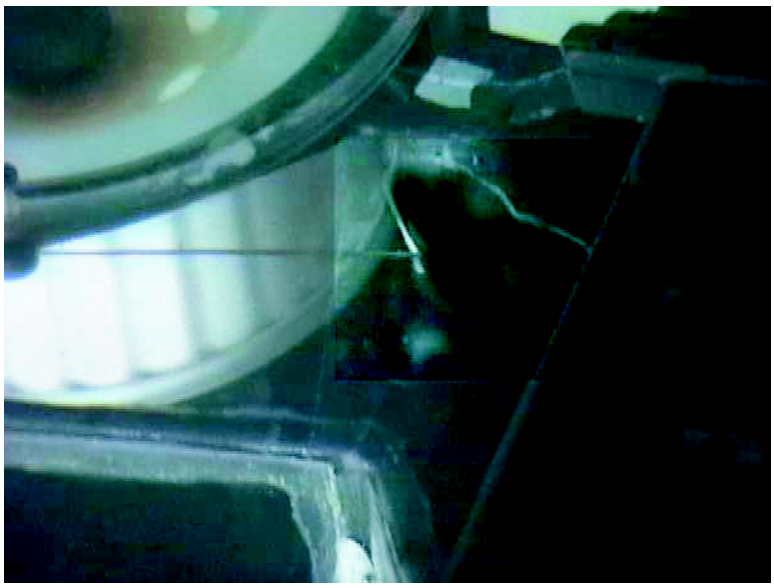

Figure 4.6: Location for the flow visualization windows on the HVAC module: Top view

cause interference with the fan's internal flow field. For example, pulsatile or unsteady oscillations in the flow field could cause flow features which are not attributable to the flow field generated by the HVAC fan when operating in an undisturbed environment.

4.6 Experimental Methodology

The technique used for the flow visualization through the HVAC module was the conventional dye injection method. This technique is relatively easy to apply and it is inexpensive, yet it has the capability of revealing important flow pattern and detailed flow structure information under various types of flow regimes.

The dye injection technique of flow visualization has the advantage of providing the localized flow field information, and when used with multiple injection techniques it can also reveal global flow pattern information. In addition, it can accurately determine flow direction in the case of a neutrally buoyant dye material. Conventional

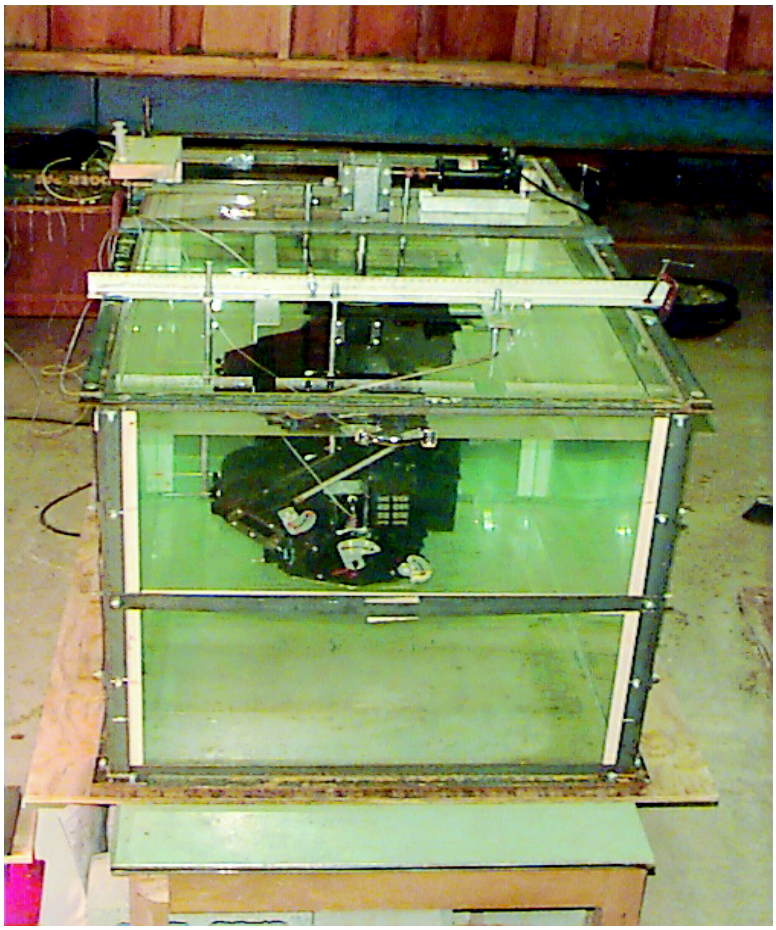

Figure 4.7: The water tank facility used for flow visualization inside an actual automotive HVAC module

dye injection is usually in a continuous mode, whereas special dye such as shear thickening dye can be produced in pulsed mode for visualization of steady and unsteady flow respectively. It is essential that the flow velocity has to be kept small (0.1 to 0.5 m/s) for proper flow visualization to be possible (Goldstein [31]).

The use of dye markers in a water tunnel is analogous to the use of smoke filaments in a wind tunnel. Flow visualization using direct injection of dye yields a streakline[2] The dye method has been used to study a very large number of two- and three-dimensional steady and unsteady flows (Werle [**?**]). The dye is injected through a hole in the surface or from the tip of a small hypodermic tube at a minimum possible relative velocity with respect to the flow velocity in the surrounding flow. The dye is typically injected using gravity-based feeding device. The critical parameters are the dye injection velocity and the density of the dye. Due to the high contrast between the colored dyes and the water flow, standard photographic techniques are sufficient to capture the detailed flow patterns. Both still and video mode photography is possible. For the flow conditions tested in the water tank experiment, video mode photography was more useful and appropriate than standard still photography using 35mm film.

In the present experiment both conventional and special dyes (i.e., shear thickening dyes Hoyt and Sellen [**?**]) were used for visualization of the internal flow. The flow features were made visible with the dye injection technique (see Appendix G using high intensity lighting, as described above. Video and still mode photography were used to record the flow features. Note a similar flow visualization technique was used by Hoyt and Sellin [**?**] to study the flow over tube banks. The results of their study showed rather unexpectedly the presence of a large bluff-body wake which was never visualized before. From their study, it was clear that the application of their technique

[2]A streakline is the locus of all fluid particles that have passed through a prescribed fixed point during a specified time interval (Goldstein [31]).

to HVAC flows (mostly unsteady) could reveal some unexpected and counter-intuitive flow characteristics that were not found or known before.

Four key areas inside the fan model were studied; they were:

- A. Fan blade exit
- B. Fan Scroll
- C. Fan cut-off
- D. Fan throat
- E. Diffuser and Upstream of evaporator core

These are shown in Fig. 4.3. The dye was injected using 1mm hypodermic needles at the locations shown in Fig. 4.3. With the conventional dye, different colors were used to highlight critical flow features such as flow swirl and vortices, and indicate flow direction and flow migration patterns inside the fan/scroll/diffuser. Manual dye injection was done using standard syringes (20-30 cc.), for the case of both the conventional dye and the shear thickening dye. In a few cases, however, a variable displacement pump was used to dispense the dye-streak flow at constant rate.

The dye injection was used for both the plan view and side view visualization video/photographs. In all cases the strobe lamps illumination was used from lamps (500-1500Watts) located outside the of the water tank. Two types of videos were used for most of the photography; they were: a standard Panasonic VHS camcorder and a professional Panasonic HVHS (with double resolution) video camera. Standard photography (35mm-film) and videos (mentioned above) documented all the flow visualization results. The video results proved to be much more useful in showing the progressive fluid motions, and in highlighting critical unsteady flow phenomena. They also showed the presence of remarkable 3-D flow patterns within the HVAC fan

module. From the videos, still images were captured using special frame grabbing software, which were digitized on a PC and placed on it in jpeg/tiff format. This method is far superior and more appropriate for still shots in unsteady flow using present-day technology, than the standard photography method.

4.7 Flow visualization results

One set of tests results was conducted by varying fan input voltage from 6 to 16 volts in steps of 2 volts, which resulted in the prototype equivalent fan speed variation from between 800 Rpm to about 3200 Rpm. The flow visualization results indicated that the local flow characteristics are strongly dependent on the fan speed. In particular, there is more recirculating flow around the fan impeller and at the cut-off region of the fan throat exit for low fan speeds (i.e., model $<$ 150 Rpm, which translates to prototype $<$ 2250 Rpm), compared to high fan speeds (model $>$ 150 Rpm) *at fixed downstream system resistance.* At the higher fan speed settings above (model $>$ 150 Rpm and prototype $<$ 2250 Rpm), the flow features were relatively insensitive to fan speed variation at fixed back pressure. (see Figs. 4.8 and 4.9)

4.7.1 Fan cut-off region

Fan cut-off region: unsteady vortical flow with flow reversal/recirculation was observed at adjacent to the cut-off at a height of 0.25H (where H is the fan throat height) from the bottom of the fan scroll and spanned an area of about 30% of the fan throat cross-sectional (see Figs. 4.10 to 4.12). The main characteristic of the flow near the cut-off is the fact that the flow reverses direction along the cut-off wall (before entering the diffuser), and flows back into the scroll area, that is, between the cut-off and the fan impeller. This has two major effects:

- First, the fan throat is partially "blocked" due to the separation region. This

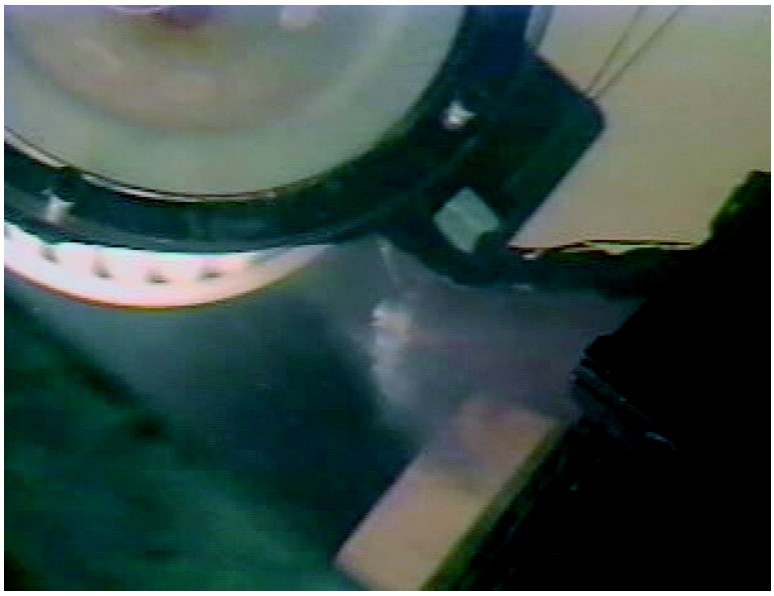

Figure 4.8: Fan throat region: 0.25H, fan operating at (8 volts and 1200 Rpm)

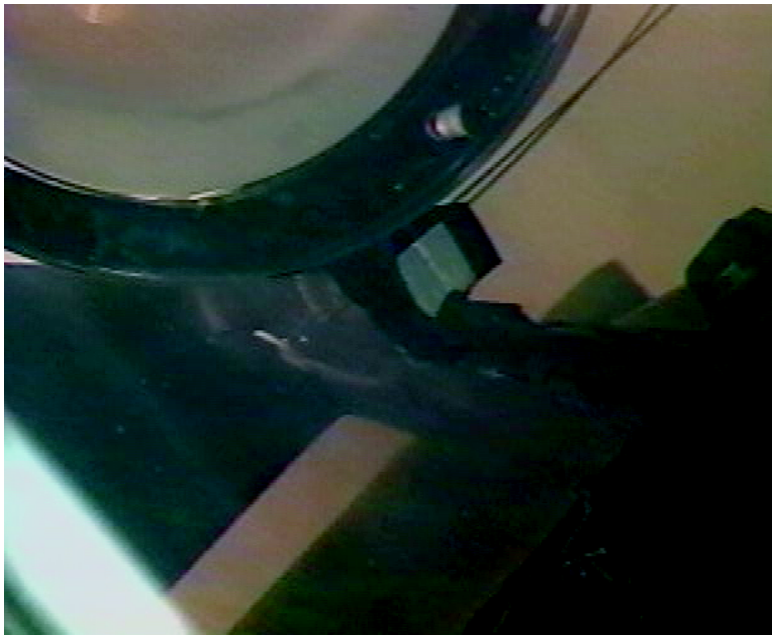

Figure 4.9: fan throat region: 0.25H, fan operating at (14 volts and 2200 Rpm)

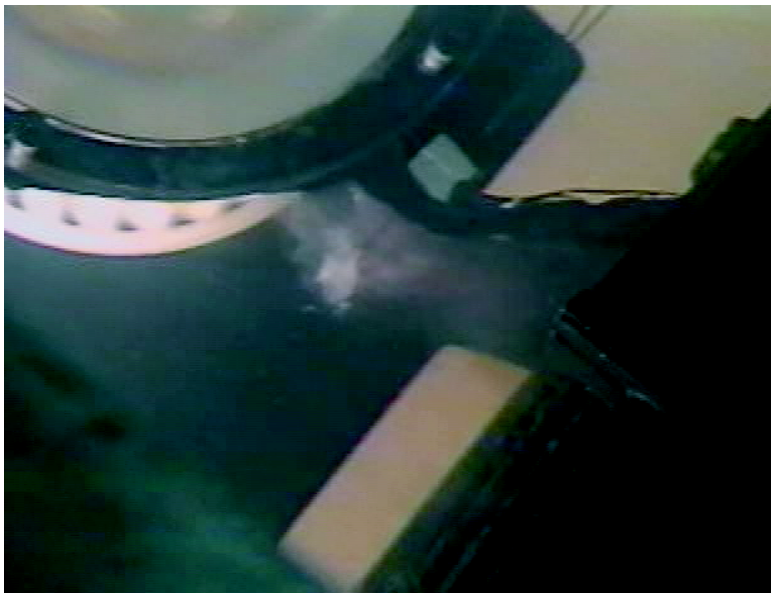

Figure 4.10: Fan cut-off region at 0.25

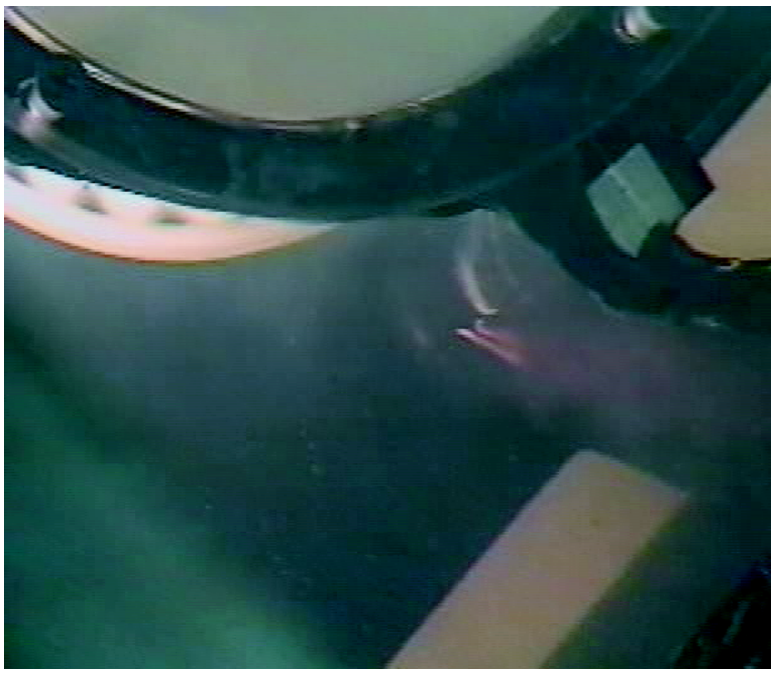

Figure 4.11: Fan cut-off region at 0.5H

Figure 4.12: Fan cut-off and diffuser inlet (cut-side) 0.25H

causes a decrease in the ability of the fan to produce higher flow coefficients, and in turn causes a loss (of static pressure) due to higher flow recirculation around the fan blade exit and scroll region instead of flowing into the diffuser and evaporator.

- Second, due to the unsteady flow pattern at the fan throat, the inlet flow to the diffuser becomes highly distorted and non-uniform causing inefficient diffuser performance.

It is well known (Kline [37]) that the velocity profile at the diffuser inlet has a major influence on the performance of 2-D channel/conical diffusers. The effects of turbulence, inlet boundary layer thickness, non-uniformity of the velocity profile also have major influences on the diffuser's ability to generate pressure recovery. This result was unexpected since previous studies using Hot-wires and LDA and Pitot

tubes indicated that the separation zone at the fan throat was more likely to occur at the top (or shroud) of the fan throat, and not at the bottom (hub region). Recall that Gessner [**?**] showed a highly loaded velocity profile at the bottom hub region at fan blade exit and a large velocity defect at the shroud side. It is to be noted, however, that the fan blade and fan cut-off geometries of the centrifugal fan previously studied were different than those of the present one.

Surprisingly, the flow remains relatively attached to the wall of diffuser downstream of the cut-off the fan cut-off at low fan speeds. A higher fan speeds on the same side-wall, the flow exhibits the famous transitory stall (detachment and reattachment). On the other hand, at the wall opposite the cut-off inside the diffuser, at lower fan speeds the flow remains attached to the diffuser wall. But at higher fan speeds the flow is completely detached, thus exhibiting a jet flow pattern similar to Kline's famous fully stalled diffusers that showed jet type of flow pattern for very high aspect and wide angle 2-D diffusers.

Flow directional information was obtained from the shear thickening dye tests at various fan speeds. The direction of the flow was observed by using the shear thickening dye which has a characteristic property of having extensional-viscosity and thereby forming long and stringy dye streaks which clearly indicate the flow direction even in highly turbulent and vortical flow conditions. It was possible to observe the flow direction beginning from the fan blade exit to the diffuser inlet, and sometimes till all the way to the of evaporator inlet region.

One of the important observation was that the major part of the scroll flow was skewed in the direction of fan rotation, towards the cut-off side wall and downstream of it. The skewness started all the way from the fan blade exit region and slightly upstream of it along the scroll (see Fig. 4.13) to the diffuser inlet. This also explains partially why the boundary layer near the diffuser wall opposite the fan cut-off is fully stalled at high fan speeds, mainly because the flow originates from that part of the

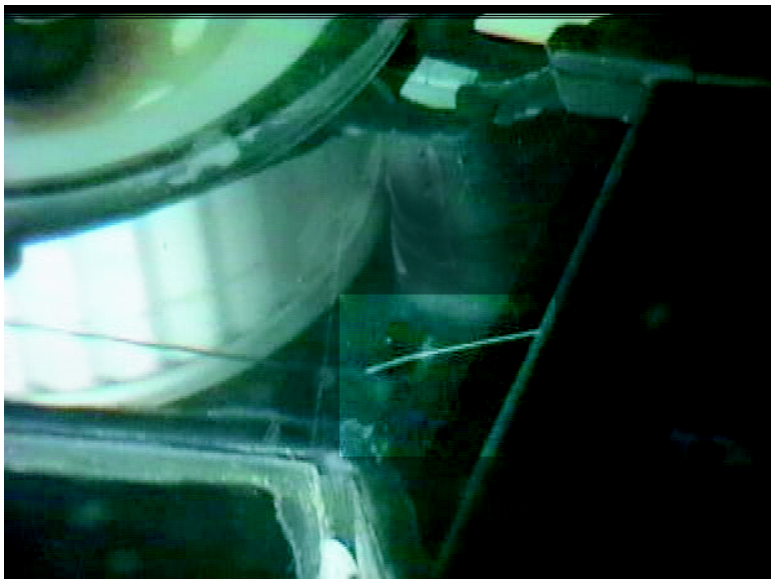

Figure 4.13: Fan throat and diffuser inlet region, (12 volts, 1800 Rpm)

scroll region, which has high momentum and is skewed away from the outer wall of the fan scroll. The resultant flow is similar to a skewed jet flow.

The video mode photography taken the fan throat region indicates that there is an unsteady almost pulsatile flow pattern, similar to the periodic vortex shedding from a cylinder. The frequency was not easy to determine using the shear thickening dye. The flow at the fan throat exit, especially at the higher fan speed settings, indicates a jet type flow pattern for bulk of the fan throat cross-section, with the occurrence of unsteady flow separation from the diffuser walls see Fig. 4.14.

Video mode photos taken at the diffuser and evaporator junction, showed an unsteady flow and highly recirculating flow pattern, which could be a strong candidate for the low frequency acoustic noise found in many automotive HVAC modules (see Figs. 4.15 and 4.16) .

At the top junction of the diffuser/evaporator flow, visualization results indicate that there was significant through flow which was was highly turbulent. At the bottom

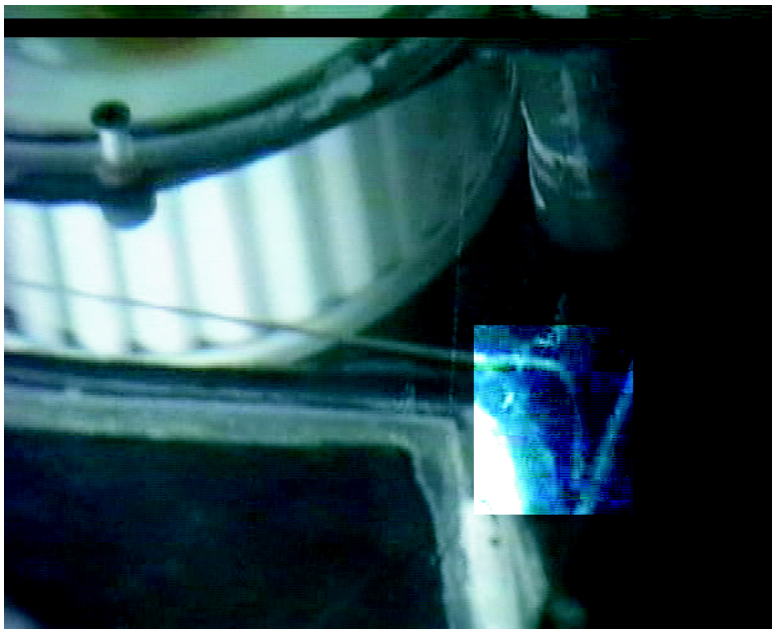

Figure 4.14: Diffuser inlet; opposite fan cut-off wall, (14 volts , 2200 Rpm)

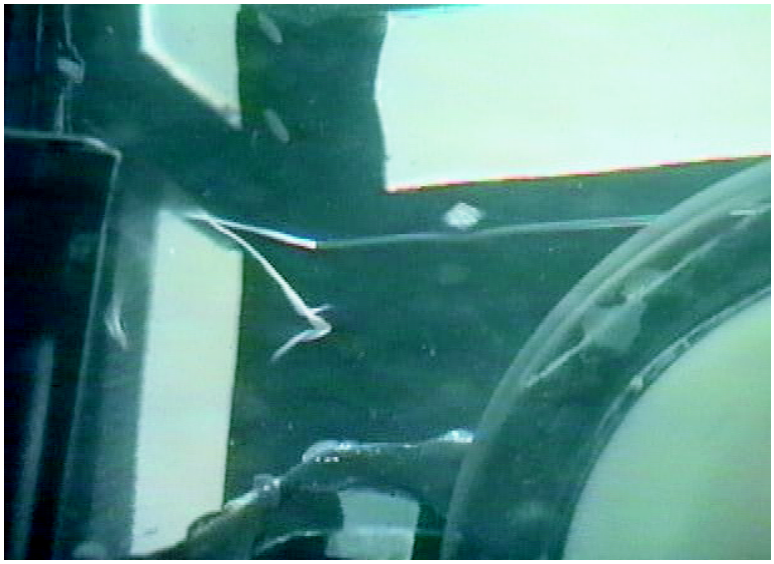

Figure 4.15: Diffuser inlet; opposite fan cut-off wall, (8 volts , 1200 Rpm)

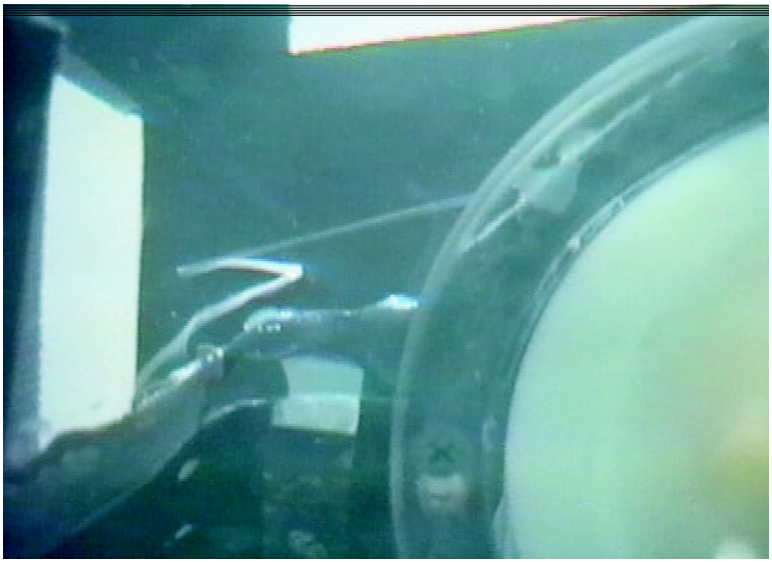

Figure 4.16: Diffuser inlet; opposite fan cut-off wall, (12 volts , 2000 Rpm)

junction, the flow was highly unsteady, and shows intermittently a "splash effect"; that is, part of the flow splits off and travels along the face of the evaporator and part of the flow enters the evaporator. This phenomena occurred at various fan speeds and at various intensities. (see Figs. 4.17 and 4.18) .

In general, the flow at the diffuser section was found to be highly turbulent, three dimensional in nature, and exhibited a considerable amount of recirculation in the side wall and bottom part of the diffuser. At the lower fan speed settings the flow reversal was more pronounced at the fan throat/diffuser inlet regions leading to back flow into the fan impeller/scroll cavity, and lower through flow into evaporator was observed. In comparison to the higher fan speed settings, there was very little back flow into the fan impeller/scroll cavity, but the flow in the diffuser region indicated a more severe flow stall on the diffuser side walls even though higher through flow was observed into the evaporator. A flow coupling was observed between the fan cut-off and diffuser side wall (on cut-off side). (see Figs. 4.19 and 4.20)

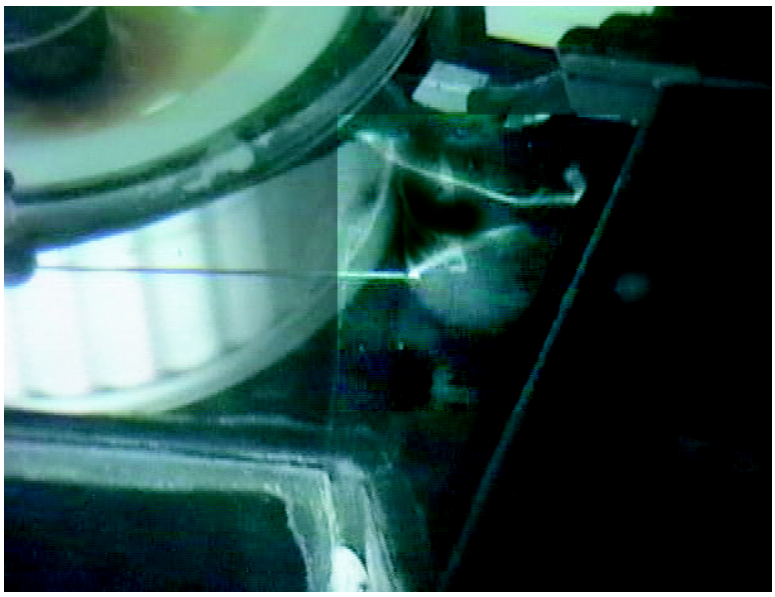

Figure 4.17: Diffuser/evaporator; top of evaporator (10 volts , 1500 Rpm)

Figure 4.18: Diffuser/evaporator; bottom of evaporator (10 volts, 1500 Rpm)

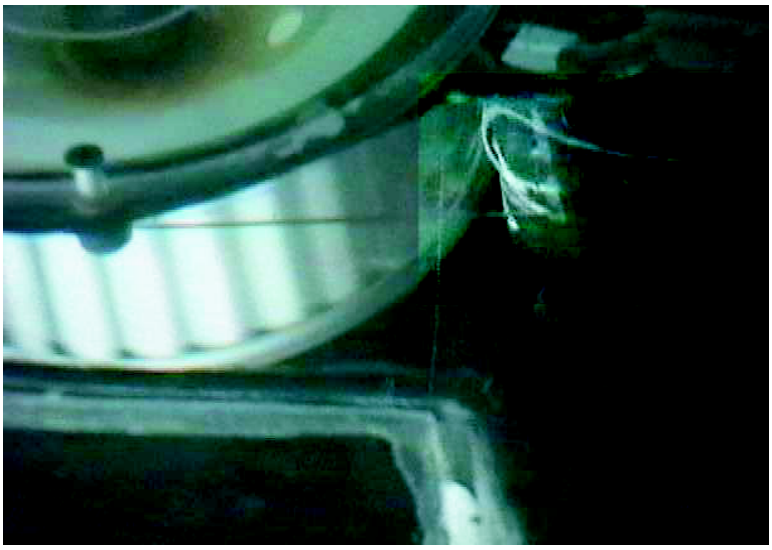

Figure 4.19: Diffuser inlet/fan throat, top side (8 volts , 1200 Rpm)

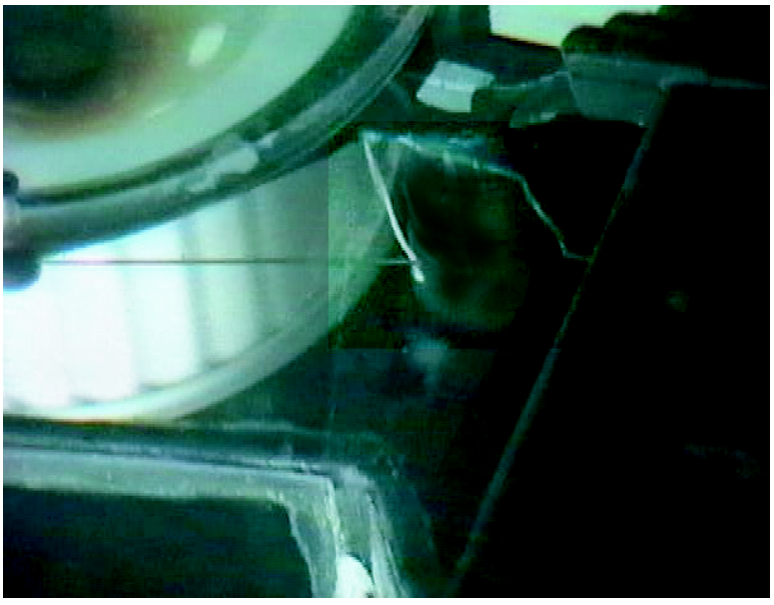

Figure 4.20: Diffuser inlet/ fan throat and fan cut-off, top side (12 volts , 2000 Rpm)

An interesting flow phenomena was observed in the region between the fan blade trailing edge and lower fan cut-off section (i.e., at the top of the fan scroll). Flow visualization results showed that the flow exiting the fan blades slightly upstream and opposite to the cut-off (see Fig. 4.21) followed a path that lead to the nose of the fan cut-off (ideally a stagnation point in this type of flow). Then the flow bifurcated (in the classical sense, see Panton, Perry) so that part of it re-entered the fan impeller/scroll cavity and the other part discharged towards the fan throat/diffuser region. This phenomenon is a classical stagnation point flow occurring at a leading edge of a blunt body (e.g., nose of a torpedo or of an aircraft). It was also observed that this stagnation point flow gets highly distorted and eventually disappears towards the bottom half of the cut-off span. It can be seen from Fig. 4.22 that the stagnation point moves off the fan cut-off solid boundary and into the flow towards the fan impeller/scroll cavity gap. The reverse flow pattern is fully established between the cut-off and diffuser inlet sections. The video mode photography shows these remarkable dynamic flow features in a very vivid manner.

4.7.2 Shear layer/Vortex formation at diffuser inlet and fan blade exit

Present results showed the existence of a large scale vortical flow structure at the fan throat, which extended well into the diffuser region. This causes a total pressure loss, and decreases the efficiency of the diffuser. The flow visualization studies on the model fan were consistent with the velocity deficit in the exit velocity profile at the fan throat of the LSB fan (described later), which had an almost similar fan/scroll/cut-off geometry. This can be interpreted as swirling flow with lower velocities in the core region. Similarly a single large scale vortex was observed at the exit of the LSB fan using the tuft flow visualization technique. Flow visualization studies using

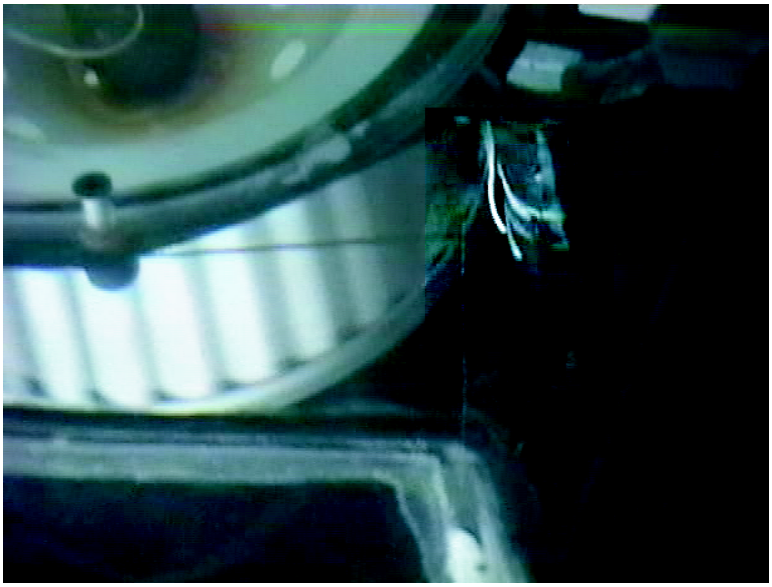

Figure 4.21: Fan cut-off, top side (8 volts , 1200 Rpm)

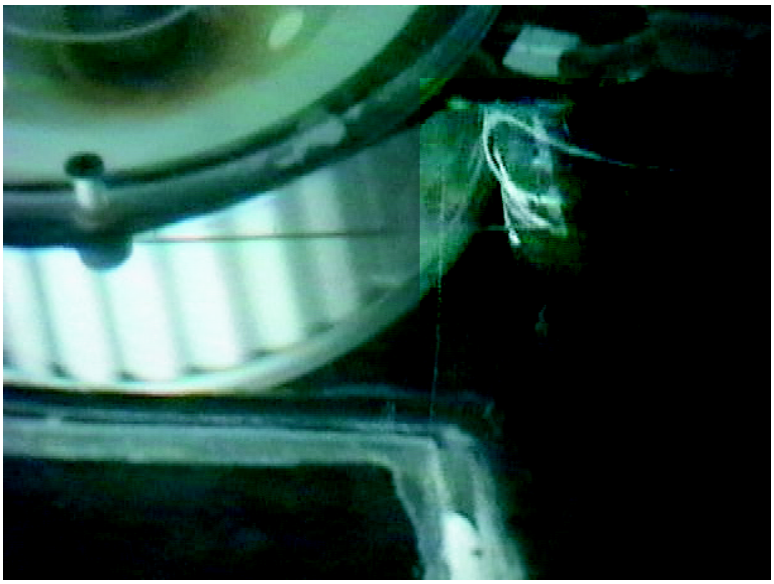

Figure 4.22: Fan cut-off top side (12 volts , 2000 Rpm

Figure 4.23: Diffuser inlet/fan throat, top side (8 volts , 1200 Rpm)

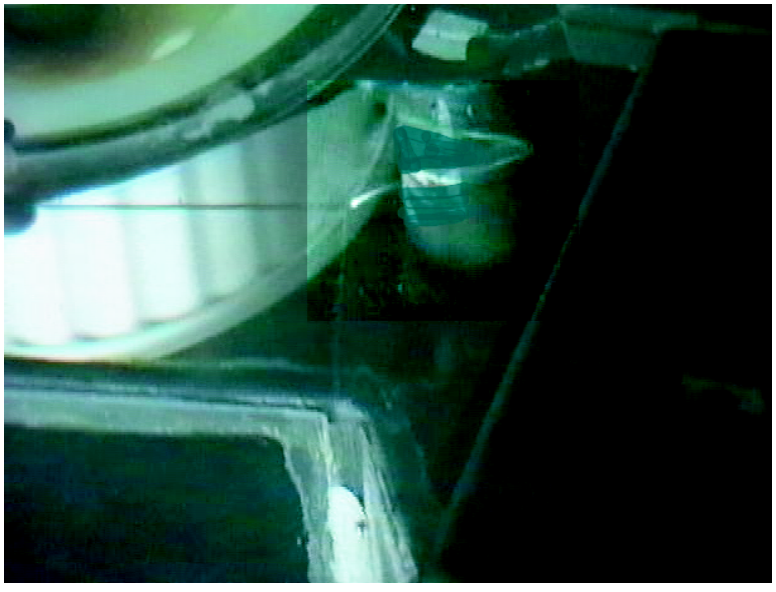

Figure 4.24: Diffuser inlet/ fan throat and fan cut-off, top side (12 volts , 2000 Rpm)

shear thickening dye also highlighted the dynamics of the vortical structure, which was unsteady in nature. Its core width and length varied, not only with fan speed but also showed variation at fixed fan speed. Identification of this type of flow phenomena was possible only with video mode photography. The unsteady vortex at the fan throat is indicative of a more complex flow interaction among the flow from the rotating fan blades, fan cut-off and fan scroll. Notice that the presence of flow swirl cannot be attributed to the diffuser, since the flow visualization tests on the LSB fan were conducted without any diffuser or extra outlet ducting, but showed precisely the presence of a single large vortex. Some researchers have noticed a double vortex structure at the exit of centrifugal fan with backward curved blades (Cau et al. [**?**]) similar to the occurrence of the classical double vortex in the circular pipes.

Flow visualization using the shear thickening dye injection can be used as an unstable/unsteady flow diagnostic technique for the detection of transitory stall, rotating stall in fan blades for centrifugal fans. The work of Chen et al. [**?**], has indicated that stall can occur in an intermittent and progressive fashion in centrifugal fans, unlike the stall in axial compressors that occurs abruptly at reduced flow rates.

Figs. 4.25 to 4.28 show flow reversal patterns at the lower fan speed than at higher fan speed. Note that at fixed downstream system resistance (at a constant load), a lower fan speed implies a lower volume flowrate. At the lower volume flowrates, flow reversal is stronger and more widespread toward the cut-off side than at higher volume flow rates (and at higher fan speeds at constant load). In fact, the the flow reverses back into the fan region from the diffuser side and from the fan impeller and cut-off side towards the fan throat.

The flow pattern observed at fan throat exit is highly skewed and shows a major shift in direction (near the cut-off wall) as fan speed is altered. The flow pattern in the diffuser region just upstream of the evaporator also changes drastically with

Figure 4.25: Fan throat region: close to inner wall

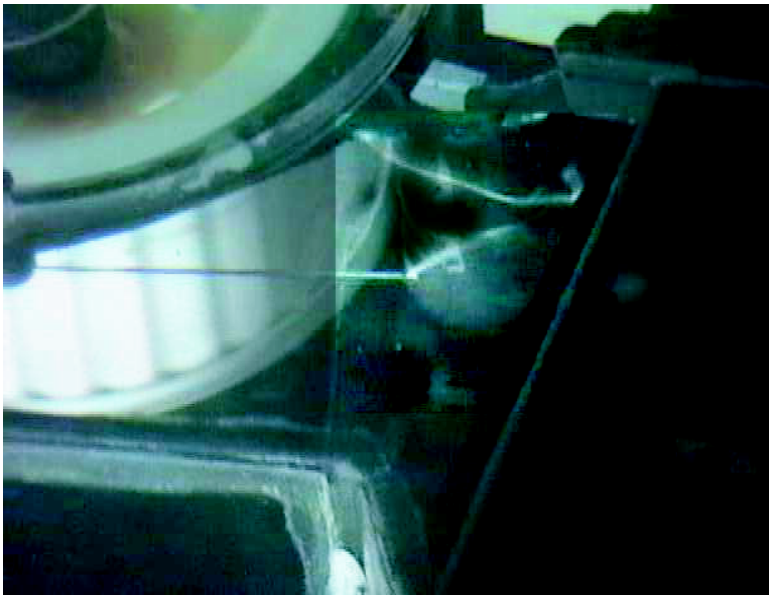

Figure 4.26: Fan throat/Diffuser inlet region

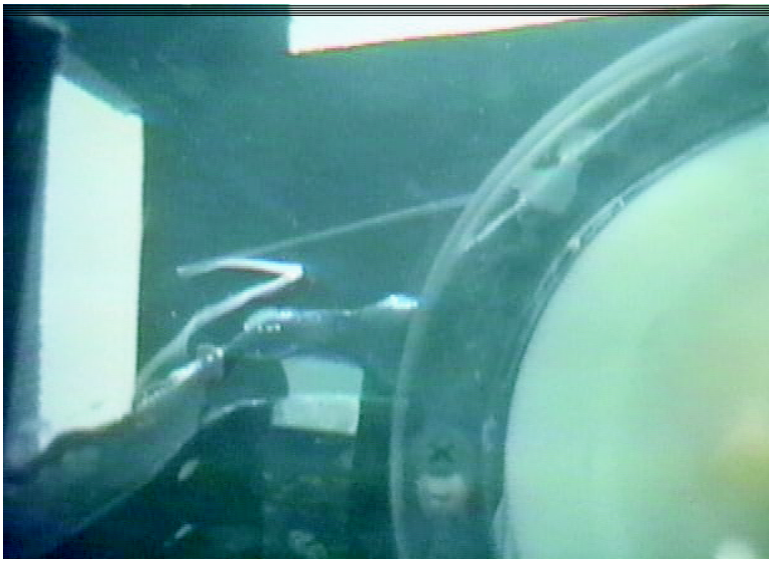

Figure 4.27: Near the the Fan scroll cut-off wall

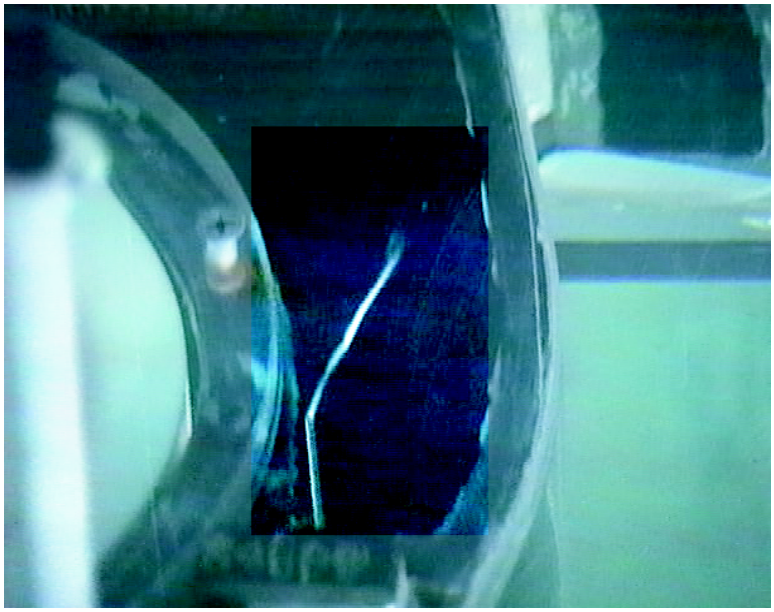

Figure 4.28: Diffuser inlet region: view 2

changes in fan speed (or voltage input to blower motor). At a fixed system resistance fan operation, a higher fan input voltage (i.e., higher fan speed) results in a much smoother flow pattern (less large scale fluctuation compared to highly pulsatile and oscillatory flow pattern observed at the lower fan speed settings) across the fan throat. In addition, at the higher fan speed (or flowrate) the flow was observed to be more uniform across the evaporator face compared to large scale fluctuation and recirculation observed at the low flowrate.

The major advantage of the using the shear-thickening dye over the convenient dye was that the shear-thickening dye was very effective in showing regions of: reversing flow, oscillatory flow, sudden changes in flow direction, the convecting flow path and presence of large shear even under very turbulent flow conditions. Conventional dye could not track the flow due it rapid diffusion characteristics and was not very useful in identifying flow features at high flow velocities.

The visualization of complex flow phenomena occurring in a HVAC fan module will be seen to enhance the understanding of the flow dynamics and the effect of HVAC component geometry on the flow structure. The flow visualization results, inconjunction with quantitative flow field data, provide a more complete understanding of the actual flow through the HVAC fan module which will lead to improvements in the overall component design. It also provides better information for efforts to calculate this flow field using CFD.

Chapter 5

Design of the LSB and the Mini-LSB Fan Test Facilities

5.1 Introduction

The small size and high fan speeds of actual HVAC components make it very difficult to investigate experimentally how the flow actually behaves. As a consequence, it is impossible to determine whether the assumptions used by the designer are valid or not. Therefore it is impossible to know, other than by trial and error, whether design changes will result in improvement of the performance. And even when improvement results, it may not be for the reasons thought. This means that even though improvements may have been achieved at great cost, little is learned to avoid the problem in the next design. The large scale centrifugal blower facility described below provides an opportunity to actually measure in such flows under near operational conditions.

An experimental investigation was conducted on a three times scale large-scale blower (LSB) of a typical automotive HVAC centrifugal fan. The LSB facility is described in detail in Appendix E. A three times scale model fan was used for two reasons: First, the flow speed must be reduced to velocities below 4m/s (Goldstein [31])

in order to perform smoke wire flow visualization studies on the fan. This can be achieved by increasing the fan size while maintaining dynamic similarity between the model and prototype as described later. This leads to a reduced fan speed resulting in lower flow velocities in the scale model. Second, the geometric (spatial) clearances need to be increased for proper application of the LDV and hot-wire flow measuring techniques in regions with complicated geometry and small clearances within the fan system. Experimental testing on the LSB was carried out to establish fan performance similarity (or dissimilarity) between the scale model and prototype, and to identify qualitatively and quantitatively the flow structures responsible for fan noise augmentation and loss of fan performance.

Additionally, the experimental testing aims to provide flow measurements with simple boundary conditions for CFD code validation that will subsequently be used in optimizing fan design for HVAC modules. For this reason, the flow characteristics were studied in detail at the fan inlet and outlet regions using a single sensor hot-wire probe. This was used to obtain the mean velocity and variance (or normal stress) in the streamwise flow direction. Tuft flow visualization was also done at fan inlet and outlet sections.

The LSB fan characteristic was evaluated in terms of the non-dimensional pressure rise across the fan and the volume flow coefficient (based on the "fan scaling laws"). This was achieved by varying the system resistance (pressure drop across the fan) using different flow resistance grids at a fixed fan speed. The static pressure was measured by multiple wall pressure taps both at the fan inlet and the fan exit. The volumetric flow rate was determined using both hot-wire and Pitot probe surveys conducted far downstream of the fan exit to achieve higher accuracy.

In comparison to the complicated prototype boundary conditions, simplified inlet and outlet fan geometries on the scale model test facility were used. Any differences between the scale model fan characteristic and the prototype are probably attributable

to differences in overall fan system geometry. The effect of boundary conditions (including fan installation effects) on the fan characteristics can be very significant (Bolton [10]). As noted in Section 2.2, in order to establish strict dynamic similarity between the model and its prototype, the fan, the fan system (including inlet and outlet geometries), and the boundary conditions must be matched exactly. To study the effects of the differences between model and prototype, it was decided that a second fan model should be built with the exact inlet and outlet fan geometry. In order to verify the effects of these differences between the LSB and prototype, a new exact 1/3-scale model of the LSB fan was constructed, the Mini-LSB. The Mini-LSB fan was used for verifying the generalized fan similarity (scaling) laws as described in Chapter 2. The experimental results for the LSB testing and their comparison with the Mini-LSB fan test results are presented later in Chapter 7.

5.2 Application of Fan Scaling Laws to Design the LSB

The application of the fan-scaling laws to design the LSB was shown in Chapter 3. The results of these fan scaling laws were summarized in Tables 3.1 and 3.4. In order to insure that the flow in the large-scale model fan behaves exactly as in the prototype (i.e., to maintain a dynamically similar flow), the new (generalized) fan scaling laws have to be applied to determine the similarity coefficients of the prototype design. These require that the Reynolds number (Re), Strouhal number (Str- equivalent to the inverse of the volume flow coefficient ϕ) and Euler number (Eu - equivalent to the diameter coefficient, δ) must be exactly the same between the model and the prototype. Table 3.4 gives the generalized fan scaling laws applied to the three times scale model. Note that these criteria differ from the classical fan laws that do not

preserve Reynolds number, as illustrated in Table 3.3.

Table **??** summarizes the flow parameters for the prototype, an automotive HVAC-type centrifugal blower. From the perspective of access and measurement, the larger the facility, the better. However, the primary constraint was the size of the room at the testing labs. In order to insure that the auxiliary equipment (like the laser doppler anemometer, for example) and duct-work could fit in the room, a three-time scale model was deemed optimal. This also coincided with the maximum size fan that could be fabricated quickly using SLA prototyping at a vendor's facility. Thus, $U_m/U_p = 1/3$, $\Omega_m/\Omega_p = 1/9$, and $\Delta p_m/\Delta p_p = 1/9$.

Table **??** also shows how the various flow parameters have changed due to the size increase. For example, in the case of the large-scale model blower, a most drastic change occurs in the rotation rate, which has been reduced by a factor of 9 from 4000 to 445 RPM. Although actual HVAC fan plots (obtained from industry) of pressure and volume coefficients display excellent collapse for high Reynolds number conditions (indicating Reynolds number independence), plots of torque coefficients and fan efficiencies do exhibit slight scatter, indicating a weak dependence on Reynolds number. Since the scale ratio is so large between the LSB model and prototype, demanding Reynolds number similarity was the safest course to pursue and was justified on the grounds of the achieving real dynamic similarity. Details of the test results for the LSB fan and comparison with the prototype fan are presented later in Chapter 7.

5.3 Geometric Similarity between Model and Prototype

Table **??**shows the prototype fan performance and geometric parameters, and also includes the model fan parameters using the fan scaling laws based on dynamic similarity as derived above. Studies demonstrating the effect of the system on fan performance (Cory [15]) have demonstrated that the effect of inlet and exit ducting on fan performance characteristics can be significant, both due to the effects of extra total pressure losses and non-uniform flow patterns, especially at the fan inlet. Typical HVAC fans operate in less than ideal conditions. The existence of nearly ideal conditions in the LSB fan can cause differences in the aerodynamic performance when compared to the air-side performance of a simple forward curved fan operating inside a HVAC module (the prototype fan) with much more complex geometry. It is important to recognize that strict geometric similarity between the prototype HVAC fan and the LSB model fan could not be maintained in the experimental apparatus. Geometric similarity implies that the model and prototype have length dimensions in a constant ratio throughout and equivalent angles are equal. This implies that both the shape and all the scaled length ratios remain constant between model and prototype. Strict geometric similarity was maintained for the fan impeller and fan scroll between the model and the prototype fan. However, the fan inlet and outlet duct shape and dimensions, and the fan blade surface roughness were different for the model fan compared to the prototype HVAC fan. Therefore, it was expected that there would be differences between the fan performance characteristics of the LSB fan and the HVAC prototype fan simply because of the dissimilarities in the fan inlet and outlet boundary conditions. Part of the motivation for the Mini-LSB investigation was to quantify these differences.

5.4 Design and Fabrication of the LSB Fan Test Facility

A three times size, optically transparent Plexiglas model of a centrifugal fan, scroll and inlet were manufactured to the original prototype dimensions. A simple fan model was chosen instead of the whole fan system in order to provide a benchmark test for CFD code validation. This model was geometrically identical to the prototype, allowing similarity to be maintained through the fan scaling laws described above. The relevant dimensions are provided in Table **??**. The LSB fan test facility design was based on AMCA design specifications in order to meet the AMCA fan testing code (i.e., the STD fan testing procedure; see Appendix D for details on the STD facility). The inlet and outlet geometries of the model fan were not modelled exactly as the inlet and outlet geometries of the prototype fan system because of both ease of manufacturing and the need to provide simple geometries for CFD code validation. It is important to recognize that the large-scale blower facility was built primarily to test the centrifugal fan *without* all the auxiliary system components, such as inlet ducting and exit diffuser-evaporator combinations. There were also some compromises made in the inlet duct design. The reasons for the difference in inlet geometry were mainly due to manufacturing, since it is difficult to manufacture a highly curved circular inlet lip from lexan or Plexiglas (although it could be done, in a second generation fan model). A simple circular duct was used without any flow conditioning or proper inlet bell mouth. The reason for installing a circular duct at the fan inlet is to ensure parallel flow immediately before the inlet-scroll junction, thus allowing easy measurements of inlet and volume flow rates. The circular inlet duct used for the fan inlet simplifies the fan inlet model geometry input to CFD codes.

The outlet fan (LSB) duct has rectangular cross-section and constitutes an extension of the fan scroll volute. The diffuser at the exit of the prototype fan was

not included in the large-scale model blower in order to provide a simple fan exit boundary conditions for CFD code validation. The straight rectangular fan exit duct is also simple to model in a CFD code, whereas the prototype diffuser has a very complicated non-symmetrical three-dimensional geometry.

The clearance gap between the top shroud of the fan impeller and the fan inlet duct was not modelled exactly to prototype geometry, but most other clearances were modelled maintaining geometric similarity. Also, it should be pointed out that, the fan blade roughness was much higher for the (SLA) model in comparison to the original prototype. These slight geometric differences may have some effect on the flow through the fan, but it is anticipated that most of these will be viscous-dominated flow phenomena which have an insignificant effect on the fan performance at high Reynolds number.

The inlet flow is one of the major candidates for blower rumble noise and thus this region needed to be investigated thoroughly. The fan literature survey (see Appendix A) indicated that the fan inlet geometry can have a significant effect on fan performance. To study the effects of the differences between model and prototype, the Mini-LSB fan was designed with the exact inlet and outlet geometry similar to the LSB fan.

5.4.1 HVAC Fan (Prototype) Geometry

Centrifugal blowers (or fans) are air-moving devices commonly used to generate airflow in automotive HVAC systems. A typical automotive HVAC system (i.e., the prototype HVAC module) consists of a fan impeller run by a motor housed in a stationary volute (scroll) casing, that is connected to the downstream evaporator and heater cores by a diffuser, as shown in Fig 5.1. In most automotive HVAC applications, forward curved centrifugal fans (fan blades are curved in the direction of rotation) are commonly used because of their small size and their lower operating fan

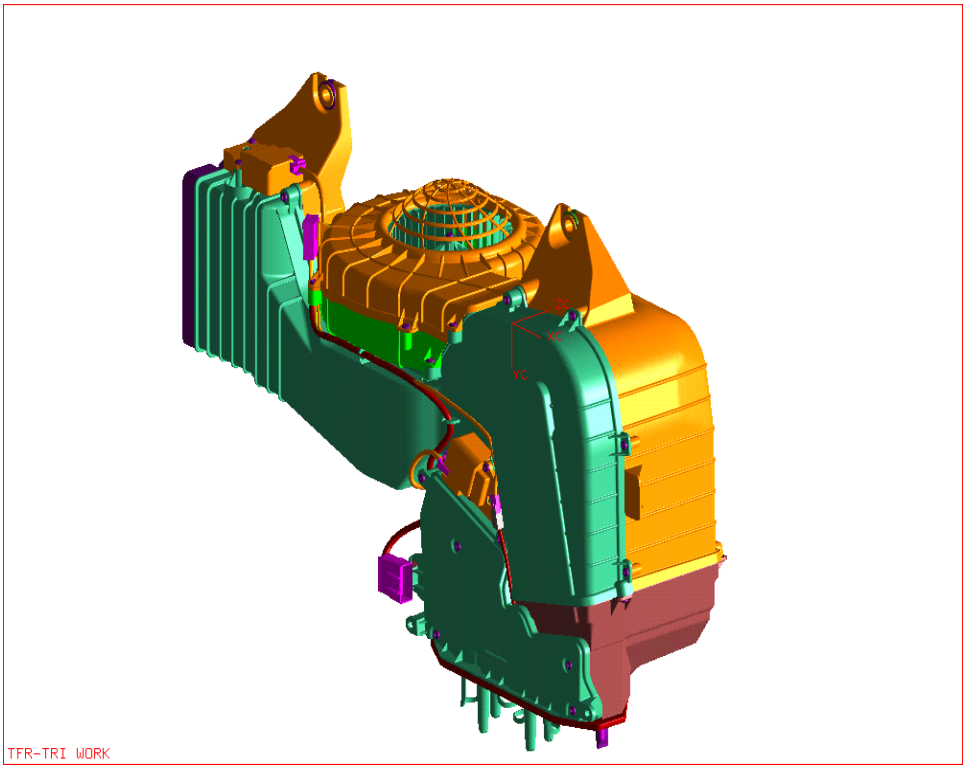

Figure 5.1: A Typical Rear HVAC module used in automotive applications

speeds at the same load in comparison to backward curved centrifugal fans. A typical forward curved squirrel cage type blower used in an automotive HVAC module is shown in Fig. 5.2.

5.4.2 Fan Impeller and Fan Scroll Geometry

A forward curved centrifugal fan impeller is made of a hub with a baseplate, top shroud and many fan blades (typically 37-60). Some blower scroll designs have an upper and a lower scroll, with the impeller/motor assembly that fits into the lower scroll using rubber isolators (Fig. 5.3). The basic size and shape of the fan impeller is defined by its outer blade diameter and the blade span (height). Blade profiles are defined by blade inlet and outlet angles, blade camber, blade thickness, aspect ratio (span to chord ratio), blade taper and blade twist. Circular arced blades are the most common blade shapes used in forward-curved bladed centrifugal fans due to cheap manufacturing costs and simple construction (See Appendix A for further details). The forward curved squirrel cage type LSB impeller (Fig. 5.4) was made of resin material and built using the SLA technique. It had 37 straight blades of three-inch chord. Fan exit diameter was 16.5 inch with a top of the blades connected via a thin shroud.

The model casing of the fan has front and back panels made out of Plexiglass sheets, which are grooved to accept a flexible Plexiglass sheet that formed the logarithmic spiral wall of the casing (see Fig. 5.5) . The cross-section of the casing was rectangular, and continued past the fan throat section, making the fan exit geometry rectangular similar to the original prototype.

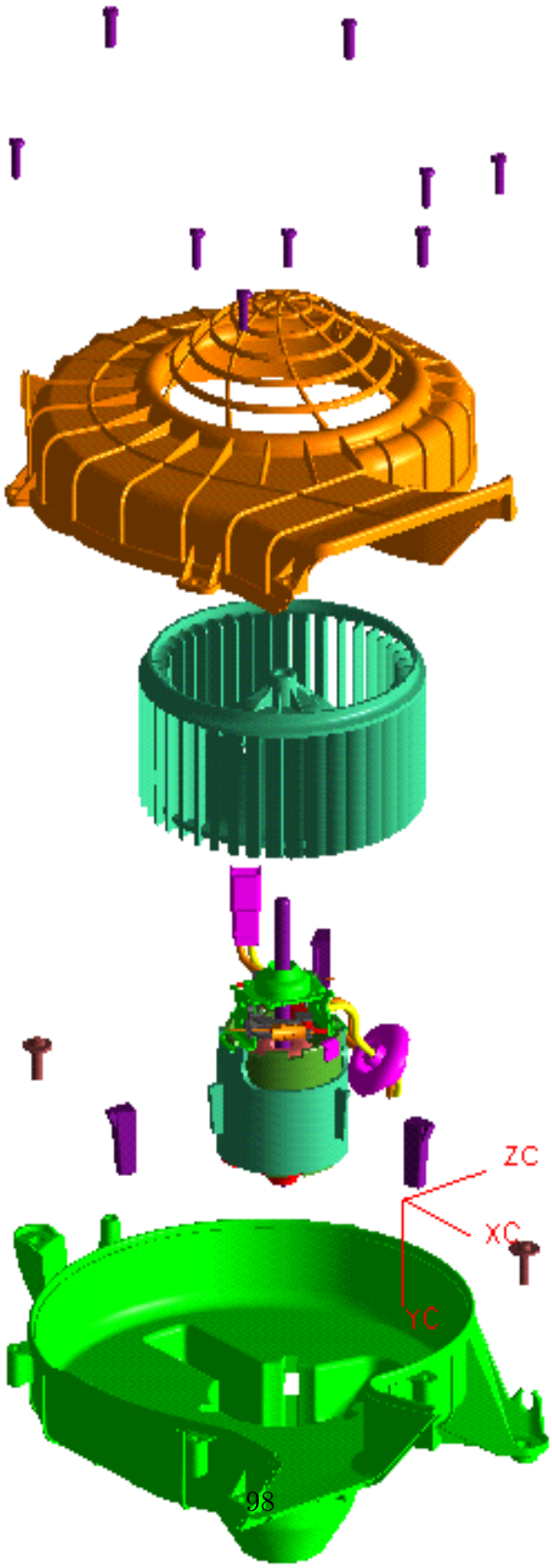

Figure 5.2: A squirrel-cage type automotive HVAC blower

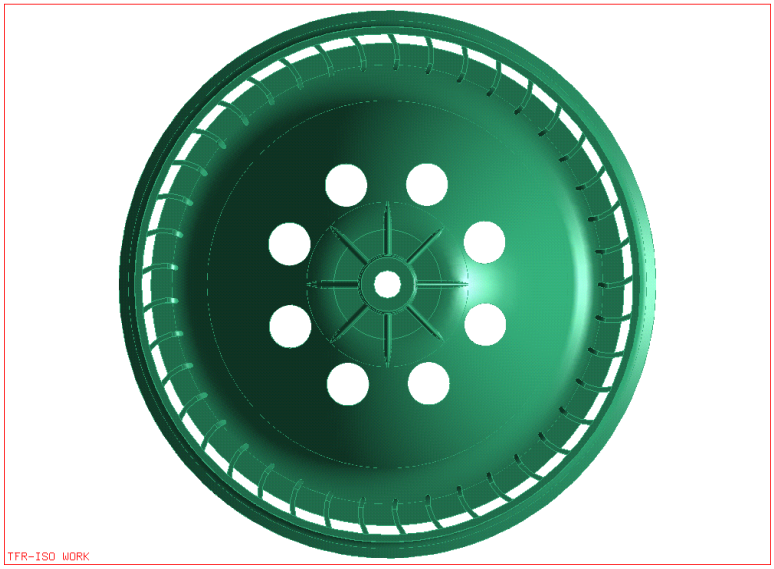

Figure 5.3: A typical squirrel-cage forward curved impeller used in automotive HVAC blowers

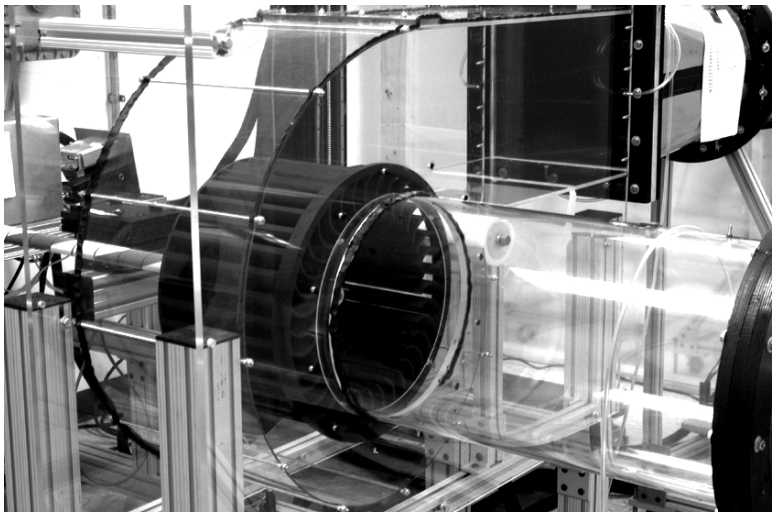

Figure 5.4: A squirrel-cage type LSB blower wheel

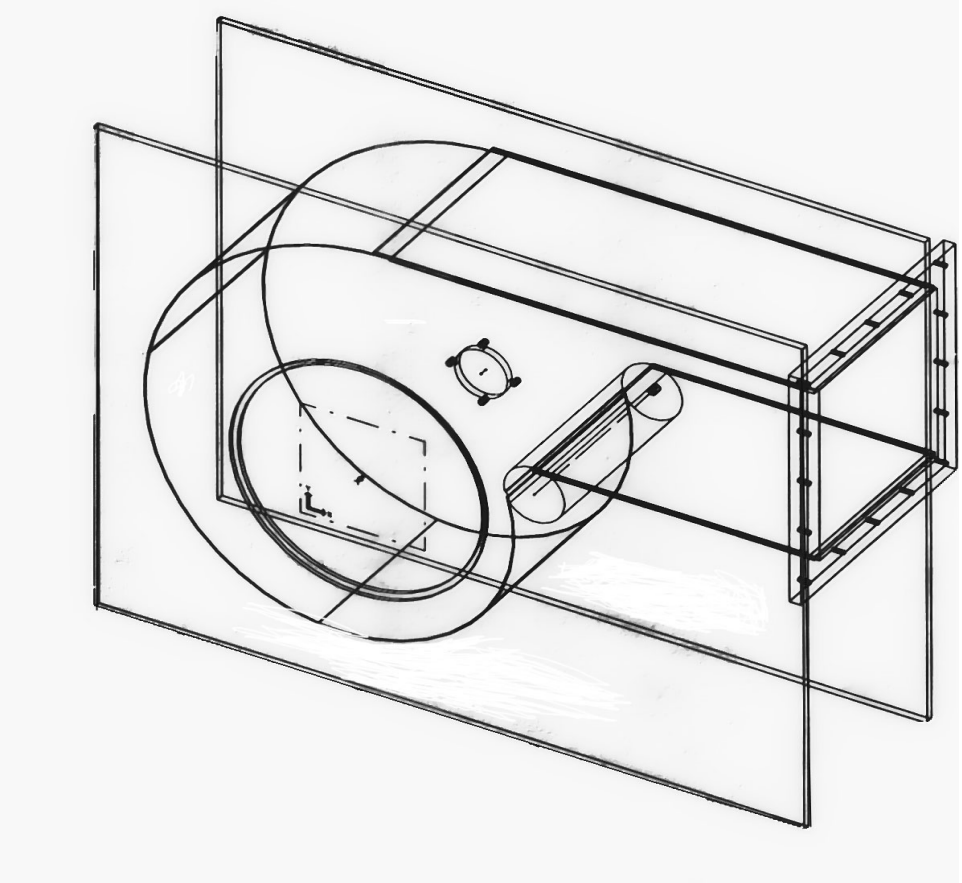

Figure 5.5: The LSB scroll casing

Figure 5.6: The LSB fan with the short and round inlet duct

5.4.3 Fan Inlet Duct Design

A 13.25 in. diameter circular duct with rounded lip was fitted to the fan's inlet opening. The fan inlet duct was directly installed into the front of the scroll at the fan orifice. This was mainly done in order to obtain preliminary inlet data the LDA and to obtain fan performance data with the same configuration. The model fan inlet duct protrudes into the fan scroll by an inch, as shown in Fig. 5.6, in contrast with the short round lip at the inlet of the prototype scroll. The locations of the boundary

conditions required for the CFD code are shown in Fig. 5.7.

5.4.4 Fan Transition and Exit Duct Design

The AMCA fan test codes recommend that volume flow rate should be determined from measurements made in a circular duct, whereas the LSB fan has a rectangular cross-section. Therefore, it was decided to build a transition duct for connecting the fan exit duct to the circular measurement duct. The transition duct was designed and fabricated according to AMCA Standards [3]. The rectangle to square aluminum transition duct was 2D long and turned out to be a converging duct. The fan discharged into a rectangular duct 18 in. long. Fan scroll exit duct cross-sectional area was approximately 147 sq in. while the downstream circular duct cross-sectional area was approximately 137 sq in. The axes of the fan exit duct and the transition duct coincided.

5.4.5 Flow Conditioner

A flow straightener was designed and fabricated according to AMCA Standards. The flow straightener was placed about 3.5D (exit duct diameters) downstream of the transition duct, as recommended by AMCA Standards. It was of 0.44D in length, 0.005D in thickness and had a 1.0 in. diameter (0.076D) aluminum circular pipes as the basic flow straightener channel design instead of the square (0.075D) channel design suggested by the AMCA Standards. The circular pipe chosen approximates the effect of the square channel, in such a way that the pressure drop was for a given flow rate remained constant. The differences between the AMCA recommended flow straightener and the one used are thought to be small.

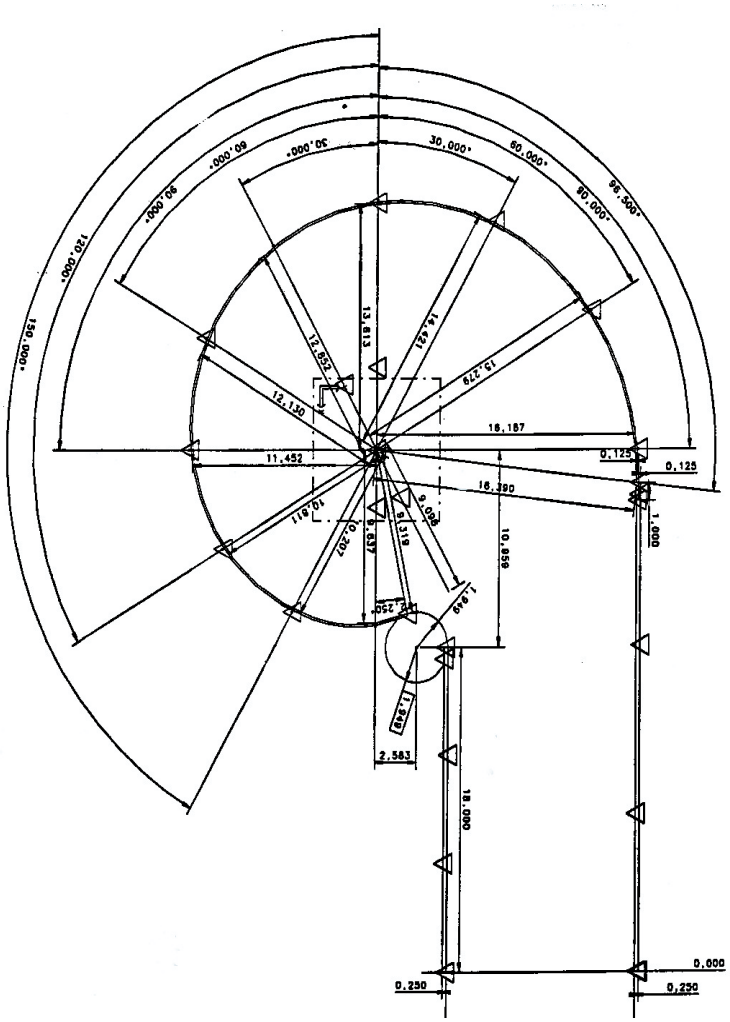

Figure 5.7: A schematic drawing of the LSB fan showing locations for measuring the inlet boundary conditions

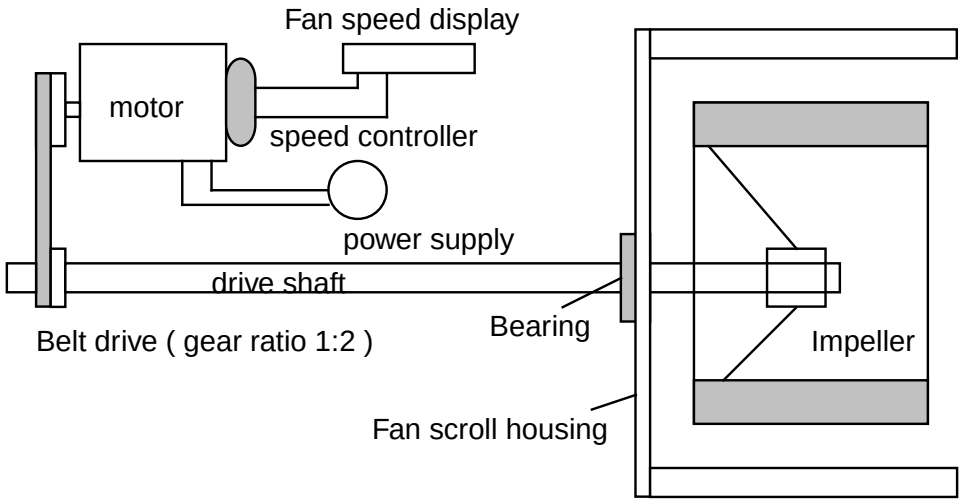

Figure 5.8: LSB fan drive system

5.4.6 System Resistance (back pressure)

Since centrifugal fan performance is dependent on its operating load point (flow system resistance), the flow resistance was varied during the experiments to determine fan performance over a range of volume flow rates. This was achieved by using perforated metal grids, of known porosity (i.e., total through flow area to total solid grid area) placed downstream (10 exit duct diameters)of the fan impeller. The following grid sizes were used in the LSB fan tests: 25%, 30%, 35%, 41% and 51%. Finally a test was also conducted with no grids (i.e. 100% open).

5.4.7 Fan Drive System

The fan is powered by a 0.5 h.p. D.C. motor (constant torque) with a variable speed drive. Fig. 5.8 shows a schematic diagram of the apparatus used for the present experiment. It consisted of a modified automotive HVAC squirrel cage fan (LSB) driven by a D.C. motor coupled to a speed controller.

5.5 Design of the Mini-LSB Experimental Test Facility

The Mini-LSB impeller was designed exactly as a 1/3-scale model of the LSB fan impeller, and was also constructed using the SLA manufacturing method. The Mini-LSB scroll volute section was fabricated using lexan sheeting of 1/8-in. thickness. This provided enough strength since centrifugal fans used in typical HVAC application produce relatively low pressures (less than 3 in. of H_2O). In addition, the 1/8-in. thickness allowed the use of a single continuous sheet in forming the logarithmic spiral shaped volute due to its flexibility. However the front and back plates of the fan scroll section were fabricated using lexan sheeting of $\frac{1}{2}$ in. thickness to provide strength to the whole fan casing enclosure, which housed both the fan impeller and fan motor.

The fan outlet ducting (straight circular pipe) was made of clear Plexiglas material, of 4.4 in. i.d. and had a total length of 72 inches. The fan scroll exit had a rectangular cross-section while the fan exit pipe duct was circular; therefore a transition piece was installed between the two sections. The transition duct was made out of thin aluminum sheet and was built similar to the LSB transition duct.

The flow conditioner was made out of soda straws that were 3 in. long and had a inside diameter of 3/8 in. The straw length and width were chosen in such a way that the Euler number (flow resistance coefficient) and Reynolds number are matched to the flow straightener in the LSB fan at max flow.

Similar to the LSB fan test facility, the Mini-LSB fan test facility, as shown in Fig 5.9 , was designed in accordance with the AMCA recommended STD fan testing procedure (see Appendix D for details on the STD facility). Both the method of fan system resistance and flow conditioning were similar to the LSB fan test facility: the system resistance was generated by using grids with variable porosity (open area), and flow conditioning was provided by circular straws and steel screen placed inside

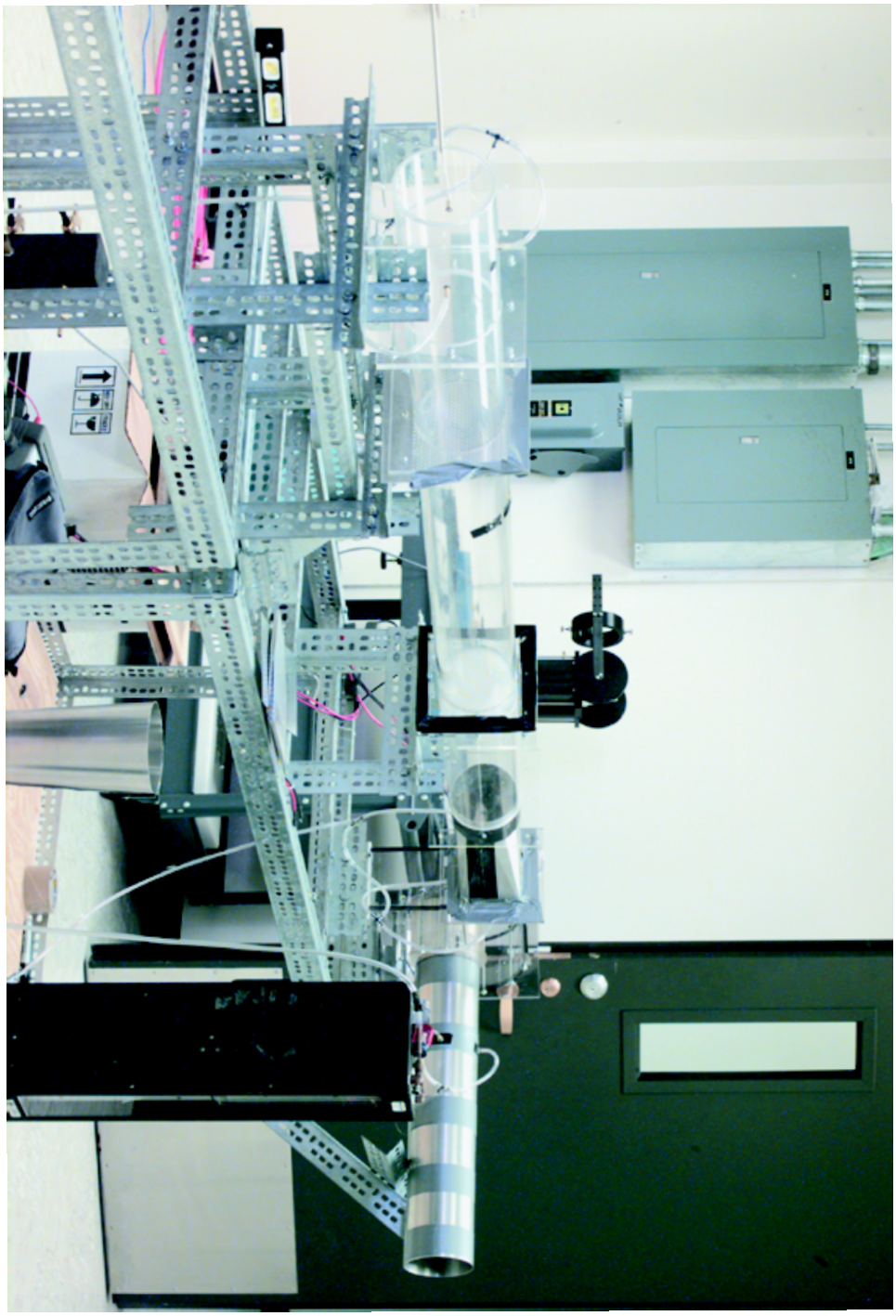

Figure 5.9: The Mini-LSB fan test facility

a long straight circular Plexiglas duct downstream of the fan impeller.

The Mini-LSB fan impeller was operated by a $\frac{1}{4}$ h.p. D.C. standard HVAC motor which ran from a variable DC power supply (voltage source). The voltage source was capable of supplying up to 30V at 20 amps. The power supply also had a digital voltage and amp meter. Thus, both the voltage supplied to the fan and the current drawn by the fan (i.e., the power supplied to the fan motor) at various fan operating points could be determined. Fan rotation rate was monitored by an accelerometer which was attached to the fan motor housing.

The Mini-LSB was subjected to various system resistances (back pressures) by use of flow resistance grids of different porosity, in the identical manner as it was done in the case of the LSB fan tests. Note, however, that the Euler number based on the resistance grid hole diameter was not matched between the two facilities. Thus, this difference in resistance grids could lead to slight differences in the Eu_{sys} number matching between the two model facilities, and hence result in some dissimilarities in fan performance matching between the LSB fan and the Mini-LSB fan.

Chapter 6

Experimental Methodology and Testing of the LSB and the Mini-LSB Fans

6.1 Introduction

The flow through a typical centrifugal fan is highly complex; in particular, the flow is highly turbulent, non-uniform (swirling) and has areas of flow separation and recirculation (Kind et al. [36] and Denger and Mcbride [17]). As a consequence, even the most sophisticated analytical techniques require the use of empirically determined factors. And although computational techniques have advanced to a high degree, the experimental validation of CFD codes for fan performance prediction is essential in order to have any expectation that they might resemble reality. In addition, CFD codes are limited by inadequate turbulence models and the complexities of the rotating fan system geometry. Also, at present the state of fundamental flow theories

for practical flows encountered in industrial settings is far from complete. For example, there are still no acceptable theories for the viscous three-dimensional separated flows that are standard in turbomachinery. Therefore experimental testing is essential in order to understand the performance of both the overall turbomachine and its individual components.

The fan laws (both generalized and classical) can help, but they can be used to predict performance *only when at least one fan has already been tested.* For a completely new fan design of a particular size, dimensional analysis allows the non-dimensional fan performance characteristic for fans of all sizes to be determined once it has been determined for one. This fan performance information allows proper fan selection to be made for a given fan application in a specific environment. In addition, it also serves to relate the fundamental aerodynamic flow parameters to the fan geometry and existing boundary conditions, so that improvements can be made in both the aerodynamic performance and acoustic performances of the fan.

Three different types of tests were conducted on the LSB fan:

- First, tests were conducted to measure fan performance characteristics; i.e., measurement of the overall static and total pressure differences between the fan outlet and inlet, and the volume flow rate for various flow resistances (system resistance) at a fixed fan speed. The system resistance was modified using various flow resistance grids of known porosity. According to the generalized fan scaling laws (GFSL), the fan testing performed at constant fan speed for a given fan implies that Reynolds number similarity is maintained throughout the fan characteristic curve. For every fan test point at a given flow resistance setting, the fan speed was maintained at 431 RPM, which corresponds to 3879 RPM on the prototype.

- Second, specific fan test rig components were tested using various pressure measuring instruments. From these pressure measurements it was possible to obtain the flow field parameters relevant for the assessment of different fan performance measuring techniques. In particular, flow field static pressure and total pressure measurements were made in close proximity to the fan inlet orifice and fan scroll exit using different types of pressure measuring instruments. This was done to show the limitations of direct measurement of flow field parameters in the near field using conventional instrumentation, and to justify more advanced measuring techniques for the accurate and direct evaluation flow field at the fan inlet and outlet (e.g., LDA and hot-wire techniques). These measurements also enabled a more direct assessment of fan performance founded on fundamental fluid dynamic theory. Additional tests were conducted using tuft flow visualization techniques to verify certain trends found in some of the flow field measurement results.

- Third, detailed flow field studies were conducted at the LSB fan inlet and exit locations. The flow characteristics were studied at the inlet and outlet regions using a single sensor hot-wire probe. The hot-wire technique was used to obtain the mean velocity and the variance in the streamwise flow direction. These results are presented in chapter 7.

6.2 Fan Testing Techniques

6.2.1 LSB Fan Testing Techniques

The LSB fan performance (pressure/flow characteristic) was determined according to the STD fan testing method (as described in Appendix D). With the exception of the static pressure measurements, the LSB fan testing procedure followed the AMCA

Standard fan test codes. This exception was because the fan exit static pressure measurements were performed at the exit of the fan scroll duct by measuring the static pressure using the average of four piezometric wall pressure taps located circumferentially around the fan scroll exit duct at $1.5D_{fan}$ downstream of the fan cut-off, instead of the AMCA Standard recommended method of measuring fan static/total pressure for the STD approach. This approach followed is believed superior since the wall measurements are less sensitive to flow velocity fluctuations than measurements made in the main stream (see the discussion on the comparison of the STD versus PLC fan test methodology given in Appendix C).

The fan test codes recommend that fan exit pressure measurements be conducted at the farthest downstream location of the fan, and be corrected back to the fan outlet conditions (see Fig. 6.1). The fan pressure rise formulations that the code uses for the outlet duct setup (AMCA standard 210-74 & ASHRAE Standard 51-75) are given by Eq. D2 (in Appendix D). It was observed from the previous fan tests (made with actual HVAC fans, refer to Appendix C) using both the STD and PLC fan facilities, that the fan scroll exit duct location was an acceptable position for direct wall static pressure measurements.

The complete fan characteristic was obtained by using different flow restrictions in the downstream duct to depict the various conditions on the fan. The AMCA/ASHRAE fan test standards suggest that eight points (pressure/volume) on the fan curve provide a sufficiently good representation of the true fan characteristic. For the LSB fan tests, six different performance points were achievable. The fan test codes also recommend Pitot tube surveys inside the exit duct downstream of the fan (in the straight duct fan test procedure, see Fig. 6.1) to determine the volumetric flow rate, and to measure the total and static pressures at constant fan speed. The fan test procedure that uses downstream circular ducting must have a sufficient length (8.5

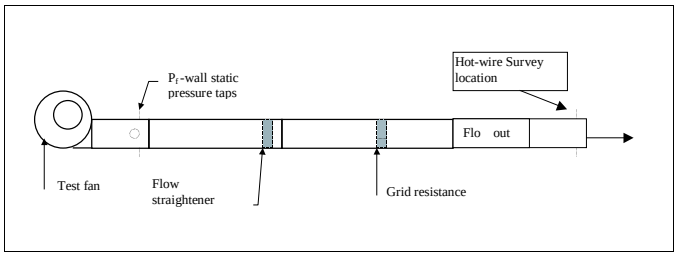

Figure 6.1: AMCA Fan testing method using the STD outlet duct approach

to 10 exit duct diameters) before flow rate or pressure information can be measured. The main reason for the extra long duct at the exit of fan is that the length of the duct smoothes out the flow towards the fully developed flow condition, mainly due to the balancing of the streamwise pressure gradient and the Reynolds or viscous stresses. In addition the flow straightener partially removes flow swirl, leading to more uniform flow conditions at the downstream measurement stations.

6.2.2 Mini-LSB Fan Testing

The experimental tests conducted on the large scale blower fan showed considerable discrepancies in fan performance when compared with the HVAC prototype. The comparison was based on the non-dimensional fan performance characteristic, the pressure (or head) coefficient versus the volume flow coefficient. It was suspected that this discrepancy in fan performance was due to the differences in fan exit geometry between the LSB fan and the HVAC prototype. In order to test this hypothesis, the near exact 1/3 scale model of the LSB fan test rig was designed and fabricated (see Section 5.4). Recall that the LSB was not (and was not intended to be) an exact model of the prototype fan (see Section 5.3).

As noted in Section 6.2.1, the same fan housed in a similar manner in different test rigs should give similar results, and any differences in the measurement of the fan performance characteristic curve are mainly due to measurement error (including instrumentation inaccuracies) or improper measuring technique. To help in identifying these errors, the performance of the Mini-LSB test facility was measured by using two different measurement techniques. One of the fan performance measuring techniques (the AMCA recommended STD approach) was identical to the one used in the LSB fan test experiments, while the other was a more accurate technique especially for this particular application (the STD approach combined with the Airflow machine). The experimental results for the Mini-LSB from both fan test methods were compared to

each other and to the LSB fan performance to verify compliance with the generalized similarity laws and to demonstrate the importance of maintaining strict geometric similarity (including boundary conditions) when comparing model and prototype fan performance.

6.3 Instrumentation and Calibration

The large-scale blower facility was designed to accommodate a variety of experimental techniques including laser Doppler anemometry and particle image velocimetry. For the investigation reported here, however, Pitot tubes and hot-wire anemometry techniques were used. While these can not adequately resolve regions of flow separation or very high turbulence intensity, hot-wires can easily identify the overall flow characteristics, and can certainly be accurately used for the determination of volumetric flow rates in the upstream flow. This rig was initially tested at the Turbulence Research Laboratory, then moved to an off-campus facility. Therefore two different sets of measurements were made; hence two instrumentation set-ups are described.

6.3.1 The TRL Set-up for Velocity Surveys near the Fan Inlet and the Fan Exit Locations

The velocity measurements at the fan exit and inlet regions were carried out using a single sensor TSI hot-wire probe in combination with a Dantec 55M series anemometer. The hot wire sensor was standard 5-micron diameter tungsten wire. The hot wire was calibrated by placing it in the potential core of the axisymmetric jet facility of the Turbulence Research Lab at SUNY at Buffalo. The hot wire was calibrated against a pressure transducer that measured the pressure drop across the jet nozzle.

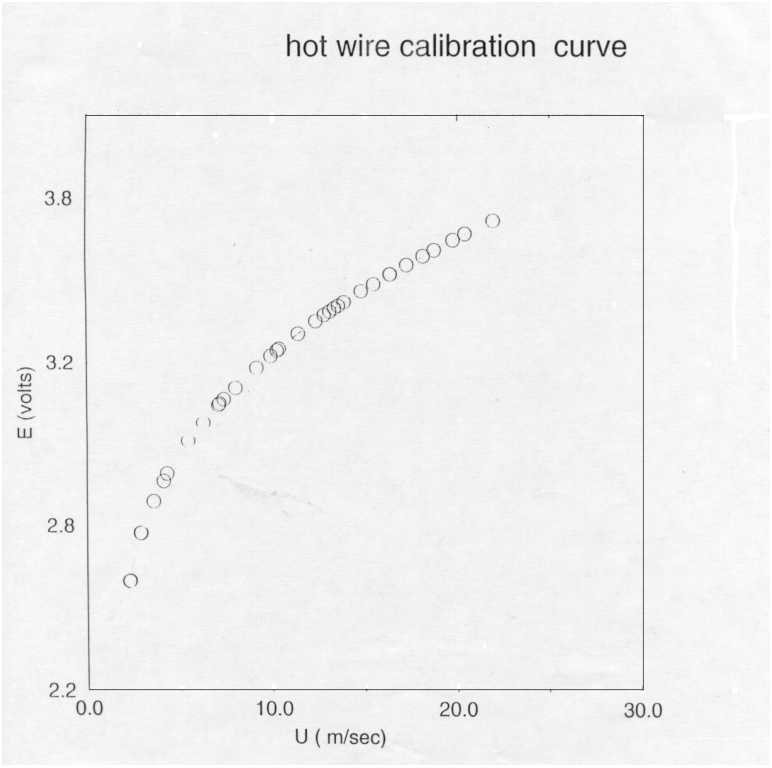

Figure 6.2: Hot-wire calibration curve

This was then converted to a reference velocity, which was used as the reference velocity for calibration of the hot wire signal output. The calibration range was from 2 m/s to 22 m/s, and spanned the given fan test velocity range. The calibration and the fan testing were conducted at around $22°C$ and standard atmospheric pressure (760 mm Hg). The calibration data was processed using the digital-linearizing scheme developed by George et al. [29]. The calibration data was curve fitted with a fourth order polynomial as shown in Fig. 6.2. The standard deviation for the polynomial fit was 0.02 m/sec with average error of 0.02 m/sec. The calibration data showed the maximum percentage error of 2% to occur at the lowest end of the velocity range.

Data acquisition and signal processing were done using in-house software on a Sun workstation and an A/D converter. The post-processing of the data was carried out

using computer software (RECDAT) available at TRL. The data was sampled at 100 Hz, which was more than adequate since no spectral analysis was done (using this data). The main parameters recorded in the fan test were the hot-wire voltage signal output, and the fan drive shaft rotation rate. For the fan operating point considered, the free delivery (zero back pressure) point, the static pressure rise was too low to be measurable with standard pressure transducers, hence, the use of the piezometric sensors. It is important to note that the volumetric flow rate was estimated from the mean velocity hot-wire survey at fan inlet,and is estimated to be accurate to within 5%.

6.3.2 The Off-campus Set-up for Velocity and Turbulence Measurements

The velocity measurements at the fan exit and inlet regions were carried out using a single sensor TSI hot-wire probe in combination with a TSI IFA 300 hot-wire anemometer. The hot-wire sensor was standard 5-micron diameter tungsten wire. The hot-wire was calibrated using the TSI hot-wire calibrating facility, which utilizes the potential core of an axisymmetric jet exit flow. The hot-wire was calibrated against a pressure transducer that measured the pressure drop across the jet nozzle. This was then converted to a reference velocity, which was used as the reference velocity for calibration of the hot wire signal output. The calibration range was from 0.5 m/s to 30 m/s, which spanned the given fan test velocity range. The calibration and the fan testing were conducted at around 21.5° C and standard atmospheric pressure (760 mm.Hg.). The TSI calibration scheme was used; this scheme also uses data fitted using a polynomial fit of velocity as a function of voltage. The standard deviation for the polynomial fit was 0.03 m/sec with average error of 0.04 m/sec. The calibration data shows the maximum percentage error of 4% occurred at the lowest end of the

velocity range.

Data acquisition and signal processing was done using TSI IFA-300 hot-wire anemometer software using an IBM-compatible PC and a 16 bit A/D converter. The sample frequency based on fan exit duct diameter and highest mean velocity and was estimated to be 27 Hz. Thus a 200 Hz data sampling frequency was sufficient for obtaining independent samples for estimation of mean flow statistics (George [26]). The post-processing of the data was done using computer software (TSI IFA 300). The main parameters recorded in the fan test were the hot-wire voltage signal output and the fan drive shaft rotation rate (i.e., number of revolutions per second). It is important to note that *the volumetric flow rate was estimated from the mean velocity hot-wire survey at fan outlet*, and was estimated to be accurate to within 6%.

6.3.3 The Off-campus Set-up for Volumetric Flow Rate Measurement

For the off-campus LSB tests, flow rate measurement was conducted at approximately 10 exit duct diameters *downstream* of the fan impeller using the flow velocity measurement grid as shown in Fig. 6.3. The recommended location assumes that the flow is fairly uniform, without swirl, and of low turbulent intensity. Three hot-wire velocity surveys were conducted at intervals of 60 degrees with 8 grid measurement points per survey following a logarithmic distribution of the measuring points.

The representative plots of the velocity profile show the flow is fairly uniform with very low turbulence intensity in the core flow, and higher levels only in the pipe wall boundary layers where the velocity reduces significantly towards the wall. The velocity data at fan exit was indicative of a developing flow which has not reached the classical fully-developed turbulent velocity profile in a circular pipe. Note that, the resistance grids were placed at least three exit duct diameters upstream of the

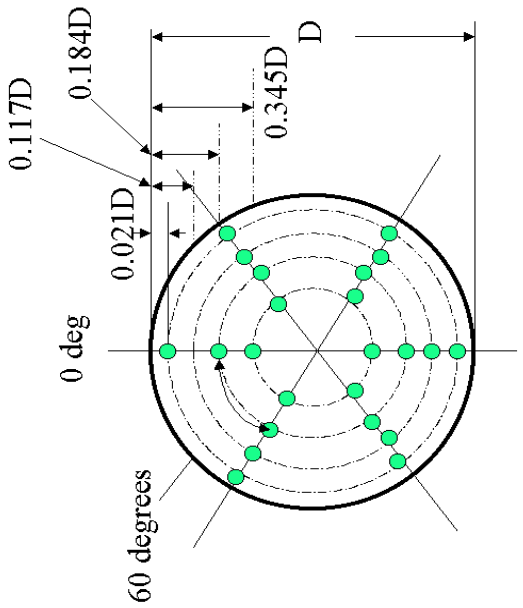

Figure 6.3: The measurement grid used for the calculation of volumetric flowrate based on the STD outlet duct approach

hot-wire survey location.

The average mean velocity, U_{avg}, was obtained by averaging over all the velocities, and subsequently a volumetric flow rate, Q, was estimated using the duct cross-sectional area, A_d. A total head probe was also used at the same location as the hot-wire to obtain mean flow velocity information.

When the fan was tested with inlet and outlet ducting (the off-campus LSB setup), both static and total head probes were used to get preliminary data in the fan inlet duct. It was observed that the wall static pressure taps gave readings very close to those from the static pressure vertical surveys across the inlet duct, see Fig. 6.4. The total pressure surveys at the inlet duct, however, showed larger fluctuations and asymmetries in the inlet profiles (see Fig. 6.5) , thus justifying the use of a hot-wire in the inlet duct to obtain both the mean velocity profiles and to determine the turbulent intensities upstream of the fan orifice inside the circular duct. Surprisingly, the turbulent intensities were found to be on the order of 15 percent, which is quite high compared to an average of 3 percent far downstream of the fan after flow conditioning. This clearly indicated that the inlet flow had to be cleaned up before reasonable inlet boundary conditions could be provided for ideal CFD validation purposes; and also provided another source of error between calculation and experiment when these effects are not accounted for.

In order to reduce the turbulence intensities at the inlet of the LSB, the inlet duct was extended and a bell mouth was installed the mouth (entrance) of the inlet duct. This reduced the flow separation inside of the inlet duct and lead to lower turbulence intensities.

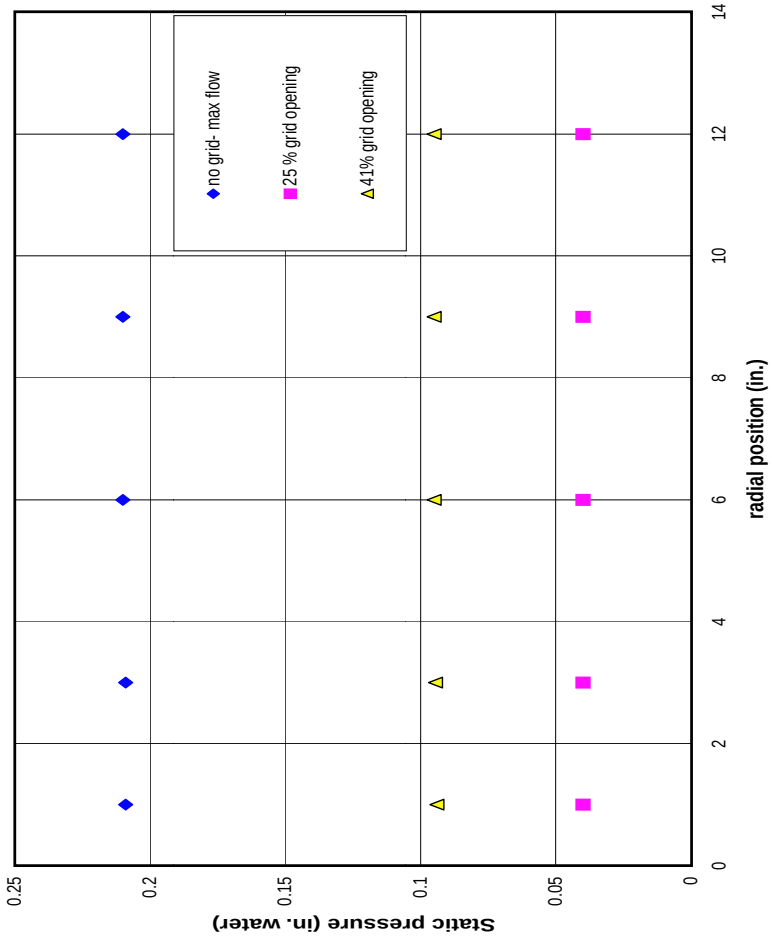

Figure 6.4: Results from static pressure survey conducted inside the LSB fan inlet duct

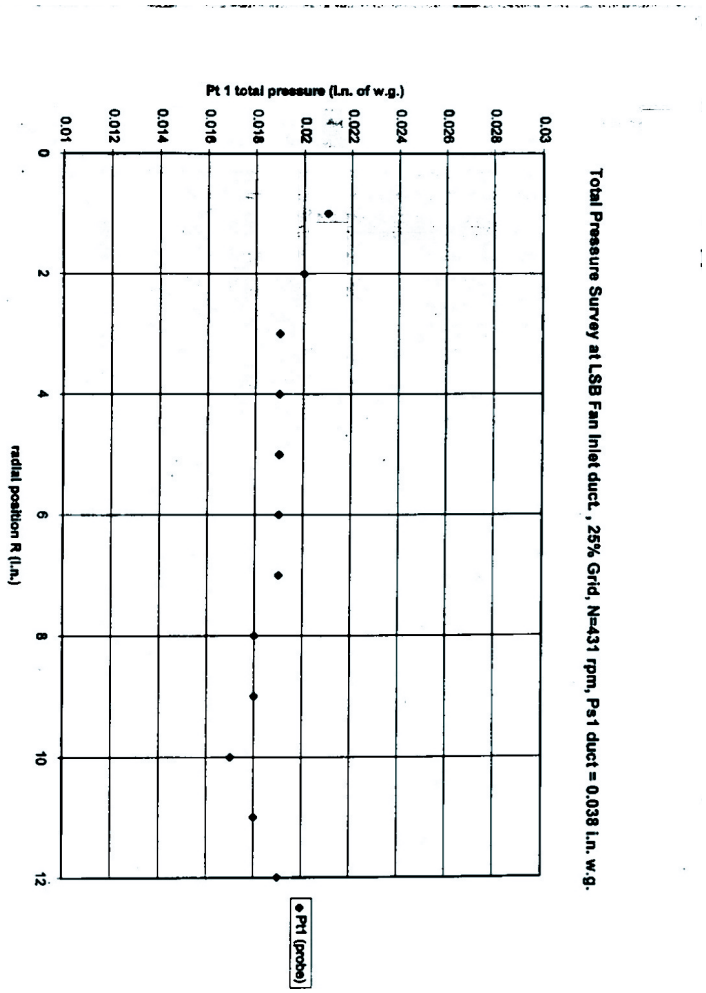

Figure 6.5: Results from total pressure survey conducted inside the LSB fan inlet duct

6.3.4 The Off-campus Set-up for Fan Static/Total Pressure Measurement

The test rig instrumentation consisted of four wall static pressure taps at the exit of the fan impeller (2 fan diameters downstream of the fan cut-off) and two wall pressure taps at the inlet to the fan (1.5 fan diameters upstream of the fan orifice). In the case of the LSB fan tests, since negligible temperature (and hence density) differences were observed between fan inlet and fan outlet, Eqs. D2 and D4 were used to obtain the fan pressure characteristics (Appendix D). The dynamic pressure was determined using Eq. D12. Thus the total pressure at both the fan inlet and fan outlet could be obtained, thereby permitting an evaluation of fan performance. A similar fan test and measurement strategy was employed in the case of the LSB fan, and subsequently for other model fans for which performance evaluation was required. The test setup for the LSB fan is shown in Figs. 6.6,6.8 and 6.7, 6.9.

Note that both total and static pressure measurements were taken across the LSB fan using different kinds of pressure probes; in particular, a 7-hole probe, a Kiel probe, and a Pitot probe. These were done for the purpose of comparison between instruments in order to evaluate their usefulness in such complex flow environments. Some of these results are presented in Appendix D.

6.3.5 Mini-LSB Fan Instrumentation

The Mini-LSB fan testing was conducted using two different experimental techniques. The first technique (similar to the off-campus LSB-fan testing) used a TSI hot-wire anemometer (at the fan exit) for volume flow rate estimates and micro-manometers for static pressure measurements. In the second technique, the measurement of volume flow rate was obtained using the Airflow machine (see Section **??** for details). The measurement of pressure was identical to the methods used in the LSB fan tests

Figure 6.6: LSB fan setup: view 1

Figure 6.7: LSB fan setup: view 2

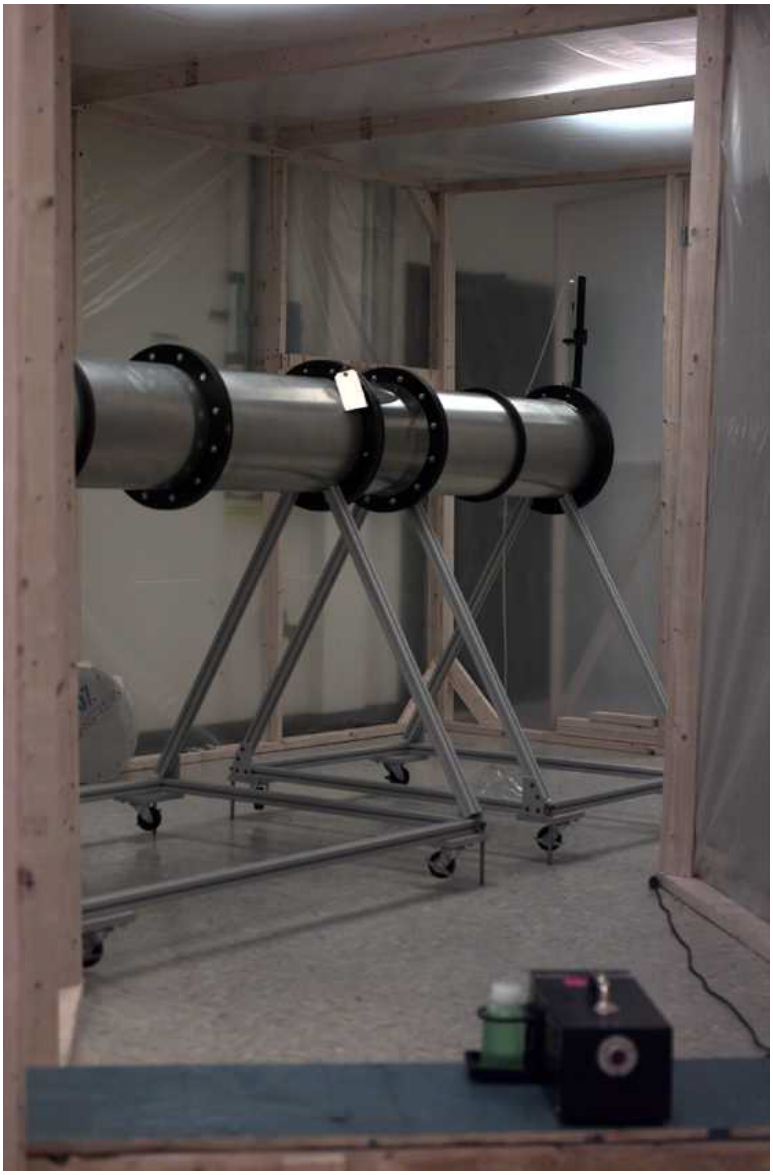

Figure 6.8: LSB fan setup: view 3

Figure 6.9: LSB fan setup: view 4

(except that pressure transducers were used instead of micro-manometers).

When using the first method for testing the Mini-LSB, the static pressure across the fan was measured using the multiple wall static pressure taps, circumferentially flush mounted at the fan inlet and fan outlet cross-sections as shown in Fig.5.9. These were connected to a micro-manometer similar to the LSB fan tests. The hot-wire instrumentation used in the testing the Mini-LSB was identical to that used in the off-campus LSB experiments. The same TSI IFA 300 anemometer was used to measure the volume flow rate downstream of the fan impeller. The measurement of volume flow rate was also obtained from hot-wire velocity traverses at 10D downstream of the Mini-LSB fan impeller inside the fan outlet duct (similar to the LSB tests) at three different radial locations at the same cross-section.

In the second method, however, the same wall static pressure taps were connected to pressure transducers (Setra model). The pressure transducers had a range of +/- 2.5-in.of H_2O, and a resolution of 0.01 inch of water. The inlet diameter of the wall taps was 1/16 inches. The static pressure at the fan exit was obtained by averaging the pressure obtained from the four wall taps at the fan outlet and two wall taps at the fan inlet locations. The flow rate was determined using the Airflow machine. The Airflow machine was used to obtain volume flow rate data, and also the static pressures.

For both methods, measurement of fan static pressure and calculation of dynamic and total pressure rise across the fan were made using a similar technique to that used in the LSB fan tests. The static pressure was measured with wall static pressure taps connected to a micro-manometer, the dynamic pressure was calculated using the volume flow rate, and the total pressure rise was calculated from the two pressures across the fan.

In both methods of fan testing, the fan rotation rate was determined by a stroboscope and verified by a digital tachometer. Motor performance was not evaluated

before conducting the Mini-LSB fan tests, thus, fan torque could not be determined. Overall efficiency, however, could be determined since it can be calculated from the combination of fan power input, IV, and fluid power across the fan, ΔpQ (see Appendix B.1); i.e.,

$$\eta_{overall} = \frac{\Delta pQ}{IV} \tag{6.1}$$

6.4 TRL-LSB Fan Testing: Mean Flow Field and Flow Visualization Studies

Detailed flow field studies were carried out in the TRL-LSB fan test facility. These included mean velocity and turbulence intensity measurements at the fan inlet and fan outlet sections. From the the mean velocity surveys conducted on the TRL-LSB fan, the volume flow rate was estimated. The study also included tuft flow visualization at the fan inlet and fan outlet ducts.

The LSB fan attached with a short circular inlet duct, but without any downstream ducting (Fig. 5.8) was driven by a D.C. motor at 192 RPM with free delivery (i.e., zero back pressure). The hot wire measurements were made both in the circular fan inlet duct at 1.5 inlet diameters upstream of the fan impeller and at 0.5 inlet diameters downstream of the fan throat (cut-off) section. The ambient temperature was $22°C$ (as in the calibration). The measurement locations were chosen to provide adequate boundary conditions for CFD code validation and to aid in understanding the flow dynamics through the fan. The measurements of mean velocity and normal stresses were taken at different radial positions for two reasons: first, in order to get mean velocity profiles and to obtain a more accurate estimate of the volumetric flow rate through the fan; second, in order to identify any swirl velocity components across the cross-section of the fan inlet duct. Similarly, the exit test measurement location

was selected downstream of the fan throat in order to avoid the separated flow region near the cut-off. Both the mean velocity and the variance were measured at fan exit.

The fan inlet velocity results show that the mean velocity is fairly uniform, in fact to within 95%. The mean flow velocity at the fan inlet and exit can be numerically integrated over their respective areas to obtain the volumetric flow rate through the fan at a given fan speed and system back pressure. Once the volume flow rate, Q, is estimated, then the volume flow coefficient, ϕ, can be determined. Table **??** provides the fan volume flow coefficient information based on the fan inlet velocity measurements. Only one inlet radial velocity profile was used in estimating Q since the facility was designed to insure that the inlet velocity profiles were homogeneous in the azimuthal direction. The fan inlet measurement grid covers up to 88 percent of the inlet duct area. The average velocity was estimated to be 6.3 m/s. This was obtained by assuming a linear velocity profile (from 6.3 to zero) at the wall for the outer 12 percent of the duct area. The procedure for calculating volumetric flow rate and volume flow coefficient is given by Eq. 6.5. Mean velocity and turbulent intensity measurements were also made downstream of the fan throat region in a rectangular duct using a rectangular measurement grid as shown in Fig. 6.10. .

Flow visualization was also conducted at both the fan inlet and exit sections using tufts. The flow visualization results at the fan exit region showed the presence of strong cross-stream velocity components and flow swirl, indicating probable secondary flow. A few measurements were taken at the fan exit to study the effect of flow angle variation on the output of a single sensor hot-wire.

The orientation of the single sensor hot wire applied to the flow at the fan exit is important, since the cross flow components change the effective velocity the hot wire measures. Standard hot-wires will operate fairly accurately in a flow with turbulence intensities of 20 percent or less. However the issue of misalignment of the flow with the hot-wire sensor is a major concern in a complicated multi-dimensional turbulent

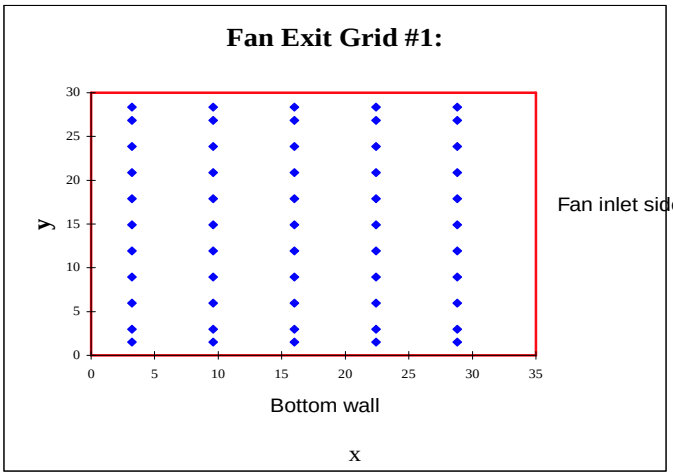

Figure 6.10: TRL-LSB fan exit grid for volumetric/velocity measurements

flow since the hot-wire sensor is sensitive to the flow angle. The effective cooling velocity past the sensor is increased by the misalignment of the absolute flow vector with the sensor (compared to the single component sought). Higher inclination of the flow to the sensor causes higher output velocities, therefore biasing the hot-wire signal output.

In the present investigation, a comparison of the mean velocity measured by a hot wire sensor aligned with the x-axis with the mean velocity signal measured from a hot wire aligned with the y-axis in the regions of large flow swirl (i.e. flow angle variation of 15-25 degrees), showed a difference of about 10 percent (see Table (6.4) 6.11). The sensor aligned with the y-axis located both in the upper and lower sections of the fan exit duct shows a higher mean velocity value compared to the sensor-aligned x-axis. It was also noticed, however, that hot-wire orientation did not significantly affect the mean velocity output in the flow regions where flow visualization showed the flow to be parallel to the fan exit duct (i.e., swirl-free), for example, at the duct centerline. It is important to note that the velocity bias due to different hot wire orientation is location-dependent in the fan exit duct due to the secondary flow in the x-y plane.

The application of a single (straight) hot-wire in a multidimensional flow cannot resolve the individual components (as shown in Fig. 6.12, i.e.; U_x, U_y and U_z); however, it can resolve the mixed components, for example, U_{zx} and U_{zy}. The actual flow vector, $\vec{U_f}$, and the measured flow velocity, U_{mx} (using a single straight hot-wire), are related by the following relations: Let $\vec{U_f}$ be the actual absolute flow vector in duct coordinates and let U_{my} and U_{mx} be the velocity measured by the hot-wire when aligned with the y and x axis respectively (see Fig. 6.12). $\vec{U_f}$ can be written in a component form:

$$\vec{U_f} = U_x\vec{i} + U_y\vec{j} + U_z\vec{k} \tag{6.2}$$

Assuming conduction losses and variance across the hot-wire are negligible, it follows that for a hot-wire aligned with respect to the x-axis (duct cross-stream direction)

location in fan exit duct	Hot wire orientation	Mean Velocity (W) m/s	Variance (m/s)	Flow direction
top center	Py	6.55	0.523	towards inlet side, X-Z plane
top center	Px	5.95	0.522	
centerline	Py	5.06	0.485	parallel to centerline, Z axis
centerline	Px	5.19	0.559	
bottom center	Py	6.39	0.381	towards fan hub, X-Z plane
botto center	Px	5.776	0.345	

Figure 6.11: Affect of single sensor hot-wire orientation on flow parameters

Figure 6.12: 3-dimensional flow over a single hot-wire sensor

the measured velocity is given by:

$$|\vec{U}_{mx}| = \sqrt{U_z^2 + U_y^2} = U_{zy} \tag{6.3}$$

Similarly for the y-direction, the measured velocity is given by:

$$|\vec{U}_{my}| = \sqrt{U_z^2 + U_x^2} = U_{zx} \tag{6.4}$$

Note that Eq. 6.3 is independent of U_x and Eq. 6.4 is independent of U_y.

By combining the results of the hot-wire study, the tuft flow visualization, and theoretical prediction of Eqs. 6.3 and 6.4, it can be inferred that the magnitude of the cross-stream velocity component in the y-direction is larger than the one in the x-direction in the location tested. Using the hot-wire measurements carried out at the duct centerline and combining them with the theory suggests that Eq. 6.3 and Eq. 6.4 are approximately equal. Equality of Eqs. 6.3 and Eq. 6.4, however, can imply one of two things; either the cross-stream velocity components are negligible; which suggests that the flow is perfectly straight and aligned with duct centerline; or that the magnitude of the cross-stream velocity components are equal, which suggests that the flow is not aligned with duct centerline. Flow visualization (using tufts) conducted at the fan exit showed that the flow is almost aligned with the duct centerline, which implies that the cross-stream components are negligible.

Thus a single straight hot-wire placed in three-dimensional flow can provide information about the relative magnitudes of the cross-stream velocity components (in the plane normal to the flow), but cannot resolve the individual magnitudes of the secondary velocity components. Hence alternate measurement techniques are needed. The difference in the magnitude of the velocity obtained from the two different hot-wire orientations can be attributed to the flow swirl, which causes a cross-stream flow on the hot-wires. This causes a bias in the measured velocity at the fan exit, which overestimates the actual velocity due to the contribution of the secondary components.

The flow rate is given by:

$$Q = \frac{\sum_{i=1}^{N} U_z}{N} \left(\frac{\pi D_{duct}^2}{4}\right) \tag{6.5}$$

The errors discussed above will result in overestimating the actual volumetric flow rate through the fan unless accounted for or eliminated, since the flow rate, Q, depends on U_z only and not U_{zx} or U_{zy}. Therefore, it was essential to map out the flow direction at the fan exit by using multiple hot-wire sensors (for example X wires) to determine the individual velocity components.

Note that this problem can be avoided by using cross-wires or triple wires. When using multiple hot wires it is important to note that the mean flow must lie inside a cone of acceptance around the probe axis in order to avoid ambiguity in the interpretation of the direction of the turbulence components (see Beuther et. al [8]). Note that hot-wires cannot resolve reversed flow regions at all, so an alternate measuring technique is necessary under reverse flow conditions (e.g., the LDA). A preliminary LDA study [1] was conducted on the off-campus LSB fan test facility that confirmed the presence of high flow swirl (or large secondary flow) at the fan exit.

Therefore, to avoid the necessity for this level of complexity, it was decided that the fan inlet (for the TRL-LSB facility) location would be more appropriate for flow rate measurements (since low turbulence intensity and no flow swirl were observed), instead of the fan exit location that suffered from high swirl.

[1] Vendor provided data

Chapter 7

LSB and Mini-LSB Experimental Test Results and Discussion

7.1 Introduction

This chapter presents the test results from the LSB and Mini-LSB fan performance measurements including the TRL-LSB hot-wire velocity surveys and tuft flow visualization. The individual test results are discussed. Also, comparisons of fan performance and system characteristics are made between the LSB and Mini-LSB to show how they conform to generalized fan scaling laws.

Detailed flow field studies of mean velocity and turbulent intensities at the fan exit and inlet of the TRL-LSB are presented and discussed in relation to the overall fan performance characteristics and measurement accuracy. Velocity profile observations and comparisons were also made at the far downstream location from the fan impeller using both the LSB and Mini-LSB fan test facilities. In addition, results are presented from the tests conducted using the Mini-LSB. These are used to illustrate the effect of the Reynolds number on fan performance, both in terms of pressure coefficient and overall fan efficiency.

7.2 Fan Installation Effects and System Characteristics

Generally fans do not operate in isolated environments, but rather fans have to work against a system resistance (the load) while generating an increase in the total pressure head at some capacity (volume discharge). The system resistance can be characterized by the difference in the total pressure losses from fan inlet to fan outlet. Generally the system elements operate under high Reynolds number conditions, thus system total pressure losses can be modelled similar to the losses occurring due to turbulent flow. Therefore, the system curve can be approximately characterized as a parabola with its origin at zero; i.e., as a pressure head that varies with the square of the volume flow.

A typical system characteristic for fan applications is shown schematically in Fig. 7.1. The fan operating point for a given fan at a given speed is given by the intersection of the fan characteristic and the system characteristic. At the fan operating point, the fan delivers enough pressure rise at a certain capacity to exactly overcome the system losses; i.e., the energy required to produce the flow exactly matches the energy delivered by the fan.

A fan's system characteristic in dimensionless form, can be obtained by plotting systems Euler number (equivalent to the inverse of the throttle coefficient), Eu_{sys} (Eq. 2.49), versus systems Reynolds number, Re_Q (Eq. 2.50). The system characteristic can generally be varied using outlet damper control; e.g., throttle (chokes), butterfly valve, gate valve (for high-pressure ratio fans), diffuser cones, grid resistance, etc. Changing the upstream or downstream resistance alters the system characteristic, and shifts the fan operating point. The fan characteristic (the pressure head/volume flow curve) changes independently of the system resistance. For example, the use of variable-inlet vane control causes the fan characteristic to change independently of

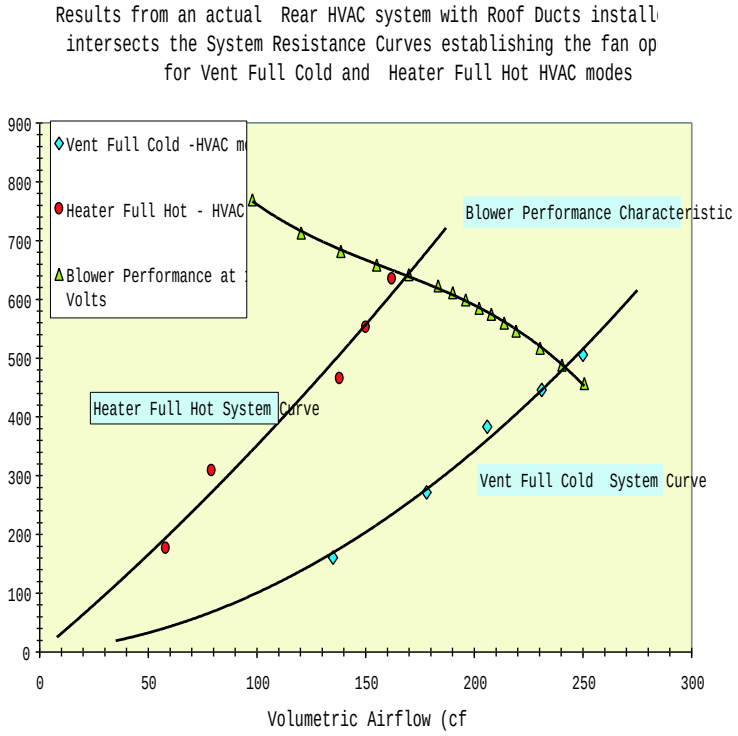

Figure 7.1: A typical HVAC module system characteristic versus a fan characteristic

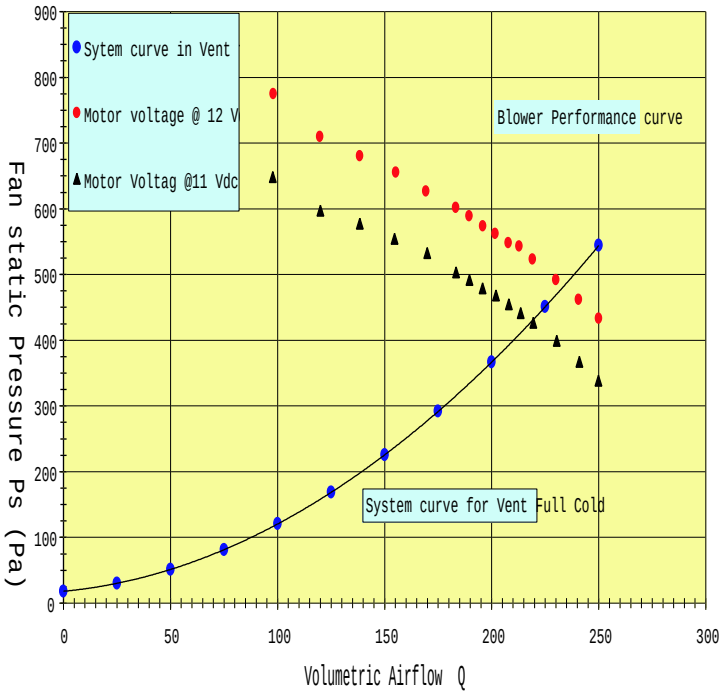

Figure 7.2: Fan performance characteristic of forward curved type blower: pressure/volumetric flow curve as a function of fan speed (or voltage shift)

the system characteristic because of the pre-rotation (or pre-whirl) of the flow entering the fan orifice (Jorgensen [35]). The variable speed method (i.e., changes in fan speed when everything else is kept constant) of changing fan capacity (volume flow) simply shifts the fan characteristic when plotted in dimensional form, as shown in Fig. 7.2. Variation in fan speed at constant system resistance does not affect the system characteristic, rather it is the fan operating point that moves along the system curve.

In general, the effects due to fan installation can be of two types:

- Effects that alter the fan performance characteristic completely, thereby modifying the aerodynamic characteristics of the fan, in addition to shifting the fan operating point.

- Effects that alter the fan system resistance, thus leading to a shift in the fan operating point only, while preserving aerodynamic fan performance.

In certain situations, it is possible to have system elements located at different sections of the fan system. These not only cause a variation in system characteristics, but also affect the fan characteristic by significantly modifying the local flow field. Examples include inlet bends (which can cause pre-whirl in addition to pressure losses), complicated inlet ducting, downstream wide angle diffusers, etc. *Only experimental testing can discern the effects on fan performance due to system effects and/or due to aerodynamic reasons.*

The effects of inlet and outlet ducting on the overall fan performance characteristics can be significant ([10], [15] and [71]). Free inlet or outlet means that the fluid enters or leaves the fan scroll directly to or from the undisturbed free environment. For the case of free entry (no inlet duct), fluid dynamic theory suggests that a potential flow-like pattern exists, similar to a suction flow into an orifice positioned in a plane wall. Depending on the fan orifice lip geometry, and in the absence of any swirl devices (inlet vanes or meshes), the bulk of the flow behaves as a three dimensional potential sink. It is important to recognize that a pressure difference alone in a potential flow cannot generate any flow swirl *since in the absence of density variations, viscous effects are required to generate or introduce vorticity into the main flow.* These can be introduced by the surfaces or solid boundaries, whether stationary or rotating.

Fan inlet ducting can be a source of swirl and flow non-uniformity for a variety of reasons; e.g., the inlet lip geometry of the inlet duct is not properly rounded, the

inlet duct has bends, the inlet duct diameter does not match the diameter of the fan inlet orifice, or the length of the duct is not long enough so that a fully developed symmetrical and straight flow occurs at the fan inlet (Cory [15]).

The velocity profile at the outlet of a centrifugal fan is highly non-uniform and exhibits considerable flow swirl. Thus the long and straight ducting at the fan outlet can allow the flow to sufficiently diffuse and become more uniform. Because of high flow swirl and non-uniformity at the exit of the fan, however, additional flow conditioning is usually required to obtain reasonably uniform pressure and velocity profiles. Since the dynamic pressure at the fan exit is quite high, especially for high specific speed fans, attachment of a straight duct (of larger diameter than the fan throat) at the exit of the fan allows for further diffusion (conversion of dynamic pressure into static pressure) to occur inside the outlet duct (*at least as long as there is no flow separation*). For the case of a fan outlet duct of the same diameter as the fan throat, the average *dynamic* pressure generated by the fan is conserved (for a constant density flow) inside the straight outlet duct. The fan outlet *static* pressure is not conserved, because of the static pressure losses in the ducting (at least for the case of constant density flows of constant cross-sectional duct area). For the LSB, the fan throat cross-sectional area was slightly larger than the exit duct cross-sectional area.

The presence of a diffuser at the exit of the fan (as in the HVAC prototype) alters both the static pressure and the dynamic pressure available at the fan exit. Real (viscous) flows through real diffusers generally have efficiencies of conversion of dynamic pressure (kinetic energy per unit volume) into static pressure that are less than unity; i.e., there is a loss of total pressure across the diffuser that implies that static pressure recovery was incomplete.

In summary, different fan inlet and fan outlet geometries present different inlet and outlet boundary conditions. These can have significant effects on the flow field

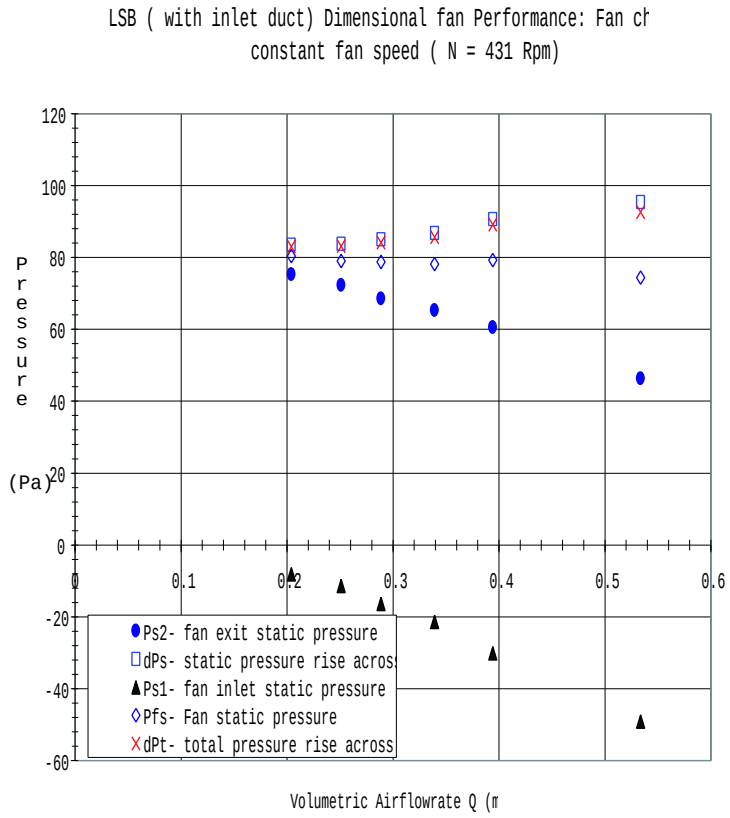

Figure 7.3: LSB fan (with an inlet duct) performance characteristics

through the fan, and can alter the fan performance characteristics in addition to the alterations due to the system characteristics.

7.3 LSB Fan Performance Results

7.3.1 Pressure/Flow Characteristics

Fan performance testing conducted on the LSB fan showed the typical characteristic behavior of a forward curved centrifugal fan. The LSB fan (with an inlet duct) performance characteristics are shown in Fig. 7.3 in terms of the standard fan performance

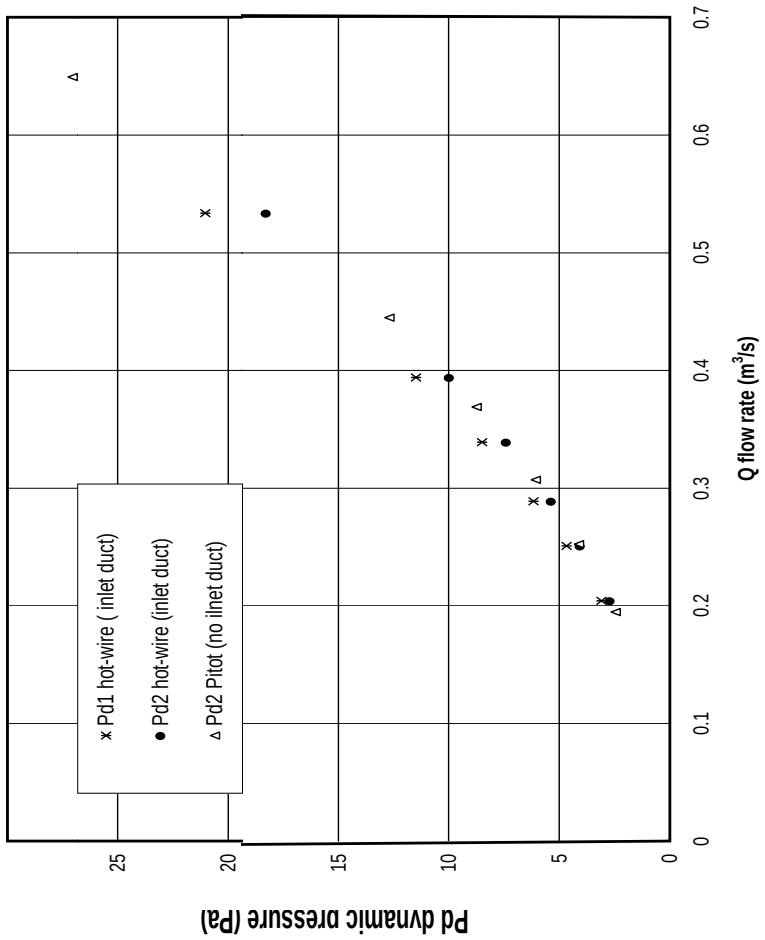

Figure 7.4: Dynamic pressure measurements across the LSB-fan inlet and exit

parameters, pressure and volume flowrate. For all measurements, the fan inlet duct axis was aligned with the fan scroll inlet orifice axis. Dynamic pressure variations with flow coefficient are plotted in Fig. 7.4.

It can be observed from Fig. 7.3 that both the static and total pressure rise across the fan follow similar trends, with some small variation apparent at the higher flow coefficients. The Δp_s and Δp_t both increase with the flow coefficient over the range of volume coefficients tested. The differences between Δp_s and Δp_t are mainly due to

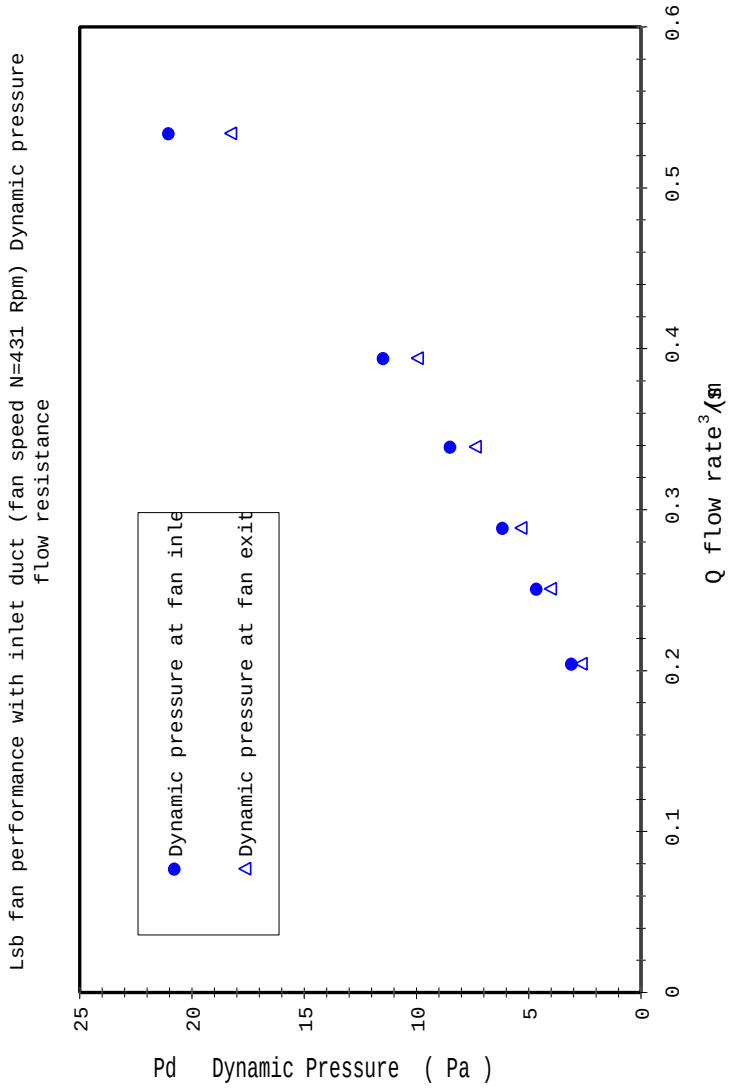

Figure 7.5: Dynamic pressure measurements across the LSB-fan inlet and exit based on flowrate measurements conducted 10D downstream of LSB

the differences between the dynamic pressure at the fan inlet (P_{d1}) and the fan outlet (P_{d2}). As can be seen in Figs. 7.4 and 7.5, the differences between the fan inlet and fan outlet dynamic pressures increase in a nonlinear fashion. Notice that the dynamic pressure variations (for an incompressible flow) between the fan inlet and fan outlet are mainly due to differences in fan duct diameters. Also P_{d1} is greater than P_{d2} for the flow range tested.

The dynamic pressure P_d can be expressed in terms of the volume flow rate (or equivalently the volume coefficient) as in Eq. D.5. The result is:

$$P_d \propto \rho\phi^2(\omega D)^2 \tag{7.1}$$

This can also be expressed as a dynamic pressure coefficient:

$$\Psi_{P_d} = \frac{P_d}{\rho\omega^2 D^2} = \phi^2 \tag{7.2}$$

Eq. 7.2 shows that the dynamic pressure curve is a parabolic function of flow coefficient.

In addition it can also be shown (for a circular duct with diameter, D) that

$$P_d = \rho\frac{Q^2}{8\pi^2 D^4} \tag{7.3}$$

If the flow rate and density remain constant between the fan inlet and outlet (which is generally the case for a fan operated at constant speed inside the stable operating range), then Eq. 7.3 can be used to obtain the difference between the P_{d1} at the fan inlet and P_{d2} at the fan outlet. It follows from Eq. 7.3 that:

$$P_{d2} - P_{d1} = \rho\frac{Q^2}{8\pi^2}(\frac{1}{D_2^4} - = \frac{1}{D_1^4}) \tag{7.4}$$

Since D_2 is larger than D_1 (for the LSB, $D_1/D_2 = 0.93$), Eq. 7.4 implies that $P_{d2} < P_{d1}$. The experimental results shown in Fig. 7.4 are consistent with the theoretical result from Eq. 7.4, as noted above.

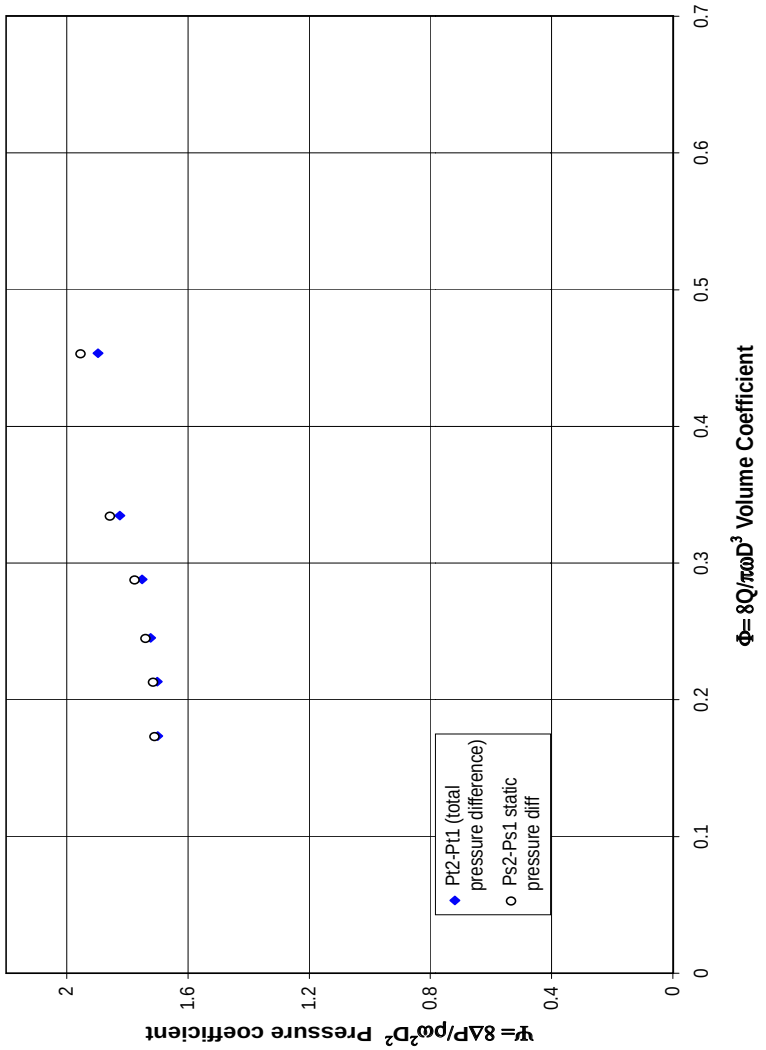

Figure 7.6: LSB-fan Non-dimensional performance characteristics curve (i.e.,$\psi - \phi$): differential static and total pressure rise across fan

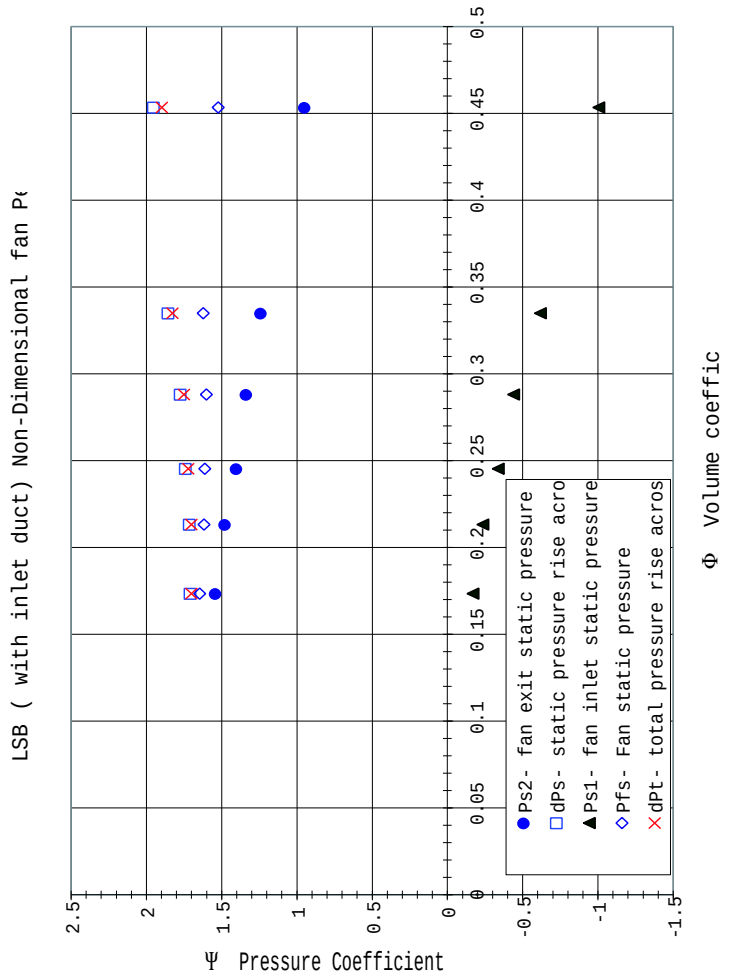

Figure 7.7: LSB-fan Non-dimensional performance characteristics curve (i.e.,$\psi - \phi$)

The LSB fan performance characteristic curve is presented in a non-dimensional form (i.e.,$\psi - \phi$ curve) in Figs. 7.6 and 7.7.It is interesting to note that the fan outlet dynamic pressure, P_{d2}, in the case of the LSB fan without any inlet duct follows almost an identical trend to the LSB fan with inlet duct. The values of the volume coefficient, however, are different, especially at high flow coefficients. Note the LSB fan-exit static pressure results are shown in Fig. 7.7.

Figure 7.8 shows the non-dimensional plot of the LSB fan performance characteristics. The static pressure rise across the fan, Δp_s, and the fan exit static pressure, P_{s2}, and the fan static pressure, P_{fs}, are plotted in Fig. 7.8. Representing fan performance data using P_{fs}[1] instead of Δp_s is a standard practice of adopted industry (ASHRAE Equipment Handbook 1988). Note that P_{fs} is lower than the Δp_s. Usually P_{fs} equals P_{s2} only if $P_{t1} = 0$, which is generally true for fans without any inlet duct.

A dimensional plot of fan static pressure (P_{fs}) verses volume flow rate (Q), is shown in Fig. 7.8. It can also be observed that $P_{fs} > P_{s2}$. This can be explained as follows: For case of the LSB fan with an inlet duct, results indicate that $P_{t1} < P_{atm}$ since the inlet static pressure is below atmospheric, i.e., $P_{s1} < P_{atm}$ (Fig. 7.3). This result was expected since the fan impeller causes a suction flow at the fan scroll orifice. In addition the value of the static pressure at the fan inlet duct will vary with the location away from the fan orifice. Generally the maximum suction pressure is achieved just upstream of the fan impeller inlet shroud. This implies that $P_{fs} > P_{s2}$.

The suction pressure at the fan inlet causes a positive contribution to the overall fan static pressure rise, Δp_s, across the fan, making it more positive as flow coefficient increases. This trend in Δp_s can be observed in Fig. 7.3. This also explains why the fan exit static pressure, P_{s2}, is a continuously decreasing function of the flow

[1]Fan static pressure is defined as: $P_{fs} = \Delta P_t$-P_{d2}; which is equivalent to P_{s2}-P_{t1}. Note that the fan static pressure is not equal to the static pressure difference for fans with inlet ducts. For fans without an inlet duct, however, fan static pressure simply equals fan exit static pressure

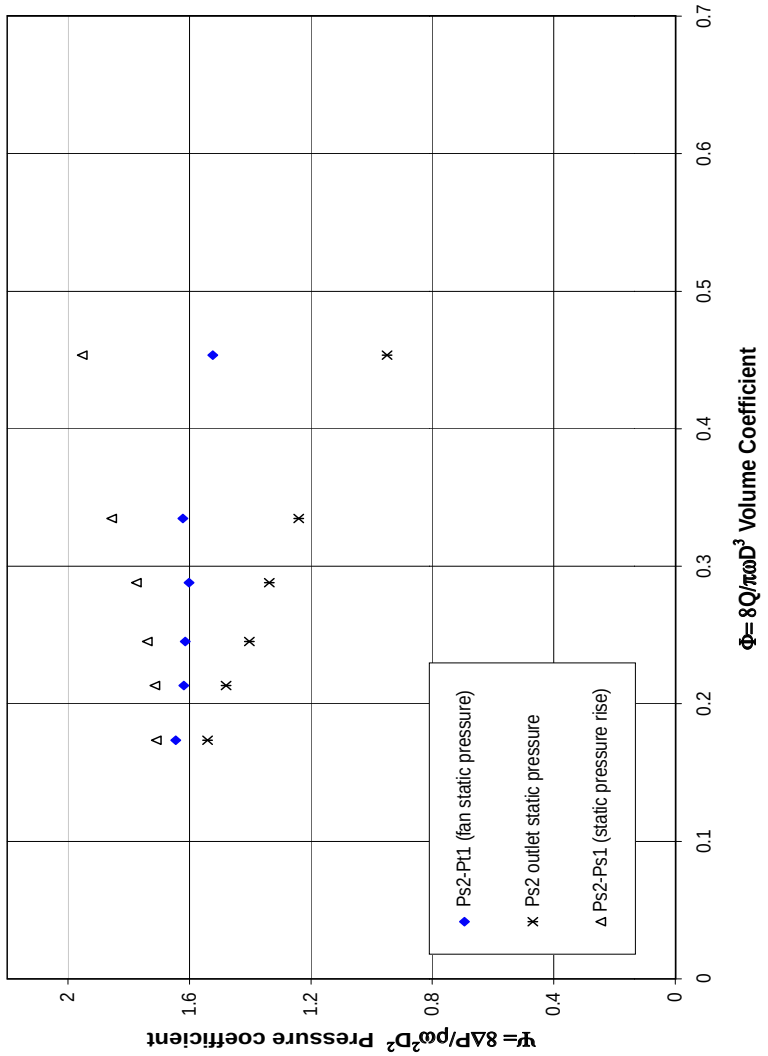

Figure 7.8: LSB-fan (with inlet duct) static pressure characteristics: fan static pressure, fan exit static pressure and static pressure differential

coefficient for the fan tested without an inlet duct. This can be contrasted with the static pressure rise across the fan, Δp_s, which shows an increasing trend with an increase in flow coefficient (at least for within flow range tested), because of the positive contribution of the static pressure at fan inlet. This was true both for fan tests with and without the inlet duct.

Fig. 7.9 shows the $\delta - \phi$ fan system characteristics using both the static pressure rise across the fan, δ_s, and, the total pressure rise across the fan, δ_t. Fig. 7.9 shows that the system resistance decreases while the volume flow coefficient increases. It can be seen clearly from Fig. 7.9 that δ is almost independent of the pressure rise, consistent with its weak power dependence (see Eq. 2.86).

Figure 7.10 shows the Euler number, Eu_{sys}, versus the Reynolds number, Re_Q, based on flow rate. Notice that the Euler number is also a function of $\Delta p/Q^2$, similar to the diameter coefficient, and that both parameters are independent of fan blade rotation rate. Thus Fig. 7.10 represents the system characteristic for the LSB fan test facility. As expected the Euler number decreases as the pipe or systems Reynolds number increases. Note that Euler number becomes independent of the systems Reynolds number as the systems Reynolds number (which is independent of fan rotation) increases. This also agrees with the fact that at very high Reynolds number, system losses become independent of viscous effects. Note that the systems Reynolds number, Re_Q, is related to the rotational Reynolds number (for rotating blades), R, through the volume flow coefficient factor, as shown by Eq. 2.55.

Fan performance tests for the LSB fan without a fan inlet duct indicate that the fan exit static pressure is a continuously decreasing function of the flow coefficient. The total pressure curve, however, is fairly flat for higher resistance settings, but then increases slightly over the flow coefficient range that was achievable in the LSB fan facility. The fan characteristic is incomplete, however, since the maximum achievable flow coefficient is only 0.5. It is expected that the fan characteristic based on total

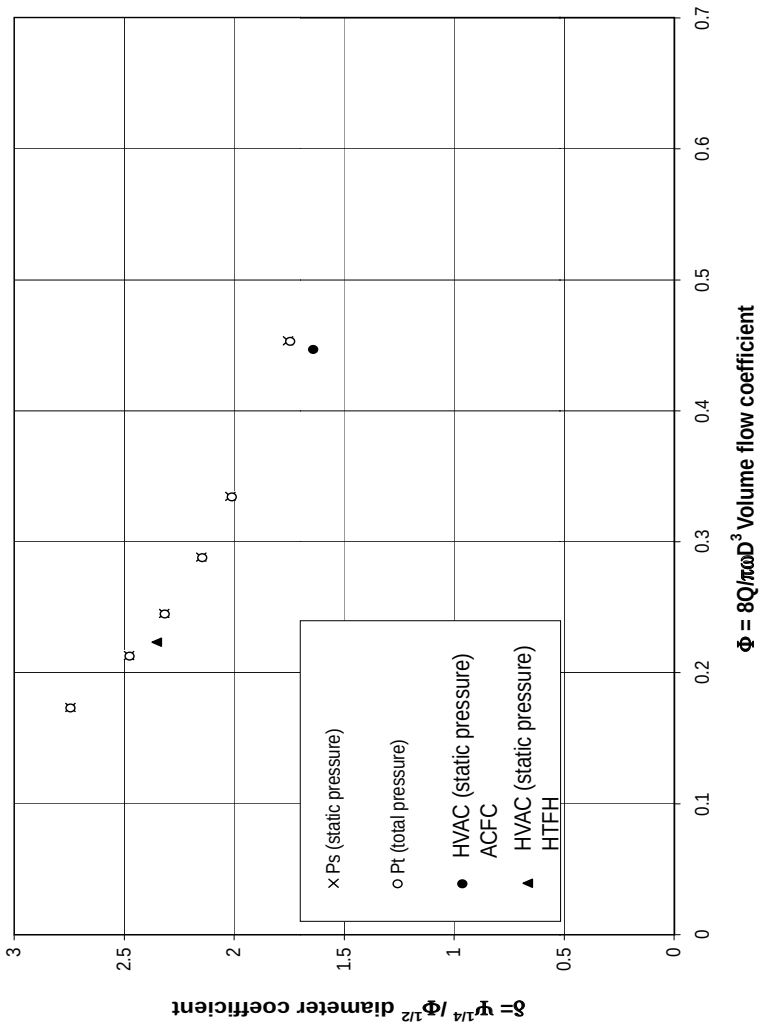

Figure 7.9: Plot shows the LSB-fan diameter coefficient versus volumetric coefficient characteristic

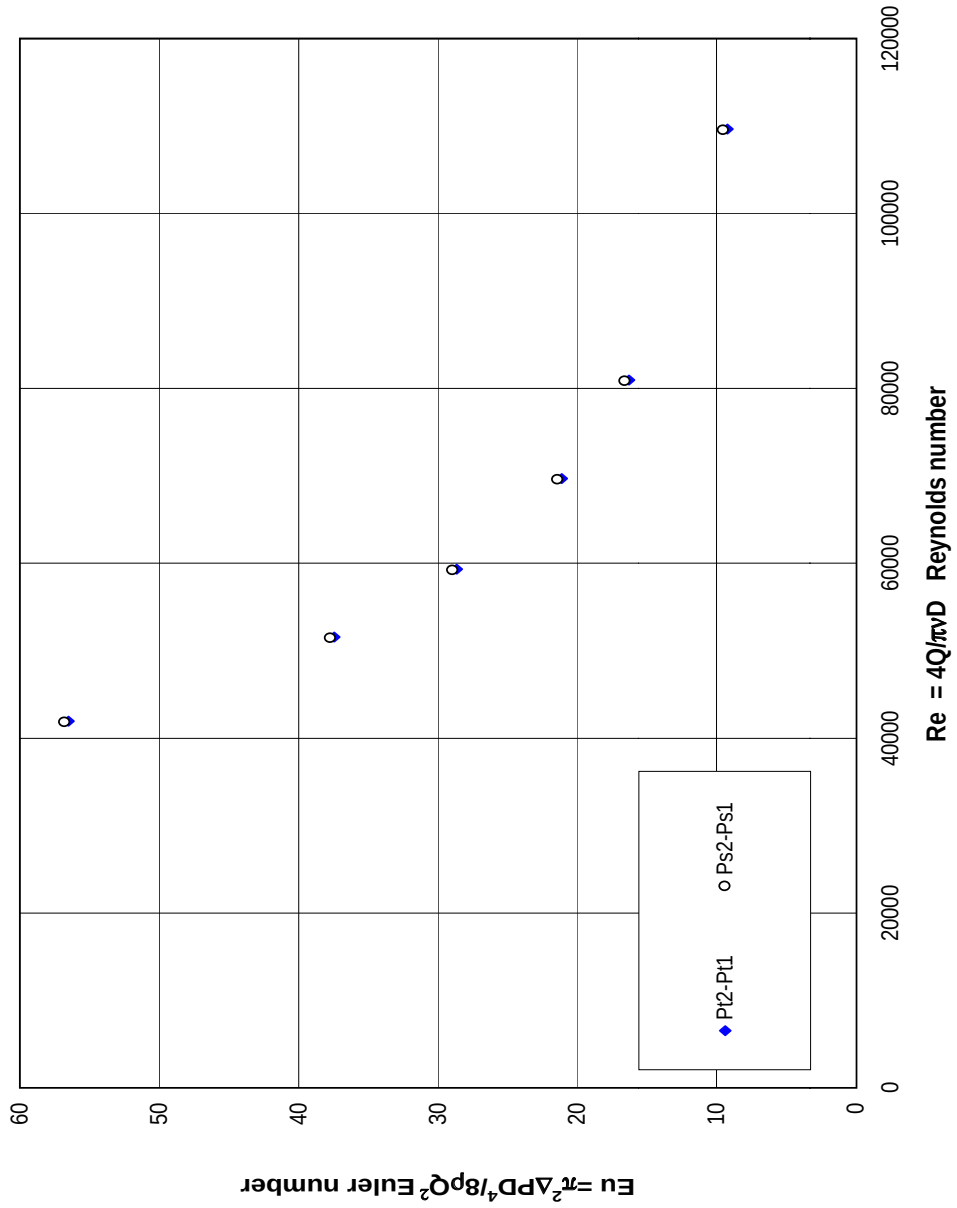

Figure 7.10: Plot shows the LSB-fan Euler number versus flow (system) Reynolds number

pressure will decrease after reaching a maximum. This can only be achieved, however, by using an auxiliary fan which will reduce the exit static pressure, thereby increasing the flow coefficient range to allow the complete fan characteristic to be mapped. This was easily accomplished on the Mini-LSB fan using the AirFlow machine which has the auxiliary fan to extend the range of flow coefficient (refer to Chapter 6 and Appendix C).

7.3.2 Effect of System Resistance on the velocity profiles far downstream of the fan impeller

The mean velocity measurements at the fan exit (exact locations are shown in Fig. 5.7) under different grid resistance settings are shown in Figs. 7.11 and 7.12. These measurements were made at a duct cross-section across the vertical and 60 degrees from the vertical. From Fig. 7.11 it is observed that the mean velocity profiles are slightly skewed (less than 8% variation from wall to wall) except in the outer 5% of the duct cross-section area near the walls. They show that the flow in the outlet duct is slightly non-uniform, and indicate the presence of a weak swirl. Turbulence intensity levels were on the order of 3 percent or less for 90 percent of the duct cross-section. The turbulent intensity was higher (10 to 30 percent) very near the wall (at 90% duct diameter). The near wall region is the well-known boundary layer region in which the mean velocity rapidly falls from the free stream velocity in the pipe core region to zero at the pipe wall in order to satisfy the no-slip condition.

Velocity surveys were made at the fan inlet duct (Off-campus LSB facility). For some of the tests, the fan inlet region (for the case of a long inlet duct) showed a much higher turbulence intensity of about 15%. This could be traced to the flow separation at the leading edge of the inlet duct. Note that for the fan tests under consideration, the LSB fan test facility did *not* have a proper bell-mouth to make the flow more

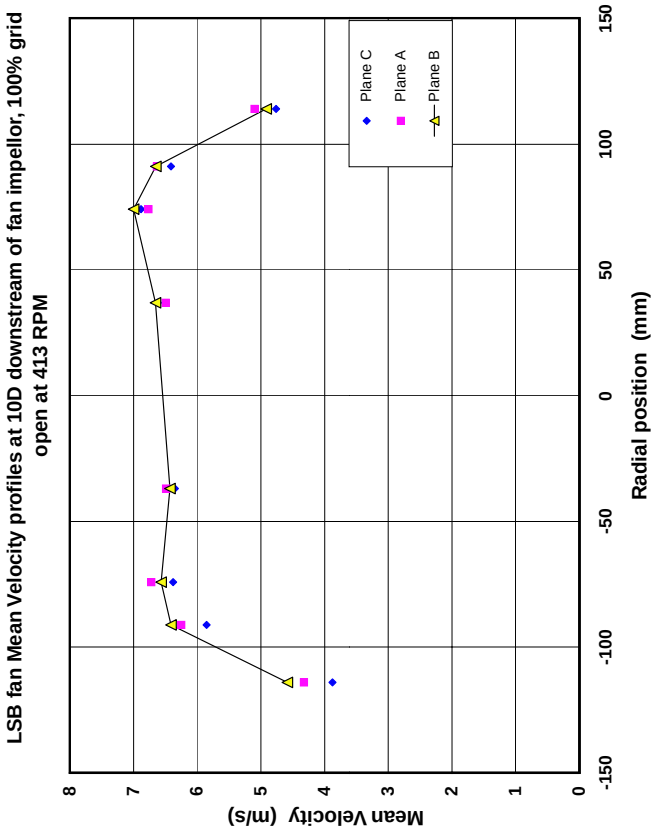

Figure 7.11: Plot shows the hot-wire based mean velocity measurements downstream of the fan exit: at 100% grid open area

Figure 7.12: Plot shows the hot-wire based mean velocity measurements downstream of the fan exit

uniform and avoid the flow separation at the inlet. This was installed later as noted below. The turbulence intensities observed at the fan inlet were considered too high for reliable volume flowrate estimates from the hot-wire data, so the volume flow rate was estimated using velocity surveys at the fan downstream location in accordance with AMCA fan test codes, as mentioned earlier. It addition, inlet velocity traverses using total head tubes were also conducted for few fan operating points (different resistance settings) to obtain independent estimates of the dynamic pressure at the fan inlet. These are presented in Fig. 7.13. Surprisingly (in view of the high turbulence intensity at the inlet), the results indicated that the volume flow measurements at fan inlet were within 7% of the estimates based on fan outlet measurements.

This result was unexpected, and differs significantly with results obtained from both, the fan inlet velocity surveys conducted on the TRL-LSB; that indicated very low values of turbulence intensities (2-4%), and those obtained from same fan's exit region; which also indicated low turbulence intensities (on the order of 3%) as mentioned above. A possible reason for these differences in the LSB fan's inlet turbulence intensity values, could be due the extra ducting (both on the inlet and exit side of the LSB fan) in the case of the Off-campus test facility, in addition to the much higher back-pressures encountered in the Off-campus LSB in contrast to the TRL-LSB which was operated at the free delivery condition.

Fan exit velocity profiles surveyed at 10 fan diameters downstream of the fan impeller are shown by Figs. 7.12 and 7.10. These indicate a non-uniformity and skewing of the velocity profiles. A considerable overshoot was observed in the magnitude of velocity towards the outer peripheral region of the circular cross-section for the case of highest system resistance (25% grid open area), whereas more skewing was observed in the velocity surveys conducted at various cross-sectional planes for the case of low resistance (51% grid open area and no grid at all). The mean flow patterns observed at 10 diameters downstream of fan impeller indicated that the velocity profiles were

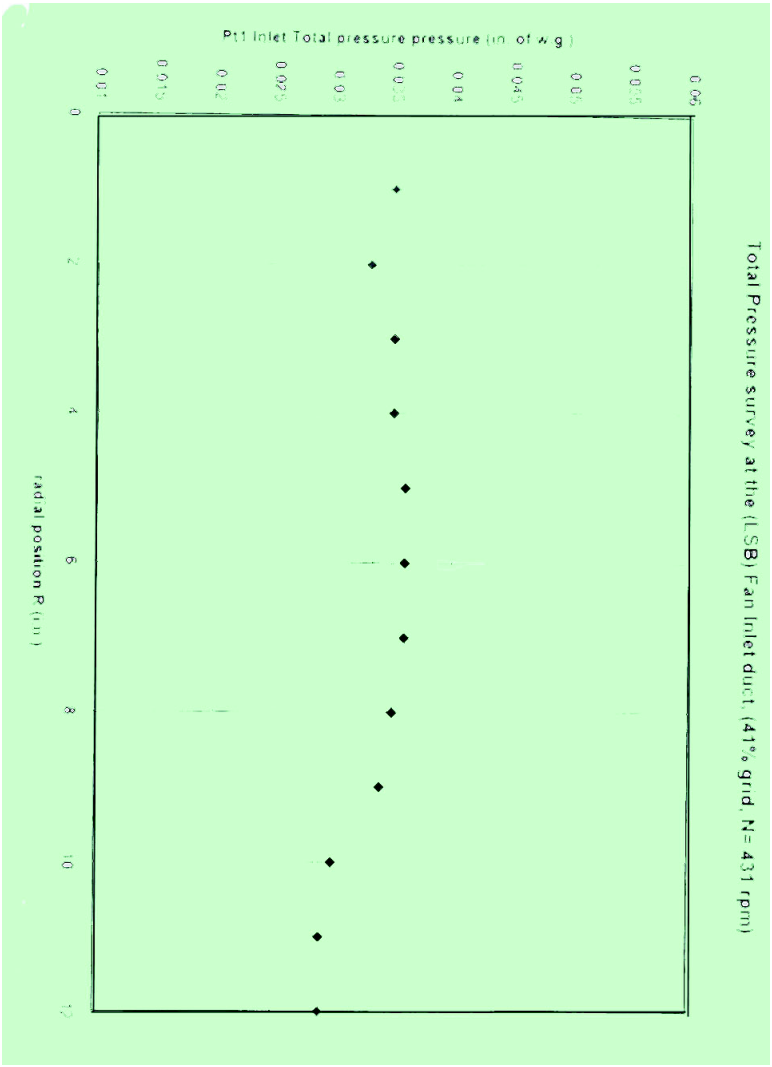

Figure 7.13: Plot shows the total pressure (based on a Pitot tubes) at the fan inlet

Figure 7.14: Plot shows the turbulence intensity profiles surveyed at 10 fan diameters downstream of the LSB-fan impeller

not fully developed, but rather were still developing.

Turbulence intensity profiles surveyed at 10 fan diameters downstream of the fan impeller are shown in Figs. 7.14 and 7.15 . The turbulence intensities range between 3 to 20 percent, with low values in the core flow of the circular duct and increasing turbulence levels towards the duct walls. For the fan exit region (i.e., far downstream at 10 diameters), a turbulence intensity of 3% was achieved for the bulk of the flow. Thus this location is appropriate for the measurement of volume flowrate as required for the mapping fan performance.

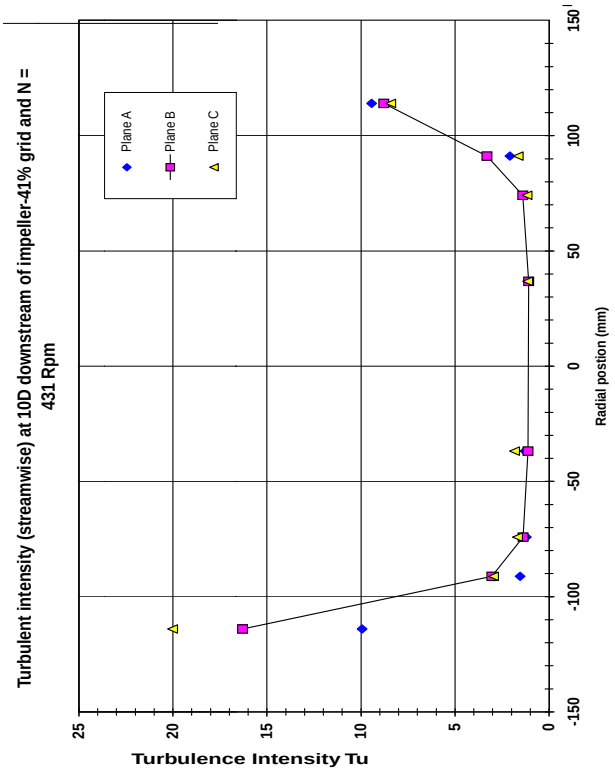

Figure 7.15: Plot shows the turbulence intensity profiles surveyed at 10 fan diameters downstream of the LSB-fan impeller

7.3.3 Alternative method of fan data representation including kinetic energy effects across the test range

An important observation was made while representing fan data in terms of the *total* pressure rise across the fan, by contrast with the *static* pressure rise across the fan. The fan performance curve takes a distinctly different shape, depending on which is used. There is both a different slope of the characteristic for high flow coefficients and for the flow coefficient at which the fan curve reaches its peak (maximum pressure rise). From the LSB fan tests it is clear that in order to accurately characterize true fan performance, *both* the static pressure head *and the dynamic pressure head contributions should be included in the analysis.* The fan causes the total pressure to change from inlet to outlet. The relative contributions of the static pressure increase compared to the dynamic pressure increase (i.e., the kinetic energy component) can vary significantly as the system resistance (or back pressure) is varied. This can significantly affect the choice of the best operating point of the fan (the intersection of the fan performance and the fan efficiency curve with the system characteristics). To understand the effects of the fan's dynamic pressure characteristics on the best operating point (and in motor selection), both the fan static and total efficiency data are required. The choice of the best operating point of the fan can affect motor selection, since the static and total efficiencies intersect the system characteristic at different points (see schematic drawing in Fig. 7.16).

The inclusion of kinetic energy represents a markedly different approach compared to the traditional method of representing fan data, but would seem to provide a better indication of a fan's potential. From the point of view of system characteristics and fan selection, it is generally advisable, and safer to use the fan total pressure for the estimation of system pressure losses, which allows proper fan selection. The danger of using static pressure to estimate system losses (and system characteristics) can

Figure 7.16: Plot shows the effect of fan operating point based on static efficiency or total efficiency

result in the improper fan selection (i.e., the fan selected will not produce the desired pressure rise at the required capacity). System loss estimation based on static pressure could be done when the differences in dynamic pressure across the system (resistance) component are negligible.

One possible rationalization of the traditional approach using only static pressure is that many fans are followed by diffusers that are so poorly designed that they give no pressure recovery at all. In such cases, inclusion of kinetic energy in the analysis would be misleading, since the kinetic energy contribution is effectively thrown away. For a properly designed diffuser, however, the new approach would seem advantageous. Regardless, the new approach gives a better indication of exactly what is lost by bad design.

7.4 Comparison of fan performance between the scale model (LSB) and the HVAC prototype fan

The experimental results shown in Fig. 7.17 indicate that the LSB fan pressure head characteristics based on static pressure are in agreement with the established fan curves for the typical forward curved centrifugal (squirrel-cage) fans. The LSB fan operating range with the large scale fan test facility is wide enough to simulate both operating modes of the actual automotive HVAC fan: heater full hot and air-conditioning full cold.

In Fig. 7.17, the actual HVAC fan performance (based on industry tests using the AMCA Plenum chamber method) are plotted together with the model LSB fan performance. It is observed that the LSB fan static pressure coefficient is higher than that produced by the HVAC fan prototype. In Fig. 7.18, the fan/system charac-

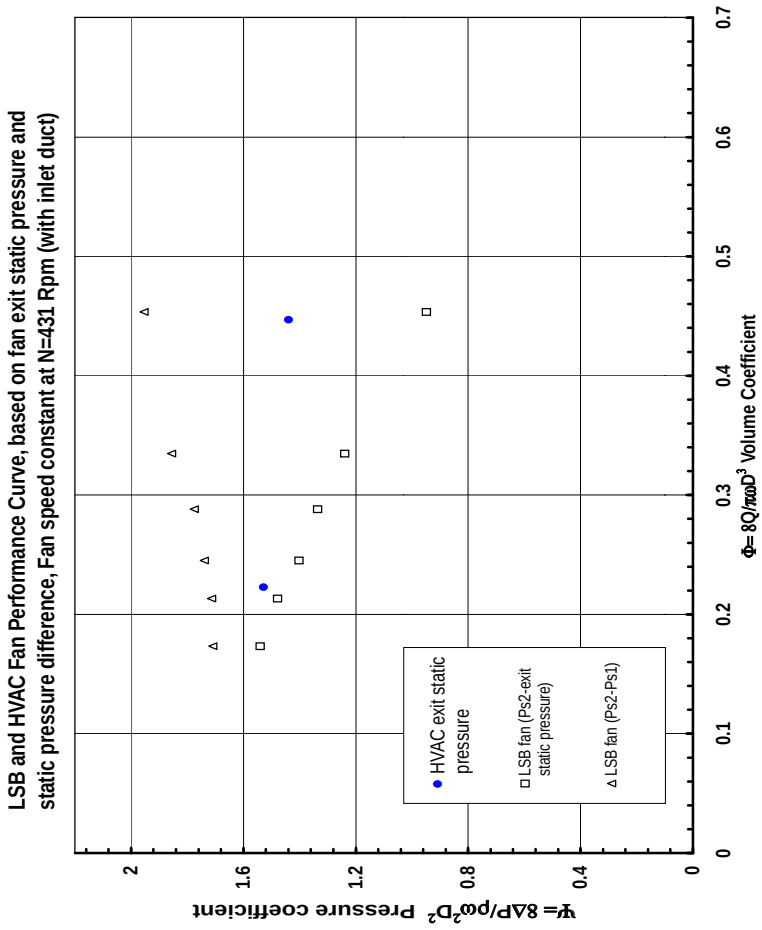

Figure 7.17: HVAC prototype module fan performance characteristics for Vent and heater modes

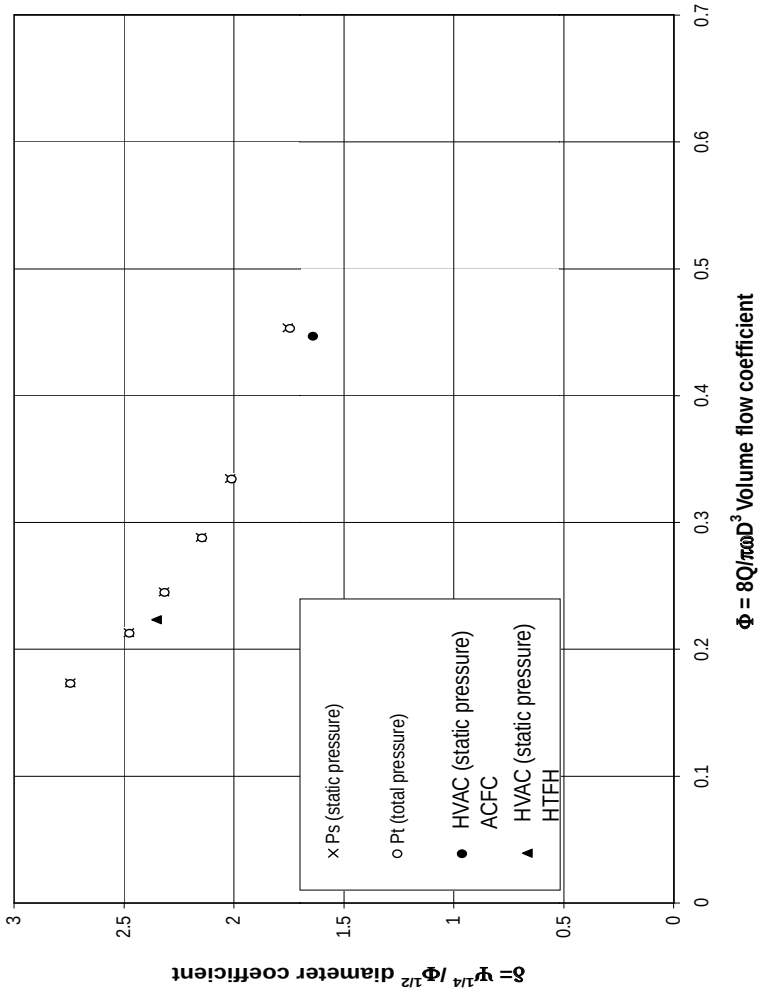

Figure 7.18: Comparison of HVAC prototype module and LSB fan performance characteristics: diameter verses volume coefficient

teristics (diameter versus flow coefficient) for the LSB fan and the HVAC prototype are plotted. Again, from Fig. 7.17, it is clear that the discrepancy between the LSB and prototype fans is significant. As noted earlier, true similarity between the LSB fan performance and the prototype HVAC fan performance characteristics cannot be expected since the both the inlet, and especially the exit geometry, of the combined fan-duct system of the prototype HVAC module are not identical to the LSB fan test facility. In order to confirm that these differences arise from geometry and not a failure of the generalized fan scaling laws, the LSB fan performance should be compared to an exactly similar geometric model of the large-scale facility while maintaining both geometric and dynamic similarity between the two facilities. This is exactly the point of the Mini-LSB, the exact 1/3 scale model of the LSB described in Chapter 6. These Mini-LSB fan test results are presented in Section 7.5.

7.5 Mini-LSB Fan Performance Results

7.5.1 Mini-LSB fan performance results in classical and new variables

The Mini-LSB fan efficiency, η, is plotted versus flow coefficient, ϕ, in Figs. 7.19 . The Mini-LSB overall efficiency is also plotted against the Reynolds number based on fan speed (see Fig. 7.20 . Also, the the overall efficiency is plotted against the flow (system) Reynolds number as shown in Fig. 7.21 . In addition, the diameter coefficient versus the flow coefficient is shown in Fig. 7.22 .

The Mini-LSB pressure coefficient measured using the hot-wire-micromanometer (HTW-MIC) method shows some scatter and non-smooth variation across the flow range. In this method, the pressure measurements were obtained using a micromanometer, whereas, for the Airflow-machine method pressure transducers were used.

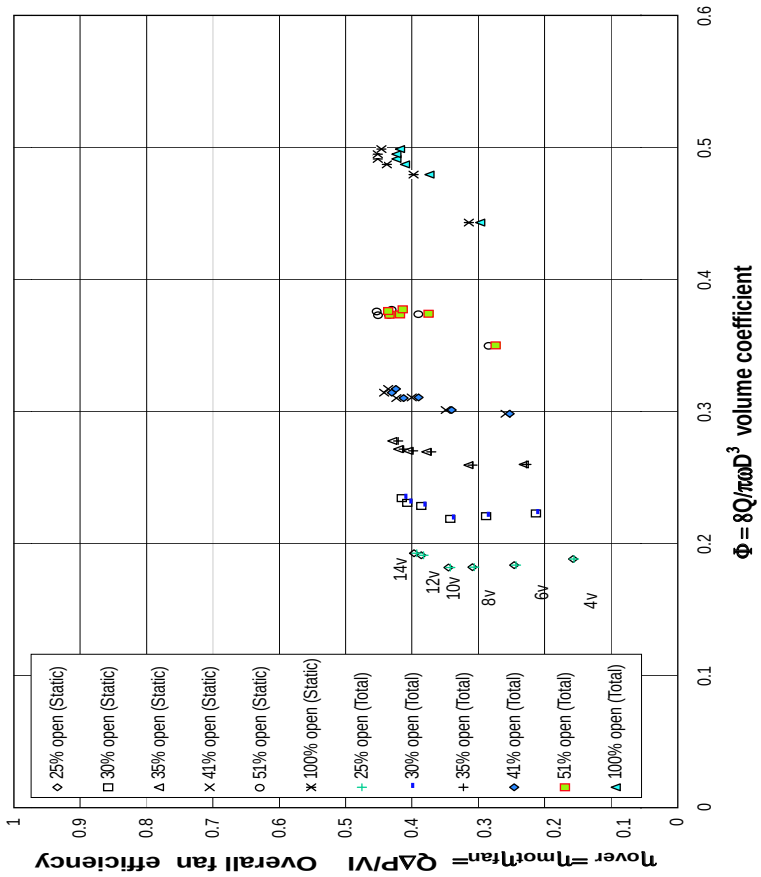

Figure 7.19: Plot shows the Mini-LSB-fan overall efficiency versus volumetric coefficient

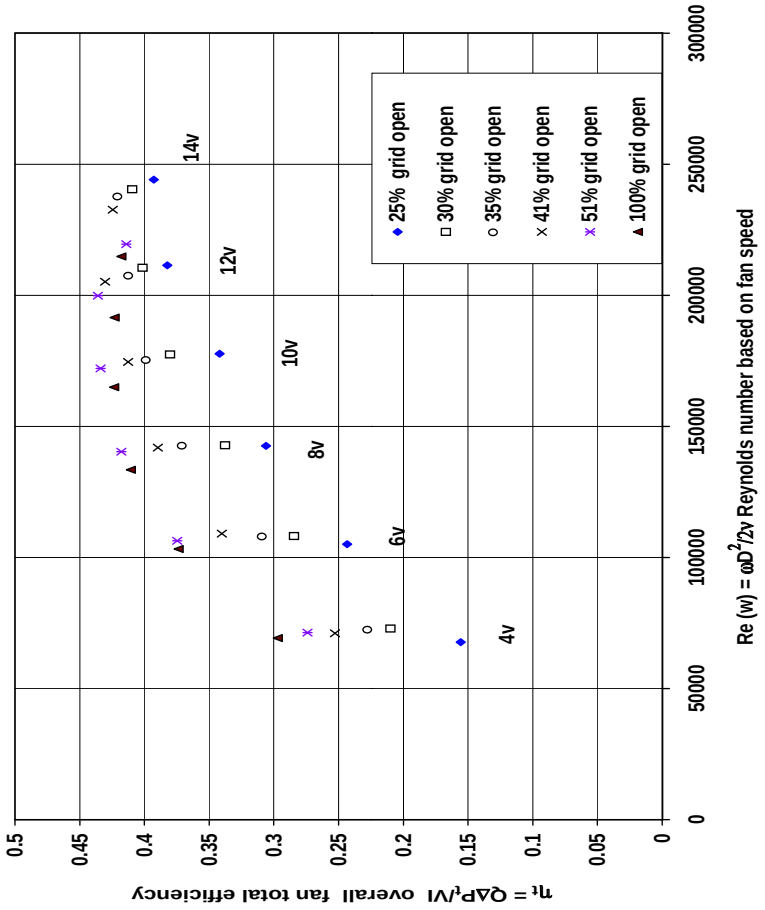

Figure 7.20: Plot shows the Mini-LSB overall efficiency versus the Reynolds number (based on fan speed)

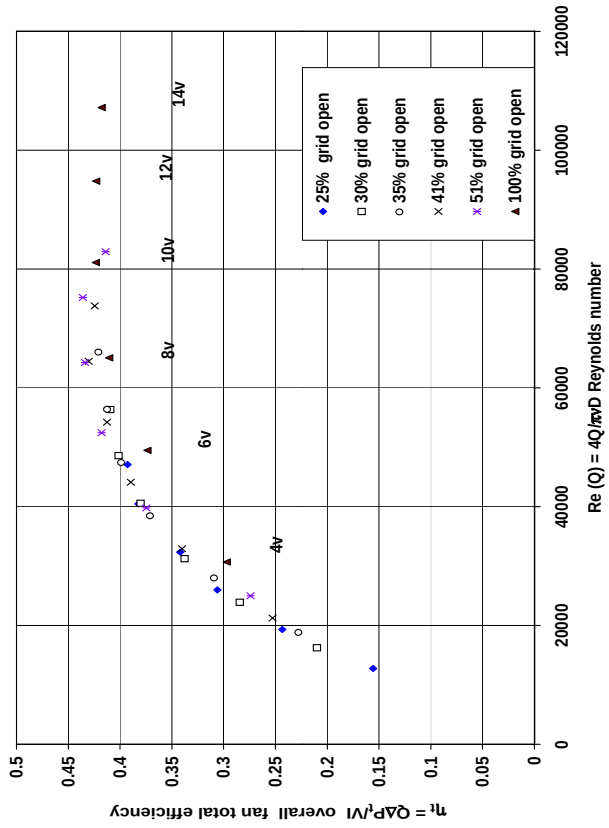

Figure 7.21: Plot shows the Mini-LSB-fan overall efficiency versus Flow Reynolds number

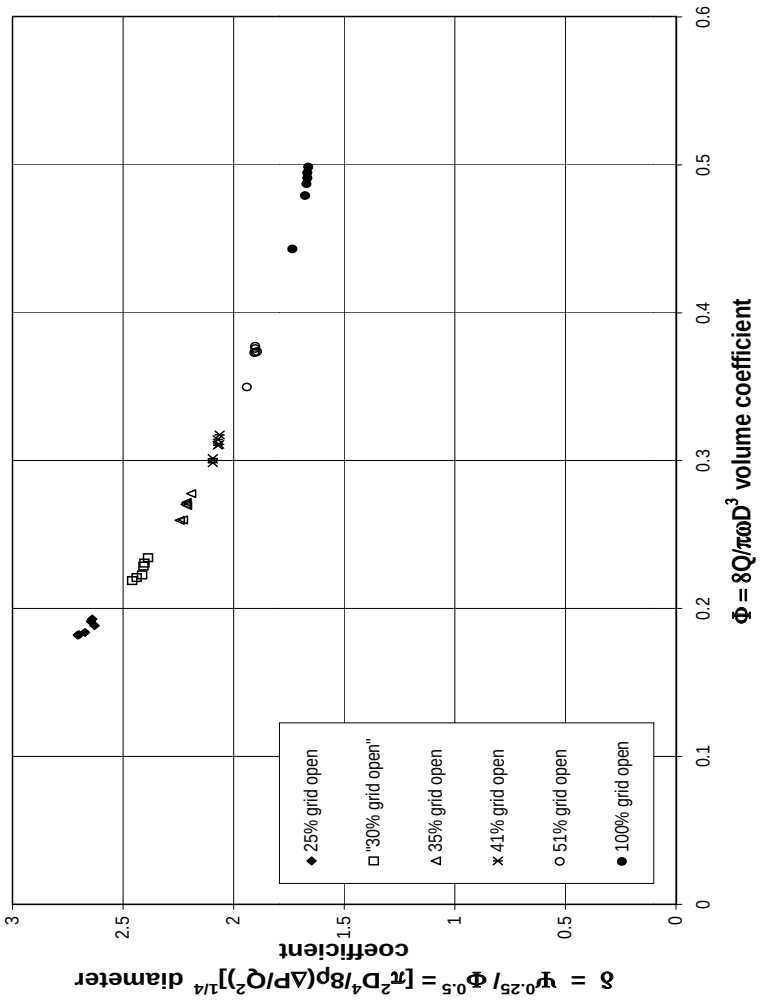

Figure 7.22: Plot shows the Mini-LSB diameter coefficient versus volumetric coefficient characteristic

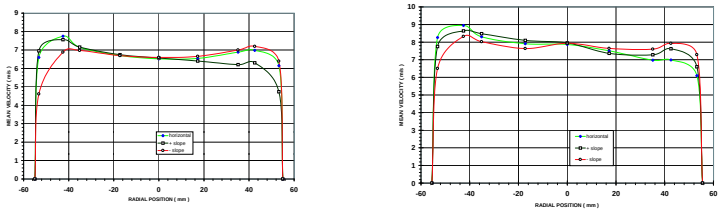

Figure 7.23: Plot shows the Mini-LSB mean velocity profiles at 10 diameters downstream of the fan impeller

The Airflow method produced much more accurate pressure readings compared to the micromanometer. This difference in pressure readings between the two methods occurred because of the fluctuations in pressure readings based on the micromanometer, which were difficult to average. Thus all pressure measurements used henceforth are based on the Airflow method.

For the HTW-MIC method, volumetric flowrates were based on hot-wire surveys conducted at 10 diameters (i.e., the Mini-LSB exit duct diameter). The volumetric flowrate measurements based on HTW-MIC method, showed slight differences compared to those measurements obtained with the Airflow-method. Also, it can be observed from Figs. 7.23 and **??** that the non-uniformity and skewing of the velocity profiles can bias the estimated value of the flow rate. Note that these results were similar to the hot-wire surveys (at 10D downstream of fan exit) obtained from the off-campus LSB facility. Streamwise turbulence intensity measurements were also obtained at 10D downstream of the at the fan exit (See Figs. 7.24 and **??**) .

In the case of the Airflow method, the volume flow rate was estimated from mass flowrate measurements (using ASME designed flow nozzles having different diameters), which are believed to be more accurate (especially for low subsonic flow) than the multi-point velocity surveys at the fan exit as made in the HTW-MIC method.

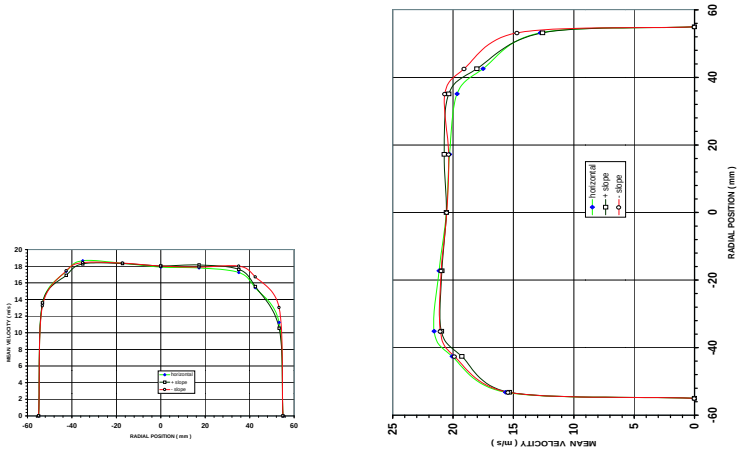

Figure 7.24: Plot shows the Mini-LSB mean velocity profiles at 10 diameters downstream of the fan impeller

Therefore, all further Mini-LSB fan performance results and comparisons will be made using the fan test results based on Airflow method only.

7.5.2 Mini-LSB fan performance test results with/without fan inlet duct

Fig. 7.25 represent the pressure/flow characteristics of the Mini-LSB fan performance results with and without a fan inlet duct in place. The trends are different since P_{fs2} (with inlet) is different from P_{fs2} (without inlet). Note, however, that the characterization of P_{fs2} (with inlet) is dependent upon the location where it is measured along the fan inlet duct. Inclusion of an inlet duct changes both the system resistance (due to the additional duct resistance) and the flow pattern at the fan inlet orifice, and even possibly the flow inlet angles at leading edge of fan blades. Thus, the inclusion of an inlet duct causes not only a change in the fan operating point, but also causes a shift in the trends of the fan exit static pressure.

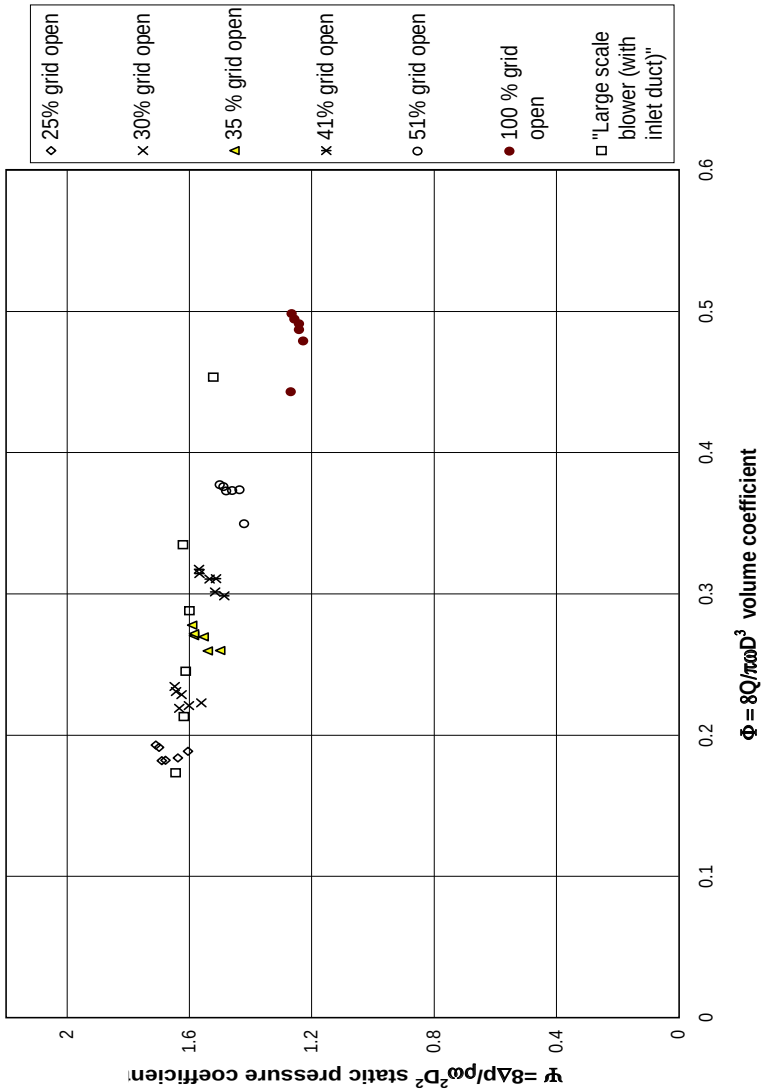

Figure 7.25: Plot shows the Mini-LSB-fan pressure coefficient versus volumetric coefficient based on inlet and outlet pressures

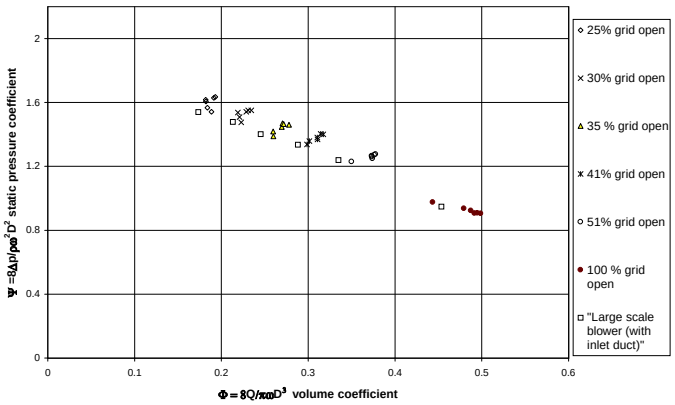

Figure 7.26: Plot shows the LSB-fan and Mini-LSB fan performance, i.e., the pressure coefficient versus the volumetric flow coefficient

7.5.3 Comparison of the LSB and the Mini-LSB fan performance

Figure 7.26 shows a comparison of the non-dimensional plots of the LSB fan and Mini-LSB (with inlet duct) fan performance characteristics, i.e., the pressure coefficient, ψ (based on the fan exit static pressure) is plotted against the volume flow coefficient, ϕ. Fig. 7.27 shows the non-dimensional plot of the total pressure rise,Δp_t, across the LSB and the Mini-LSB fans. Similarly, Fig. 7.28 shows the non-dimensional plot of the static pressure rise,Δp_s, across the LSB and the Mini-LSB fans.

Fig. 7.29 shows comparison of the non-dimensional plots of systems Euler number, Eu_{sys}, versus the systems Reynolds number, Re_Q, the LSB fan and Mini-LSB system performance characteristics. The diameter and flow coefficients are presented in Fig. 7.30.

From Fig. 7.28 and 7.26 it is clear, that the trends of fan performance between

Figure 7.27: Plot shows both the Mini-LSB-fan total pressure coefficient versus volumetric coefficient characteristic at different voltages and LSB fan total pressure coefficient curve

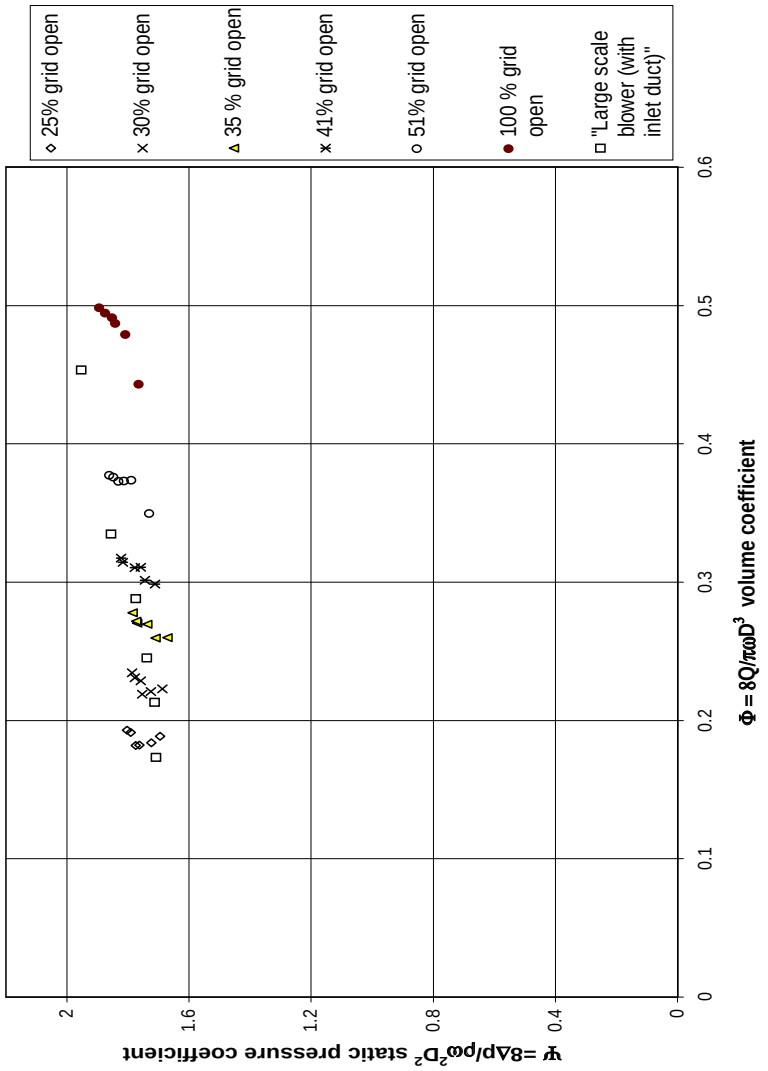

Figure 7.28: Plot shows both the Mini-LSB-fan static pressure coefficient versus volumetric coefficient characteristic at different voltages and LSB fan static pressure coefficient curve

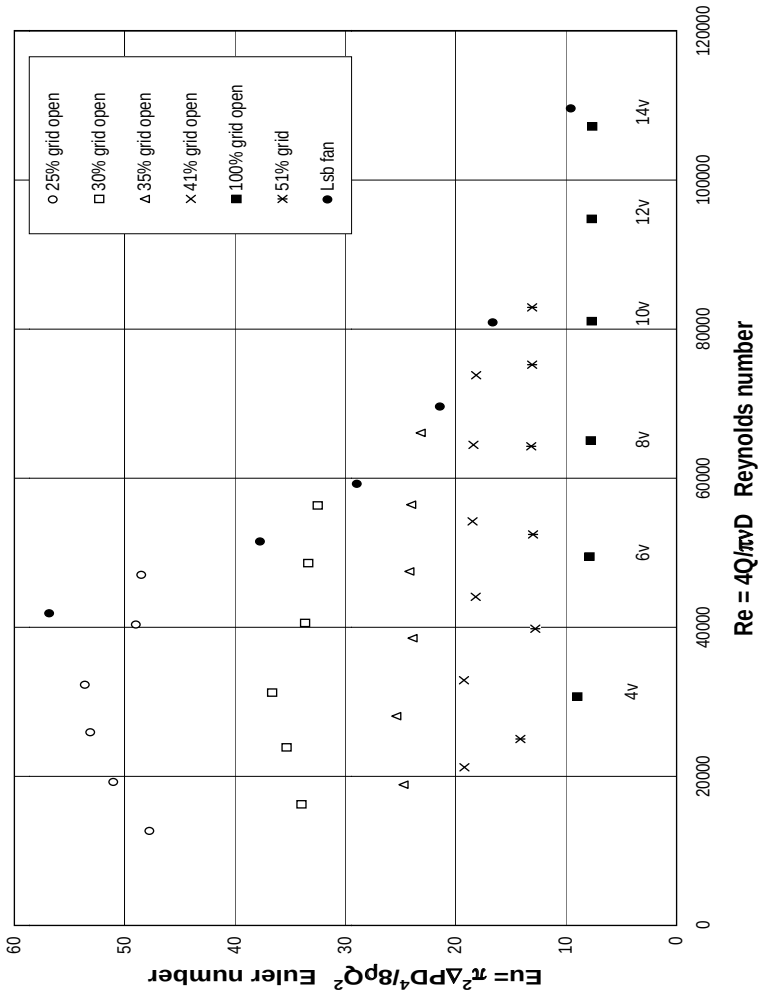

Figure 7.29: Plot shows the Mini-LSB Euler (systems) number versus Flow (systems) Reynolds number

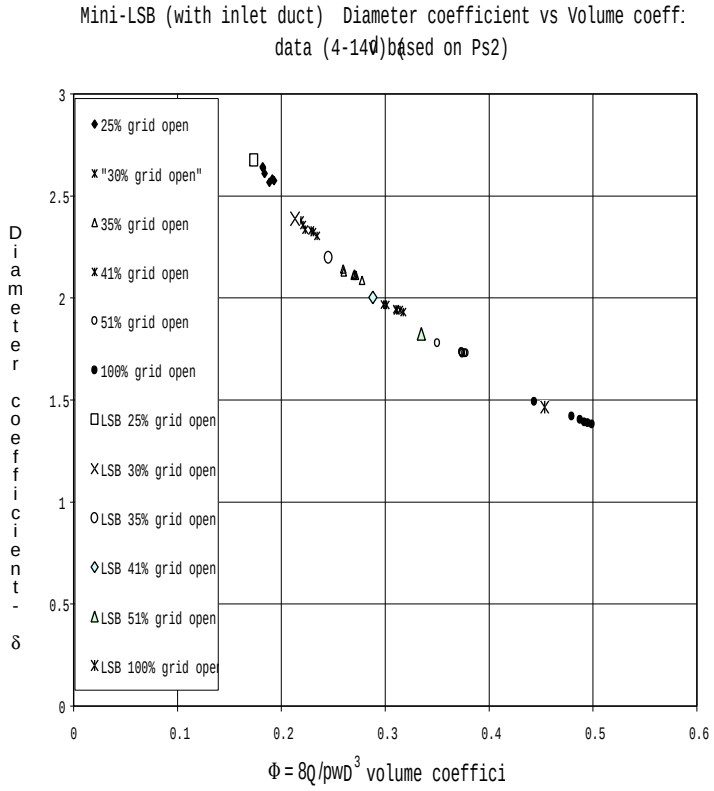

Figure 7.30: Plot shows the Mini-LSB diameter coefficient versus volumetric coefficient characteristic

the LSB and MINI-LSB fans are similar. Therefore the Mini-LSB fan is a legitimate model of the LSB fan. There exist, however, slight discrepancies between the volume flow coefficients obtained from the two fan facilities, especially at the higher flow coefficient region. Also, as the volume coefficient increases (or as the system resistance decreases), the difference between the two volume coefficients also increases in an almost parabolic (non-linear) manner. From Fig. 7.29, it can be observed that the system characteristics for the Mini-LSB tests made at 14 volts closely match the LSB system characteristics. Note that some discrepancies do exist at the higher system resistance settings since the systems Euler number *could not be exactly matched* between the LSB and Mini-LSB fan test facilities. This was because the $\Delta p/Q^2$ (or Euler/Reynolds number) characteristics of the resistance grids and flow conditioning elements for the LSB and Mini-LSB fan test facilities were not exactly matched. Fig. 7.29 also highlights the differences in the system characteristics over the range of volume flow rates.

Two additional reasons are proposed for the difference between the fan performance of the two fan facilities. First, the measurement error in the estimation of volume flow rate for the LSB fan increases as the flow coefficient increases, i.e., as the system resistance decreases. This is mainly due to the skewing and non-uniformity of the velocity profiles at the fan exit location, especially for the high volume flow rates. Second, the LSB fan tests were conducted at constant fan speed (for practical reasons), whereas the Mini-LSB fan tests were made at constant voltage and were made over a whole range of voltages. Fig. 7.31 shows the Mini-LSB fan speed plotted as function of motor voltage. It can be observed that there is variation of about 50 Hz for the whole range of tests conducted between 360 Hz at 4 volts to 410 Hz at 14 volts. This variation in fan speed will cause a shift in the fan operating point, thus leading to a shift of the volume coefficients. Also note that the volume flow coefficient is a function of both the volume flow rate and fan speed (assuming constant fan size).

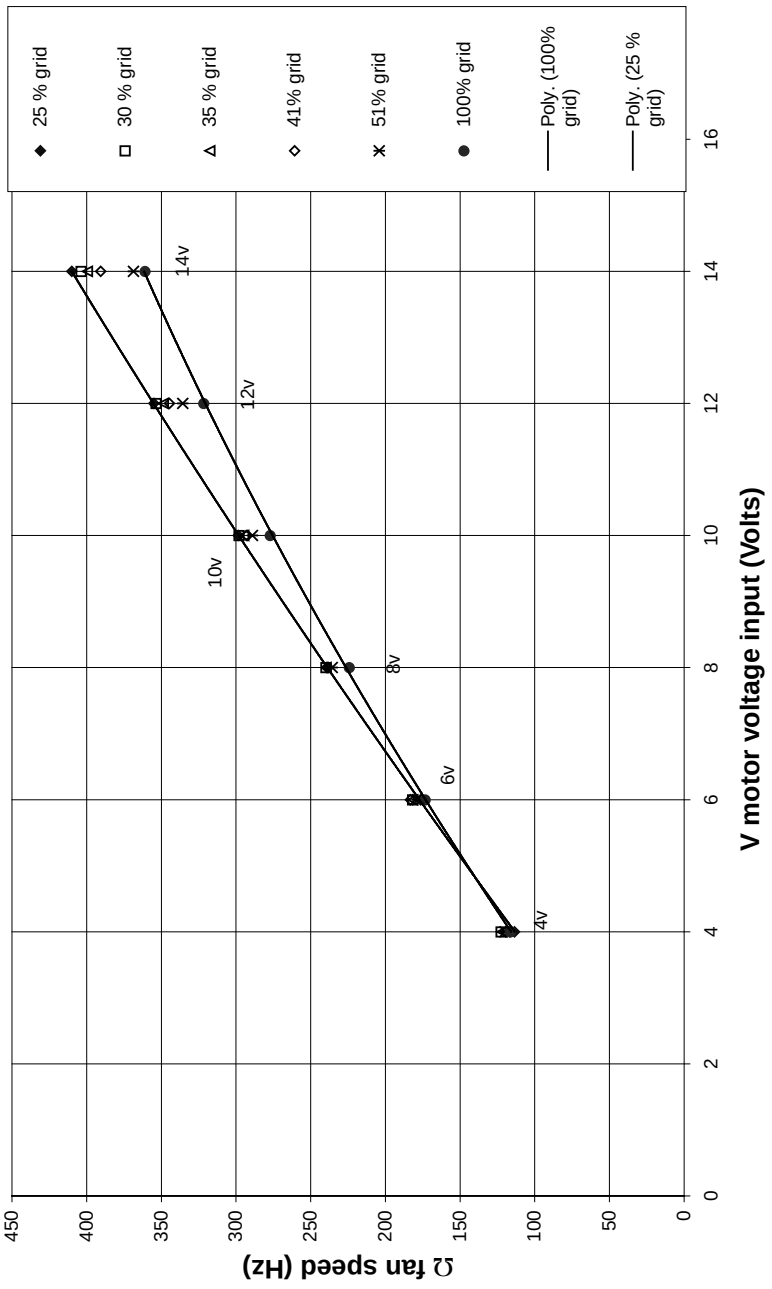

Figure 7.31: Mini-LSB-fan speed variation with fan motor input voltage

From the theoretical standpoint, the Euler number (systems), the flow coefficient (or the Strouhal number) and the pressure coefficient are all related by the following expression:

$$\psi = Eu_{sys}\phi^2 = \frac{Eu_{sys}}{Str^2} \tag{7.5}$$

It is obvious from Eq. 7.5, that any discrepancy occurring in the LSB and Mini-LSB fan's Euler number will directly affect the fan pressure coefficient. Similarly any discrepancy in the flow coefficient matching (which in general is a function of both the fan rotation speed, Ω, and flow rate, Q, and the Re_Q) will affect the fan characteristic. For high Reynolds number flows the flow coefficient becomes independent of Reynolds number. The theory also suggests that, in general, the Euler systems number, Eu_{sys}, is also a function of Reynolds number. Thus it should be recognized that the performance of individual system (resistance) elements can show Reynolds number dependence quite independent from that of the fan impeller.

7.6 Dynamic Measurements in the TRL-LSB Fan using Hot-wire Anemometry and Tuft Flow Visualization

7.6.1 The Fan Inlet Region

It is important to recognize at the outset that only qualitative information about the flow can be obtained with flow visualization methods. Nonetheless, many features of the flow are made immediately obvious, and considerable insight can be obtained as to what is really happening. Fan inlet flow visualization using tufts was conducted far upstream of the fan impeller inside the circular inlet duct. These showed a very uniform and symmetric flow distribution going into the fan inlet. At 1.5 fan inlet

diameters upstream of the fan scroll, the effect of the fan impeller on the inlet flow is insignificant for all practical purposes. In fact, the inlet flow pattern outside the fan inlet duct in the absence of swirl is very similar to the entrance flow into a "Borda Mouthpiece", which is a three-dimensional potential (inviscid) flow solution for a flow into an inlet duct connected to a plenum, see Fig. 7.36from Batchelor [6]. Close to the scroll inlet lip (approx. 0.2 D_{in}), however, the rotating fan blades cause an induced velocity upstream of the fan blades. This causes an irrotational swirl in the incoming flow. Note that in an inviscid (incompressible) flow, vorticity cannot be generated by pressure forces alone, but requires some type of solid boundaries to generate it.

At the fan inlet, one could also observe (by varying the flow rate through choking the fan exit) that as the system back-pressure was increased, the effect of the induced velocity was felt at a much further upstream region (on the order of 0.4 D_{in}) in the fan inlet duct. This kind of sensitivity of the flow pattern at the *inlet* due to the alteration in the *exit* boundary condition is typical of incompressible *non-boundary layer flows*, where a slight modification of the boundary conditions affects the whole flow field.

It is worth mentioning another aspect of the effect of boundary conditions on an incompressible flow: if the flow is assumed to be inviscid and not of boundary layer type, then the effect of changes in the boundary conditions are transmitted to the whole flow almost instantaneously, since the governing equations are elliptic. For example, in the case of very high back pressure it was observed that a flow recirculation region develops inside the fan inlet duct that was asymmetric with respect to the circumferential direction. Most of this flow reversal was occurring near the fan cut-off side of the inlet duct. Tufts applied to the inside of the fan impeller showed that in the upper part (shroud) of the fan impeller, the flow has mostly an axial velocity component (i.e., towards the hub) instead of turning into the fan blades. However, the flow direction near the hub or bottom of the fan was radial. This causes the flow

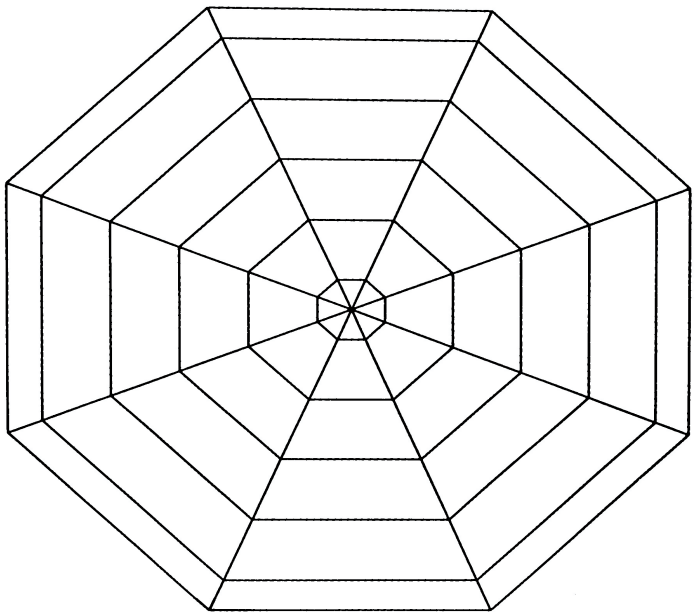

Figure 7.32: Plot shows the grid used for velocity measurements at fan inlet for the TRL-LSB facility

to enter the fan blades at the proper angle of attack (known as a 'shockless entry' into the fan impeller). It is thus this lower half of the fan impeller that is producing most of the through flow and carries the most of the energy converted from fan to fluid. In view of the above, a more detailed flow measurement study was necessary to characterize the complete flow field at the entrance to and at the exit of the fan blades.

The measurement grid for the fan inlet velocity survey is shown in Fig. 7.32. The flow measurements shown in Fig. 7.33 indicate the flow in the inlet duct is very uniform with the turbulence intensity levels on the order of 1.0 percent or less for 90 percent of the duct cross-section. Very near the wall (at 90% diameter), however, the turbulence intensity is about 10 percent.

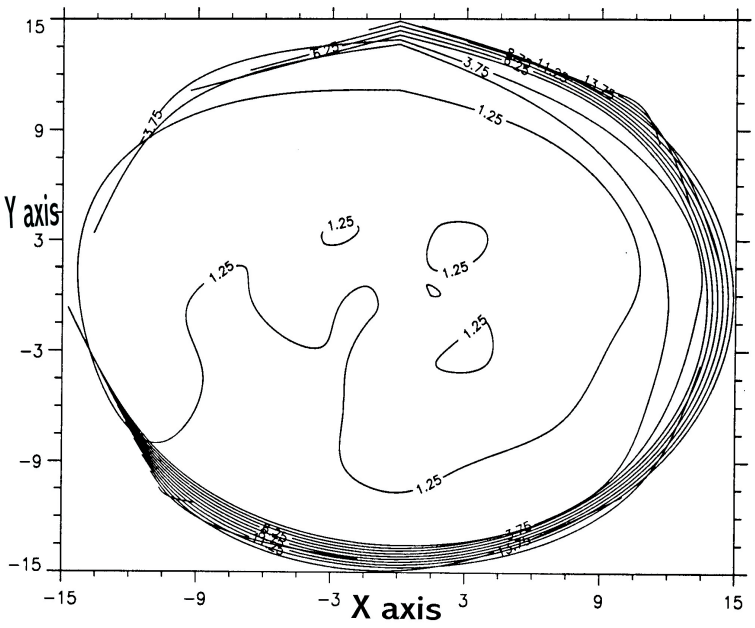

Figure 7.33: Plot shows the TRL-LSB-fan turbulence Intensities at the fan inlet (using a short inlet duct)at maximum flow-no restriction

Mean velocity profiles were taken at four different radial cross-sections. From Fig. 7.34 it can be observed that the mean velocity profiles are nearly flat (6.3 m/s %) except in the outer 5% of the duct cross-section area near the walls. This indicates that a 'potential' like flow pattern is established in the inlet region far upstream of the fan impeller. The measurements confirm that the inlet region far upstream of the fan impeller the flow is almost laminar and uniform (as shown in Fig. 7.35 .

The flow statistics at the inlet show no sign of swirl. Measurements were made at different radial cross-sections with fixed hot wire orientation, and showed no sign of any variation of mean flow velocity indicating the absence of flow swirl. In addition, changing the hot wire orientation at these radial locations did not alter the velocity statistics, also indicating a uniform mean flow velocity distribution with no swirl. Thus the inlet velocity profiles can serve as a possible upstream boundary condition for straight-form CFD code validation.

When a high back pressure is imposed on the fan system, however, flow visualization studies show that flow recirculation occurs at the lip of the fan inlet duct, thus altering the flow field. Flow visualization also shows that operating the fan under high system resistance causes the flow to swirl at a much larger distance upstream of the fan blades. The basic inlet flow test measurement results suggest that the tested fan inlet location is an appropriate location for determining the volumetric flow rate using a single point velocity measuring instrument.

It is reasonable to deduce that a Pitot probe survey would suffice for obtaining average velocity at the fan inlet since the velocity profile is very uniform and almost laminar in character. In order to map the complete fan performance range, however, a fast and accurate method of determining the volumetric flow rate at each back pressure setting is required, simultaneous with the velocity and pressure measurements. This has already been designed into the complete fan test facility (the off-campus LSB facility) described in section 6.3.2.

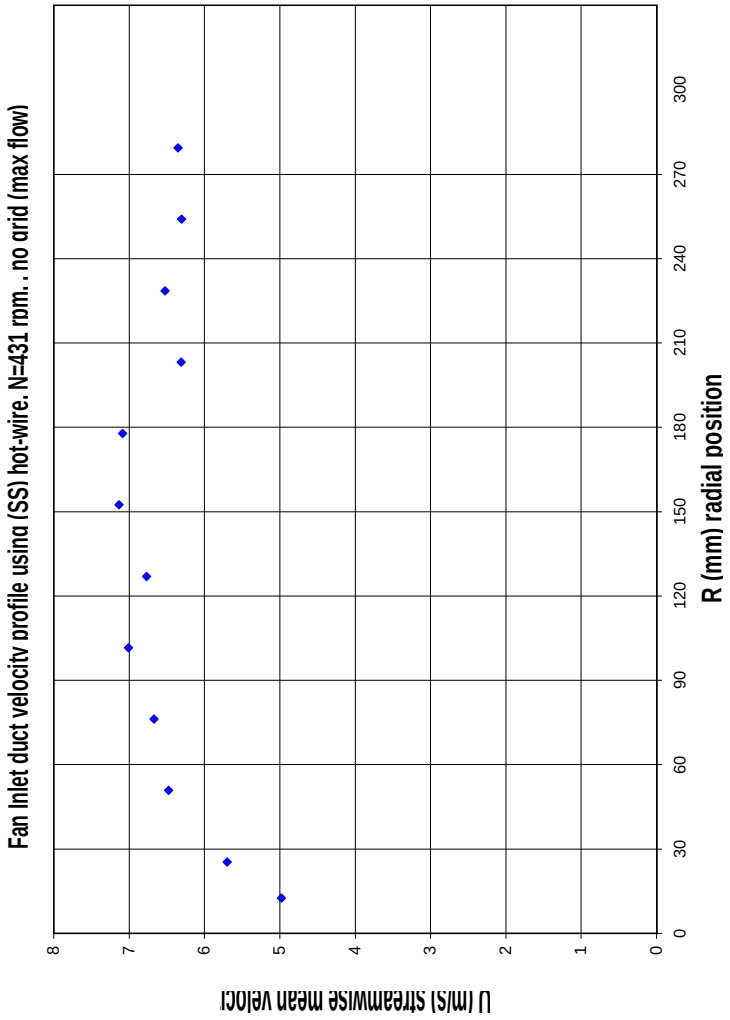

Figure 7.34: Plot shows the mean velocities at a radial cross-section across the fan inlet of the TRL-LSB using a short inlet with no restriction

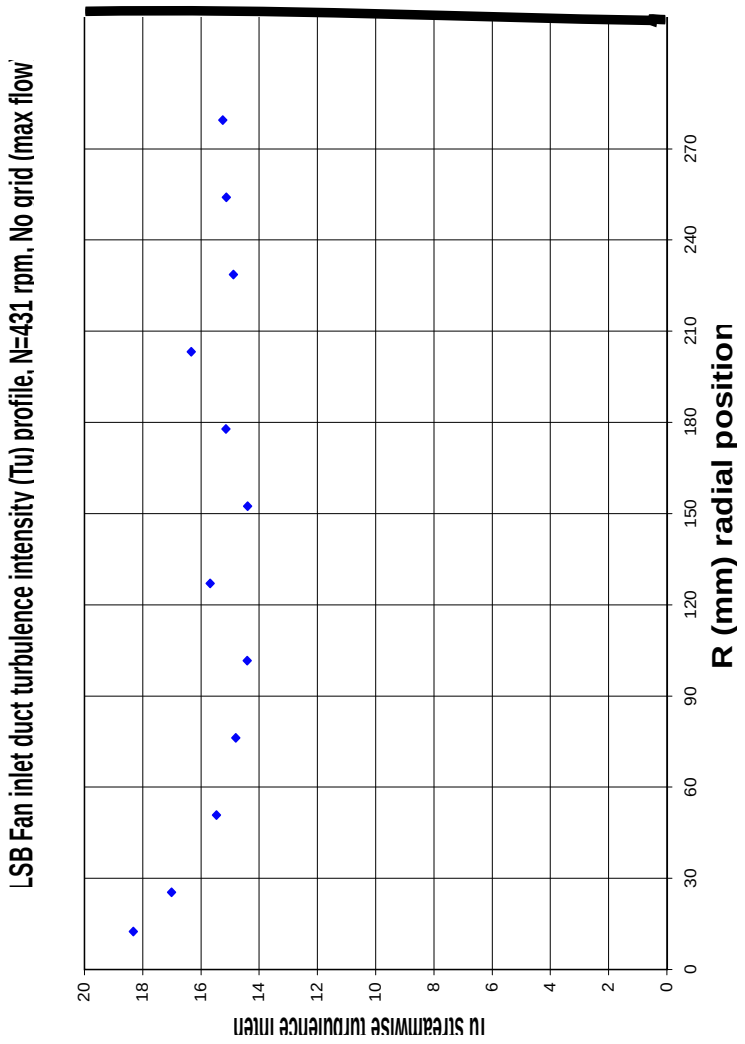

Figure 7.35: Plot shows the streamwise turbulence intensity at a given radial cross-sections across the fan inlet of the TRL-LSB using a short inlet with no restriction

7.6.2 The Fan Exit Region

Tuft flow visualization was also used near the cut-off at the fan blade exit region. These results showed that a large area of flow reversal covered *almost 40 percent* of the fan impeller from the inlet shroud to fan hub. The flow near the cut-off wall and close to the inlet fan shroud showed a stagnation region with very little through flow in either direction. The flow increases, however, as one moves away from the cut-off side wall towards the top of the scroll duct. This is the bulk flow from the fan scroll which contains the major portion of the momentum, part of which the volute scroll converts to a static pressure rise. The flow recirculation is believed to be caused by fan blade stall in the upper part of the fan impeller; the flow simply cannot make the turn into the upper part of the blades. This result was anticipated in light of the centrifugal fan literature survey (v., Appendix A), and suggests there may be real advantage to decrease the blade aspect ratio, and skew them for the proper angle of attack.

Tuft flow visualization was also done to roughly estimate the flow angle distribution downstream of the fan throat. There is evidence of the presence of strong swirl in the fan exit flow that causes appreciable flow angle variation across the duct. The velocity vector varied by as much as 25° from the exit duct centerline axis along the span-the plane formed between the fan impeller and fan scroll (volute) wall-from fan hub to shroud. The flow velocity vector at fan exit also varied along the cross-stream direction. In the top half (and center)of the exit duct, the flow vector had an upward velocity component; while in the lower half (and center), the flow vector was observed to have a downward component. The tuft flow visualization results in the fan exit duct suggest that a secondary flow exists in the x-y plane (cross-stream direction). The clockwise swirl with respect to the primary flow direction is illustrated in the Fig. 7.36.

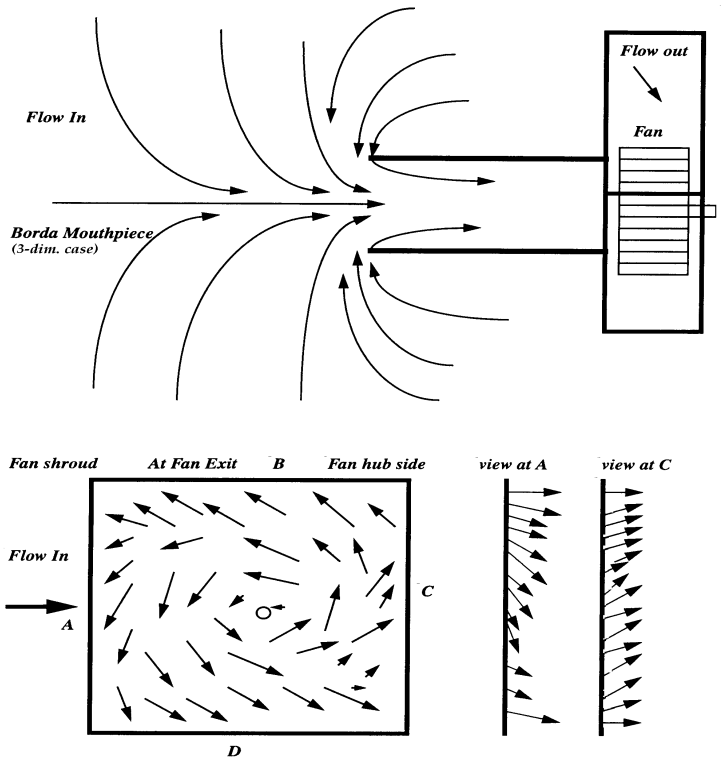

Figure 7.36: An illustration of the swirl pattern at exit of the TRL-LSB fan (maximum flow-no restriction)

Since hot-wires are sensitive to the cross stream velocity components, an investigation was conducted to study the effect of hot-wire sensor orientation on the measured value of the mean velocity and turbulent intensity at the fan exit. Results from the upper and lower parts of the duct show that the orientation denoted by Py in Fig. 7.37 gives a 10 percent higher velocity output compared to orientation Px. In the center of the duct, however, both hot-wire orientations give nearly equal mean velocity results. This is consistent with the fact that the flow visualization shows high swirl in the upper part and lower part of the duct, but the flow is almost parallel to the velocity vector at the center of the duct, an area of no swirl. As expected, the flow swirl due to the cross-stream velocity components causes a bias in single sensor hot wire signal output. It was observed that the velocity bias is location dependent within the measurement grid in the fan exit duct.

Flow visualization using tufts was also conducted between the fan cut-off and blade trailing edge towards the fan exit duct. As expected, the direction of flow near the cut-off (just at the beginning of the cut-off) was observed to be pointed back towards the fan blades and towards the gap formed between the fan scroll and impeller. Note that the flow in the gap forms part of the recirculating flow around the impeller inside the fan scroll and contributes to the losses (mostly viscous) in total pressure across the fan.

It was also observed from the flow visualization studies near the cut-off region that the flow recirculation (flow reversal) spans the cut-off side wall to about 0.3 fan exit diameters downstream. Note that this result was obtained for zero system resistance. It is expected that the flow (near the fan cut-off) will become more non-uniform, with an increase in the recirculation area (i.e., the exit blockage factor will increase) as the system resistance (back pressure) increases on the fan. An indirect proof for this hypothesis is the fact, as noted earlier, that for the case of maximum system resistance (or load), a large region of the flow at fan (for the off-campus LSB facility)

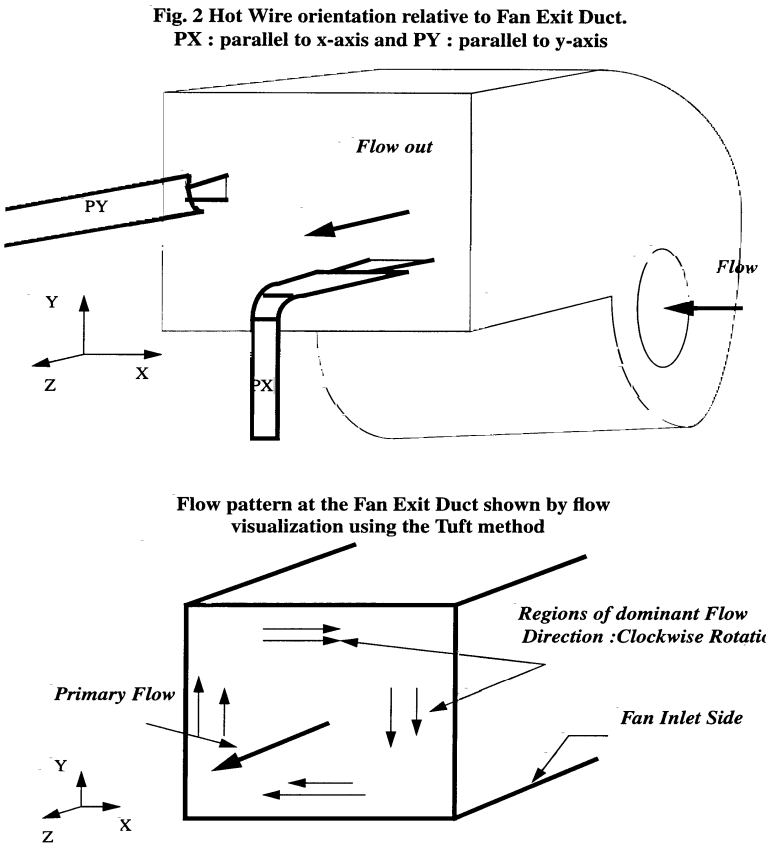

Figure 7.37: Orientation of the hot-wires used for flowrate/velocity measurement at the exit of the TRL-LSB facility

inlet duct just upstream of the fan impeller was recirculating (with flow reversal) towards the cut-off side of the inlet duct.

Mean velocity and turbulent intensity measurements were also taken downstream of the fan throat region in a rectangular duct using a rectangular measurement grid as shown in Fig. 6.10. The mean velocity results show a much more complicated picture compared to the fan inlet characteristics. As can be seen in Figs 7.38 and 7.39, the flow field is partitioned into regions of a high speed and low speed flow. Basically a flow deficit is observed in center and left parts of the duct closer to the fan shroud side. The high speed zone is thought to be associated with the flow through the hub section (lower part of the fan impeller). High speed flow also occurs in the "other three" corner regions of the rectangular exit duct. The large gradient in mean velocity on the shroud and center regions is a consequence of the flow deficit due to flow separation in the upper part of the fan blades. The mean velocity profiles also indicate that a weak velocity gradient exists in the y-direction (scroll top to cut-off wall). However the velocity gradient in the x-direction from the fan shroud to the hub is much larger and is asymmetric with respect to the y-location. The low speed area is believed to be associated with flow through the fan shroud section (upper part of the fan impeller) where the flow is separated off the fan blades. Flow visualization shows the presence of a vortical structure whose center location corresponds to the minimum fan exit velocity point as shown in Fig. 7.38.

The 2-D mean velocity contour plots of Figs. 7.38 and 7.40 show that even though there is a velocity deficit in the velocity profiles at the shroud side of the exit, pockets of high speed flow can be observed in the corners of the rectangular duct. Further investigation is required to resolve the regions near the walls, but these are probably dominated by corner vortices and scroll wall boundary layer interactions. Also, they may be influenced by the inlet duct protrusion into the fan scroll at the fan inlet. This is usually the region of leakage flow in centrifugal turbomachinery, and its direction

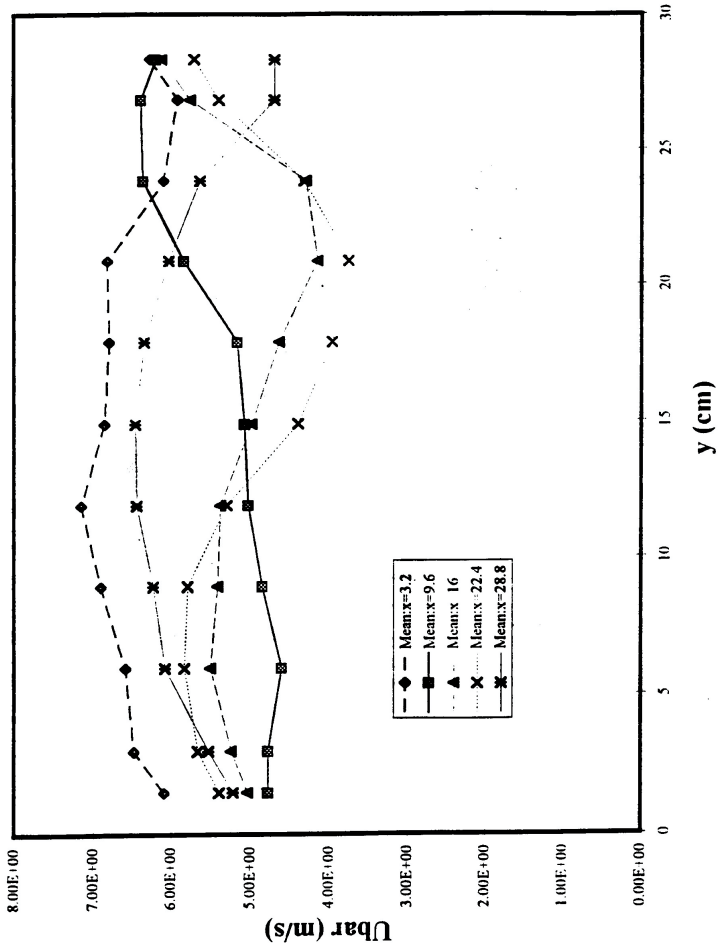

Figure 7.38: Plot shows the mean velocities across the exit of the TRL-LSB fan (using a short inlet and having no flow restriction)

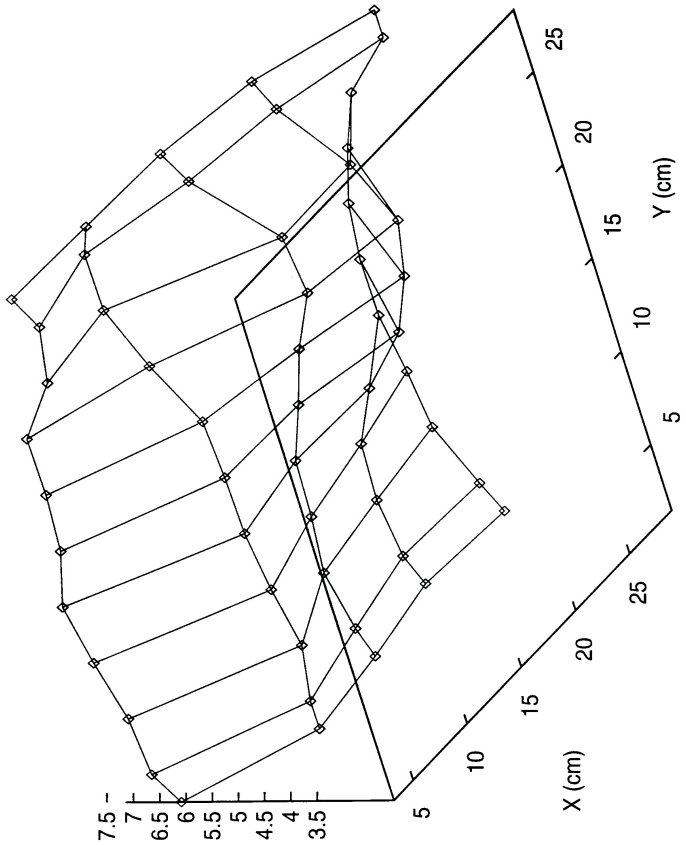

Figure 7.39: Plot shows the surface velocity contour across the fan exit of the TRL-LSB (using a short inlet and having no flow restriction)

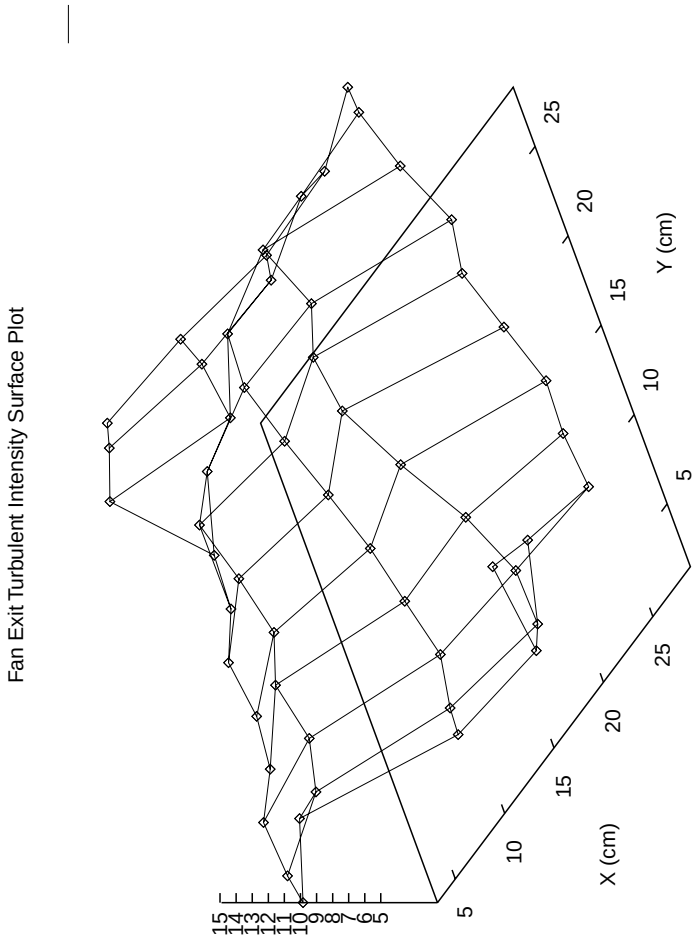

Figure 7.40: Plot shows another view of streamwise turbulence intensity contours at the exit of the TRL-LSB fan

depends mostly on the static pressure gradient across the fan inlet lip and fan shroud (Wright [71]).

The surface velocity plot at the fan exit is shown in Fig. 7.38. It shows that the flow deficit begins in the upper shroud section and continues to 60 percent of fan impeller height (measured from the top). The remaining 40 percent of the fan impeller region is seen to be a region of the high speed flow. This flow trend was expected since it was established from the centrifugal fan literature review (see Appendix A) that for squirrel cage fans the upper half of the impeller is stalled. Thus, most of the through-flow is from the lower half of the fan impeller, in agreement with previous measurements (Kind and Tobin [36], Raj and Swim [55], Denger and Mcbride [17]). It is important to note that the flow at the fan cut-off region (towards the exit) is not a simple 2-dimensional flow. It rather is a complicated 3-dimensional flow which is inherently unsteady. A simple flow model like the famous jet-wake model proposed (by F.K. Moore 1974) and observed from the impeller exit of high speed centrifugal compressors (or even centrifugal pumps) cannot be proposed for the LSB since the geometry is considerably different from both high speed centrifugal compressors and low speed hydraulic centrifugal pumps. For example, the LSB has a round and blunt cut-off, whereas the centrifugal pumps have very sharp and thin cut-off with very low fan impeller exposure. Also,the impeller blades on the LSB fan are of straight 2-D design, whereas modern pumps and compressors have complex 3-D skewed blade design. In addition, most of the high performance centrifugal compressors have short vane-less or vaned diffusers at the exit of the impeller. There is no such device at the exit of the LSB; rather the flow is simply collected and diffused in the scroll volute casing and discharged directly to an exit duct.

In the case of the LSB, flow visualization studies suggest the flow at the fan exit is affected by three major flow mechanisms: first, the flow from the fan blades, second, the recirculating flow around the impeller-scroll gap, and third, the leakage (and

recirculating) flow from the inlet orifice to the fan cut-off between the top shroud of the fan impeller and scroll wall. Note that as system resistance is varied, both the fan blade loading (and thus the angle of attack at the blade leading edge) and the through flow are affected. This causes a modification in the local fan-scroll flow patterns so that at high flow coefficient (low system resistance), lower blade loading (or low pressure coefficient) is encountered and thus more through flow (with less recirculation). On the other hand,for the case of low flow coefficient (high back pressure and low through flow)), the blade loading (or pressure coefficient) increases and the fan speed increases to generate the higher pressures in order to match the higher load. This in turn causes higher adverse pressure gradients across the blades that result in blade stall and increased flow recirculation. In light of the above and the complicated nature of the flow at the fan cut-off/exit, this flow region needs to be investigated by more sophisticated flow measurement techniques, such as LDA and PIV. The unsteady nature of the flow through the fan can be characterized through both spectral measurements, and sophisticated dye injection flow visualization techniques.

Another important characteristic of flow that was measured at the fan exit was the streamwise variance. Fig. 7.41 shows the variance (normal stress) of the flow downstream of the cut-off section. The variance (i.e., normal stress) in the core flow is not high (0.4 m^2/sec^2 at most, which corresponds to an intensity of 14%). Sudden jumps often occur, however, in the Reynolds stress and mean velocity gradients profiles when the flow changes from a region of uniform flow to a highly turbulent shear layer. Examples are separated boundary layer flow and the turbulent wake from a stalled fan blade. No such trends were observed in the fan exit flow at the location tested which was downstream of the fan throat at the given operating point (full-open). *The absence of sharp gradients in the mean velocity and variance suggests that there are no flow separations or strong shear layers in the core flow.* As a consequence, flow measurements with hot-wires are suitable in this region of low turbulent

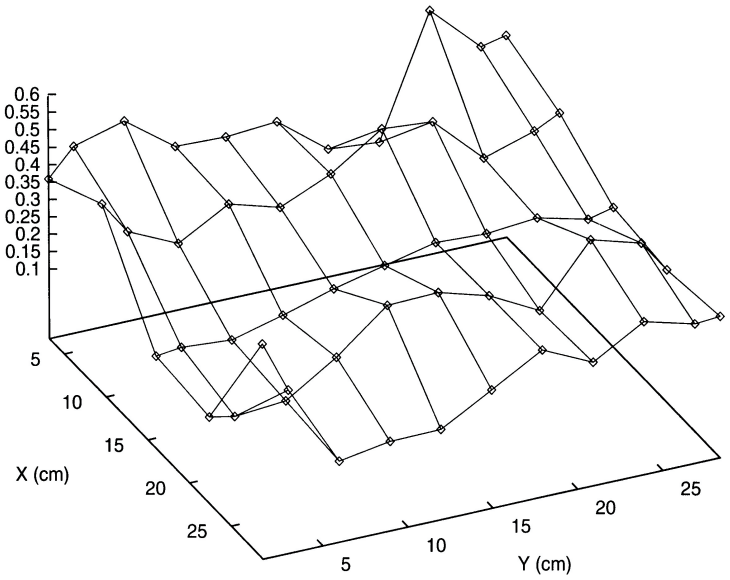

Figure 7.41: Plot shows the streamwise variance at the exit of the TRL-LSB fan (with no flow restriction)

intensity flow with no flow reversals downstream of fan throat. However, under high back pressures the flow at the fan exit may separate and cause flow reversal, in which case an LDA method is more suitable for flow measurement.

By combining the results of the flow visualization and the effect of hot wire orientation on the velocity measurements at the fan exit, one can conclude that there are strong cross-stream velocity components in the x-y (cross-stream) plane, probably caused by secondary flows in the exit duct. Figs. 7.41 and 7.42 show the direction of the trends of the flow in the exit duct. The observed clockwise flow swirl at fan exit can be predicted assuming the flow to be inviscid and incompressible. The basic fluid dynamic equations combined with the present flow information (initial and boundary conditions) show that a swirl will be generated in the opposite direction of the fan inlet. From Fig. 7.42 it can be seen that a hypothetical velocity profile gives swirl with the correct direction of rotation and predicts the location of the velocity deficit in the correct quadrant of the fan exit duct. It can be concluded based on flow visualization at the fan exit that *there is a single secondary flow cell pattern (vortical structure) and not the classical double cell secondary flow pattern that occurs in the flow through a curved duct.* Also, at the exit of fan downstream of the fan throat, i.e., X-wire sensors should be used to obtain the individual velocity components and resolve the flow regions more accurately because of the multidimensionality of the flow.

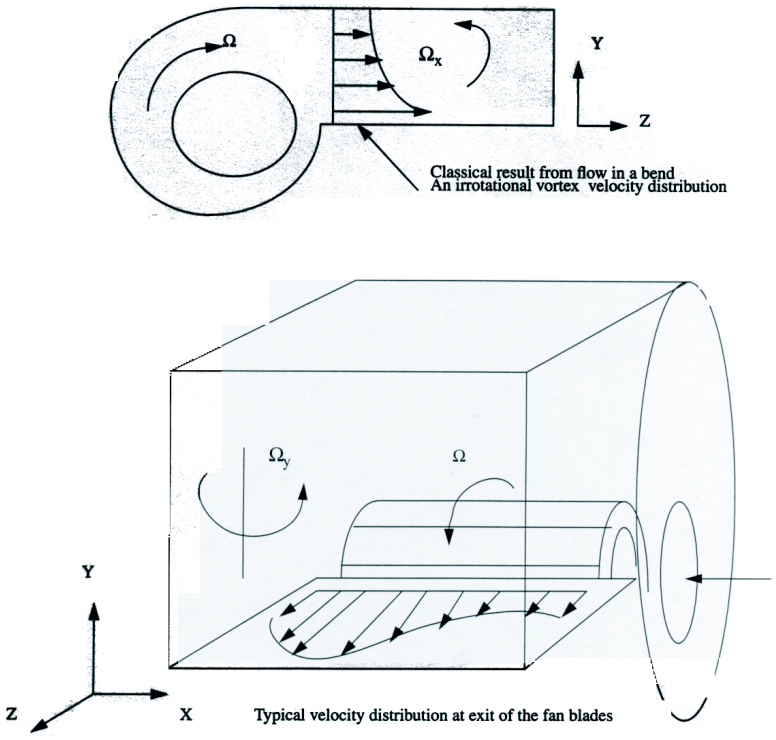

Figure 7.42: Hypothetical plot of the swirl pattern at LSB-fan exit; based on flow visualization and dynamic measurements

Chapter 8

Investigation of the instantaneous flow field inside an actual HVAC module

8.1 Introduction

8.1.1 The noise "rumble" problem in an automotive HVAC module.

Overall sound level tests conducted on automotive HVAC modules, both in the vehicle and in the anechoic chamber, reveal the presence of blower "rumble" noise. Blower rumble noise occurs at the low frequency end of the noise spectrum (Fig. 8.1) , typically in a band around the 80 to 130 Hz. For example, when in VENT mode the HVAC module radiates a distinctive rumble sound when the temperature control is switched from FULL COLD to FULL HOT. Previous experimental investigations have established that the rumble noise generation is a system phenomena. If the fan

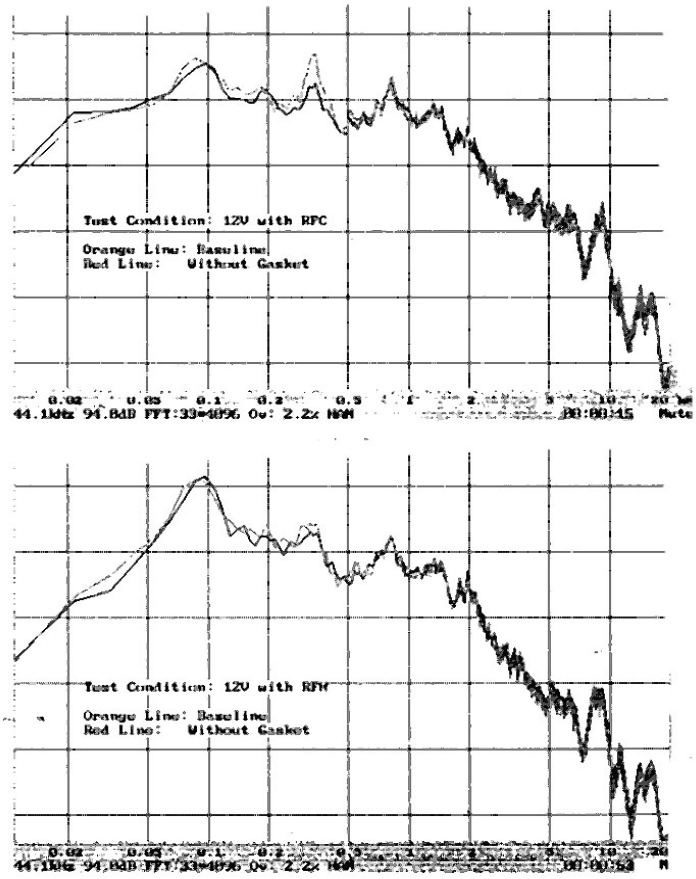

Figure 8.1: HVAC module noise spectra

and scroll assembly are isolated with a similar back pressure to maintain flow coefficient similarity, the rumble noise is not present. It was also noticed that the rumble disappears when the heater core is removed. This is in agreement with previous experience that indicates rumble is closely associated with a high system resistance. User dissatisfaction due to blower rumble noise inside the vehicle cabin has been a main impetus for identifying the sources of blower rumble noise. Since many different types of HVAC modules reveal similar blower rumble noise characteristics, it is important to understand the fundamentals of the physics underlying the sources of the rumble noise. Hot-wire measurements and tuft flow visualization in the automotive indicate that the area of flow separation at the diffuser may be coupled to the recirculating flow at the fan blade inlet region opposite to the cut-off point. If so, this may lead to design changes which will affect all HVAC modules exhibiting blower rumble.

Some basic flow mechanisms can be identified that are possible sources of flow-induced noise ([9] and [49]):

- random background turbulence; causes broad band noise
- fan blade wake shedding (blade passage frequency); usually discrete tonal noise is generated especially if the shed wakes interact with solid boundaries. For example, centrifugal fan rotor wakes chopping the fan scroll cut-off area
- fan blade flow separation: causes broad band noise
- large scale flow recirculation regions: causes broadband noise
- jet shear layer noise: causes pressure peaks in noise spectra
- vortices: causes discrete tonal noise
- any type of vortex shedding, due to obstacles in the flows or flow over the edges of cavities: causes both discrete tonal noise and excites higher order structural

(duct) acoustics modes.

A review of the literature ([47], [48], and [39]) on centrifugal fan noise and "in house" testing suggests that the blower noise is not characterized by discrete tonal noise like axial fans, but is dominated by broad-band noise. In general broad-band noise is aerodynamically generated and is characterized as a random noise source usually linked with turbulence. The work of Moreland [44] on the housing effects on centrifugal blower noise contained a number of interesting findings. Among them::

- Sound power spectra from a forward curved fan exhibited major speed-independent spectral peaks which corresponded to the Helmholtz resonance frequency of the blower housing (i.e., 315 Hz for that particular blower).

- The double inlet blower radiates less noise at resonance than its single inlet counterpart.

- The noise spectral peaks were not due to characteristics of a backward faced centrifugal fan. Wright also suggested that severe inlet flow distortion was a probable candidate for rotating stall in centrifugal fans. In addition, recent studies conducted on high speed centrifugal compressors (Zverdrup [**?**]) indicated the negative effects of poor inlet flow on compressor performance.

Characterization of these different zones of flow is essential for understanding their effects on the fan performance. System components placed downstream of the fan/scroll combination can have considerable effects on the upstream behavior of fan itself. This is especially true for low speed (i.e., incompressible flow regimes) internal ducted flows where flow disturbances at the downstream location can affect the upstream flow behavior depending on the strength of the disturbance. Weak disturbances generally decay much faster than strong ones due to viscous diffusion. Strong flow disturbances, however, can be affected by the internal duct geometry so that various types of flow

regions can be formed in different parts of the ducted geometry with distinct flow characteristics. It is clear from the above that a detailed investigation of the instantaneous flow field inside a centrifugal fan is essential in order to identify key areas within the fan geometry. Identification of problem areas and their elimination can lead to design improvements resulting in more efficient fans. A more efficient design in turn leads to cost savings which can be important for products that are produced in a high volume; e.g., HVAC centrifugal fans, automotive HVAC modules, heat exchangers, etc. Instantaneous flow field characterization can be used to understand the "interaction" between the fan impeller and system elements. The system elements (e.g., exit diffusers, inlet ducts, evaporators, etc.) can have basically two type of effects on fan performance:

- First, an increased system resistance that results in a shift of the operating point of the fan, but has no effect on the aerodynamics of the fan itself.
- Second, a flow coupling between the additional system elements and the fan impeller that can change the performance characteristics of the fan, both in terms of the shape and slope of the fan characteristic.

Flow field characterization can also identify possible large scale flow structures which couple between the different regions of the overall HVAC module. Typical examples of flow regimes that occur in internal ducted flows are:

- flow after a sudden expansion,
- flow through a short wide angle diffuser,
- flow through rotating elements (causing large centrifugal and Coriolis forces),
- flow in a corner,
- flow in bend with a short radius of curvature.

These examples indicate that many types of flow regime can coexist in complicated internal ducted flows. The typical HVAC fan system generally consists of a fan, scroll, wide angle diffuser, evaporator, etc. There is a possibility of a strong mutual interaction or perhaps 'interference' between the fan and the system components. This interaction between the fan impeller/scroll combination and the additional system components either at the fan inlet or the fan outlet can be characterized in terms of the flow field and fan/system parameters (e.g., system resistance , fan speed, pressure rise and flow rate). This chapter describes the methodology for such a characterization. The results of the application of a new experimental approach to study the flow coupling phenomena inside a particular HVAC module are reported. Also presented are the results of applying frequency domain analysis (i.e., Power Spectral measurements) to the flow field inside the HVAC fan in order to study the characteristics of the distribution of unsteady flow energy as function of system resistance. Finally, the coherence function and cross-spectra measured using two single hot-wire sensor probes at different spatial locations within the fan scroll and diffuser regions are presented.

8.2 Experimental Methodology

Low speed aerodynamic flow field analysis is usually confined to flow velocity and static pressure measurements. These can be done either locally using intrusive or non-intrusive measurement techniques (e.g., Pitot-tubes, hot-wires, pressure probes, LDA, etc.) or globally using non-intrusive experimental measuring techniques (e.g., PIV (particle image velocimetry), PTV (particle tracking velocimetry), etc.). All these various methods of velocity measurement are typically used to obtain only mean flow field statistics, (i.e., mean velocity, standard deviations and higher order statistics). In many cases it useful to obtain the temporal (or spatial) frequency content

of the flow field in order to highlight or identify certain unsteady flow phenomena. Frequency domain analysis of turbulent flows is usually concerned with spectral measurements using fast response velocity or pressure probes. Such measurements reveal the frequency distribution of either flow energy or pressure energy. A typical example of such spectral measurements is in rotating turbomachinery where the blade passing frequency caused by the multiple fan blade wake shedding exhibits itself as a single discrete peak in the frequency domain analysis. This can be observed with even a single point spectral measurement. Sometimes it is important to estimate the coherence between two signals for noise detection in order to establish a relationship between them. For example, in a system generating aerodynamic sound, correlation and coherence measurements (in the frequency domain) can be made between different sound signals to obtain estimates about the noise sources [49].

8.2.1 Role of system resistance (back pressure) on fan performance

In the following discussion the terms VFC and VFH will be used. VFC means "VENT FULL COLD" mode while VFH means "VENT FULL HOT" mode. The VFC and VFH fan operating points are shown schematically in Fig. 7.2 interaction of fan performance curve versus the system characteristic. The fan operation in VFH mode is against a high system resistance, and the flow rate decreases as the fan speed increases. The VFC mode is just the opposite due to lower system resistance, and the fan speed decreases as the flow rate increases. The coherence and spectral measurements discussed later will show that the higher flow rates (as in the VFC mode) will have a tendency to generate stronger shear layers in the wide angle diffuser. By contrast, large recirculation exist for the low flow rate cases (as in the VFH mode), even though the fan speed is higher.

In the VFH mode the fan adjusts to the higher load by increasing fan speed and increased current draw at a given motor voltage, thus indicating an increase in power consumption. In the VFC mode the trend is just the opposite. A fan producing higher flow rates at lower fan speeds indicates that fan blade loading is low, thus resulting in lower pressure rise across the fan impeller, and most of the energy at the fan exit is in terms of the kinetic energy. This behavior is consistent with the trend indicated by the Euler pump (or fan) equations (see Appendix B.1). Higher fan speeds generate larger centrifugal pressure gradients, thus increasing the pressure rise across the fan blade. Higher fan speeds, however, do not necessarily imply higher flow discharge from the fan, since the through flow characteristics will dictate the flow discharge from the fan. Through flow characteristics are dependent on the volume flow coefficient (or the velocity ratio ($U/\Omega D$). The flow coefficient, in turn, is a function of fan blade geometry in addition to the fan scroll parameters. Simple one dimensional inviscid flow analysis (Refer to Eq. B27 in Appendix B.1), shows that the fan's theoretical pressure rise characteristic is a function of the flow coefficient and fan blade and fan scroll geometric parameters.

Typical HVAC fans are connected to diffusers at the fan throat exit for flow diffusion and decelerations purposes upstream of the evaporator core. A change in the flow rates (and the corresponding change of the flow pattern across the fan) changes the Reynolds number of the flow and velocity profile at the inlet of the diffuser. It is well known from various diffuser studies ([37],[?] and [?]), that the most important parameter affecting diffuser performance (or effectiveness) for a given geometry is the inlet blockage parameter[1]. Another key inlet flow parameter that has been observed to have a strong influence on the diffuser pressure recovery coefficient, is flow swirl at diffuser inlet [?]. The observed flow patterns from flow visualization studies and

[1]inlet blockage parameter is: $1 - A_{eff}/A_{geom}$ where A_{eff} is the effective flow area at the inlet of diffuser and, A_{geom} is the diffuser throat (inlet) area.

spectral measurements conducted inside the HVAC diffuser show the presence of flow recirculation at the inlet of the diffuser in case of high system resistance setting. These should be expected to decrease the overall performance of the fan system. For the case of moderate fan speeds and low system resistance, the flow patterns observed indicated less recirculation and higher through-flow across the fan and the diffuser. In the case of very low fan speeds, flow visualizations studies with HVAC fans indicated that a much more global unsteady and almost pulsatile flow pattern exists. For these measurements, however, the fan operating point was well below the range for standard HVAC fan operation.

8.2.2 Power Spectral Measurements

In the present study, the frequency domain analysis approach was used to obtain single point flow velocity spectral information at various locations within the automotive HVAC module. Flow visualization and hot-wire studies conducted in HVAC fans have shown the flow (in the inertial frame of reference) across the fan is mostly turbulent and unsteady. Turbulent flows exhibit a characteristic power spectral shape which consists of three main frequency sub-ranges [64]: the low frequencies (that contain most of the energy), the mid-range (or the inertial-advective sub-range which rolls off approximately as $f^{5/3}$), and high frequencies (or the equilibrium range).

Note that one should not be fooled by the fact the spectrum appears to have energy at very low frequencies since this is an artifact of the spectral aliasing in the one-dimensional spectrum (v. [64]). In reality the spectral energy peaks near the roll-off point and almost everything below it is aliased from smaller scale motions. In the large scale spectral range (or low frequencies), energy is extracted from the mean flow by large scale eddies and transferred to smaller scale eddies (see Batchelor [5]). The presence of coherent (organized) structures, appear mainly in the large scale (low wave number) spectral range, and can alter the asymptotically flat character of the

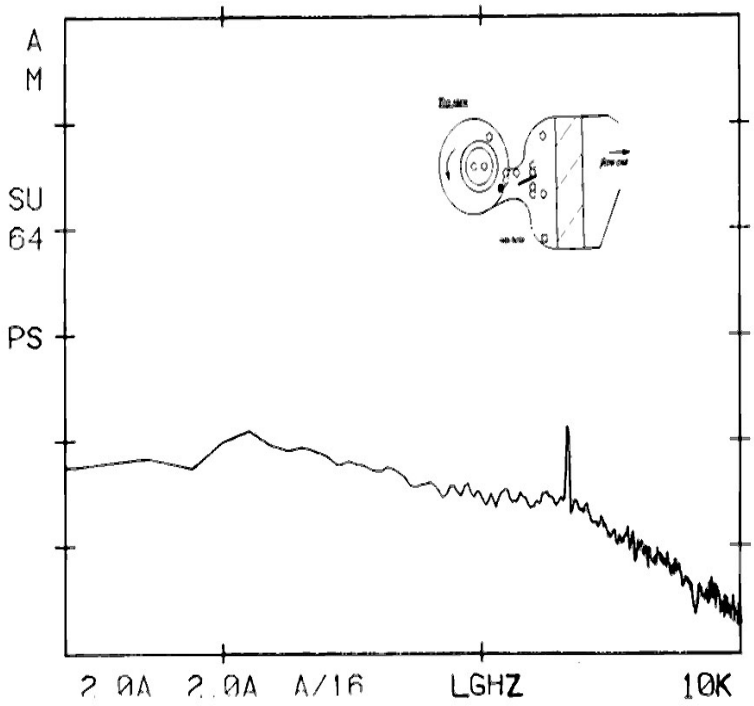

Figure 8.2: Power spectrum at fan blade exit (H2) vent full cold 14V blower Z1 (in) = 2.25

spectrum as shown by (George et. al. [28]).

The presence of spikes (Fig. 8.2) and humps (Figs. 8.3 and 8.4) in the lower end of the energy spectrum obtained from the automotive centrifugal fan studies can be associated with many different causes. The presence of the spike in the power spectrum in Fig. 8.5 , is probably due to rotor imbalance since the balancing clip was removed at that stage of testing. The hump observed in the power spectrum measurements is probably be due to the presence of a shear layer. It is characteristic of shear layers (locally large velocity gradients) to have spectral signatures in the form of spectral humps in the frequency domain. By contrast, the spectral signature of a localized flow phenomena related to the fan rotation rate shows up as discrete spectral peaks at well defined frequencies. A typical example of a flow phenomenon

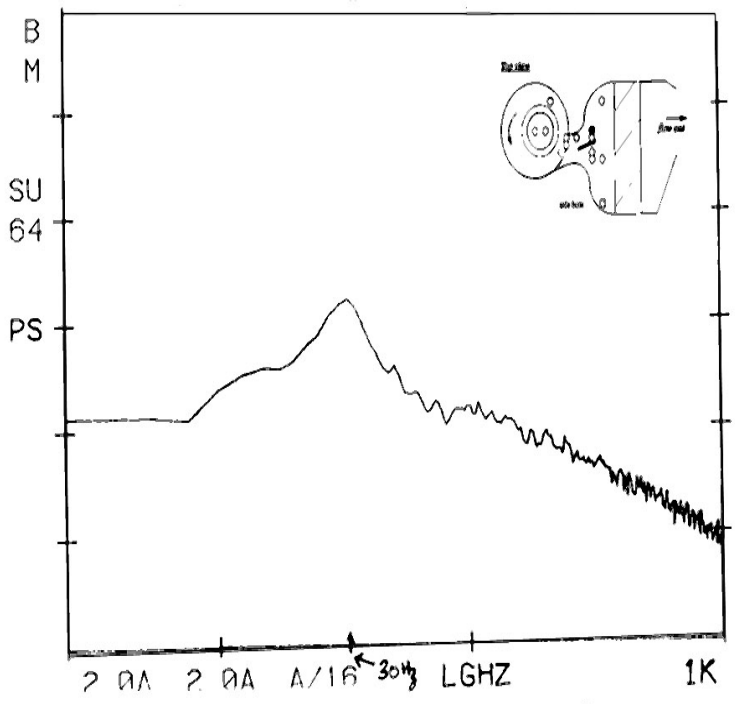

Figure 8.3: Power spectrum at diffuser inlet (H9) vent full cold 14V blower Z2 (in) = 8.0

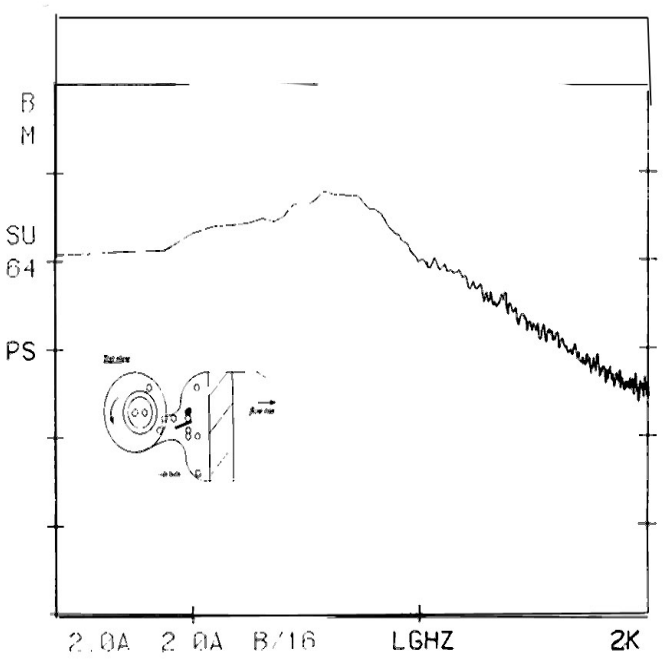

Figure 8.4: Power spectrum at diffuser inlet (H9) vent full cold 14V blower Z2 (in) = 5.75

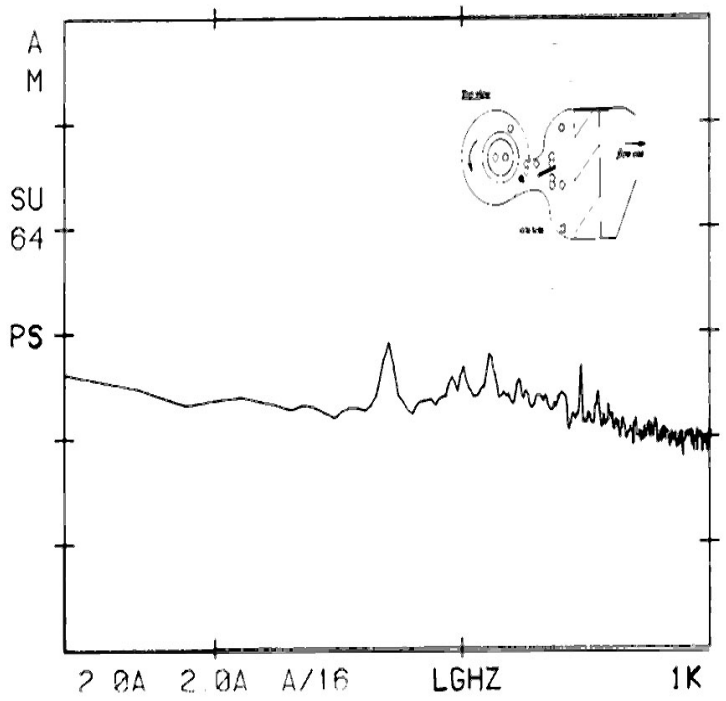

Figure 8.5: Power spectrum at fan blade exit (H2) vent full hot 14V blower Z1 (in) = 2.75

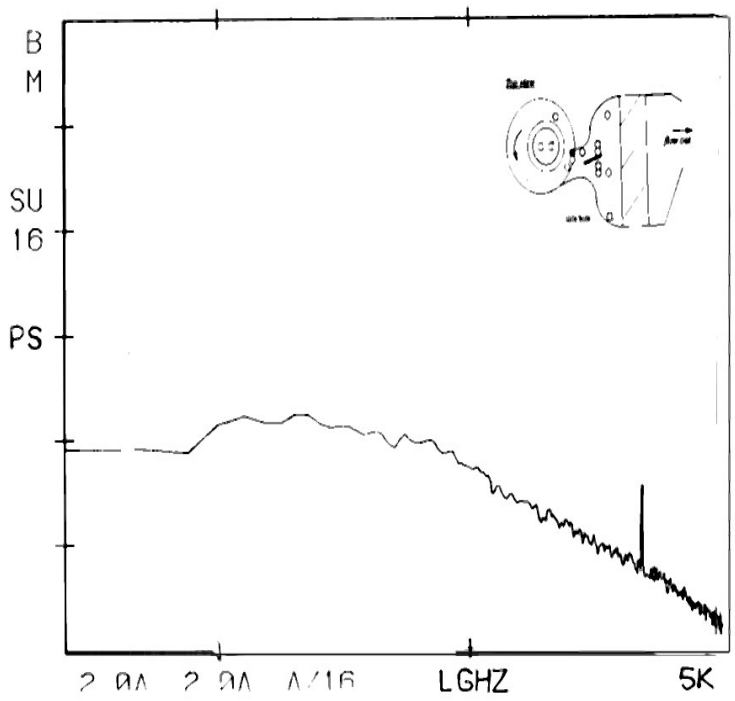

Figure 8.6: Power spectrum at fan blade exit (H4) vent full hot 14V blower Z2 (in) = 2.25

linked with the blade passing frequency (see Fig. 8.6) is the shedding of wakes from the fan blades.

The noise literature on centrifugal fans suggests that the sound generated by the fan has both discrete and broad-band components. The discrete tonal sound is a function of fan speed and the number of blades used on the fan rotor. It occurs at the blade passing frequency and its associated harmonics. In addition, discrete tonal components exist at the shaft (fan) rotational frequency and its harmonics. Both trends were observed in the power spectral measurements conducted on the automotive module at the fan blade exit position (Figs. 8.2 and 8.6. It is observed that the blade passing components dominate certain narrow frequency bands, whereas the overall power spectral levels are similar to typical turbulence spectra with flow

energy distributed over a broad-band of frequencies.

The noise literature on centrifugal fans also indicates that the overall sound levels are often dominated by the broad-band aerodynamic noise. Generally the broad band aerodynamic noise is associated with vortex shedding, turbulence, flow separation regions, etc. Noise studies performed in pipe/duct flows [49] have shown that if the peaks in the noise power spectrum are due to vortex shedding, etc., then one would expect all spectral peaks to be at the same Strouhal number, Str, for all flow speeds. In some ducted flow configurations, however, acoustic resonances independent of flow rate are encountered. A typical example of this type of resonance phenomenon is the flow through a gate valve [49]. In the particular case of the gate valve, the spectral peaks result from an acoustic response, such as cavity resonance combined with vortex shedding from the edges of the cavity. Sources of noise generation in flows through complex (ducted) geometries can be attributed to both flow-induced (aerodynamic noise sources) and acoustic duct resonances.

8.2.3 Two-Point Coherence Measurements

In the present study, two-point velocity cross-correlation measurements were also made using two single sensor hot-wire probes between various locations within the fan-scroll-diffuser area. The two-point cross-correlation measurements are presented using the coherence function. The coherence function is defined as the ratio of the squared modulus of the cross-spectral density function to the auto-spectral density functions; i.e.,

$$\gamma^2_{AB}(f) = \frac{S_{AB}(f)S^{\circ}_{AB}(f)}{S_{AA}(f)S_{BB}(f)} \tag{8.1}$$

where $\circ$ denotes complex conjugate. The definitions of the cross-spectrum, S_{AB} and the power spectrum, S_{AA} and S_{BB}, are given in Appendix F. The coherence function provides a non-dimensional measure of the correlation between two random signals

A(t) and B(t) at each frequency similar to the correlation coefficient (Bendat and Pieresol [7]). An important property of the Coherence function is its boundedness between 0 and 1, i.e.,

$$0 \leq \gamma^2_{AB}(f) \leq 1 \tag{8.2}$$

In analyzing coherence plots, it is important to recognize that low coherence is expected between the input signal and the output signal from a system for the following reasons [7]:

- measurement noise
- additional inputs to the system
- non-linearities in the system causing energy to be generated at additional frequencies

When the coherence function is zero at a particular frequency, the random signals A(t) and B(t) are uncorrelated at that particular frequency, suggesting that the signals are incoherent. Note that lack of correlation does not imply statistical independence. The analysis of the variance of cross-spectral estimators [34] has shown that the variance approaches zero when the coherence function is unity, and increases as the coherence tends to zero. Note that low coherence amplitudes imply large noise levels and inefficient estimates. Further, it was also shown [34] from analysis of the variance of the cross-covariance estimators that very large cross-covariances were generated, mostly artificially, between two uncorrelated stochastic processes as a result of large auto-covariances within the two processes. It is also important to note that the two-point velocity coherence function will be finite for a periodic process which is cyclostationary [**?**], i.e., a process X(t) with period T which has statistical properties that are invariant to a shift of the origin by integer multiples of T [53]. Typical numbers range between 0.8 to 1.0 for perfectly coherent signals, indicating that the signals are linearly related.

By contrast, a maximum correlation coefficient of 0.4 is found in jet shear layers in regions where the flow structures are highly organized [27]. Typically, the coherence between two random velocity signals at different spatial locations within a turbulent flow field containing organized flow structures is between 0 and 0.5. Certain discrete flow phenomena such as vortex shedding or blade wake chopping are expected to show a much higher degree of coherence; e.g., coherence values anywhere between 0.2 to 0.8 are typical. For hot-wire velocity signals spatially separated by a finite distance, the coherence function may be considered to be a measure of flow-eddy[2] correlation.

Finite coherence can also be linked to the passage of large scale coherent (organized) structures which pass by the hot-wires. Some degree of coherence would also be present if the time it takes for an eddy to traverse the distance separating the two hot-wires is much smaller than eddy turn over time. Another possibility is if the eddy length scale is larger than the probe separation distance, but the probe locations are not in the convection path of the coherent eddy. An eddy may also undergo convection, diffusion, or interaction (non-linear) mixing on its flow path before it reaches the second probe, so that the coherence is low (on the order of 0 to 0.1).

Note that the vortex stretching mechanism can alter the eddy structure and therefore its length scale, for example in a contraction or expansion region in the flow. This could severely modify the velocity coherence between the two probes. If the eddy length scale is much smaller than the probe separation distance, then this translates into a zero coherence, especially if the eddies do not cross both probes located within the flow. A typical example would be the small eddies that are shed off the fan blades due to flow separation. These would show no coherence between probes located at the fan blade inlet and at the exit of the blade trailing edge because of the convection and diffusion processes within the blade stage. The eddies embedded in the fan

[2]A flow eddy can be defined as a region in which flow conditions are similar and within the eddy flow quantities are well correlated, i.e., eddy dimension is given in terms of a correlation scale [19]

blade wake, however, show high coherence (0.4-0.60) at the blade passage frequency, as shown in Fig. 8.6.

8.3 Experimental facility and Instrumentation

Experimental testing was conducted on an automotive HVAC module without recirculation doors or vehicle airflow ducting using two single sensor hot-wire probes. The automotive HVAC fan was operated at both the 12 volt and 14 volt settings. Table 1 gives the relevant HVAC fan dimensions. The Auspex 5 micron tungsten hot-wire sensors were powered by two DANTEC 55M anemometers. The DANTEC anemometers have a very high frequency response (on the order of 100 KHz) compared to the hot wires or the highest frequency present in the HVAC flow field. The frequency response of the hot-wire sensors was much higher than the highest frequency present in the HVAC flow field. The spatial resolution of the hot-wire probe is limited to 5mm, except for one probe which had a 90 deg bend and offered a maximum spatial resolution of 7mm.

The anemometers were connected to a Nicolet Dual channel FFT Spectrum analyzer which was used to measure the instantaneous time signals, the single point power spectrum, and the coherence function. The dual channel FFT Spectrum analyzer is limited to a 1024 point FFT in the dual channel mode and a 2048 point FFT in the single channel operation. Thus all coherence measurements were done on a 1024 point FFT basis with the number of block averages (N) being an independent variable. Note that the record length determines the extent to which spectral peaks can be distinguished in the data so data acquisition must be done with several sampling frequencies so that the relevant frequencies of interest can be captured and resolved. For example, in order to capture the blade passage frequency (2400 Hz) the data was sampled at 5 KHz with a frequency resolution of 5 Hz. But in order to

resolve the coherence data, sampling was done at 500Hz or 1 KHz (with a frequency resolution of 0.5 Hz and 1.0 Hz respectively) since it was known that blower rumble occurs in the 50 to 200 Hz range depending on fan operating conditions. Note that the variance of the spectral estimator is inversely proportional to the bandwidth of the spectral window.

8.4 Experimental procedure

The selection of the measurement locations for the coherence study is critical to understanding the possible noise-related flow structure in the HVAC module. Previous results (both from flow field hot-wire velocity measurements at the fan throat and upstream of the evaporator core and the flow visualization study using the tuft technique) identified areas of flow recirculation (back-flow), flow separation, and jet-type (shear-layers) flows within the HVAC module. This aided in the selection of hot-wire positions for the coherence measurements. Another important factor in probe location selection was the overall geometry of the HVAC module. For instance, in the diffuser region after the fan throat, a shear-layer was anticipated at the edges of the fan throat exit. These experiments showed that there are shear-layers present around the four edges, although not of equal intensity, due to the fact that the core flow at the exit of the fan is highly skewed towards the fan cut-off side in the direction of fan rotation. The possible areas of shear layer formation and flow separation are shown schematically in Fig. 8.7.

Two point velocity-velocity coherence measurements were conducted between various locations in the automotive HVAC module. Power spectral measurements were also conducted at various locations within the fan module. In view of the fact that blower rumble occurs at low frequencies, the measurement locations were selected in order to capture possible large scale eddies that remain coherent over a certain

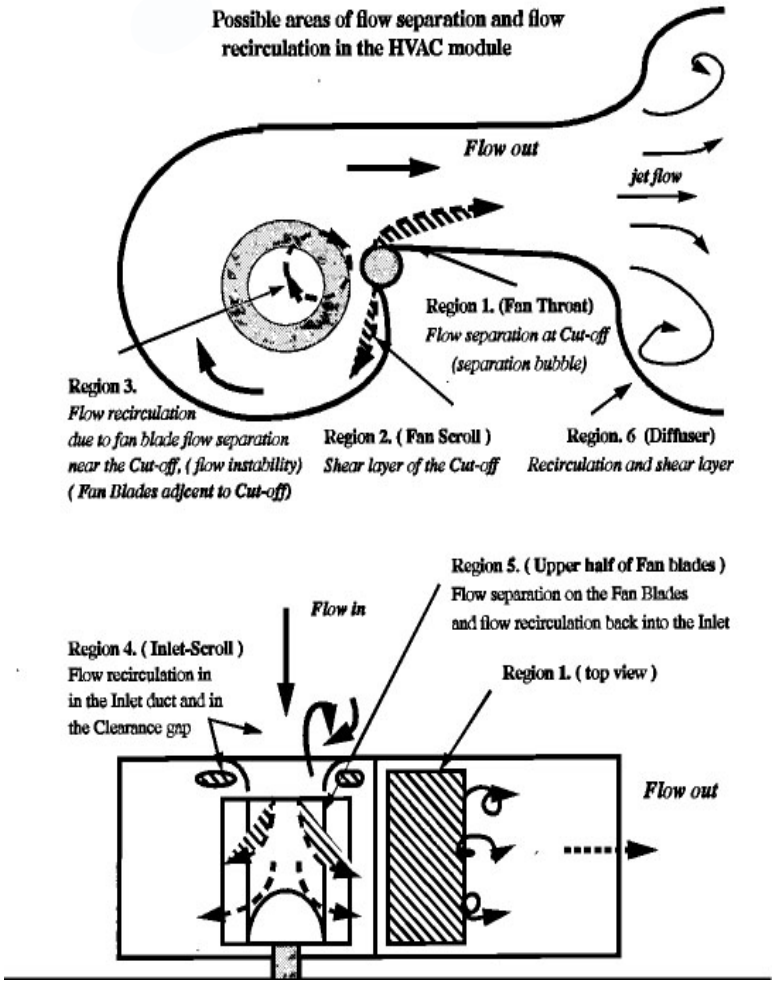

Figure 8.7: Possible areas of flow separation and flow recirculation in the HVAC module

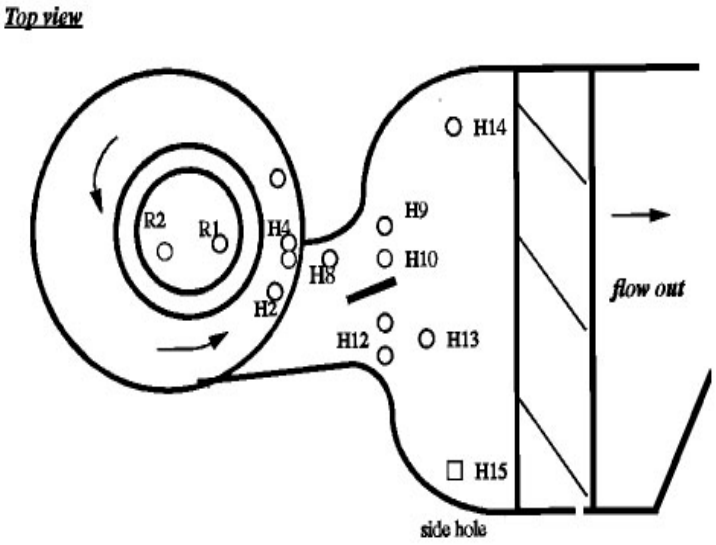

Figure 8.8: HVAC fan module geometry and measurement locations

finite distance within the fan-scroll-diffuser duct system. The measurement locations within the fan module are shown in Figs. 8.8 and 8.9, and are also listed below:

- Region 1: fan blade inlet (probe location R1 adjacent to the fan cut-off)
- Region 2: fan blade inlet (probe location R2 opposite to the fan cut-off)
- Region 3: fan blade exit (probe locations H2,H3 and H4, at the fan exit)
- Region 4: fan throat (probe location H8, towards the cut-off side wall)
- Region 5: inlet to diffuser (probe locations H9 and H12, jet exit shear layer region)
- Region 6: inlet to diffuser (probe locations H10,H11, core flow region)
- Region 7: upstream of evaporator (probe locations H13 and H14)

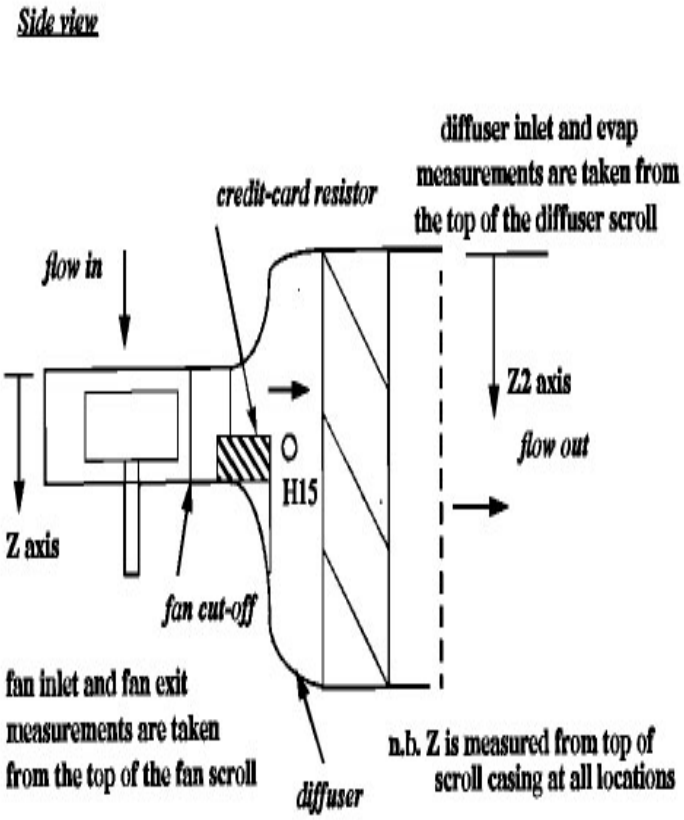

Figure 8.9: HVAC fan-scroll-diffuser-evaporator geometry

- Region 8: inlet to diffuser (probe location H15 to study the fan throat exit, side shear layers)
- Region 9: diffuser recirculation zones (probe locations used were H9, H10, H12, H13 and H14).

Spectral measurements were conducted in all the nine key regions. In addition coherence measurements were conducted between the following regions:

- fan blade inlet versus fan blade exit (Region 1 - Region 3)
- fan blade inlet versus diffuser inlet (Region 1 - Region 5)
- fan throat (cut-off side wall) versus diffuser inlet (Region 4 - Region 5)
- fan blade exit versus diffuser inlet (Region 3 - Regions 5,8 and 9)
- fan blade inlet versus diffuser inlet (Region 2 - Regions 5 and 6)
- diffuser inlet versus upstream of evaporator (Regions 5 - Regions 6 and 7)

In the figures presented below, all power spectrum figures are denoted by (PS) and all coherence figures are denoted by (COH). The vertical axis of the power spectrum figures is plotted on log axis, while the horizontal axis is plotted either as log of the frequency in Hertz, (x-axis is marked as LHZ) or as linear frequency (x-axis is marked as Hz). All velocity coherence figures are plotted as linear-linear with the vertical axis ranging from 0 to 1. The horizontal axes scaling varies from zero to 500 Hz, 1000 Hz and 2000 Hz for highlighting low frequency experimental results, whereas the high frequency data are plotted on a zero to 5 KHz or a 10 KHz range.

8.5 Results and Discussion

8.5.1 Fan Blade inlet versus Fan Blade Exit (R1 - H2, H3, H4)

Tuft flow visualization done in the fan blade inlet area (Region 1) showed a region of flow instability (flow recirculation in the circumferential direction) adjacent to the fan cut-off at approximately 1.0 in. along the blade span from the scroll top (see Figs. 8.8 and 8.9). The flow pattern (in VFH mode) at this location showed a strong localized recirculation region similar to the vortical structure observed by Denger and McBride [17], and Kind and Tobin [36]. In order to obtain spectral information about this region, one hot-wire was placed directly at this flow instability region and another at the fan blade exit to study the coherence across the fan rotor.

Figs. 8.10 and 8.11 (VFC[3] at 1.75 and 1.0 in.) to Figs. 8.12 and 8.13 (VFH at 1.75 and 1.0 in.) show the variation of the spectra (both in shape and magnitude) with the fan blade span. The upper part of the blade span showed lower spectral levels, but the lower blade span regions showed higher low frequency content. This is also the region of high through-flow across the fan rotor. Since the fan produces a higher flow rate in the VFC mode in contrast to the VFH mode, more flow energy is expected in the VFC mode, even though the turbulence intensities could be higher in the VFH mode because of the low mean velocities (form stalled flow) in the upper part of the fan rotor. Note, the flow instability region at fan inlet does not allow an easy interpretation of the flow phenomena observed. The individual spectra at the inlet to the fan blades (cf. Figs. 8.13 and 8.11) show an increase in turbulence levels in the VFH mode compared to the VFC mode. The power spectrum shown in Fig. 8.10 indicates no spectral peak at the BPF (blade passing frequencies) in the VFC mode.

[3]Abbreviations defined in Section 8.2.1

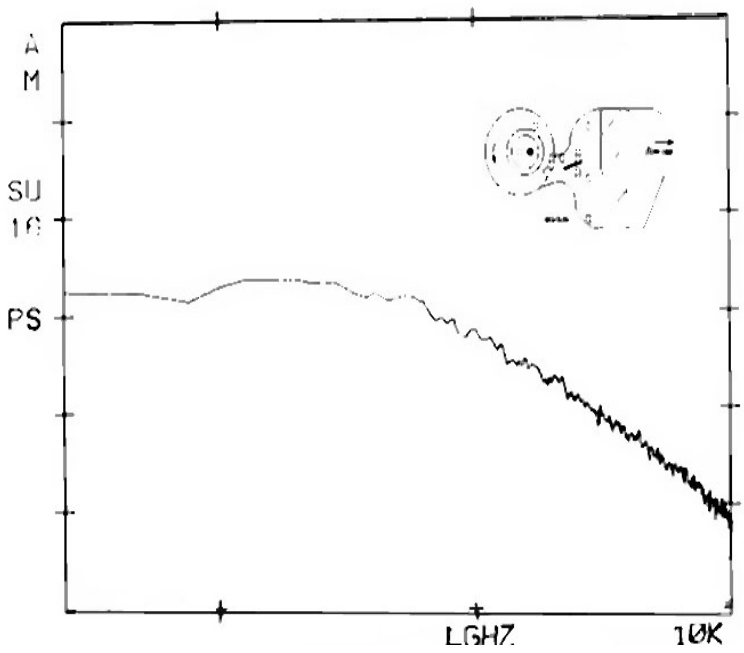

Figure 8.10: Power spectrum at fan blade inlet (R1) vent full cold 14V blower Z1 (in) = 1.75

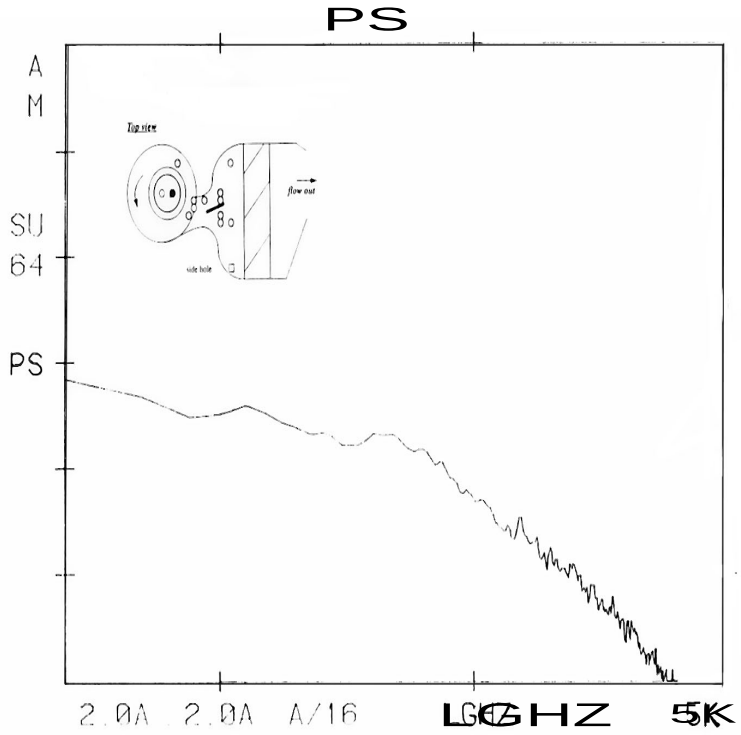

Figure 8.11: Power spectrum at fan blade inlet (R1) vent full cold 14V blower Z1 (in) = 1.0

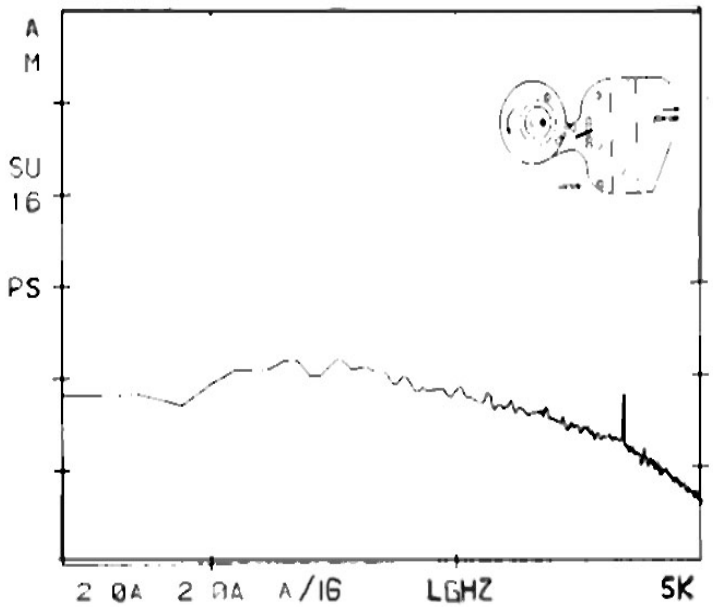

Figure 8.12: Power spectrum at fan blade inlet (R1) vent full hot 14v blower Z1 (in) = 1.75

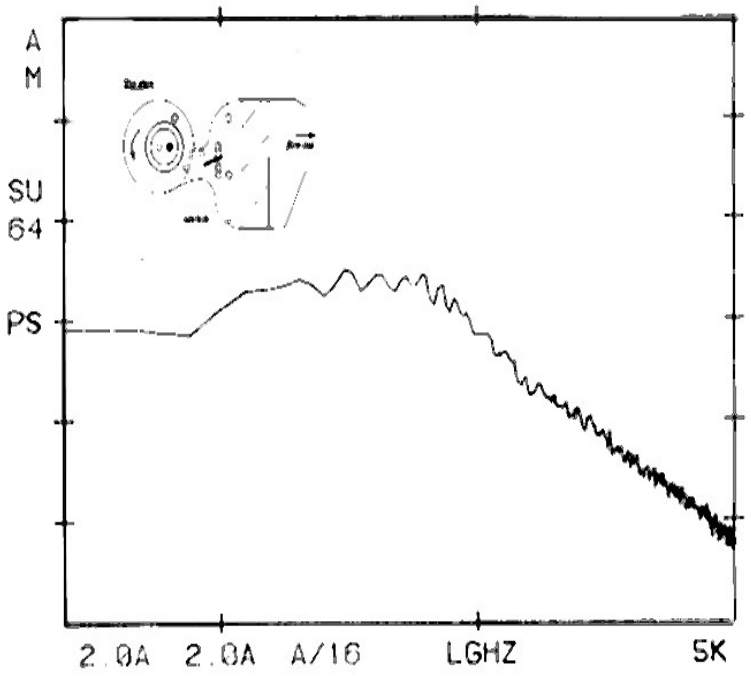

Figure 8.13: Power spectrum at fan blade inlet (R1) vent full hot 14V blower Z1 (in) = 1.0

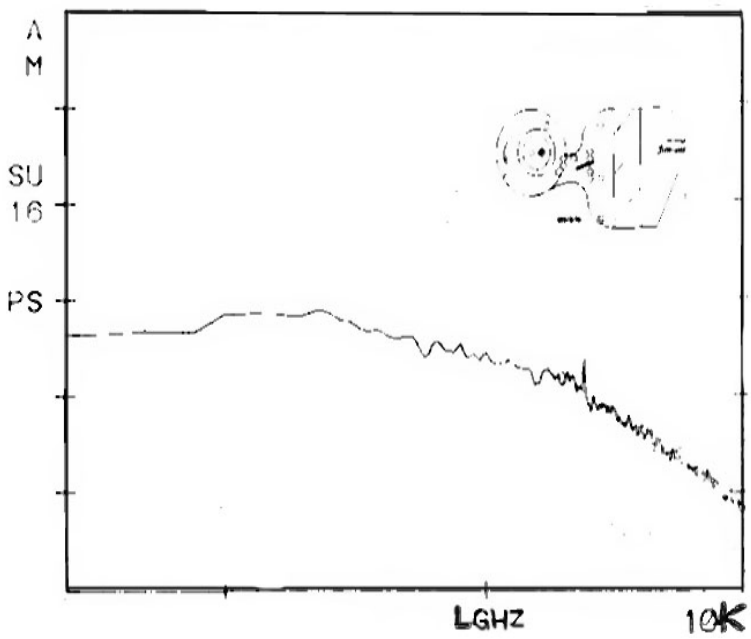

Figure 8.14: Power spectrum at fan blade inlet (R1) vent full hot 14V blower Z1 (in) = 1.75

This could be with high enough energy levels at the (Z= 1.75 in, at fan inlet) to mask any peak at the BPF, in contrast to lower levels found in the VFH mode (Fig. **??**) at the same location. The opposite trend is observed in the spectral energy levels in the fan inlet region (closer to the top of the fan, i.e., Z= 1.0 in.) compared to the lower position along the fan blades (Z = 1.75 in.). The occurrence of higher spectral levels for the VFC mode (in comparison to those in the VHF mode as function of blade height) is possibly due to the fact that most of the through flow occurs from the bottom 50 to 60 percent of the fan rotor, with the upper half of the rotor being stalled. A high value of velocity coherence across the fan blades in VFH mode would suggest possible flow reversal through the fan blades with flow separation. In the VFH mode, however, the coherence measurements shown in Fig. 8.15 show a strong correlation only at the blade passage frequency (BPF = 2436 Hz), whereas the power

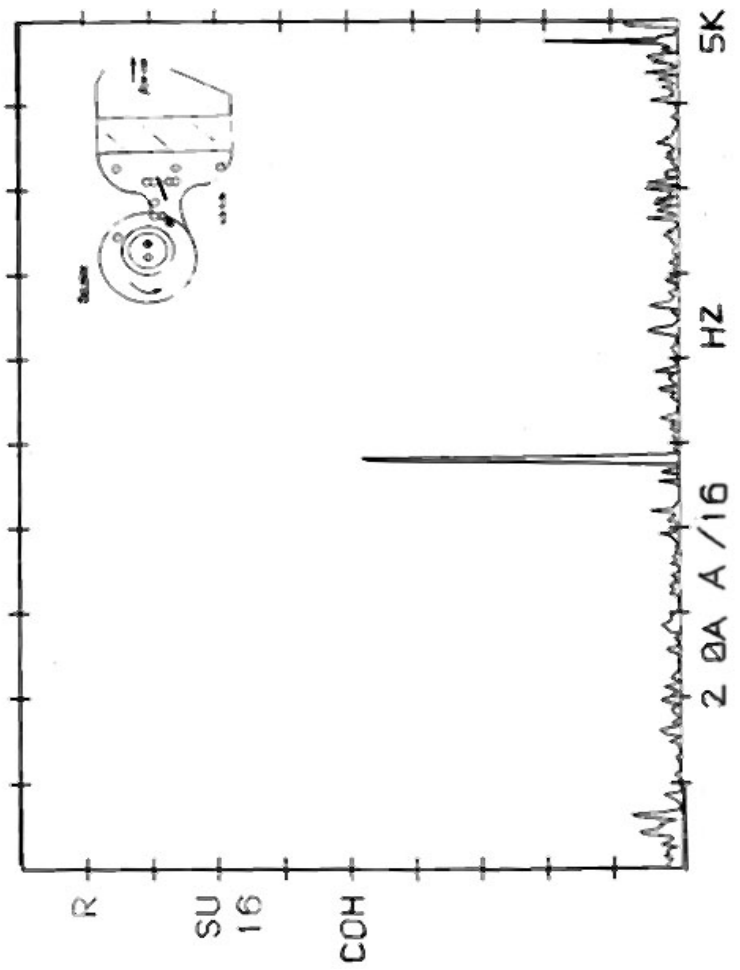

Figure 8.15: Coherence between fan blade inlet (R1) and fan blade exit (H2) vent full hot 14V blower Z1 (in) = 1.75 Z2 (in) = 1.75

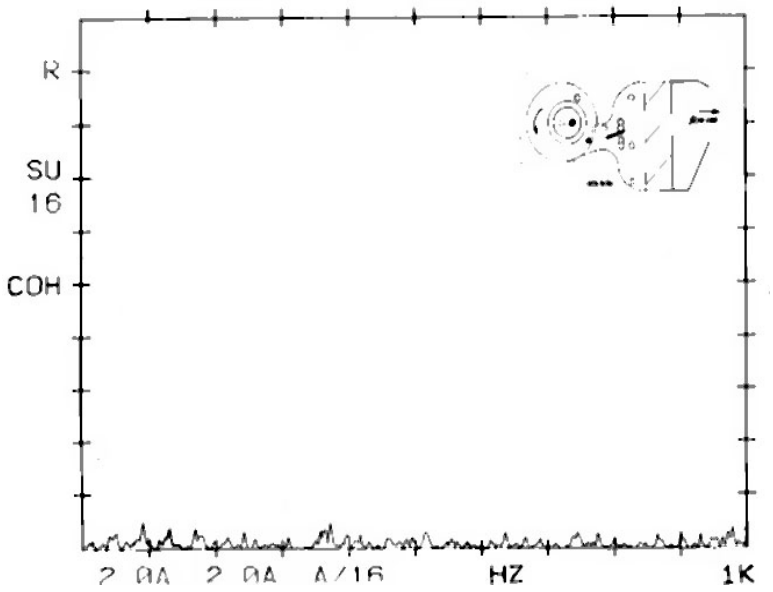

Figure 8.16: Coherence between fan blade inlet (R1) and fan blade exit (H2) vent full cold 14V blower Z1 (in) = 1.75, Z2 (in) = 2.75

spectrum measurements (Fig. 8.6 and Fig. 8.12) show discrete peaks at the BPF at both fan blade inlet and exit. However in the VFC mode, there is no coherence at the BPF or any other frequency (Fig. 8.16) .

The overall flow picture across the fan blades is consistent with the various results from the literature review (see Appendix A); in particular, studies of squirrel-cage type centrifugal fans indicate that 40 percent of the upper part of the fan rotor is stalled and very little through flow is present. In addition, the stalled region of the fan blade span, there exists a vortical structure adjacent to the cut-off which induces some flow back towards the inlet, so some flow is forced through the narrow gap between fan blade trailing edge and scroll volute near the cut-off point. From the point of view of fan rumble noise, there is no velocity coherence across the fan rotor in the broad band rumble frequency range for either the VFH or the the VFC modes. It is plausible, however, to suggest that the presence of vortical structures in the fan

blade inlet region might be correlated to the rumble noise, since the fan inlet flow pattern can be interacting with the inlet to the fan impeller independently of the fan blade exit. This hypothesis should be verified using either pressure transducers or microphones in conjunction with hot-wires in this region.

It should be noted that the presence of spectral peaks at the fan rotation frequency or the blade passage frequency is related to the orientation of the hot-wire sensor with respect to mean flow direction (probe orientations shown in Fig. 8.17) and the positioning relative to the fan blades. The results from the fan blade inlet (R2) location with the sensor pointing towards the flow (orientation-P2) as shown in Fig. 8.18 show a spectral peak at 333 Hz (which is an integer multiple of the fan rotational frequency). The spectral peaks disappear when the probe is aligned to the blade leading edge at the R2 location (orientation-P1). The opposite trend, however, was observed for the R1 location which is adjacent to the cut-off section. The power spectral measurements at the R1 location showed the existence of a peak at the BPF in the VFH mode operation with the hot-wire probe aligned with the leading edge of the fan blade (orientation-P3). This BPF peak disappeared when the probe was aligned to the flow (opposite to the direction of fan rotation). The R2 location at the fan inlet is an area of laminar flow with very low velocity fluctuations compared to the R1 location which is directly 180 degrees opposite to the R2 position. The R1 fan inlet position is adjacent to the fan cut-off and is thereby suffering from high turbulence and recirculating flow.

8.5.2 Fan Throat and Diffuser Inlet, H8 - H9

The coherence between the fan throat (H8) and diffuser inlet (H9) as shown in Fig. 8.19 indicates insignificant coherence in all frequency bands. The measurements

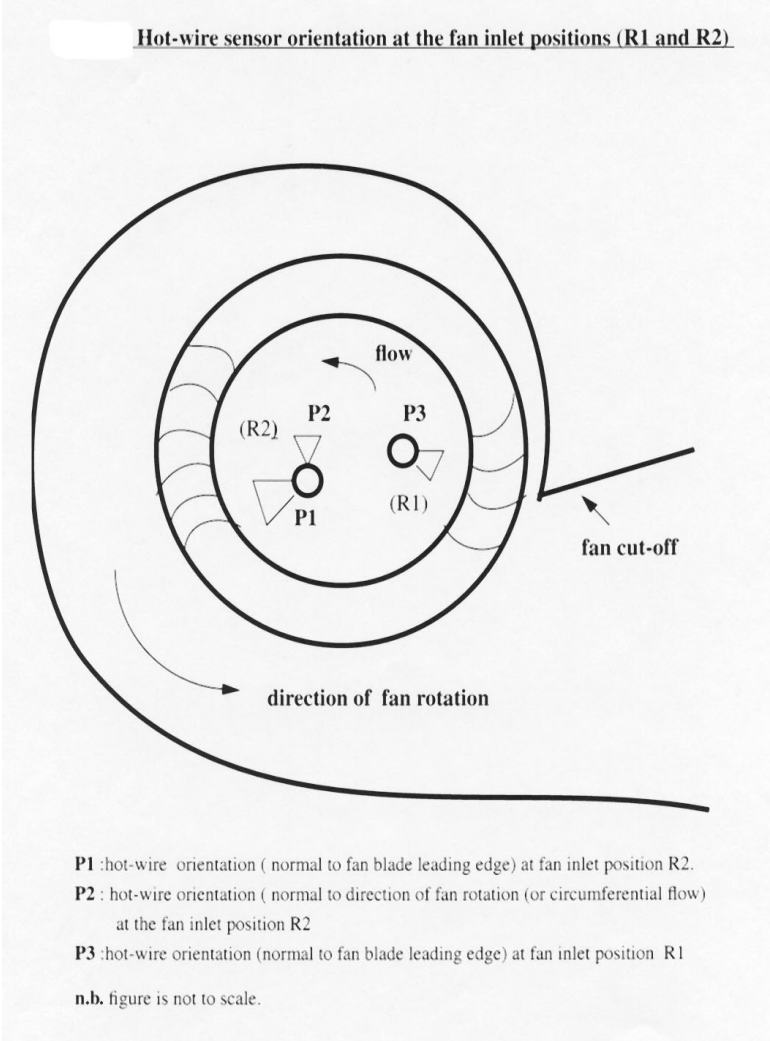

Figure 8.17: Hot-wire sensor orientation at the fan inlet positions (R1 and R2

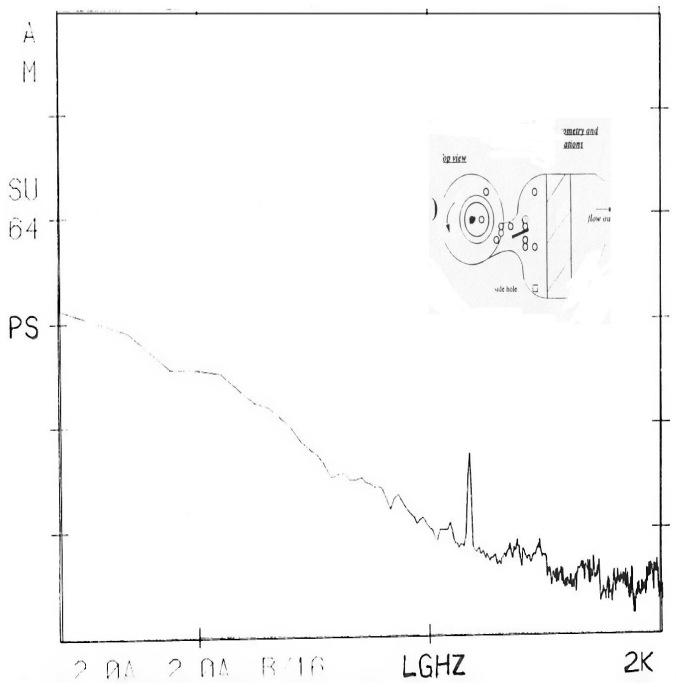

Figure 8.18: Power spectrum at fan blade inlet (R2) vent full cold 14V blower Z1 (in) = 1.5

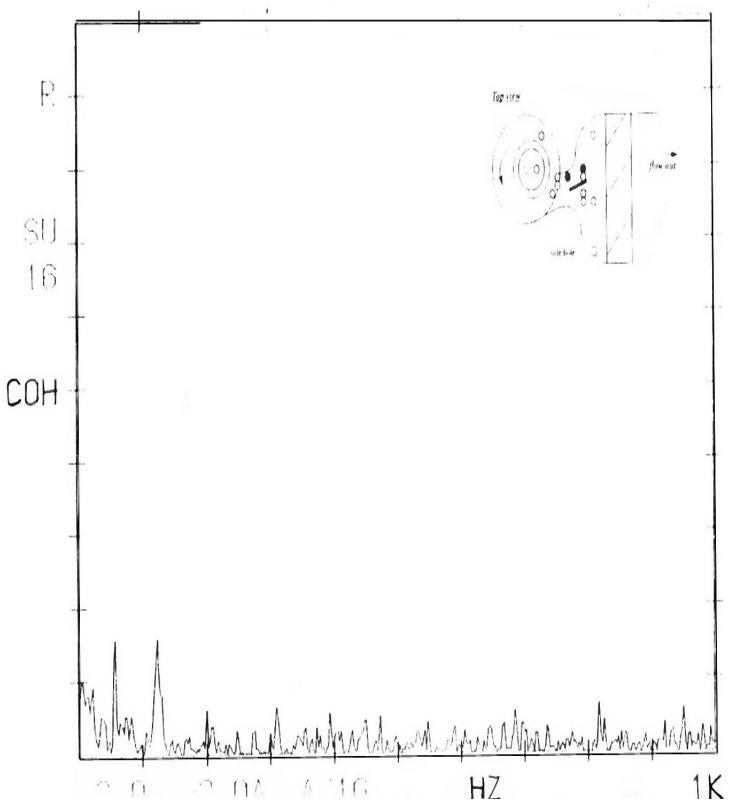

Figure 8.19: Coherence between fan throat (H8) and diffuser inlet (H9) vent full hot 14V blower Z1 (in) = 1.75 Z2 (in) = 5.5

are complicated, however, because of the presence of a small separation bubble attached on the cut-off side of the fan throat. This was observed by tuft flow visualization. Local flow reversal was also observed in part of the fan throat in previous hot-wire measurements as shown in Figs. ??, ??, and ?? and ?? ??, and ??. The measurements showed a complicated flow pattern at the fan throat with at least two flow deficit regions in the throat cross-section plane. A jet type flow pattern is indicated with possible flow reversal regions (due to very low velocities and very high turbulence intensities). Note that no coherence measurements were made between the fan blade exit and the side opposite to the cut-off at the fan throat. A moderate level of coherence was observed between the fan blade exit (H2) position and diffuser inlet (H9) in the VFH mode 8.20, in contrast to the negligible coherence seen in Fig. 8.19. Note that data for Fig. 8.20 was taken at a lower sampling rate to increase the resolution at low frequencies. These results indicate that the flow in the vicinity of the cut-off side wall of the fan throat is a probable flow recirculation zone with a dividing streamline. As a result, there are two zones of flow: one with recirculation next to the wall and one with the core flow from the fan rotor and scroll region. The hole position H8 is located inside the recirculation zone. A hot-wire placed in the recirculation zone would not be expected to show coherence with a hot-wire placed in the mainstream core flow, since the flow patterns are very different and are decoupled from one another. However when the two hot-wires are placed in the same flow path then velocity coherence should be expected, and is observed, between the two hot-wire signals in these different locations. Finite coherence also exists between the fan blade exit location (H2) and diffuser inlet (H9) as shown in Figs. 8.21 and 8.22 in the VFC mode.

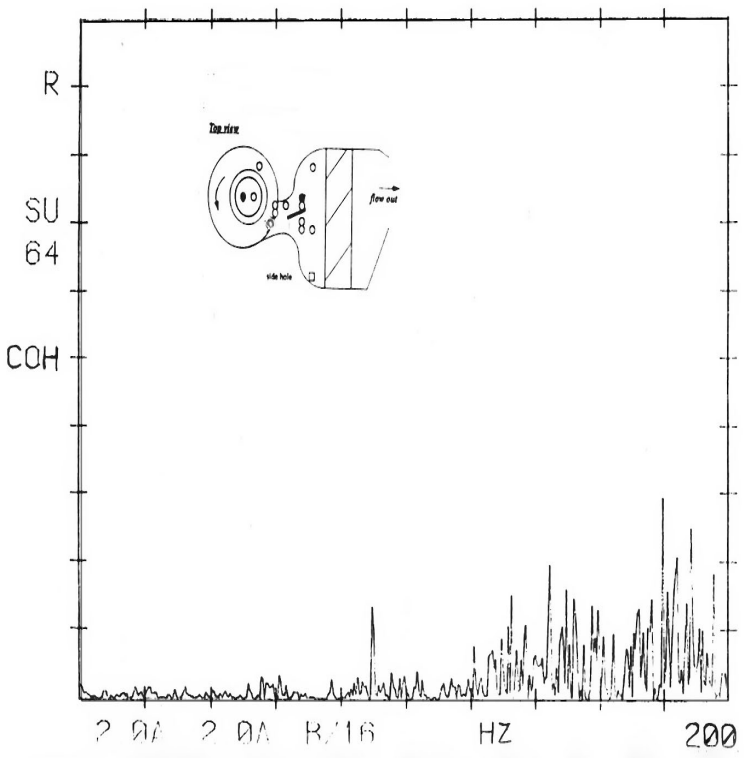

Figure 8.20: Coherence between fan blade inlet (R2) and diffuser inlet (H9) vent full hot 14V blower Z1 (in) + 1.5, Z2 (in) = 6.75

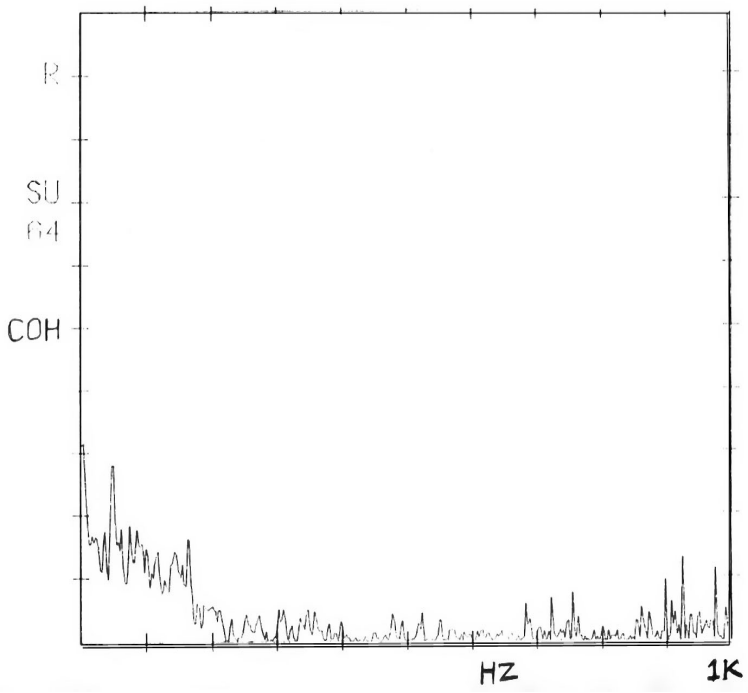

Figure 8.21: Coherence between fan blade exit (H2) and diffuser inlet (H9) vent full cold 14V blower Z1 (in) = 2.0 Z2 (in) = 5.75

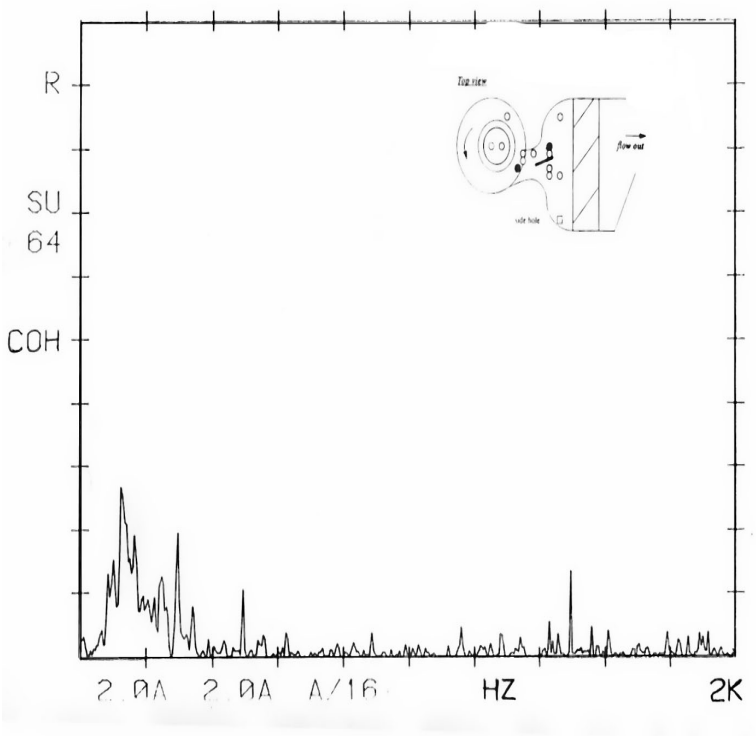

Figure 8.22: Coherence between fan blade exit (H2) and diffuser inlet (H9) vent full cold 14V blower Z1 (in) = 2.25 Z2 (in) = 6.5

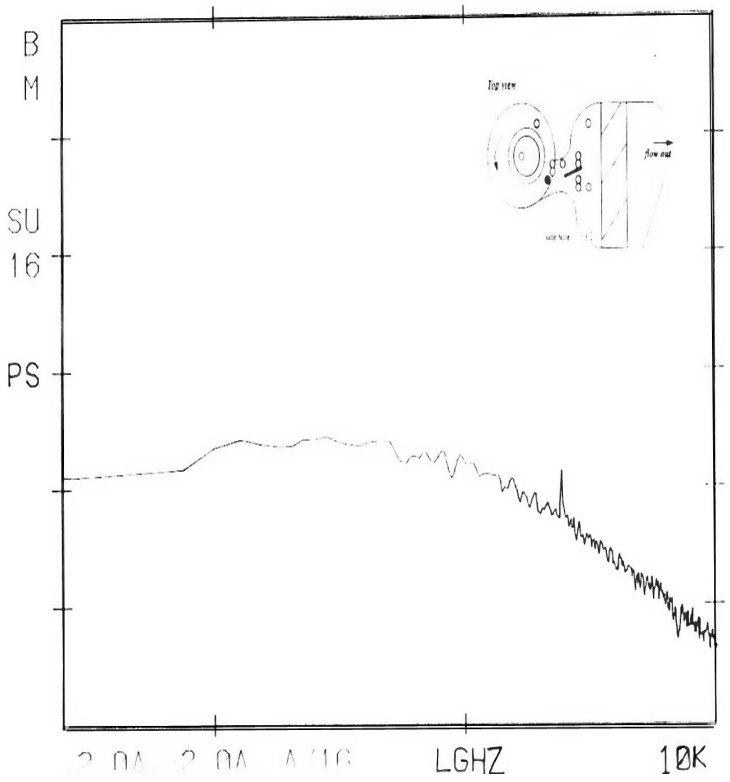

Figure 8.23: Power spectrum at fan blade exit (H2) vent full hot 14V blower Z2 (in) = 2.75

8.5.3 Fan blade exit and diffuser inlet, jet shear layer and core (H2- H9)

Power spectral measurements at the fan blade exit indicate a frequency peak at the blade passage frequency for both VFH and VFC modes (Figs. 8.23 and 8.24) . Comparing the broad band turbulence level in the VFH mode to that in the VFC mode, as shown in Figs. 8.23 and 8.24, makes it clear that the VFH mode has higher energy levels (above 100 Hz). Also, at the fan blade exit, as shown in Figs. 8.25 and 8.24, the flow energy level increases with increasing distance down the fan blade span. The coherence between fan blade exit and diffuser inlet (fan throat exit) in the VFC

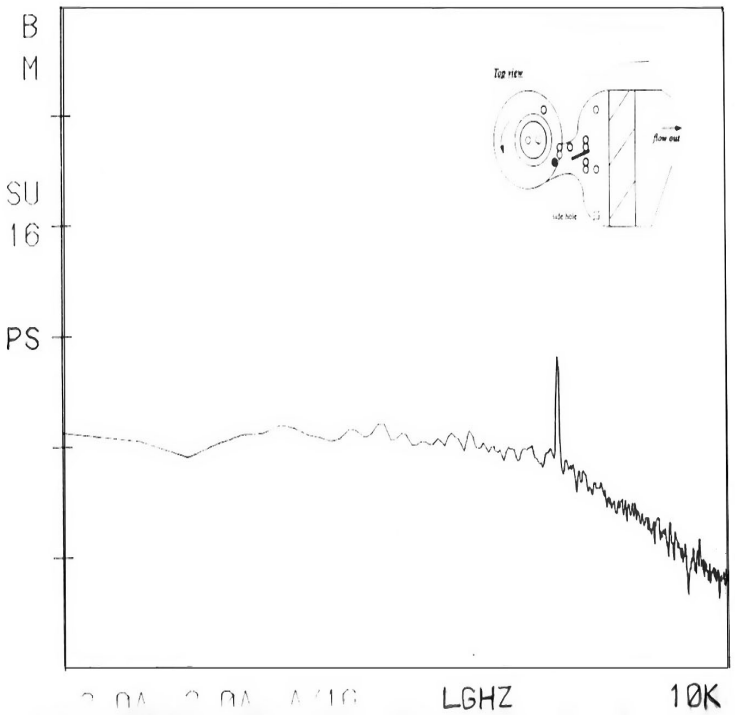

Figure 8.24: Power spectrum at fan blade exit (H2) vent full cold 14V blower Z2 (in) = 2.75

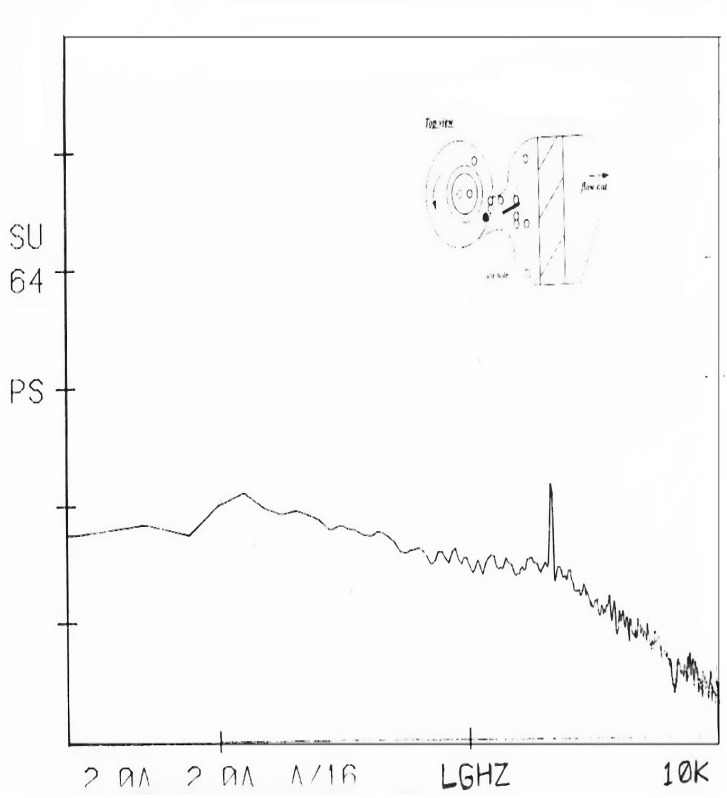

Figure 8.25: Power spectrum at fan blade exit (H2) vent full cold 14V blower Z1 (in) = 2.25

mode is shown in Fig. 8.21. This shows strong coherence when the second probe is located inside the shear layer generated at the exit of the fan throat and the wide angle diffuser at Z2 = 5.75 inches. It is interesting to note that the coherence is stronger in the VFC mode than in the VFH mode. Figs. 8.21 and 8.22 show that the coherence between the two velocity signals occurs in the 0 to 200 Hz range which includes the rumble frequency band. Another observation made with flow visualization at the fan throat exit was that the flow field is skewed towards the cut-off side wall in the direction of fan rotation. This leads to asymmetric side shear layers at the inlet to diffuser. Previous hot-wire measurements [**?**], in the fan throat (Figs. **??** and **??**) indicate that the flow is a type of strong jet flow skewed towards the upper corner of the fan throat. S.J. Kline [37] in his discussion of stall in diffusers has identified three different flow regimes which can occur under different plane walled diffuser area expansion ratios and pressure gradients:

- first, the occurrence of a large transitory stall (a time dependent three dimensional flow). Slightly wide angle diffusers are characterized by large areas of stall that attach and detach from the walls. For example, a diffuser with a wall length to throat width (aspect ratio) of 3 and a 30 degree expansion angle will produce a transitory stall.

- Second, a fully developed stall which is characterized by nearly steady recirculating flow on the side walls. For example, a diffuser with an aspect ratio of 3 and expansion angle of 50 degrees will generate a steady stall pattern.

- Third, a jet flow resulting from extremely wide angled diffusers. For example, expansion angles larger than 60 degree covering a range of aspect ratios from 3 to 25 fall into this category. The jet flow pattern will generate large steady recirculating flow regions on both side walls with a jet type of flow discharging from the inlet core, almost as if the walls were absent.

Kline's two-dimensional diffuser geometric parameters can be used to evaluate automotive HVAC diffusers. The HVAC diffuser under consideration has a diffuser wall length-to-throat width ratio (L/W) equal to 1.6, a diffuser expansion angle (2θ) equal to 78 degrees, and operates at a Reynolds number (Re) based on fan throat height equal to 100,000. By Kline's plane walled diffuser stall criteria, a jet type of flow pattern is expected across the diffuser with the presence of large regions of steady flow recirculation on the diffuser side walls. This is consistent with the hot-wire measurements described earlier. This type of flow pattern is also likely in the VFC mode which has a higher volumetric flow rate through the fan.

A different type of flow regime occurs when the walls of the diffuser are wide angled; the flow first attaches itself to one of the side walls, then separates and/or attaches to the other side wall. This transitory stall pattern also causes large scale recirculation zones within the diffuser. Although it is not possible to identify diffuser transitory stall phenomena by using spectral measurements alone, knowing that such a phenomena occurs in wide angle diffusers under certain boundary conditions helps explain the complicated flow patterns upstream of the evaporator in different fan operating modes.

In the VFC mode, the distribution of spectral energy occurs over a wider frequency band (0 to 120 Hz frequency bandwidth) than in VFH mode. The individual spectra at the shear layer of the jet exit show (Figs. 8.26 and 8.27) that in VFH mode, the low frequency end (below 70 Hz) of the power spectrum is heavily loaded compared to VFC mode (Fig. 8.28). The VFC mode spectra, by contrast, exhibit a slight hump at the bandwidth characterizing rumble noise, but contain less energy in the low frequency end. The power spectral levels for the flow in the core flow region at the diffuser inlet (Fig. 8.29) are lower than those in the jet exit shear layer (Fig. **??**) in the rumble noise bandwidth in VFC mode.

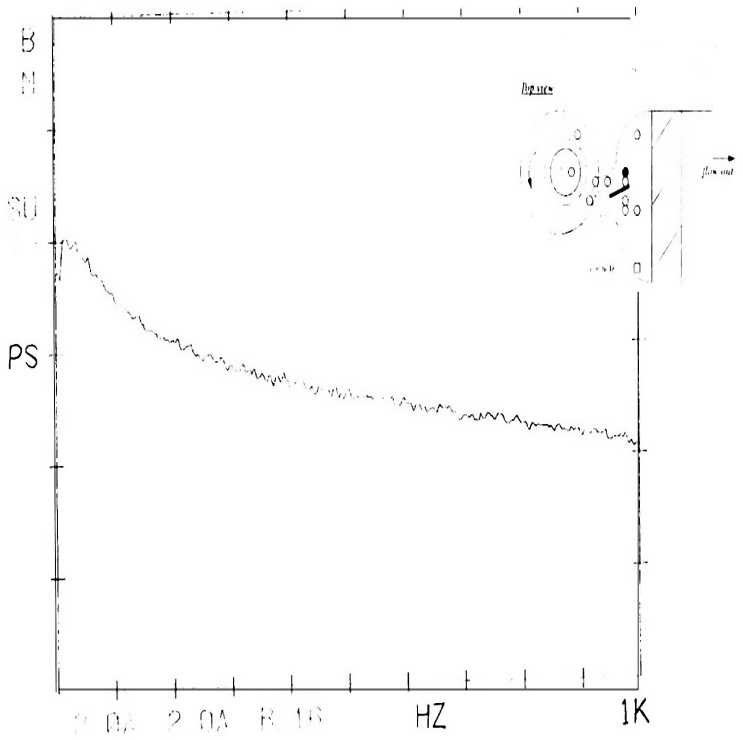

Figure 8.26: Power spectrum at diffuser inlet (H9) vent hot 14V blower Z2 (in) = 7.0

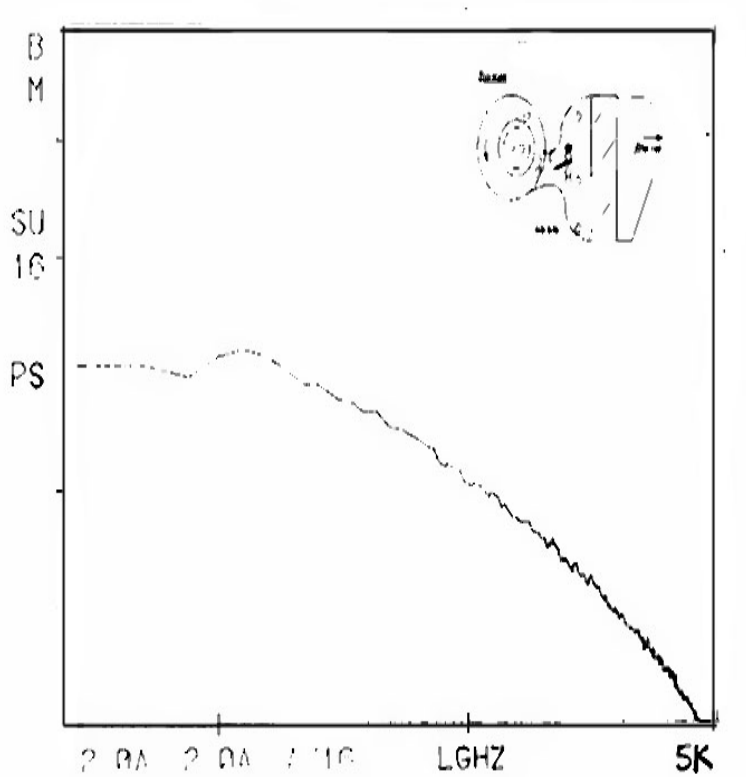

Figure 8.27: Power spectrum at diffuser inlet (H9) vent full hot 14V blower Z2 (in) = 1.75

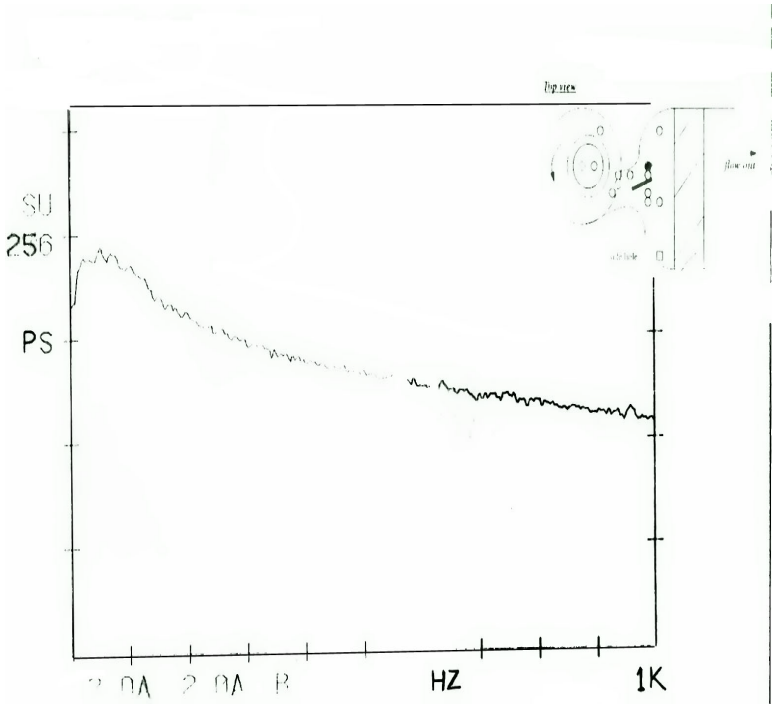

Figure 8.28: Power spectrum at diffuser inlet (H9) vent full cold 14V blower Z2 (in) = 7.0

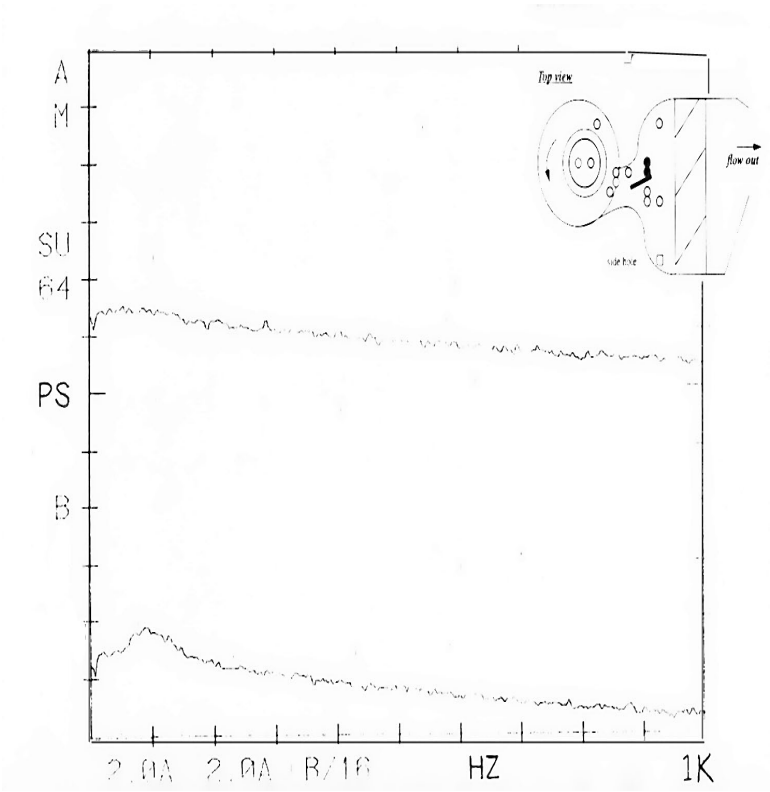

Figure 8.29: Power spectrum at diffuser inlet positions (H9 - H10) vent cold 14V blower Z1 (in) = 2.5 Z2 (in) = 2.5

It is well known that the turbulent fluctuations are much higher in the region of flow with larger velocity gradients (shear layers). This means that the power spectral levels are higher for higher turbulence levels, and more concentrated around those frequencies that are due the turbulent shear layers. The experimental results indicate that such shear layers occur at the junction of the fan throat exit and the inlet to the HVAC diffuser. More energy at the lower frequencies could also be due to the presence of larger scale coherent structures in the flow (e.g., large flow separation and recirculation zones with lower mean velocities).

Due to the high aspect ratio of the HVAC diffuser, the diffuser inlet is analogous to a sudden expansion with strong shear layers generated as the flow exits the fan throat region and enters the diffuser. These shear layers not only reduce the fan aerodynamic efficiency, but also serve as potential sources of noise generation, especially if the jet velocity is high. The flow across a sudden expansion (wide angle diffuser) is analogous to a flow over a backward facing step in terms of the flow recirculation characteristics which are mainly caused by the abrupt change in the solid wall geometry. Fig. 8.30 depicts a flow over a backward facing step with a uniform upstream velocity U_j and a step height H. The bulk of the flow over the step re-attaches to the bottom wall at distance b, whereas some of the flow recirculates in the corner region. An approximate characteristic recirculation frequency, fr, can be derived from the velocity U_j and recirculation zone height h, that is, $(fr = U_j/h)$. For example, in case of the HVAC diffuser, if the average velocity at the fan throat exit is 15 m/s and a recirculation height of the diffuser (or the width of the fan throat exit) can be taken as 4 inches (0.1 m), a characteristic recirculation frequency of 150 Hz is obtained.

It was originally thought that the experimental evidence of the concentration of flow energy around the 100 Hz frequency at the jet exit shear layer in VFC mode, as shown in Fig. 8.26, was linked to the natural shedding frequency of the jet flow at the fan throat exit, (see Fig. 8.30). However, a natural shedding frequency of a turbulent

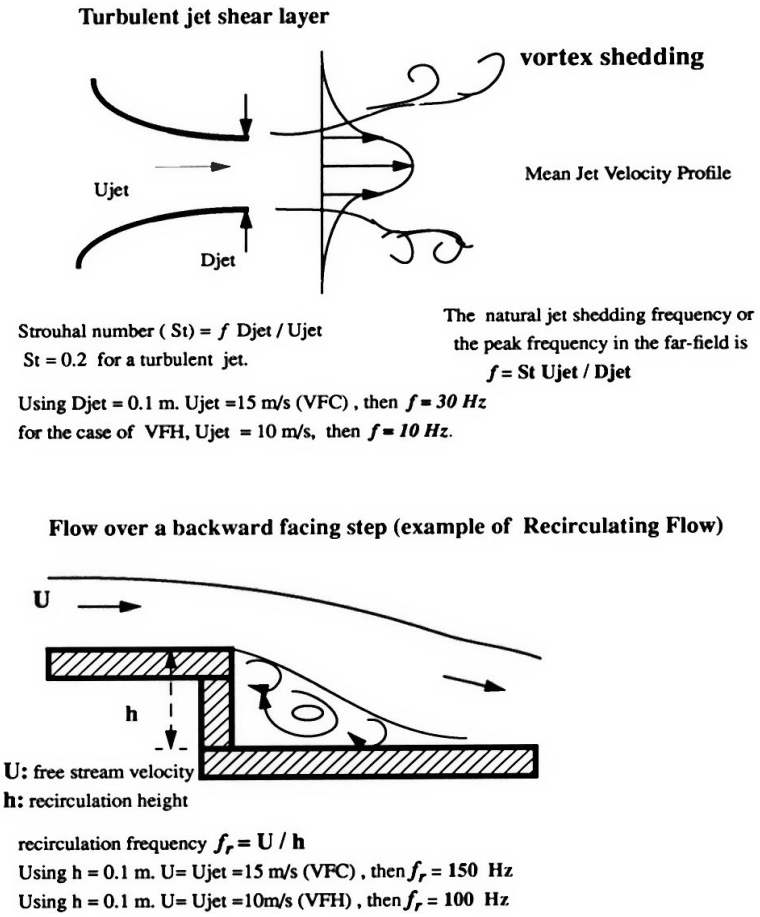

Figure 8.30: Shear flow and recirculation flow model

jet was derived from the Strouhal number ($Str = fD/U$) for a round turbulent jet ($Str = 0.2$, [49]). A typical fan throat exit velocity of U= 15 m/s and the fan throat height D= 0.1 m (4 in), results in a jet natural shedding frequency of 30 Hz. It is also noticed that the jet flow occupies around 40 percent of the fan throat, according to the velocity measurements done in the automotive HVAC module (Figs. **??** and **??**). If the characteristic jet diameter D used to obtain the jet natural shedding frequency is reduced by 40 percent, then the shedding frequency obtained is 75 Hz.

The VFC mode exhibits a high energy content in the 70 to 120 Hz range. So the characteristic frequencies obtained from both flow models indicate that the recirculation frequency is higher than the jet natural shedding frequency when applied to the automotive HVAC diffuser section. Given the very wide angled geometry of the HVAC diffuser and the power spectrum results obtained at diffuser inlet (inside jet shear layer), it is highly likely that recirculation is occurring in both VFC and VFH modes inside the diffuser. In contrast to the VFH mode, however, the VFC mode exhibits higher mean velocities in the jet shear layer, thus causing a shift in the frequency band dominated by high energy flow. The coherence measurements at the diffuser inlet in VFC (Fig. 8.31) and VFH modes (Fig. 8.32) indicate a shift in the coherent band to lower frequencies when in the VFH mode in contrast to the VFC mode, consistent with the power spectral results.

One of the conclusions that can be made from both the coherence and power spectral measurements of Region 5 is that in the VFH mode the flow energy distribution shifts to much lower frequencies (below 70 Hz) and does not show significantly high flow energy content at the bandwidth of the rumble noise. Both the flow energy distribution and coherence results in the jet shear layer region (diffuser inlet) of the fan, however, show significant concentration at and around the rumble frequency band in the VFC mode.

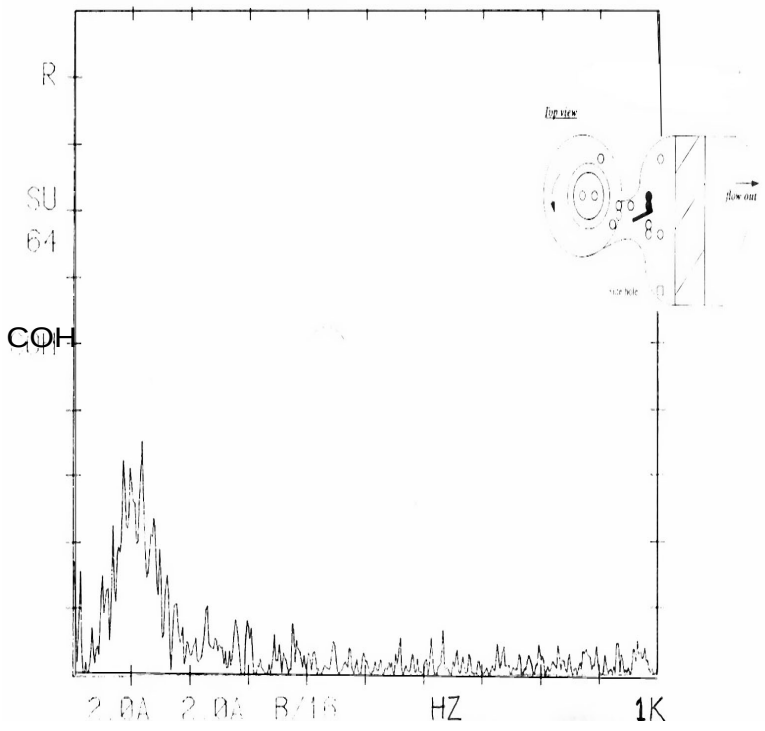

Figure 8.31: Coherence between diffuser inlet positions (H9 - H10) vent full cold 14V blower Z1 (in) = 3.0 Z2 (in) = 3.0

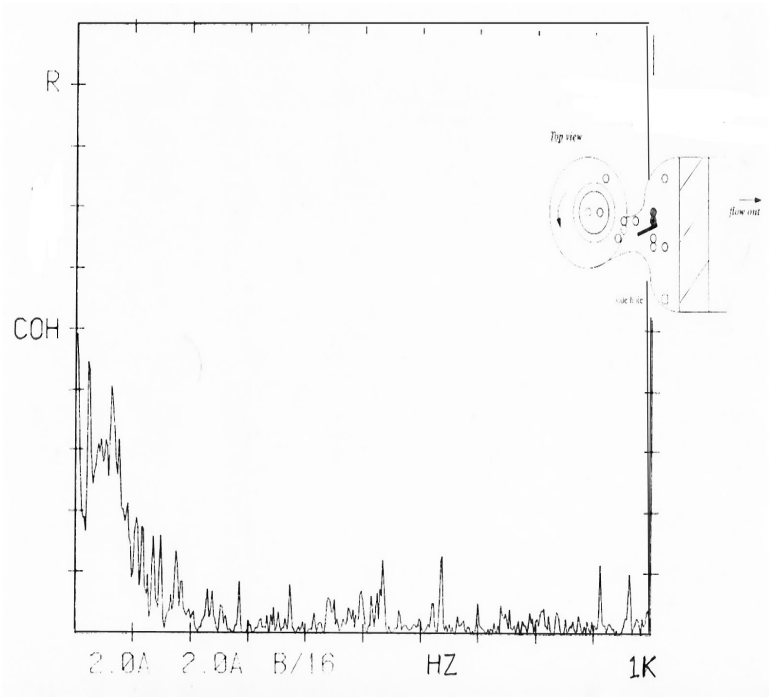

Figure 8.32: Coherence between diffuser inlet positions (H9 - H10) vent full hot 14V blower Z1 (in) = 3.0 Z2 (in) = 3.0

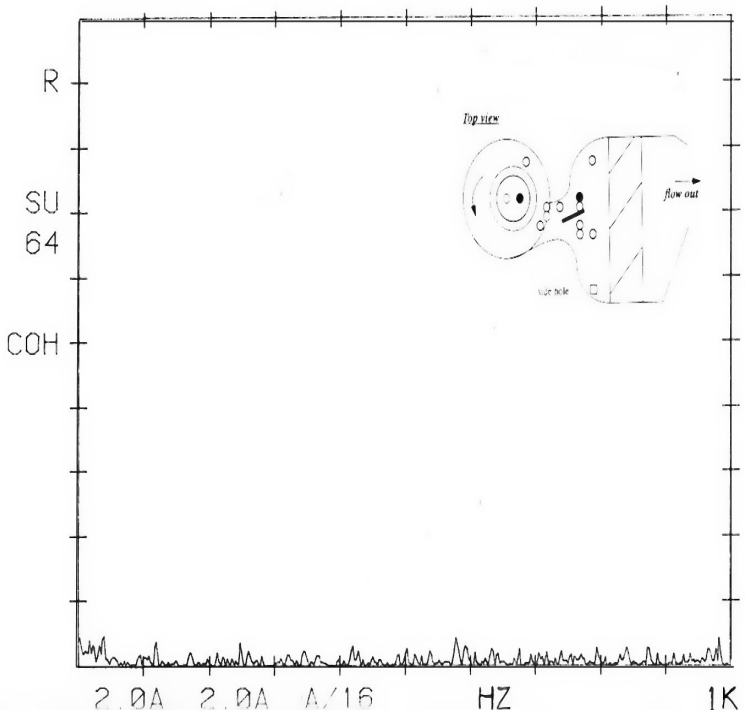

Figure 8.33: Coherence between fan blade inlet (R1) and diffuser inlet (H9) vent full hot 14V blower Z1 (in) = 1.75 , Z2 (in) = 3.5

8.5.4 Fan Blade Inlet (adjacent to fan cut-off) versus Diffuser Inlet (R1 - H9)

Coherence was measured between the fan blade inlet and at different heights in the diffuser inlet section covering both the shear layer region and the core flow. Coherence measurements made between the HVAC fan blade inlet (R1) location (at the flow instability region) and the HVAC diffuser inlet (H9) do not show any coherence in any frequency band for either the VFH mode or the VFC modes (Fig. 8.33) . In particular, all the positions tested showed zero coherence in both the rumble frequency bandwidth (0 to 1000 Hz) and in the fan blade passage frequency band (1000 to 5000 Hz), both in the VFH and VFC modes. Fig. 8.33 is a plot chosen typical of the

coherence for both the VFH and VFC modes. Similar tests were conducted between fan blade inlet position R1 and other diffuser positions such as H10, H12 and H14. No combinations showed any significant coherence in the rumble noise frequency range.

The presence of a flow instability area at the fan inlet adjacent to the fan cut-off is a well-established fact in forward curved squirrel-cage fans ([36], [17]). The existence of flow recirculation regions in the diffuser investigated here has been established from both the tuft flow visualization and the hot-wire measurements. The original hypothesis was that the flow instability region at the fan blade inlet was flow coupled to the recirculation area in the diffuser through a feedback mechanism. The coherence measurements conducted between fan inlet and diffuser inlet suggested that no such flow coupling exists. The power spectral results previously cited have shown that the energy levels are changing both with fan speed and fan operating modes, which indicates that the flow structures are being modified. Smoke flow visualization, together with velocity and total pressure measurements [36] have shown that the flow instability area grows and shifts in position with respect to the fan rotor adjacent to the fan cut-off at off design fan operating.

From both coherence results and previous work on forward curved centrifugal fans, it can be reasonably concluded that the identified flow structures (at the fan inlet and the diffuser) are not strongly flow coupled to each other and are probably being altered independently with varying fan operating conditions. This does not necessarily mean that these flow structures are not contributing to the noise generation process, but it does imply that the flow phenomena are decoupled from each other (at least in the flow areas tested).

In light of the experimental evidence presented, an alternative hypothesis can be proposed for the mechanism generating "rumble" noise: namely, that the identified flow structures at fan blade inlet and in the HVAC diffuser excite certain duct (cavity) acoustic modes at resonant frequencies which cannot be identified by purely fluid

dynamic testing. It is therefore recommended that vibration analysis of the fan casing and the diffuser cavity be conducted to determine the model response. Vibration analysis would indicate if there is a structural resonance both at the blade passing frequency and at the "rumble" frequency range.

One such study was carried out by Koopman et.al.[**?**] who used the boundary element method to compute the acoustic pressures on the surfaces of a 6-bladed backward curved centrifugal fan casing in terms of the surface vibration (which was measured experimentally). Their results indicated, that the aerodynamic noise sources at the BPF generated near the entrance plane of the inlet to the fan dominated the noise spectrum in the field. Also, at the first sub-harmonic of the blade tone, the sound power generated from the inlet and the fan casing were within 3dB of each other. Although, Koopman's investigation concentrated at the blade passing tone of the fan, their approach can be applied to the automotive HVAC module in order to investigate the influence of fan casing and diffuser cavity structural resonances on the overall sound radiation, in order to see whether any coupling exists between cavity resonance and fan "rumble" noise.

8.5.5 Fan Blade Inlet (Opposite to the fan cut-off) versus Diffuser Inlet (R2 - H9)

Another area surveyed with hot-wires was at fan blade inlet (the R2 location), which is 180 degrees opposite to the cut-off side of the fan scroll. The individual velocity spectra at fan inlet (R2) location are shown in Fig. 8.34 (VFH) and Fig. 8.35 (VFC). The instantaneous time traces at fan inlet location, R2, showed that the flow is very nearly laminar with insignificant turbulence levels in the VFC mode, but an increase in turbulence intensity takes place in VFH mode operation. The coherence between the fan inlet position, R2, and the diffuser inlet position, H9, as shown in Fig. 8.36,

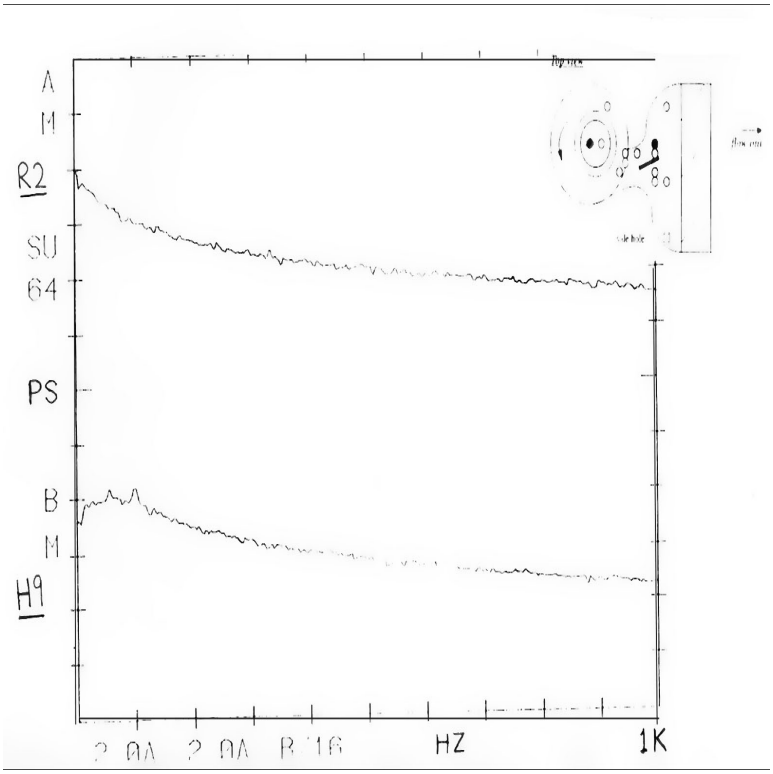

Figure 8.34: Power spectrum at fan blade inlet (R2) and diffuser inlet (H9) vent full hot 14V blower Z1 (in.) = 1.75 , Z2 (in.) = 2.5

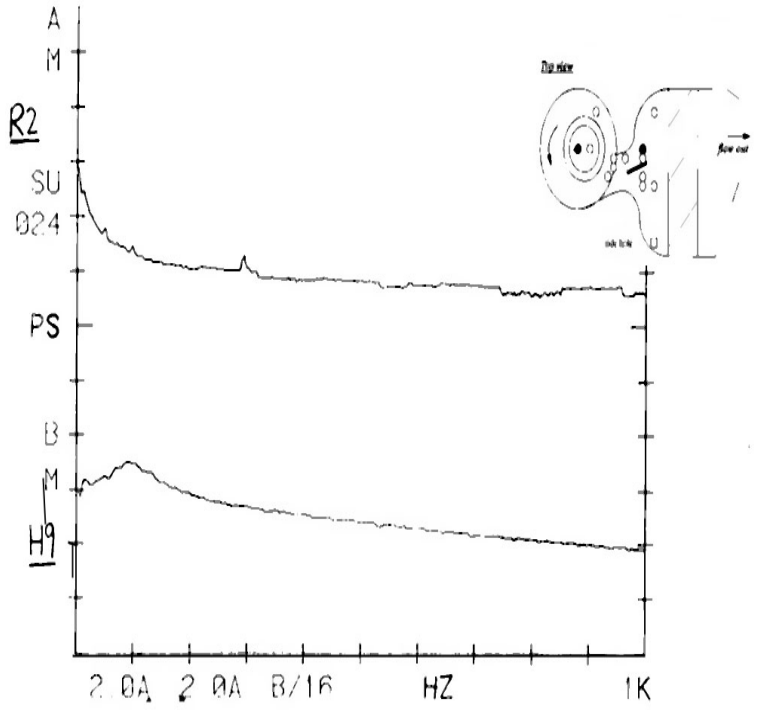

Figure 8.35: Power spectrum at fan blade inlet (R2) and diffuser inlet (H9) vent full cold 14V blower Z1(in.) = 1.75, Z2(in.) = 2.5

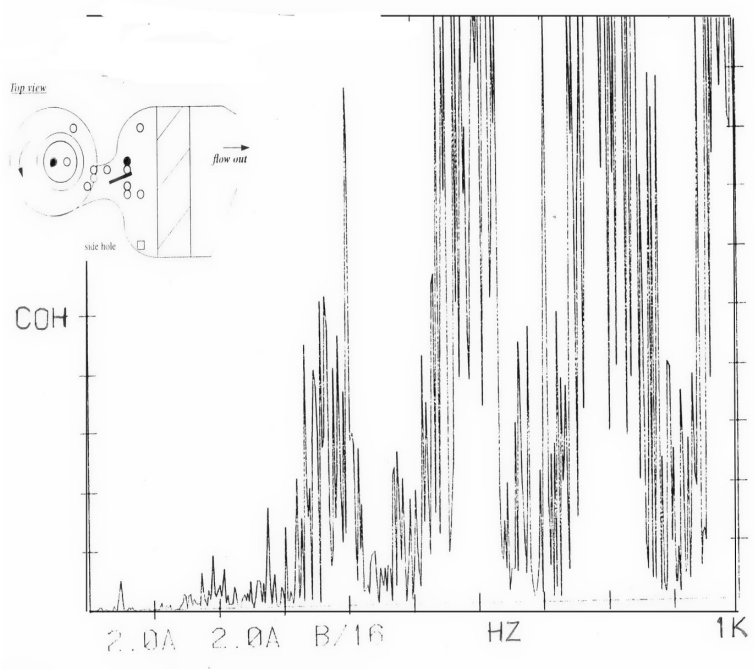

Figure 8.36: Coherence between fan blade inlet (R2) and diffuser inlet (H9) vent full cold 14V blower Z1 (in.) = 1.5 , Z2 (in.) = 7.0

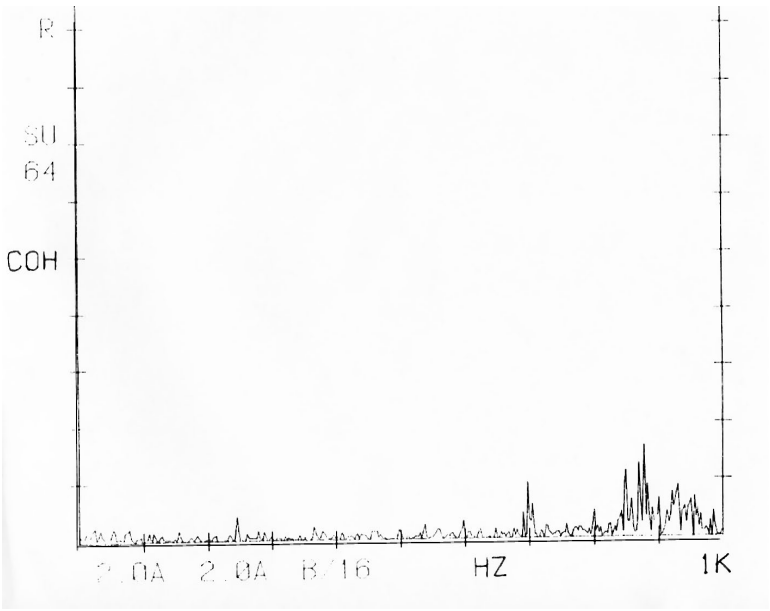

Figure 8.37: Coherence between fan blade inlet (R2) and diffuser inlet (H9) vent full hot 14V blower Z1 (in.) = 1.5, Z2 (in.) = 1.75

indicates that the there is moderate to high coherence (0.3 to 0.6) in the 200 to 300 Hz frequency band in the VFC mode, and a very high coherence (0.8 to 1.0) in the range above 700 Hz. In the VFH mode there was insignificant coherence between the R2-H9 test locations in the low frequency band, although some weak coherence did exist around the 900-1000 Hz frequency band as shown in Fig. 8.37.

It must be noted that the individual power spectral levels are so low at the fan blade inlet position R2, that the coherence results of (R2-H9) cannot be given much credibility. This is because it can be shown that if the magnitudes of the individual power spectra (the denominator) are very low, the magnitude of the coherence function can be very high due to random errors in the spectral estimates. Such is the case of a power spectrum for a nearly laminar flow (with the signal dominated by noise) like that at position R2 opposite the cut-off. The idea of the effect of very low power spectrum levels on the measured coherence function is supported by the fact that the

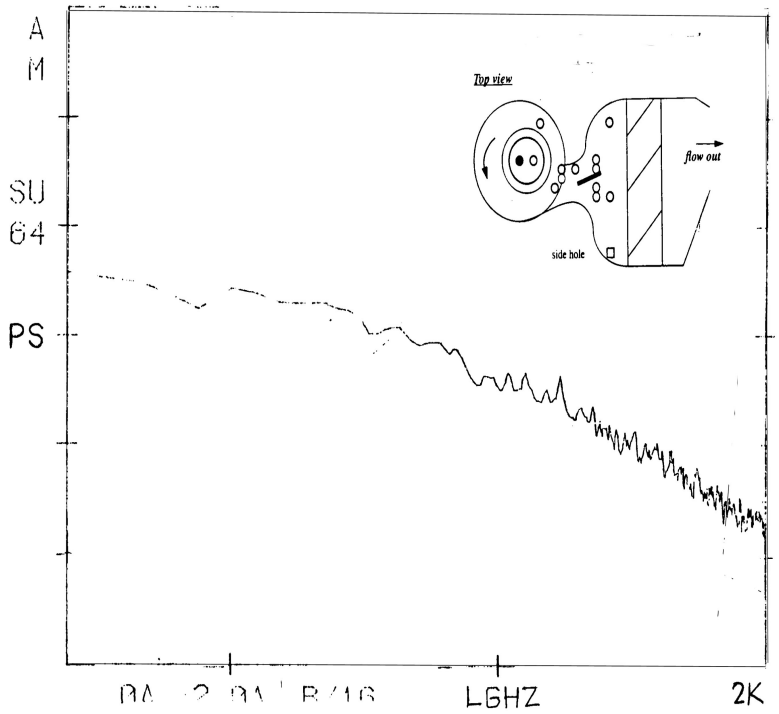

Figure 8.38: Power spectrum at fan blade inlet (R2) vent full hot 14V blower Z1 (in) = 1.5

difference in the magnitude of the power spectrum in VFC mode compared to VFH mode, as shown in Figs. 8.34, 8.35 and 8.38 , is of the order of two, whereas the VFH energy levels are much higher, thus making the coherence unusually high in case of VFC.

It is thus concluded that emphasis should not be put on the coherence results for the R2- H9 test location. The difference in the individual power spectra at the fan inlet position, R2, does indicate a change in flow phenomena occurring in that region, especially the fact that turbulence levels increase significantly going from VFC to VFH modes.

The other significant observation from the R2-position spectra is that a discrete frequency peak occurs at approximately six times the fan rotation speed, 333 Hz,

as shown in Fig. 8.18 (VFC). This possibly occurs in VFH mode also as shown in Fig. 8.38, but if so it is embedded in the high level broad band turbulence. Whether this spectral peak is due to flow reversal out of the fan blades or some other phenomena is not clear.

Interpreting the coherence function (see equation 1) to extract the flow physics is not a trivial matter. One reason for the unusually high coherence could be an insufficient number of block averages used to compute the coherence function. It was noticed that the coherence levels were significantly altered when a higher number of block averages was taken. For example, increasing the block averages from 16 to 256 reduced the unusually high coherence levels over a wide frequency range. Certain areas, however, remained coherent at similar levels even after increasing the number of block averages. For periodic flow phenomena which are coherent, for example at the blade passage frequency, increasing the block average size reduces the coherence levels at all frequencies except at the discrete blade passage frequency. This is a theoretically predicted result for the coherence of cyclostationary processes [**?**]. The theoretical/numerical studies (Jenkins and Watts [34]) on the bias in coherency and cross-spectral estimates suggest:

- First, even if the theoretical cross-spectrum is zero the mean smoothed coherency estimate can be large (assuming the the biases in the autospectral estimators are ignored).

- Second, the bias in the coherency estimate increases as the bandwidth decreases; thus for larger spectral window sizes the variance increases. In fact, it was shown that the coherency estimator approached unity as the bandwidth approached zero for the case of two uncorrelated autoregressive time series.

- Third, the bias in the coherency estimator is also directly proportional to the first derivative of the phase spectrum and to the coherency itself. Thus large

time delays (or lags) will cause very inaccurate coherence estimates.

These reasons for the bias in the sample coherency estimate may be the cause of the large coherence observed in the VHC mode between the laminar flow region, R2, and the turbulent flow region at the diffuser inlet, H9. From a qualitative perspective, the significant result in Region 1-5 is that the range of frequencies where coherence occurs is different for the VFC and the VFH modes between fan blade inlet (laminar region (R2)) and the diffuser inlet (H9). This implies that the flow structures are changing in magnitude and that the flow path is being altered at the different fan operating modes. The fact that there is finite coherence in the VFC mode while there is almost none in the VFH mode at Region 1-5 is interesting, since this probably implies that the flow structures are being convected from the inlet region to the diffuser region with less restriction in the case of VFC fan operation. This is in contrast to the resultant zero coherence measured between the other fan inlet region (flow instability area adjacent to the cut-off, R1) and the diffuser inlet (H9) in both VFH and VFC modes.

This flow picture is consistent with the fact that the flow adjacent to the cut-off is decoupled from the flow downstream of the fan throat since a large area of flow recirculation (vortical structure) exists at the flow instability region (see Fig. 8.7). This forces fluid into the scroll area or back towards the fan inlet on the side close to the cut-off, thereby disconnecting it from the flow downstream towards the fan exit. This basically means that the fan inlet region adjacent to the cut-off and the diffuser region are not on the same flow path. It is the bulk flow from the exit of the scroll region and the part of the flow from the exposed area of the fan rotor which mainly contributes to the discharge flow into the diffuser downstream.

Comparing the coherence and power spectral measurements between the two fan inlet positions and the diffuser inlet region, it can be concluded that the flow instability region next to the cut-off at the fan inlet (which is also the flow re-entrant

area) is flow decoupled from the downstream recirculation region inside the diffuser. It was expected that these two regions might be strongly coupled due to a feedback mechanism which would force some flow to re-enter the fan throat and subsequently even though the fan blades towards the fan inlet region.

It has also been observed that replacing the HVAC module with an identical system resistance eliminates the "rumble" noise. This would seem to demonstrate a potential feedback phenomena between the fan/scroll and diffuser/module. The coherence results, however, have demonstrated the opposite trend, suggesting that the flow instability area at the fan inlet is probably a localized phenomena. If this flow model is correct, it would be reasonable to state that flow instability area at the fan inlet and the recirculation-shear layer combination at the diffuser section could be independent sources of noise, quite possibly radiating aeroacoustic noise in common frequency bands. The key question would then be, which of the identified flow structures is the primary contributor to "rumble" noise. These questions cannot simply be answered by fluid dynamic testing alone. Rather a joint flow-acoustics testing is necessary to reasonably identify the source of "rumble" noise.

8.5.6 Diffuser and Upstream of Evaporator (H9-H10, H12-H13 and H2-H15)

Hot-wire surveys were conducted in the HVAC diffuser inlet region, both over the diffuser height (see Figs. 8.28, 8.26, 8.39 and 8.40 at location H9, H10, H12 and H13) and across the diffuser width (see Fig. 8.41 at location H15). This region includes the jet, shear layer and recirculation zones. As shown in Figs. 8.28 and 8.26, in the VFC mode the energy is distributed over a narrower range (especially at the lower frequencies) than in the VFH mode. Also, the VFH spectral energy exhibits a shift to lower frequencies compared to the VFC mode. Since the volumetric flow rate through

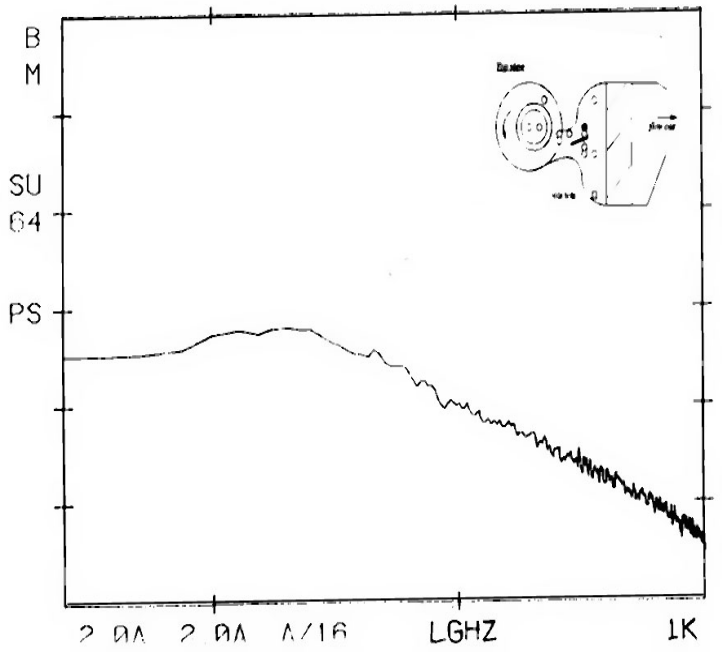

Figure 8.39: Power spectrum at diffuser inlet (H9) vent full hot 14V blower Z2 (in) = 8.0

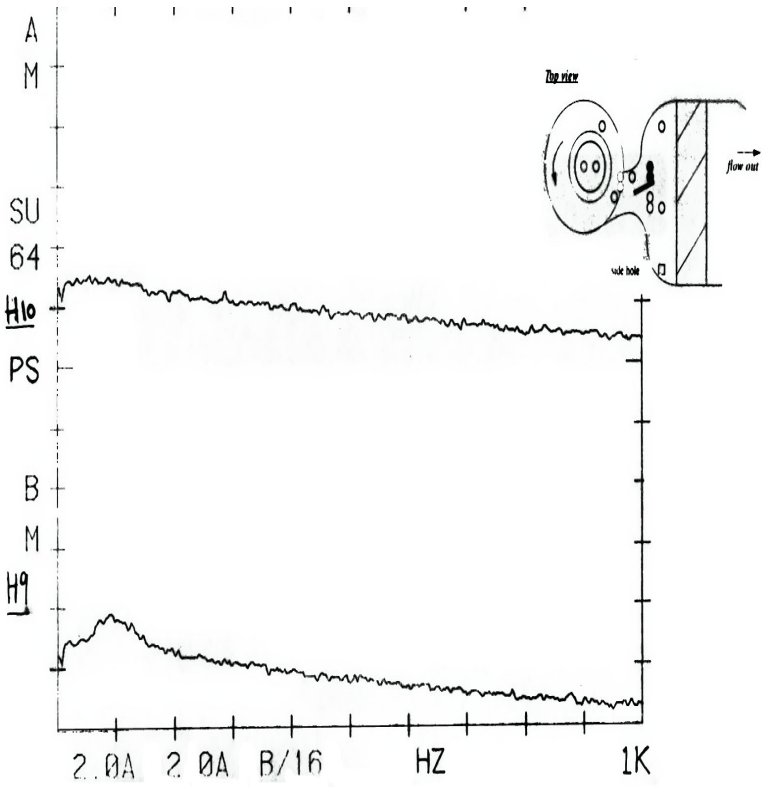

Figure 8.40: Power spectrum at diffuser inlet positions (H9 - H10) vent cold 14V blower Z1 (in) = 2.5 , Z2 (in) = 2.5

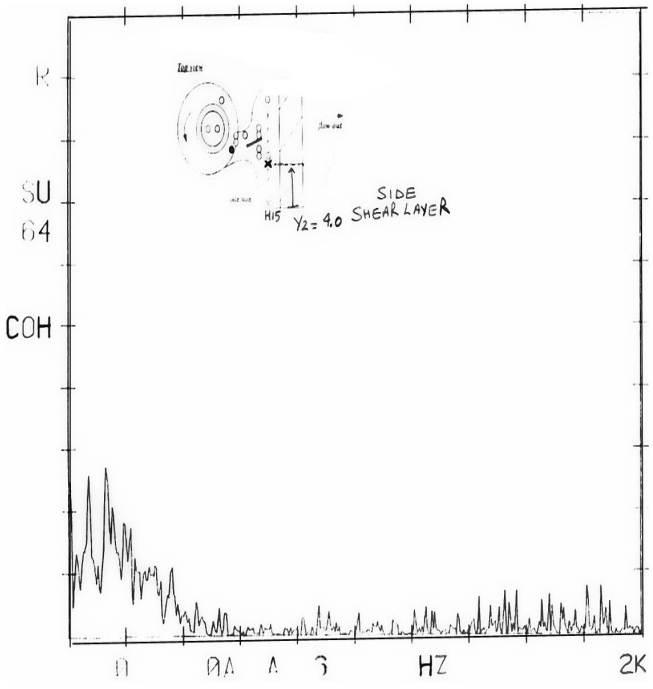

Figure 8.41: Coherence between fan blade exit (H2) and upstream of evaporator core (H15) vent full cold 14V blower Z1 (in) = 1.75 , Y2 (in) = 4.0 , Z2 (in) = 5.5

the fan is higher in VFC than in VFH mode, the shear layers will be more prominent and would be expected to have a narrower spectral width at the same location inside the fan compared to the lower flow rate case in VFH mode. The change in fan operating conditions, especially the alteration of the system resistance, results in a shift in the mean velocities throughout the fan. The VFH mode represents the higher system resistance setting compared to VFC mode even though the fan speed is higher in the VFH mode than that in the VFC mode.

Taylor's frozen field hypothesis (see Townsend [65]) can be applied to a typical convecting flow eddy through the HVAC fan to understand the effect of increasing mean convection velocity on the frequency shift in the spectral plots of Figs. 8.28, 8.26 and 8.39. When this hypothesis is applied to a flow eddy crossing the fan, a relationship can be formed between any time scale (t) of the flow eddy and a length scale (L) by L=Ut, or $f = U/L$, where $f(1/t)$ is the corresponding frequency. Thus, the frequency increase of the spectral peak in the energy plots at jet exit shear layer is due primarily to higher convection velocities (VFC mode). By contrast, in the VFH mode the mean convection velocity is lower due to lower volumetric flow rate, so the energy spectra peak at lower frequencies. The coherence measurements in the jet shear layer shown in Figs. 8.31 and 8.32 demonstrate two essential features of the flow: first, the coherence is high when the hot-wires are placed in the shear layer region on both sides of the fan exit; second, the coherence decreases in magnitude and shifts down in frequency in the VFH mode compared to the VFC. In general the velocity coherence within the shear layers occurs in the 0 to 200 Hz frequency range which includes the rumble noise frequency range.

Figure 8.42 shows the coherence between hot-wire signals from the side shear layer at the exit of the fan throat (region of H12 and H13). The results from the side shear layer (Fig. 8.41) are similar to the results of the top and bottom shear layers which show high coherence in the VFC mode, in comparison to the weaker coherence found

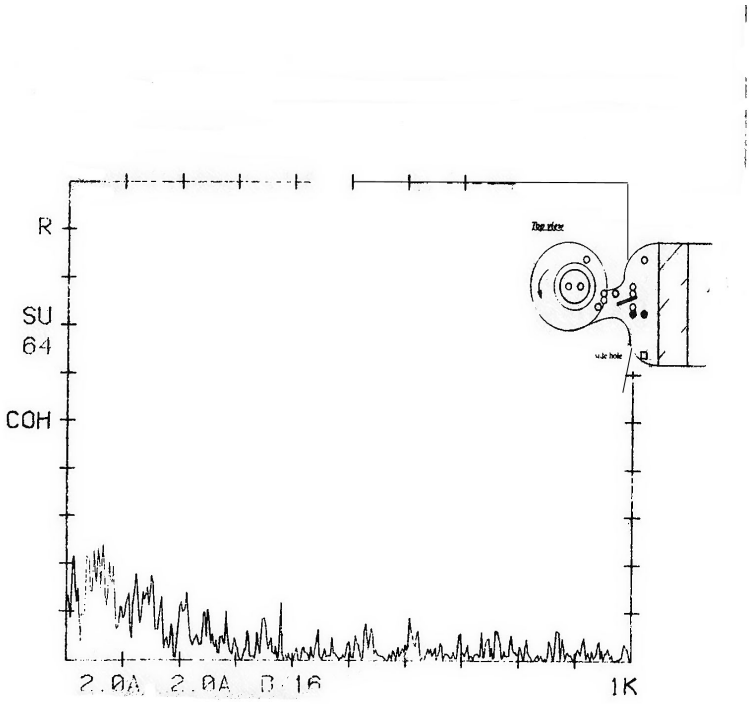

Figure 8.42: Coherence between diffuser inlet (H12) and upstream of evaporator core (H13) vent full cold 14V blower Z1 (in) = 1.75 , Z2 (in) = 1.75

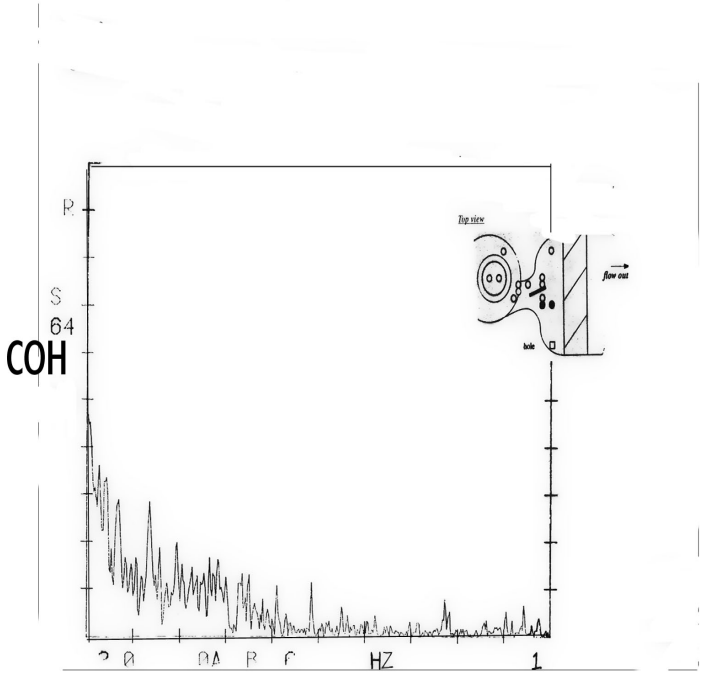

Figure 8.43: Coherence between diffuser inlet (H12) and upstream of evaporator core (H13) vent full hot 14V blower Z1 (in) = 1.75 , Z2 (in) = 1.75

in VFH mode (figure not shown). In addition, the velocity coherence decreases to almost zero when the two hot-wires are closely spaced inside the core flow at the exit of the fan throat. This implies that the flow structures are not large scale coherent eddies, but mostly smaller eddies generated by the fan blade chopping in the fan scroll region upstream. Thus the rotating fan blades are very effective in reducing the size of the largest eddy and generating more broad band turbulence. When the two probes are placed in close proximity to each other inside the jet exit shear layers, however, a high coherence is observed both for VFC (Fig. 8.42) and VFH (Fig. 8.43) modes. Comparing Figs. 8.42 and 8.43, even though the coherence levels are quantitatively different (higher coherence at lower frequencies for VFH mode compared to VFC), they are similar qualitatively; i.e.,, both the VFC and VFH modes exhibit the presence

of shear layers inside the HVAC diffuser at the location tested.

8.6 Summary of Results

The experimental results indicate that the flow pattern changes significantly with the fan operating conditions. The VFC mode results indicate that shear layers present at the exit of the fan throat are more intense and well-defined compared to the shear layers in the VFH mode operation. Experimental evidence at the fan inlet region in the VFH mode indicates a large flow recirculation region is present at the fan inlet adjacent to the cut-off section. By contrast, in the VFC mode there is a significant reduction in this flow recirculation.

Under both the VFC and VFH modes there was no evidence of flow interaction between the fan inlet for R1 positions and the diffuser shear layers (H9 and H12). In addition, although the coherence results from the R2-H9 measurement location between fan inlet position and diffuser inlet showed finite coherence, the results are suspect. Even though power spectral results at the diffuser inlet indicate that the bandwidth over which high energy is concentrated shifts down in frequency in VFH compared to VFC mode, the coherence results between two points inside the jet exit shear layer show widening of the bandwidth in VFH mode compared to the VFC mode. From all the evidence, it can be concluded that no significant flow coupling exists between the flow at the fan inlet section and the flow in the diffuser region. Note that this cannot, rule out an acoustic coupling.

In the diffuser region under the VFH mode of operation, the coherence is over significantly a wider frequency range than in the VFC mode. It is hypothesized for both modes of operation that the flow in the diffuser is similar to a recirculating flow after a sudden expansion (or flow over a backward-facing step), and this dominates the fan throat exit shear layers. The noise shift to lower frequencies and a broader

bandwidth can be attributed to the lower mean velocities in VFH. This flow model for the flow in the diffuser area in the VFH mode would explain both the reduction in the coherence between flow at the fan inlet (and the fan blade exit) and the diffuser shear layer flow. It would also explain the presence of larger scale eddies in the diffuser region, as clearly demonstrated by the power spectral measurements in the diffuser section in VFH.

It can be hypothesized for VFH mode operation (the case of higher system back pressure), that the interaction of the shear layer at the diffuser inlet with larger recirculating flow inside the diffuser cavity can act as a source having both discrete tonal frequencies and broad-band noise. The non-linear interaction of the coherent eddies with each other and the walls of the diffuser could also contribute to the "rumble" noise. The higher flow rate in VFC mode (lower system back pressure) generates distinct peaks in the power spectrum compared to VFH mode. The natural jet shedding frequency was calculated to be 30 Hz for the automotive fan jet configuration. By contrast the VFC energy spectral plots exhibit a broad peak in the 100 Hz band while the VFH energy spectral plots are more widely spread (below 70 Hz). Since the natural shedding frequency of the jet shear layer is lower than the frequency band at which blower "rumble" noise occurs, it is possible that this particular type of flow induced noise generator might not be directly related to the blower rumble.

8.7 Conclusions

The main objective of this study was to identify large flow structures within the HVAC module that are responsible for noise, and in particular "rumble" noise generation. Possible mechanisms for the generation of flow-induced noise in the automotive HVAC fan module were investigated. The experiments used measurements of spectra and the coherence function between two velocity signals at different spatial locations within

the fan scroll and diffuser regions. Both the coherence function and power spectra were measured using two single hot-wire sensor probes. Power spectral measurements provide information about the broad-bandedness or discrete frequency content of these structures. A finding of strong coherence between the two velocity signals indicates the presence of an organized flow structure. Experimental results do not indicate any significant coherence between the fan inlet flow and the shear layers in the diffuser region in either the VENT FULL COLD mode (VFC) and the VENT FULL HOT mode (VFH). These results suggest there is no flow coupling between these locations under these conditions. The magnitude of the velocity coherence between fan inlet and fan blade exit is much higher, however, at the blade passage frequency in the case of both the VFH and VFC modes. The power spectral results in VFC at the diffuser shear layer location showed a much higher frequency content in the lower (rumble frequency) range in comparison to the VFH mode. The coherence between the flow at the fan blade exit and the shear layers in the diffuser region is much higher than the coherence between the fan blade inlet flow and the diffuser flow for both VFC and VFH modes.

It is important to note that the noise can also be linked to incoherent sources caused by the flow that are not due to coherent flow phenomena between the fan inlet and diffuser flow fields. In situations involving turbulence, the identification of noise sources can be more difficult since sources both convect and undergo complex interaction with the flow. In light of these facts and the experimental results, it is important to conduct further studies on the relationship between the pressure at the walls of the diffuser and flow field (velocity) and to obtain information about the coherence between the identified flow structures and the far field noise. Only then can definitive statements be made about the exact causes of "rumble".

Further investigation can also determine which of the identified flow structures are actually the generators of "rumble" noise. The measurement of the coherence between

the (far field) pressure and regions of high turbulent fluctuations inside the module could be very useful in this determination. It is also recommended that a fan/duct modal analysis be performed on the automotive HVAC module in order to determine the acoustic duct cavity resonance frequencies (both for Helmholtz resonance and higher order duct acoustic modes) in the HVAC module, since these could be a major contributor to blower "rumble" noise.

Chapter 9

Conclusions and Recommendations for Future Work

9.1 Conclusions

There are five major areas within the realm of centrifugal fan research presented in this thesis from which important conclusions can be derived. These five areas are: fan installation effects on overall fan performance and evaluation of fan testing methods, analysis of the fan scaling laws and consequences of dynamic similarity on modelling, mean velocity and turbulence intensity measurements (flow field studies) at the inlet and outlet of large scale blower, detailed flow visualization studies (in water) covering the flow path starting at the fan blade exit till the evaporator core of an actual HVAC fan scroll-diffuser module with just an attached evaporator core (include the instantaneous steady/unsteady flow field characteristics) and two point coherence and Spectral measurements conducted on an actual HVAC fan module (flow structure identification for aeroacoustic noise sources).

In light of these five areas of research, HVAC fan modules were analyzed and the

correlation were made between the key HVAC fan aerodynamic performance parameters and the flow field characteristics under the given fan test conditions. In addition the key HVAC fan component characteristics were discussed in terms of flow physics in order to suggest improvements in design for better performance.

It was demonstrated that fan scaling laws, based on principles of complete dynamic similarity, requires that Reynolds number matching is a necessary condition for developing scale model fans or fan test facilities. Physical basis was provided for the fan scaling laws derived from purely dimensional analysis and from the fundamental equations of fluid motion, that is, the Navier-Stokes equations. Note however, the classical fan laws are based on an infinite Reynolds number assumption. Comparison of the two fan scaling (similarity) approaches applied to incompressible rotating flows, indicates that the classical fan laws have two basic independent fan scaling parameters, that is the fan size ratio and the fan speed ratio, whereas the inclusion of Reynolds number into the fan scaling laws shows that there is only one basic independent fan scaling parameter, the fan size ratio or fan speed ratio. It was also demonstrated using GFSL that in order to maintain strict dynamic similarity between the model and the prototype fans, the model fan speed must be reduced by a factor of the square of the inverse of the geometric length scale ratio, even though the flow speed only drops by a factor of the inverse of geometric length scale ratio. Note however, application of CFSL between the model and the prototype fans, requires the fan speed ratio be reduced by only the inverse of the geometric length scale ratio. This is a major difference between CFSL and GFSL. This is also why the implementation of the classical fan laws usually requires corrections for Reynolds number, which is not maintained constant.

Physical analysis based on the Navier-Stokes equations applied to fans under incompressible flow conditions showed both model and prototype will have exactly the same behavior if in addition to Strouhal (or inverse of Volume flow coefficient) and

Euler number similarity, the Reynolds numbers are identical between model and prototype. In addition, the GFSL, based on purely dimensionless analysis produces a similar set of constraints to those derived from physical analysis whose basis are the Navier-Stokes. equations. Therefore it is recommended that the GFSL and not the CFSL approach be used when modelling fans (under incompressible flow conditions).

A three-times scale model of an actual HVAC centrifugal fan (the LSB) was designed and built to maintain dynamic similarity. Differences in aerodynamic performance were observed between the HVAC prototype fan and the LSB. These were mainly attributed to differences in fan inlet and outlet geometries. In order to understand differences between actual HVAC prototype and the LSB, an exact one-third model of the LSB, the Mini-LSB fan was designed and tested like the LSB. The LSB fans performance characteristic test results were observed to be similar to the Mini-LSB fans performance characteristic. In addition, the similarity of the LSB and Mini-LSB fan performance characteristics also served to verify conformance with the generalized fan scaling laws (GFSL), and, in turn the experiments themselves.

In addition to the similarity of overall performance between the LSB and Mini-LSB fans, the mean velocity and turbulence intensity profiles at fan exit also showed good agreement. After analyzing experimental pressure and velocity data obtained at both the near and far field fan region (i.e., at the fan inlet and fan exit), it was concluded that velocity measurements using hot-wires is an appropriate and accurate technique for determining both the velocity profiles and volumetric flowrate, whereas, in the near field region especially at the fan exit, the LDV method is recommended, since zones of flow recirculation are present. In the case of flow field pressure measurements, all pressure probes tested were highly susceptible to flow directionality (skewness and flow reversal) and strong pressure gradients (for example, the case of single large vortex at the fan exit) in the near field region. Thus it is highly recommended that average static pressure be measured using the classical piezometric method. In the

far field, however, Pitot/head tubes or static tubes are appropriate means to measure pressure inside fan exit ducts where the flow has less skewness and more uniform.

A flow visualization experiment was conducted to study the complex 3-dimensional, vortical and unsteady flow patterns inside an actual HVAC fan module operated in water under dynamically similar conditions as those in air. Both conventional and shear thickening dye injection methods were used in the study. The shear thickening dye injection method proved very effective in capturing the unsteady and turbulent flow features across the fan module. Note that, shear thickening dye injection method has been successfully used for flow visualization of mostly external aerodynamic flow, whereas its use on HVAC fans appears to be the first internal aerodynamic application. Flow visualization was able to indicate the large-scale flow patterns through the blower/diffuser and clearly showed areas of flow separation and recirculation within the fan module. In the case of very low fan speeds, flow visualizations studies with HVAC fans indicated that a much a more global unsteady and almost pulsatile flow pattern exists, notice however, that the fan operating point was well below the range for standard fan operation. Flow visualization also showed that the fan cut-off and diffuser region both were critical regions, which can drastically affect the blower's aerodynamic performance. Also, a flow coupling was observed between the fan throat and the diffuser region, especially at low fan speeds and low volumetric flowrates.

Possible mechanisms for the generation of flow induced noise in the automotive HVAC fan module was investigated. The main objective of the study was to identify flow structures within the HVAC module that are responsible for noise and in particular "rumble noise" generation. The experimental technique used for this purpose consisted of measuring both the power spectrum and the coherence functions between two velocity signals at different spatial locations within the fan scroll and diffuser regions

The experimental results indicated that the flow pattern changes significantly with

the fan operating conditions. The VFC (low system resistance and high flow rate) mode results indicate that shear layers are present at the exit of the fan throat which are more intense and well defined compared to the shear layer intensity in VFH (high system resistance, higher fan speed and lower flow rate) mode operation. Also, in the VFC mode, there is a reduction in the flow recirculation at fan inlet opposite to the cut-off section, where as in VFH mode a large flow recirculation region is present.

In general, it was observed that the blade passing components dominate certain narrow frequency bands, whereas the overall power spectrum levels are similar to the typical turbulence spectra with flow energy distributed over a broadband of frequencies. The individual spectra at the jet exit (inside the diffuser) show that the in VFH mode the low frequency end of the power spectrum is heavily loaded compared to VFC mode. In VFC mode, results indicate a spectral hump at around the rumble frequency band (200Hz) but containing less energy in the low frequency end. More energy at the lower frequencies could occur due to the presence of larger scale coherent structures in the flow (e.g. large flow separation and recirculation zones) and due to non-linear interaction between the flow eddies. Also, flow visualization clearly showed the presence of large-scale flow structures inside the fan throat and diffuser inlet regions and the diffuser side-walls for the case of low volumetric flowrates.

It was observed that for fan operation in VFH mode, a high system resistance corresponds to a lower flow rate, while the fan speed increases. In the VFC mode the trend is just the opposite; fan speed decreases as the flow rate increases due to lower system resistance. In light of the results obtained from both the coherence and spectral measurements, higher flow rates (as in the VFC mode) will have a tendency to generate stronger shear layers in the wide angle diffuser, where as large recirculation is evidenced for low flow rate cases, even though the fan speed is higher (as in the VFH mode). In VFH mode the fan adjusts to the higher load by increasing fan speed (increases current draw) at a given motor voltage, thus indicating an increase

in power consumption. While in VFC mode the trend is just the opposite.

A fan producing higher flowrates at lower fan speeds indicates that fan blade loading is low, thus resulting in lower pressure rise across the fan impeller, while most of the energy at the fan exit is in terms of the kinetic energy. This behavior is consistent with the trend indicated by the Euler pump (or fan) equations (see Appendix **??**). Higher fan speeds generate larger centrifugal pressure gradients thus increasing the pressure rise across the fan blade. Notice, however that higher fan speeds do not necessarily imply higher flow discharge from the fan, the through flow characteristics will dictate the flow discharge from the fan. Through flow characteristics are dependant on the volume flow coefficient (or the velocity ratio ($U/\Omega D$). The flow coefficient is a function of fan blade geometry in addition to the fan scroll parameters. A change in the flow rates (and a corresponding change of the flow pattern) across the fan will change the Reynolds number of the flow and velocity profile at the inlet of the diffuser. It is well known from various diffuser studies (Kline, Dean et al), that the most important parameter affecting diffuser performance (or effectiveness) is the inlet blockage parameter for a given geometry. In terms of the observed flow patterns from flow visualization studies and spectral measurements conducted inside the HVAC diffuser, flow recirculation at the inlet of the diffuser in case of high system resistance setting tends to decrease the performance of the overall fan system. The addition of a well-designed and efficient diffuser (in case of sufficient packaging space) placed after the fan scroll augments the static pressure rise across the fan without significantly increasing fan motor power consumption, thus leading to a more aerodynamically efficient HVAC module. In addition, based on the spectral and coherence measurements inside the HVAC module, it can be inferred that a more efficient fan/diffuser combination reduces the possibility of rumble noise which is partially linked with the flow coupling between the fan scroll and the diffuser. Recognize that a combined pressure and aeroacoustic study is necessary to properly evaluate and identify the

actual sources of aeroacoustic noise ("rumble" in particular).

A three times scale model (large-scale blower) fan was designed and tested using the modified AMCA Standard (straight outlet duct setup) fan testing method. A different location (and measurement technique) was used to measure fan exit static pressure in comparison to the location recommended by the fan test code. The alternate location was situated at the fan exit scroll duct. The technique used, was the classical piezometric static pressure wall taps located at downstream of the fan cut-off. The static measurements obtained from this new location on an actual HVAC fan was verified with an AMCA/ASHRAE Standard plenum chamber fan test facility. One of the important conclusions that can be drawn from the fact there is consistency in fan static pressure measurements between the STD and PLC methods indicates that the location for piezometric static pressure measurement at the fan outlet duct (in the STD approach) is an appropriate location for purposes of fan performance measurement. This static pressure measurement approach presents an alternative to the one recommended by the AMCA/ASHRAE fan test codes.

In addition it was verified that the AMCA designed Plenum chamber static pressure is an accurate measure of the static pressure of a flow that is uniform and swirl-free (for both laminar and turbulent flow cases). However in case of HVAC fan without any passive resistance, static pressure obtained by the plenum chamber did not agree with the fan exit static pressure. Some reasons are suggested for this discrepancy, yet further testing is required to confirm the result and suggest possible flow mechanisms. The testing of fans with extra ducting using the plenum chamber fan test method demonstrates that, even in that case the plenum chamber accurately predicts duct exit static pressure just upstream of the plenum.

9.2 Some Recommendations for Future Work

Due to the existence of a strong secondary flow pattern at the fan exit, the hot-wire velocity signal output is biased since both the u and v components are contributing to the normal component of the velocity as measured by the single wire probe. Therefore, flow field measurements should be conducted using multiple hot-wire sensors in order to determine the three components of the fluid velocity at a given point in space. It should be possible to resolve the flow field far downstream of the fan throat since the turbulent intensities are relatively low, on the order of 10 percent, and without flow recirculation. Consequently the application of multiple hot wires seems feasible in the regions of the flow with low turbulent intensities and no flow reversal. In regions of flow reversal and very high turbulent intensities however, flow measurements using the LDA technique are more appropriate since they can resolve the reverse flow regions and can handle very high turbulent intensities. The main issue in using the LDA technique is to insure that the seed particles follow the flow, and this will be one the main source of inaccuracy in estimating the mean velocity vector in the flow field. This problem can be greatly alleviated by using scaled models, because of the greatly reduced velocities in the model fan as compared to prototype fan.

Smoke or dye visualization is recommended for a more detailed picture of the critical flow areas within the fan scroll and around the fan impeller. In order to understand the generation and evolution of the flow pattern at the fan exit, the flow field closer to the fan impeller should be further investigated. The critical areas are as follows: near the fan blade leading edge, at the fan blade trailing edge around the fan throat region (also the region for maximum flow capacity), in the space between the fan impeller and volute scroll, and at the fan throat itself. An example of such an investigation using dye injection in a prototype fan in water was presented in Chapter 4.

Presented below are additional recommendations (for future work) concerning aeroacoustic issues within HVAC fan modules:

- Explore the correlation between far field noise and flow velocity using a microphone and hot-wire.
- Study the interaction of the flow induced noise and the duct acoustics to obtain information about whether certain flow structures are exciting certain higher order duct modes and resonant frequencies.
- Map the inlet flow along the blade span and circumferential direction along with the flow incidence angle variation along the blade span. This information could be crucial to understanding the flow instability and flow interaction across the rotor, which changes drastically with fan operating modes, as well as the resulting drastic changes in HVAC fan noise characteristics.
- Test the HVAC module for acoustic resonances and any mechanical resonance phenomena in order to improve the assessment of the low frequency fan noise characteristics (i.e., "rumble"), preferably *before* mass production.

References

[1] S. Akaike and K. Kikuyama. Noise reduction of pressure type fans for automobile air conditioners. *Journal of Vibration and Acoustics*, 115:216–220, April 1993.

[2] S. Akaike, M. Kitada, T. Matsushima, and K. Kikuyama. Study of noise reduction of automotive cooling fans. In *Symposium on Flow Induced Vibration and Noise*, volume 4 of *PVP 243*, pages 15–25. ASME, 1992.

[3] PTC-11 AMCA Bulletin 210-85. Laboratory methods of tesing fans for rating. Technical report, ANSI/AMCA/ASHRAE Standard.

[4] O. E. Balje. A study on design critera and matching of turbomachines. *Journal of Eng. for Power*, 84:83, 1962.

[5] G. K. Batchelor. *Theory of Homogeneous Turbulence.* Cambridge University Press, 1953.

[6] G. K. Batchelor. *An Introduction to Fluid Dynamics.* Cambridge University Press, London, 1967.

[7] J. S. Bendat and A. G. Piersol. *Random Data: Analysis and Measurement Procedures.* John Wiley and Sons Inc, 1971.

[8] P. D. Beuther, A. Shabbir, and W. K. George. X-wire response in turbulent

flows of high intensity turbulence and low mean velocities. In *Proc. of Symp. on Thermal Anemometry*, Cinn., OH, 1987. ASME.

[9] W. K. Blake. *Mechanics of Flow-Induced Sound and Vibration.* Academic Press, 1986.

[10] A. N. Bolton. Installation effects in fan systems. *Proceedings of the Institution of Mechanical Engineers*, 204:201–215, 1990.

[11] P. W. Bridgeman. *Dimensional Analysis.* Yale University Press, New Haven Connecticut, 1922.

[12] M. V. Casey. The effects of reynolds number on the efficiency of centrifugal compressor stage. 84-GT-247, 1984.

[13] M. V. Casey. The effects of reynolds number on the efficiency of centrifugal compressor stage. *Journal of Eng. for Gas Turbines and Power*, 107:541–548, 1985.

[14] O. Cordier. Similarity considerations in turbomachines. Technical report, VKI.

[15] W. T. W. Cory. The effects of inlet conditions on the performance of a high specific speed centrifugal fan. In *The effects of inlet conditions on the performance of a high specific speed centrifugal fan*, number 84 in C115, London, 1984. IMechE, Mechanical Engineering Publications.

[16] G. T. Csanady. *Theory of Turbomachines.* McGraw-Hill., 1964.

[17] G. R. Denger and M. W. McBride. Three-dimensional flow field characteristics measured in a forward-curved centrifugal blower using particle tracing velocimetry (PTV). In *Proceedings of the Fluid Measurement and Instrumentation Forum*, volume 95, pages 49–56. ASME, 1990.

[18] S. L Dixon. *Fluid Mechanics and Thermodynamics of Turbomachinery.* Pergamon Press, London, second edition, 1978.

[19] A. P. Dowling and J. E. Ffowcs Williams. *Sound and Sources of Sound.* Ellis Horwood, 1982.

[20] B. Eck. *Ventilatoren.* Springer-Verlag, Berlin, 4. auflage edition, 1962. First English Edition, Pergamon Press Ltd., 1973.

[21] H. S. Fowler. An investigation of the flow processes in a centrifugal compressor impeller. Mechanical Engineering Report ME-220, National Research Council of Canada, 1966.

[22] H. S. Fowler. Some experiments on the flow processes in simple rotating channels. Mechanical Engineering Report ME-229, National Research Council of Canada, 1969.

[23] H. S. Fowler. Aerodynamic tests on a centrifugal fan impeller model with swept-back blades. Mechanical Engineering Report ME-238, National Research Council of Canada, 1971.

[24] H. S. Fowler. Comparison of thin plate and thick aerofoil blades in a centrifugal fan. Mechanical Engineering Report ME-240, National Research Council of Canada, 1972.

[25] E. B. Gardow. *On the Relationship Between Impeller Exit Velocity Distribution and Blade Channel Flow in a Centrifugal Fan.* PhD thesis, State University of New York at Buffalo, Feb 1968.

[26] W. K. George. Processing of random signals. In *Proceedimgs of the Dynamic Flow Conference*, 1978.

[27] W. K. George. Private communication. 1997.

[28] W. K. George, B. D. Buether, and R. E. A. Arndt. Pressure spectra in turbulence free shear flows. *Journal of Fluid Mechanics*.

[29] W. K. George, B. D. Buether, and A. Shabbir. Polynomial calibrations for hot-wires in thermally-varying flowsits control. In *ASME Symposium on Thermal Anemometry*, Cincinati, Ohio, 1987.

[30] M. N. Glauser. *Coherent Structures in the Axisymmetric Turbulent Jet Mixing Layer*. PhD thesis, State University of New York at Buffalo, Sept 1987.

[31] R. J. Goldstein. *Fluid Mechanics Measurements*. Hemisphere Publishing Corp., 1983.

[32] A. Goulas and B. Mealing. Flow at the tip of a forward curved centrifugal fan. *ASME Paper No. 84-GT-222.*, 1984.

[33] J. H. G. Howard and E. Lenneman. Measured and predicted secondary flows in a centrifugal impeller. *Journal of Engineering for Power*, 93(1):126–132, January 1971.

[34] G. M. Jenkins and D. G. Watts. *Spectral Ananlysis and its applications*. Holden-Day, 1968.

[35] R. Jorgensen. *Fan Engineering*. Buffalo Forge Company, Buffalo, New York, 8 edition, 1983.

[36] R. J. Kind and M. G. Tobin. Flow in a centrifugal fan of the squirrel-cage type. *ASME Journal of Turbomachinery*, 112:84–90., January 1990.

[37] S. J. Kline. On nature of stall. *Journal of Basic Engineering*, pages 305–320, Sept. 1959.

[38] S. J. Kline. *Similitude And Approximation Theory.* McGraw-Hill, 1965.

[39] Krishnappa. Centrifugal blower noise studies literature survey and noise measurements. Mechanical Engineering Report ME-244, NRC of Canada, December 1976.

[40] E. Lenneman and J. H. G. Howard. Unsteady flow phenomena in rotating centrifugal impeller passages. *Journal of Engineering for Power*, 92(1):65–72, January 1970.

[41] S. Madhavan and T. Wright. Rotating stall caused by pressure surface flow separation on centrifugal fan blades. *Journal of Engineering for Gas Turbines and Power*, 107(84-GT-35):775–781, July 1985.

[42] G. B. McDonnald, E. Lenneman, and J. H. G. Howard. Measured predicted flow near the exit of a radial-flow impeller. *Journal of Engineering for Power*, 93(11):441–446, October 1971.

[43] L. F. Moody and Zowaski. *Hydraulic Machinery Section 26 of Handbook of Applied Hydraulics.* McGraw-Hill, ed. c. v. davis and k. e. sovarn edition, 1969.

[44] J. B. Moreland. Housing effects on centrifugal blower noise. *Journal of Sound and Vibration*, 36(2):191–205, 1974.

[45] Air Movement and Control Associated Standard 210-74. Laboratory methods of tesing fans for rating. Technical report, AMCA Standard 210-74/ASHRAE Standard 51-75.

[46] Munson. *Fluid Mechanics.* McGraw-Hill, 1998.

[47] W. Niese. Noise reduction in centrifugal fans : A literature survey. *Journal of Sound and Vibration*, 45(3):375–403, 1976.

[48] W. Niese. Review of noise reduction methods for centrifugal fans. *Journal of Engineering for Industry*, 104:151–161, May 1982.

[49] M. P. Norton. *Fundamentals of Noise and Vibration Analysis for Engineers.* Cambridge University Press, 1989.

[50] Y. Ohta, E. Outa, and K. Tajima. Characteristics of the blade-passing frequency noise of a centrifugal fan, and a method for noise reduction. *JSME International Journal*, 32, 1989.

[51] K. Okada. Excellent low frequency noise due to the rotating stall of centrifugal fan. In *Proceedings of Inter-Noise*, pages 793–796, Avignon, France, 1988.

[52] W. C. Osborne. *Fans.* Pergamon Press Ltd., Oxford, second edition, 1977.

[53] A. Papoulis. *Probability, Random Variables and Stochastic Processes.* McGraw-Hill Inc., 3rd edition, 1991.

[54] J. J. Phelan, S. H. Russel, and W. C. Zelluf. A study of the influence of reynolds number on the performance of centrifugal fans. *Journal of Engineering for Power*, 101:670–676, October 1979.

[55] D. Raj and W. B. Swim. Measurements of the mean flow velocity and velocity fluctuations at the exit of an FC centrifugal fan rotor. *Journal of Engineering for Power*, 103:393–399., April 1981.

[56] J. M. Randall, D. Berckmans, and R. P. White. A methodology to compare the performance of low pressure fan test rigs using n0n-dimensional fan characteristics. *Journal of Agricultural Engineering Research*, 65:235–246, June 1996.

[57] J. A. Schetz and A. E. Fuhs. *Handbook of Fluid Dynamics and Fluid Machinery.* John Wiley and Sons Inc, 1996.

[58] D. G. Shepherd. *Principles of Turbomachinary.* Macmillan, 1956.

[59] Ian C. Shepherd, R. Frank La Fontaine, Laurie W. Welch, and Ron J. Downie. Velocity measurement in fan rotors using particle image velocimetry. *Proceedings of the Advances and Applications of Laser Anemometry*, 191:179–183., 1994.

[60] R. A. Strub, L. Bonciani, C. J. Borer, M. V. Casey, S. L. Cole, B. B. Cook, J. Kotzur, H. Simon, and M. A. Strite. Influence of the reynolds number on the performance of centrifugal compressors. *Journal of Turbomachinary*, 109:541–544, 1987.

[61] S. Suzuki and Y. Ugai. Rotating stall noise generated by centrifugal fan and its control. In *Proceedings of Inter-Noise*, pages 797–800, Avignon, France, 1988.

[62] S. Suzuki, Y. Ugai, and H. Harada. Noise characteristics in partial discharge of centrifugal fans. *Bulletin of the JSME*, 21(154):689–96, April 1978.

[63] D. Taulbee, J. Sonnenmier, and K. Jensen. The design and fabrication of the asme/ashrae standard plenum chamber fan test facility. Technical report, Harrison-Delphi Thermal Systems.

[64] H. Tennekes and J. L. Lumley. *A First Course in Turbulence.* M.I.T Press, 1972.

[65] A. A. Townsend. *The Structure of Turbulent Shear Flow.* Cambridge University Press, Cambridge, UK, second edition, 1976.

[66] W. Traupel. *Die Theorie der Stroemung durch Radialmaschinen.* Braun, Karlsruhe, 1962.

[67] H. Tsurusaki, K. Imaichi, and R. Miyake. A study on the rotating stall in vaneless diffusers of centrifugal fans (1st report, rotational speeds of stall cells, critical inlet flow angle). *JSME International Journal*, 30(260):279–287, 1987.

[68] F. R. Weisner. A review of slip factors for centrifugal impellers. *Journal of Fluids Engineering*, 66-WA/FE-18.

[69] F. M. White. *Fluid Mechanics.* McGraw-Hill, New York, 1994.

[70] G. F. Wislicenus. *Fluid Mechanics of Turbomachinery.* Dover, 2 edn., 1965.

[71] T. Wright. Centrifugal fan performance with inlet clearance. *Journal of Engineering for Gas Turbines and Power*, 106(84-GT-186):906–912, October 1984.

[72] T. Wright. Comments on compressor effeciency scaling with reynolds number and relative roughness. *Journal of Engineering for Gas Turbines and Power*, (89-GT-31), 1989.

[73] T. Wright, S. Madhavan, and J. DiRe. Centrifugal fan performance with distorted inflows. *Journal of Engineering for Gas Turbines and Power*, 106(83-JPGC-GT-5):895–900, October 1984.

[74] T. Wright, K. T. S. Tzou, and S. Madhavan. Flow in a centrifugal fan impeller at off-design conditions. *Journal of Engineering for Gas Turbines and Power*, 106(84-GT-182):913–919, 1984.

Appendix A

THE AERODYNAMICS OF CENTRIFUGAL FANS AND BLOWERS A Literature Survey

A.1 Introduction to the problem and purpose of review

Centrifugal fans are rotodynamic machines used for moving air continuously against moderate [1]t one time, a compression ratio of 1.1 was the demarcation line between fans and compressors, but recently a compression ratio of 1.3 was being considered as the upper limit, however AMCA has removed even this limit. Fans or blowers, can produce pressures ranging from a few millimeters of water up to pressures equivalent to 3/10 of an atmosphere (up to 45 inches of water) according to present Industrial fan classification standards (see Jorgensen [8]). pressures through ventilation and air conditioning systems. The applied research and development efforts on centrifugal

[1] A

fans over the past fifty years have lead to higher fan efficiencies with improved noise characteristics. The development, however, has largely been of a trial and error nature, with the primary objective being an improvement in overall performance for fans working under specific environments. The high manufacturing costs, which arise due to complex, design with high tolerances often results in major design compromises in commercial fan design. Thus, the product development programs are of a limited nature. Therefore, the design of a centrifugal fan for a specific application stems from the experience of the designer based on established results from previous tests (mostly concerning the overall performance of the fan), rather than from a thorough understanding of the internal fluid mechanics.

The literature survey on centrifugal blowers (fans) covers both the aerodynamics and flow field studies, and the relevant acoustical measurements connected to the flow field through the blower. In contrast to the numerous reviews concerning noise production of blowers for example, (Niese [1,2] and Krishnappa [3]), one of the striking outcomes of the survey was that there is not a single review paper on the aerodynamics of centrifugal blowers. The work concerning the flow field through blowers up to 1967 is listed in Gardow's thesis [4], which clearly shows the lack of detailed experimental studies as well as theoretical analysis. Much of the earlier research originated from Germany, referenced mainly in the standard text books by Eck [5] and Traupel [6], both in German and the book by Osborne [7] in English. In the last thirty years there has been considerable progress in centrifugal fan development both from fundamental research (mostly gained from other types of turbomachinery and cascade experiments), and from Industrial interest mainly aiming for noise reduction. Papers on noise reduction evidenced little interest in understanding centrifugal fan aerodynamics for purposes of improving fan efficiency as compared to industrial publications on both centrifugal pumps and compressors, and axial fans and compressors. The book on fan engineering by Jorgenson [8] (published by the Buffalo Forge

Company), and the works of T.Wright et al [9,10,11,12,] of Westinghouse (describing the experimental investigation on the flow field through blowers) clearly show the Industrial interest in improving the aerodynamic and noise characteristics of centrifugal blowers. There is significant interest in this area by the Japanese automotive industry [13, 14, 18], along with the specific areas of sound and vibration [15, 16, 17, 19]. The British publications in this area are mostly associated with industrial applications [20] in building ventilation systems and concentrate on the areas of noise and power consumption. However there has been some progress in the area of centrifugal fan aerodynamics by a few British researchers [21]. Early Canadian research in this field was of a pioneering nature, which came about due to studies on low speed centrifugal compressors in the late sixties and early seventies initiated by Fowler [22,23,24,25] and Howard et al [26, 27, 28]. Fowler used hot wire anemometry to conduct detailed flow field studies on centrifugal fans including the blade passage area. It appears that most of the experimental research conducted on centrifugal blowers in the last twenty years was due to impetus from industry and very little basic research has been pursued. With the advent of LDA instrumentation, PIV analysis and powerful CFD packages with high-speed computers, research is being directed towards understanding the complex flow patterns and the interaction of the aerodynamics with the acoustical field, that is, flow induced noise. Examples are the recent PTV study done by Denger and McBride [29], the PIV study done by Shepard et al. [30], and LDA studies of Goulas and Mealing [31]. It should be mentioned that the LDA studies are now successfully being applied to rotating turbomachinery both in axial flow and centrifugal turbomachines.

- Centrifugal fan aerodynamics The centrifugal blower is a turbomachine which produces a moderate static pressure rise, operating against a given system resistance. If there are no upstream obstacles or guide vanes of any sort (which are usually present in centrifugal compressors and pumps) the flow enters the inlet

section in almost an axial direction (parallel to axis of shaft rotation), flowing smoothly and without whirl. The flow then turns due to the curvature of the inlet lip towards the radial direction entering the impeller. The rotating impeller consists of multiple blades either of circular arc shape (chosen due to ease of manufacturing and cost effectiveness) or of highly cambered airfoil profile section. The primary function of the rotating blades is to transfer mechanical energy to the fluid flowing through the turbomachine and the secondary function is to provide flow guidance through the impeller. The blades transfer the energy to the fluid by deflecting the flow thereby increasing the pressure across the impeller, analogous to the generation of aerodynamic lift. From flow momentum considerations, the impeller increases the energy level of the fluid by whirling it outwards, thereby increasing the angular momentum of the fluid (Dixon [32]). Once the flow has exited the impeller both the static pressure and the kinetic energy have increased compared to that at the inlet. The blower housing design subsequently dictates how the flow will be collected and discharged from the blower. The scroll casing, usually designed as a log spiral volute, both collects the flow for discharge and converts part of the kinetic energy into a useful static pressure rise across the blower. This pressure rise is achieved primarily by the divergence of the collector scroll, causing flow diffusion and an exchange of kinetic energy for static pressure head. The blower casing geometry can have a considerable affect on blower performance, especially the static pressure rise characteristics.

The flow through a centrifugal blower can be considered to be incompressible but inherently unsteady. Similar to other turbomachines, the blower suffers from losses of efficiency and performance due to different fluid dynamic mechanisms. The main loss occurs due to flow separation caused by boundary layer separation off the blade surface or at the blower casing wall at the inlet and at

the cut-off region, resulting in high levels of turbulent dissipation. Other causes of recirculating flow can be attributed to sudden changes in geometry and excessive flow blockage in restricted regions within the blower. Additional loss mechanisms include fluid friction due to viscous effects, flow leakage through clearances between shroud and inlet section and losses at the inlet shroud (at entrance to the impeller) due to the improper matching of the flow angles to the inlet blade setting angles causing leading edge flow separation. The losses mentioned above are internal to this particular turbomachine, other external factors that effect the flow field pattern and blower performance to a varying degree are free stream turbulence, ingestion of large eddies (coherent vortical flow structures), downstream obstacles causing excessive back pressure and exit diffuser geometry. These external factors can be categorized under blower installation effects, see Bolton [20]. It is important to recognize the effects of the mutual interaction of the different upstream and downstream components of any aerodynamic system, especially in an incompressible flow where downstream flow disturbances can instantaneously affect the upstream flow conditions.

- Detailed review of the aerodynamic tests performed on Centrifugal Blowers: Flow through a Squirrel-cage (forward curved) type of Centrifugal Blower

The majority of the published research related to centrifugal fans has been done on backward curved centrifugal fans (BCC fans), refs. [4,9,10,11,12,13,16,17,24,25,43], where as forward curved centrifugal fans (FCC) fans refs. [31,36], and squirrel-cage type centrifugal fans (SCFC) fans refs. [29,33,34,35,44,63] have received much less attention. The flow through SCFC fans is quite different to the flow through BCC fans and other types of FCC fans. It should be mentioned that SCFC fans are one particular type of FCC fans. In terms of fan performance, the FCC fans produce higher pressure rise then BCC fans for the same rotor diameter and speed as well as

higher volume flow. Thus FCC fans are generally used in air delivery systems requiring compactness. However this is achieved at the expense of reduced efficiency for the FCC fans, typically in the range of 55 to 75 percent while efficiencies of the order of 90 percent have been achieved for BCC fans with airfoil section blades (Osborne [7]). The major differences in the flow characteristics of FCC, SCFC and BCC arise due to the differences in blade geometry, blade setting angles and rotor exit to inlet area ratio as suggested by Kind and Tobin [33]. Their study on SCFC fans clearly shows two major loss regions, one being flow separation at the upper inlet shroud region and the other being a large recirculation zone near the cut-off causing reverse flow back into the rotor inlet. Similar results for SCFC fans showing major inlet shroud separation were obtained by Denger and McBride [29] using the PIV approach, Raj and Swim [34] using hotwires, as well as Gessners [35] study of the inlet of a SCFC fan with a single hot wire. The experimental study of Cau et al. [36] used crossed hotwires and the work of Goulas and Mealing [31] used a LDA, on forward curved centrifugal fans but not without the typical squirrel-cage rotor geometry. The blade span to chord ratio was much lower than typical squirrel-cage blading, thus giving a flatter and lower width fan rotor unlike squirrel cage rotors. The flow patterns for this different geometry showed major hub flow separation at the rotor exit, instead of the expected flow separation in the shroud region observed in a typical squirrel-cage type centrifugal fans used by other workers. A literature survey of the experimental flow field studies on centrifugal blowers highlights several regions within the blower where the flow is separated from the fan blade or wall boundaries. In the following paragraphs, these regions will be identified and reviewed. The resulting effects on blower performance and efficiency will be described for the various sections of the blower geometry.

A.1.1 Blower inlet section

The main purpose of the inlet section is to provide a smooth and uniform velocity profile at the inlet to the impeller blades, thereby minimizing losses. In addition to flow guidance to the impeller blades, one of the aims of good inlet design is to establish a uniform radial velocity distribution before the flow enters the blade passages in order to achieve uniform blade loading across the span of the blades and around the whole circumference at the impeller inlet. This entails a large radius of curvature at the inlet lip. A small radius of curvature of the lip, which is the case for most industrial fans and blowers, causes high diffusion of the flow due to an adverse pressure gradient, producing flow separation on the inlet cone itself. This subsequently causes a highly distorted and nonuniform inlet flow pattern at the impeller inlet. Considering the blade aerodynamics aspect, a uniform entry to the blades is paramount for maximizing the work capacity of blades, resulting from optimum blade lift coefficients, due to a proper matching of the flow and blade angles at inlet.

The flow visualization studies of Fowler [24,25], Raj and Swim [34], Kind and Tobin [33], and Denger and McBride [31], and the hot wire velocity measurements of Gessner [35] on the inlet of the centrifugal fan, clearly show the flow separation occurring at the inlet shroud region of the impeller blades. This flow separation region almost covers the upper third of the blower width and this effect is more prominent and severe in squirrel-cage rotors used in forward curved centrifugal blowers due to large blower exit to inlet area ratios. This is attributed to the sharp axial to radial bend the flow has to take in order to enter the impeller at the correct angles. Gessners measurements revealed highly nonuniform radial velocity distributions at the inlet to the impeller, with the maximum throughflow nearer the hub region. The area near the shroud had a high axial component of velocity and minimal throughflow. Similar flow behavior was demonstrated by Kind and Tobins 5-hole pressure probe measurements at the inlet of a squirrel-cage fan, typically used in compact HVAC systems. This

nonuniformity of the inlet velocity profile and the mismatch between the angle of incidence of the flow and the blade leading edge angle cause severe flow separation of the leading edge of the blades.

Distorted inflows can be produced not only by poor inlet design but also due to fan installation characteristics and complicated ductwork preceding the fan inlet. Performance degradation of a centrifugal fan with backward swept airfoil blades, subjected to distorted (nonuniform) inlet flows, was measured by Wright, Madhavan and DiRe [10]. Their test results show that loss of efficiency and pressure rise are as much as 10 to 15 percent with highly nonuniform inflow patterns. Gessner [35] also successfully used a boundary layer suction technique on the inlet to squirrel-cage type centrifugal fan. His results show by using an edge suction technique to remove part of the flow at inlet before the flow enters the blades, that a 5 percent improvement in overall fan efficiency is possible. His test results also showed that the inlet velocity profile becomes more uniform and a higher degree of flow turning was achieved within the inlet passage when edge suction was employed. This produced a more symmetric radial velocity distribution along the width of the impeller, causing lower angle of flow incidence at the leading edge of the blades, resulting in much lower flow separation, thereby increasing the static pressure rise through the blower. This also led to reduction in brake horsepower input leading to an increase of overall blower efficiency. If the flow patterns established in the inlet region of typical industrial centrifugal blowers are compared to the flow pattern exhibited in the rotating channel experiment of Fowler [37], it is observed that the velocity profiles in the hub to shroud plane for the rotating channel is nearly uniform compared with the distorted inflow in the blower. This can be attributed to a larger radius of curvature of the inlet duct of the rotating channel compared to the sharp axial to radial bend of blower inlets. Fowler experimentally studied the distribution and the stability of the flow in rotating 2 dimensional channels having convergent, parallel and diffuser

geometries under both single and multiple channel configurations. Fowler's results show that the change of flow rate (Reynolds number) has a significant effect on the degree of nonuniformity of the flow distribution in the channels but the change of rotation number appears to have a more noticeable effect on both the stability and distribution of the flow and that the downstream flow field and the influence of adjacent channels has a large effect on the flow within the rotating channel, especially concerning flow separation from the suction side of the channel wall. The flow through curved rotating channels is even more complicated since the curvature of the walls introduces an additional body force, namely a centrifugal force perpendicular to the mean flow direction, that would effect the growth of the bounded shear layers within the channel (resulting from high wall curvature implying that the magnitude of the centrifugal effect was on the order of magnitude of the Coriolis and inertia forces) similar to flow through highly cambered blades of a centrifugal fan rotating at a high speed. The effects of rotation and blade curvature on the flow both affect the level of turbulence, boundary layer growth and flow separation off the blades. Among the mechanisms affecting turbulence, rotation and flow curvature are the most important factors modifying flows in turbomachinery. Direct numerical simulation results (see Chen and Guo [38]) indicated that the predominant affect of rotation is to decrease the rate of dissipation of turbulence and increase length scales, especially along the axis of rotation (in fan blade geometry that would imply the axial direction between the blade passage). It is well known from rotating channel experiments and direct computer simulation, that on the suction side of the rotating channel strong depression of the turbulence level and suppression and stabilization of the turbulent boundary layer occurs while on the pressure side destabilization of the turbulent boundary layer occurs due to strong rotation effects. For example if a centrifugal impeller blade boundary layer is turbulent, the principle effects of stabilization on the suction surface are reduced Reynolds stress (due to turbulent transport), wall shear

stress (producing drag on the blades), eddy viscosity and mixing losses (see Johnston [39]). Johnston also suggests that these effects are important to centrifugal impeller design since they may limit the pressure recovery (diffusion) that can be applied to the suction surface boundary layers without causing flow separation. Although Johnston's rotating channel experiments were conducted at Reynolds much lower (by a factor of 10) compared to the typical Reynolds number in centrifugal compressor flows, the basic interaction of the an important fluid mechanism of the Coriolis force with the boundary layer growth and its resulting effects on the level of turbulence provide very useful insight into the more complicated environment of flow through a centrifugal fan impeller. The effects of rotation on flow separation from curved surfaces are still not fully understood. The flow through rotating curved blades is very complex since various flow mechanisms are at work. In addition to the Coriolis and rotation effects as mentioned above there is also the effect due to pressure gradients (favorable pressure gradients occur in converging passages and adverse pressure gradients occur in diverging passages) effecting the pressure recovery and flow separation through the blade passage. Blade curvature introduces an additional component of centrifugal force perpendicular to the blade surface affecting the lift characteristics of the blades and dictating the pressure gradients within the blade passage to a large extent.

One can conclude, by reviewing the results of various experiments in the literature, that the standard inlet design of centrifugal blowers is poor because it not only produces a non-uniform radial velocity distribution at the inlet to the impeller but also creates a skewed and a 3-dimensional velocity pattern. This is in clear conflict with the manufacturing based decision to produce blade geometries based on a purely radial (2-dimensional) throughflow impeller design. Any modification done on the inlet must allow for a proper matching of the flow angle and the inlet blade setting angles. On the other hand, skewed blading could be employed when it is difficult

to make changes in inlet configurations. A good inlet design can substantially improve the flow characteristics through the centrifugal blower resulting in significant improvements in the aerodynamic efficiency as well as blower performance.

A.1.2 Blade design and stall characteristics

The performance of most aerodynamic systems utilizing rotating blades for energy transfer through aerodynamic lift generation are highly dependant on blade profile and blade setting angles for given flow environments. The function of blades whether of airfoil design or simple circular arc profile, is to do work on the fluid entering the impeller. The amount of work done on the fluid, evident from the pressure development across the blower, depends primarily on the angle of the blower blades with respect to the direction of rotation at the periphery of the impeller (see either Osborne [7] or Eck [5]). In addition to blade setting angles, flow development through compressor and turbine cascade tests (Goestellow [40]), demonstrate clearly the effect of blade camber, leading edge radius, profile thickness, and location of the maximum thickness to chord ratio from the leading edge, among other parameters, on flow quality and work capacity of the blade rows.

In order to appreciate the effects of the above blade parameters, it is essential to attain a deeper understanding of how the rotating blade affects the fluid passing over it, consequently performing work. The only movement of the impeller blade is in the circumferential direction, so only force components in this direction perform work. Thus, changes of momentum of the fluid in the circumferential direction are of concern. It is well known from the basic equations of fluid mechanics that the torque about a given fixed axis is equal to the rate of increase of angular momentum about that axis. Therefore, the torque on the fluid must be equal to the angular momentum of the fluid leaving the impeller per unit time minus the angular momentum of the fluid entering the impeller per unit time. Thus the whirl component of velocity at

inlet and outlet are of primary concern when looking at the work done on the fluid. It immediately follows that the main function of the blades is to impart a whirl component of velocity to the fluid. This requires a force in the whirl direction to be exerted on the fluid by the blades. Consequently, at a given distance along the blade the pressure at the forward face (pressure side) is greater than at the trailing face (suction side), (see Massey [41]). Thus the individual blades function like airfoils generating lift, with a pressure jump orthogonal to the blade chord. This transverse pressure gradient or lift force across the blade occurs due to the curvature of the blade profile. It is important to recognize that there are centrifugal machines with purely radial blades, that is, straight blades (flat plates) with no curvature at all. Straight bladed impellers also generate some pressure rise, but significantly much less than impellers with forward curved blades. The reason that the straight blades also generate lift is because the flow impinges the blades at an angle of attack which will create an asymmetric pressure distribution above and below the plate and due to a component of centrifugal force acting perpendicular to the blade chord (due to flow through rotating blades with stagger, that is non-radial blade inlet angle). It thus obvious why cambered plate blades typically used in centrifugal blowers performs far better than straight radial blades. The next step in improving the impeller performance would be to use airfoil blading instead of circular arc plate blades. From the literature survey, it is noteworthy that airfoil blades have been used in backward curved centrifugal fans, but there is no evidence of airfoil blading being used in forward curved centrifugal fans of the squirrel-cage type. This could be due the fact that the flow deflection achieved by forward curved short chord blades used in typical squirrel-cage rotors is much higher than that required by blowers having backward curved blades. The forward curved blades have very high blade camber, somewhat similar to turbine blade where as the blade camber of backward swept blades is slightly higher than compressor blading. Thus one would expect significant difference in the flow field around the

two different types of blading commonly used in industrial fans or blowers.

The various parameters concerning the blading geometry, relevant to centrifugal fans operating at very low Mach numbers (incompressible flow) are; inlet blade angle, exit blade angle, blade camber, leading edge radius, profile thickness, and maximum camber location. In addition, the type of blading and the number of blades is dependant on the specific application of the centrifugal fan, that is, on the flow range and type of fan characteristic required. The flow quality and fan performance are dependant to a varying degree on the choice of these parameters. The effects of these geometric parameters on flow behavior through a typical blade passage are numerous. For example, the lift coefficient produced is strongly dependant on the effects of blade geometry on blade stall characteristics (which play a critical role for fan operation at off-design conditions) and the point of flow separation off the blades (again dependant not only on inlet flow condition but also on the blade camber and maximum blade camber location). It is well known that excessive flow separation causes a loss of lift and under stalled conditions flow reversal takes place, resulting in a major loss in turbomachine performance and efficiency. The effects of some blading parameters on fan performance have been studied, but the published literature is very scarce. However the review illustrates that the trends observed in centrifugal fan research concur with established aerodynamic test results on cascades and other turbomachinery. In short, compared to other centrifugal turbomachines, the flow mechanism are similar but their interaction is different in typical centrifugal fans.

Fowler [25] conducted a detailed experimental study on a backward curved centrifugal fan impeller using both thin circular arc plate blades and airfoil blades. Flow visualization studies used smoke wires and velocity measurements of inlet and outlet profiles were taken using hot-wire techniques. His study compares the differing fan performance using circular arc plate and airfoil blading. He used the British C-4 airfoil section with 10 percent maximum thickness to chord ratio and slightly higher

blade camber with 5 percent higher blade inlet angle than that of the circular plate blades. The comparison of the two types of blading was done at design point by varying the flow rate. It is important to recognize that the optimum blade form depends on the impeller speed and the relative velocity through the blade passages. Fowler's test results clearly illustrate the superiority of airfoil blading compared to circular arc plate blades, in terms of improved fan performance and much better blade stall characteristics, which are important for off design fan operation. The general description of the flow is similar in both rotors, over the working range of flow at design point. At flow rates below design point, the inlet velocity moves towards the tangential direction, flow separation takes place over the suction side, and is observed to start at the trailing edge and moves upstream. This is expected and could be due to the well-known fact that both laminar boundary layers and turbulent boundary layers will separate off the solid boundary under adverse (positive) pressure gradients. It is important to recognize that flow separation will occur either at the leading edge of the blade due to a very high flow incidence or the flow will separate within the blade passage due to adverse pressure gradients due to either very high blade camber particularly in the pressure recovery section of the blade which acts as a diffuser, or due very low flow rates through the fan which produce boundary layers with lower momentum, unable to overcome the adverse pressure gradients within the blade passage. Rogers [56] has discussed the significance of the degree of impeller inlet to exit velocity diffusion ratio within centrifugal impellers. Rodger's results indicate that the impeller diffusion parameter can have a significant influence on the impeller efficiency and on the impeller stalling characteristics. His results based on tests conducted on centrifugal compressors with specific diffuser types, suggest that the primary factor affecting compressor surge could be the impeller inlet to exit velocity diffusion ratio, where as the flow incidence considerations become of secondary importance. In centrifugal compressors, the impeller and diffuser must be matched simultaneously

at their peak efficiencies, leading towards a wider flow range. In centrifugal fans the flow ranges are dictated by the stalling characteristics of the impeller blade and the diffuser that are inherently controlled by the blade profile design and volumetric flow rates (system resistance). Thus it is essential that blading geometry be chosen for minimizing flow separation in order to increase the flow working range of the centrifugal fans, similar to the aim of increasing flow ranges of centrifugal compressors based on design modifications related to impeller blading as mentioned above. It is interesting to compare flow separation phenomena occurring in backward curved centrifugal fans to that in forward curved centrifugal fans (of the squirrel-cage type); The Particle Tracking Velocimetry study of Denger and McBride [29] and the flow visualization studies of Raj and Swim [34] and Kind and Tobin [33] on squirrel-cage type fans both show that the flow separation occurs at design point and starts from the leading edge and not from the trailing edge as observed by Fowler and others in backward curved centrifugal fans. This signifies an important difference in the two fan types, especially since the blade camber angles of blading used in squirrel-cage fans is much higher then that for backward curved centrifugal fans. On this basis alone one would expect very different flow characteristics through these two types of fans. As the system resistance increases the flow rate is decreased further. The flow fully separates and causes severe unsteadiness in the blade passage. This is documented in many published papers. As is typical in centrifugal compressors and pumps, at very low flow rates, reverse flow is observed through the fan, into the inlet region totally disrupting the inlet flow pattern and subsequently stalling adjacent blade passages. This behavior is noticed in both forward and backward swept centrifugal fans with more vigor in squirrel-cage type fans due to their poorer inlet design. This flow characteristic causes rotating stall and fan surge similar to compressor surge Fowler [24,25]. In comparing the two types of backward curved blading, Fowler made the following observations:

- The airfoil blade rotor stalled at a much lower velocity than the circular plate blades and the design point of the airfoil bladed rotor was at a higher flow rate. This results in a much wider flow working range from maximum to stall flow, being 1.9 times higher for airfoil blade than the circular plate blades. This is very significant, since it can drastically improve fan performance.

- The stall characteristics for the two types of blading are very different. Flow separation is delayed for airfoil blades. That is, at the same flow rate much smaller flow separation takes occurs over the airfoil blades than on circular arc plate blades, this means that a higher pressure rise is achieved for the airfoil bladed rotor.

- The thin circular plate blades were much more sensitive to incidence effects (inlet velocity distribution) compared to the airfoil blades. This is primarily due to the leading edge radius being much smaller and the leading edge profile being sharper for the thin plate blades as compared to the airfoil blades. The flow separation on the suction side is greatly increased and the point of separation quickly moves to the leading edge for the thin plate blades, stalling the whole blade passage. This type of flow sensitivity to the leading edge sharpness is also confirmed by Guzy's [42] CFD simulation of flow through blade passage of fan rotors. His results show that the velocity pattern around the leading edge region for thin circular arc blades is highly sensitive to flow incidence and has a major effect on the blade stall characteristics, especially the pressure rise through the blade passage thereby effecting fan performance.

From Fowler's study, it can be concluded that the working range of the fan can be increased by either increasing the number of blades, (that is, reduce the loading per blade) or by using blades of higher Lift Coefficient. It is clear from different studies

that the second criteria can be accomplished by using an airfoil profile section in fan blading.

A.1.3 Scroll design

The flow leaving the impeller is generally 3-dimensional in nature, although most studies, Raj and Swim [34], Cau et al [36], Kind and Tobin [33], Kjork and Lofdahl [43], and Denger and McBride [29], done on flow through the fan scroll casings indicate small axial velocity components at the impeller exit discharging into the scroll. The absolute blade exit velocities are much higher than the ones at the fan inlet, especially in centrifugal fans with forward curved blading, due to the high blade exit angles. The large blade exit angles of the forward curved fan also provide a large amount of flow guidance in the direction of impeller rotation. The dominant velocity components are the radial and the tangential (circumferential) components entering the scroll casing. The main objective of the scroll is to provide flow guidance from the impeller discharge to the fan exit, with maximum conversion of the dynamic pressure at the impeller exit into a static pressure, which is added to the static pressure rise achieved in passing through blade passages. Thus the role of the scroll casing within the complete fan system can be considered as a pressure recovery device and its influence is very significant on both the overall fan performance as well as internal flow characteristics. The scroll geometry effects the flow development through the fan by prescribing a pressure boundary condition on the flow discharging from the impeller. It is also observed that the scroll geometry has a significant influence on the reverse flow pattern, especially at off design conditions and at low flow rates as suggested by Kind and Tobin [33].

From the theoretical stand point, a scroll design can be proposed on the basis of potential flow theory (inviscid flow analysis) and using correction factors for incorporating the effects of friction due to viscous effects and to turbulent mixing losses. This

approach has been taken traditionally (see the texts by Eck [5] and Osborne [7]) where one of the common approaches to scroll casing design is the free vortex assumption with a point source, both centered at the axis of rotation giving a spiral streamline pattern which needs to be matched by the shape of the volute. The combination of a free vortex and a point source results in a circumferentially uniform radial velocity distribution at the exit of the impeller, which is an ideal flow pattern compared to the real flow through the fan in which there is a considerable radial velocity gradient in the circumferential direction. This discrepancy between the theoretical flow model and the real flow can be attributed to the inability of the flow model to include the effects of blade wake shedding (a source of strong vorticity), flow separation effects within blade passages, and the effect of the scroll casing on the upstream flow pattern. The free vortex design implies that the product of the radial velocity at the exit of the impeller and the radius are a constant, thus giving a log spiral shape for the scroll casing. Roth's [44] experimentally based optimization study of squirrel-cage fans showed that narrower casings gave the maximum efficiencies for all spiral angles. Also the optimum spiral angle found by Roth was 11 degrees with an efficiency of 65 percent. It should be mentioned that Roth's finding regarding optimum casing width of 1.1 was at variance with that of 2.5 found by other workers as pointed out by Kind and Tobin [33]. However, Roth used, similar to Raj and Swim [34], squirrel-cage rotors suffering from inlet shroud flow separation, where as the other workers mentioned by Kind and Tobin used very narrow rotors, that is, with rotor exit to inlet area ratios close to 1, implying a different static pressure rise through the two types of fan rotors.

A.1.4 Blower exit (diffuser) and Cut-Off

The primary purpose of a diffuser is to convert the maximum possible fraction of the dynamic pressure (or dynamic head) into static pressure (or static head). Once the

scroll casing (volute) is designed, additional pressure recovery is possible with the use of a diffuser, caused by the deceleration of the exit velocity from the throat region of the fan scroll up to the diffuser outlet due to an increase of the cross-sectional area from diffuser inlet to diffuser outlet. In addition to the diffuser's pressure recovery function, it is also important to maintain steady and symmetric flow downstream of the diffuser. Flow leaving the diffuser and its efficiency of pressure recovery are closely related to the presence of or absence of flow separation (or stall) in the diffuser. Diffusers are very common pressure recovery devices and it is well known that optimal diffuser included angles should be between 6 degrees to 8 degrees to avoid flow separation and flow reversal within the diffuser. Regions of stalled flow creates considerable flow blockage within the diffuser causing low pressure recovery and results in asymmetric and unsteady flow detrimental to the performance of downstream components in an internal flow system. Reneau et al. [45] have shown that flow through straight 2-dimensional diffusers exhibit four major types of flow patterns depending on the diffuser divergence angle or area ratios and inlet turbulence. For very small angles and area ratios no appreciable stall is observed and the pressure and velocity profiles are fairly symmetric. As the diffuser angle and the area ratio are increased large transitory stall occurs resulting in large pressure fluctuations. At even higher diffuser angles and area ratios a fully two-dimensional stall occurs with the characteristic of being attached to one side of the diffuser and causing severe flow blockage resulting in very low performance. In this regime the flow is steady but intense turbulence and mixing areas are observed even though the stall is stable within the diffuser. The last type of flow pattern observed is the jet flow, which occurs in diffusers with extremely high divergence angles and relatively low area ratios. In this case the incoming flow separates from both diverging walls very near the throat flows straight down the diffuser, resulting in severely stalled regions at the diffuser walls which are fully attached giving relatively steady pressure and velocity profiles except

for the shear layers at the edges of the jet region and the stalled region. Reneau et al also suggest that diffuser performance becomes almost independent of the Reynolds number based on diffuser inlet geometry for the range of Re ¿ 5 x, which insures that the wall boundary layers are turbulent at the inlet. In addition to the effect of diffuser geometry on diffuser performance, the most important blower throat (that is, inlet to the diffuser) conditions that effect performance, for low subsonic inlet Mach numbers and meeting the above Reynolds number criteria, are inlet velocity profile and turbulence level.

In the case of the centrifugal fan, the flow leaves the scroll impeller region and interacts with the fan cut-off and then discharges from the throat region and finally enters the diffuser section. Qualitatively, it was found that a large vortex is present (see refs. [29,30,33,63]) and there is considerable reverse flow back into the impeller near the cut-off region signifying a complex flow pattern. The flow pattern near the cut-off region is complicated due to the interaction of various flow structures, such as blade wakes, blade passage vortex, impeller through flow and scroll flow with the core flow formed by the scroll / impeller combination. As mentioned above the inlet velocity profile to the diffuser has a significant effect on diffuser performance and so it is essential to understand the interaction of the various flow structures near the cut-off. Another region of the fan geometry that can have significant effects on the pressure recovery through the diffuser is the cut-off side of the diffuser wall towards the throat region. It is evident from the literature survey that this area of the centrifugal fan geometry has not received much attention. Some mention of it is found in the text by Eck, but a review of some of the centrifugal pump literature has indicated that the flow near the cut-off region has been under significant investigation (see the recent work by Wo and Bons [46] for a brief review on this topic).

Instability in a centrifugal pump (off-design performance) was investigated experimentally by Wo and Bons [46]. Their study shows there are primarily two reasons

for the onset of surge (instability) as the flow is reduced in the centrifugal pump they used: first, the flow in the cut-off region, and second, the destabilizing effect of the pipe diffuser. Their results show that the former is due to premature diffusion of the flow entering the cut-off region, which is manifested by increased flow recirculation through the cut-off / impeller gap and flow separation on the scroll outer side-wall opposite the cut-off. Their study also shows that flow separation occurs on the cut-off side of the diffuser wall at high flow rates through the pump. This results due to the flow leaving the impeller at a high angle of attack thus causing flow separation on the cut-off side of the diffuser wall. This flow separation needs to be minimized if not eliminated through design modifications. Flow separation on the cut-off side of the diffuser wall causes flow blockage in the throat region upstream of the diffuser inlet leading to a highly distorted flow pattern at the diffuser inlet and reducing the pressure recovery achievable by the diffuser. The published literature on centrifugal fans (see Denger and McBride [29], Kind and Tobin [33], Raj and Swim [34] and Wright et al. [9,10,11,12]) and centrifugal pumps (see Wo and Bons [46], and Elholm et al. [47] and Van den Braembussche and Hande [48]), indicate that at low flow rates or high system resistance, substantial scroll (volute) flow is recirculated around the scroll through the fan or pump impeller / cut-off gap. It is also evident from the literature that the flow near the cut-off plays a vital role in determining the onset of fan or pump system instability (both rotating stall and surge). In addition to the importance of the cut-off region, the destabilizing effect of the diffuser dominates at the onset of overall system instability since reduced flow rates drastically effect the flow through the diffuser section and cut-off compared to other fan or pump system components. It should be realized that individual component performance can be improved from applying first principles in conjunction with past experience, however the overall system performance may not yield the expected improvements due to localized component modifications, mainly because of improper component matching and also

due to a lack of basic information on the flow physics. Only when the relationship between flow regime and performance is known is it possible to evaluate the effects of proposed design modifications. The performance of flow through a typical centrifugal fan depends not only on the flow pattern but also on different geometrical parameters in different flow regimes. From the experimental aspect, the region between the cut-off and impeller blades does not offer itself for ready flow measurement, because typical clearance gaps are on the order of 3 to 8 percent of the rotor diameter. Thus none of workers could accurately quantify flow velocities near this region, however static pressure measurements and flow visualization were manageable. Improvement in flow field resolution near the cut-off region of the fan will be achieved by increasing the size of the fan facility, thereby allowing easier probing in the proximity of the cut-off. The cut-off geometry and relative positioning with respect to the fan impeller affects both the aerodynamics and the acoustics of the centrifugal fan or blower. The cut-off geometry effects the blade passing tone (BPT), which is a discrete noise that occurs due a unsteady pressure field caused by blade wake shedding (a source of high vorticity) interacting with a solid edge boundary, that of the cut-off in blower casing. This discrete noise is the main noise source in centrifugal fans and blowers Neise [1,2]. It was noticed that many acoustic researchers (refs. []) have observed that the cut-off geometry and clearance gap between the rotor and cut-off has a significant effect on the BPT and much less effect on the broadband noise spectrum. Thus it appears that a better understanding of the flow around the cut-off region can help not only the improve the flow characteristics but also lead to a better understanding of the noise features generated due to the aero / acoustic interactions. Thus it is important to able to map the velocity field near the cut-off and methods need to be developed to pursue this objective.

A.2 Towards an experimental program under the existing experimental techniques

From the review of the various experimental methods and instrumentation employed in the flow measurements through centrifugal fans or blowers, it is evident that the relative advantage of differing experimental methods must be matched to the specific areas of the complex flow field. It is clear that the first step in the experiment should consist of flow visualization studies to identify flow separation regions and areas of recirculation. This will indicate the major areas responsible for losses in both blower and impeller and also reveal the overall flow behavior in regions of the blower geometry which are critical for both aerodynamic as well as acoustic performance (such as near the cut-off region, blade wakes, and scroll casing boundary layers within the blower housing). Smoke wire flow visualization techniques have been used successfully by many workers in centrifugal fans, see refs. [24,33,34,63]. The smoke wire method of flow visualization is preferred assuming the impellers rotate at low enough speeds. Low enough fan speeds can be achieved, while maintaining dynamic similarity, by increasing the size of the fan facility. There are other flow visualization methods which can also reveal important information about the flow, such as spark tracing, tufts or bead attachment, oil surface techniques, and dye injection Yang [49] and Goldstein [62]. Air is suggested rather than water for the experimental medium, since facility construction is simpler and the simple method of smoke wire techniques can be used for flow visualization.

The choices for quantitative flow measurement techniques are more limited than flow visualization methods. The flow measurements in the centrifugal fan can be of two types, since the flow is inherently unsteady. Using probes at fixed spatial locations will reveal the absolute flow quantities, where as fixing the measuring probes to the rotating blades allows the relative flow quantities to be obtained. The relative

velocities are of more importance to the designer as well as the researcher for improved blade performance and important turbulence flow quantities. The various types of instrumentation that have been used for flow measurements in centrifugal fan research are; 5-hole pressure probes (refs. [10,11,33,35]), single hot-wires (refs. [4,22,2434,35]), crossed (X) hot wires (refs. [35,36]), hot film sensors (refs. [63]), laser Doppler velocimetry (LDV) refs. [31], Particle Tracking Velocimetry (PTV) refs. [29] and Particle Image Velocimetry (PIV) refs. [30], in addition to using pressure transducers for static pressure measurements within fan housing. In order to obtain detailed flow information through the fan, the flow measurement technique must be able to accomplish the following objectives:

- Measure the 3-dimensional velocity components, starting from the blade inlet profiles, then the flow through the blade passages and at blade exit within the fan casing, since the review of the test results of various workers suggest the flow field is three dimensional in typical centrifugal fans contrary to the assumed two dimensional flow patterns.

- Identify and quantify reversed flow regions.

- Measure flows with high turbulent intensities, as witnessed in the jet-wake structures at the blade's exit and possibly in highly separated flow zones.

- Be adaptable to regions with complicated geometry and small clearances.

The various types of instruments mentioned above, all have certain limitations when used in the flow environment of interest, namely flow through centrifugal fans. It should be mentioned that 5-hole pressure probes are of little use in flows with strong static pressure gradients transverse to the probe and also in highly turbulent flow flows. However, they are well suited in flows with slight nonuniformity and three dimensionality. It appears that turbulence measurements in flows through centrifugal

fans are scarce, with many publications presenting only simple rms velocity traces on oscilloscopes. These are of limited use to the researcher as well as the design engineer, since they can be misleading as to what is actually occurring in the flow relative to the blade due to coherent structure formation being shed off the blades caused by flow separation. The hot wire technique is very well suited to measure turbulent flow fields, even though special procedures are required to measure the multiple components of flow velocity, but many workers have accomplished this in the past. However, hot wires perform well up to 20 to 25 percent turbulence intensities, and therefore could be of limited use in very high turbulent intensity regions. Another drawback of hotwires is that they cannot detect flow reversal. For example, Goulas and Mealing [31] while conducting tests on the tip of a forward curved centrifugal fan impeller at exit with a LDV system on the pressure side of the blade measured turbulent intensities up to 50 percent in the jet structure. The study of Lofdahl and Kjork [43] recorded turbulent intensities up to 14 percent at the exit of a backward curved centrifugal fan. The LDA approach seems to be well suited for the accurate measurement of local flow velocity vector in areas of the fan's flow field characterized by high turbulence intensities and large flow reversals. The LDV technique was first applied to centrifugal turbomachinery by Adler and Levy [50] in 1979 and showed promise for future applications. Since then it has been successfully applied by many workers, on centrifugal pumps and centrifugal compressors ([51,52, 53, 54,55]) and centrifugal fans by Goulas and Mealing [31]. It is interesting to note that there has been only one such study on forward curved centrifugal fans by Goulas and Mealing, but it is important to note that the rotor design they used for the study is not a typical squirrel-cage rotor. As a consequence no single LDV study on forward curved centrifugal fans with a typical squirrel-cage rotor design has been found. One of the important considerations in using the LDV flow measuring technique in centrifugal turbomachines is that of particle seeding. Since the LDV system will measure the

particle velocity, the accuracy of the LDV is determined by the ability of the particles to follow the flow. The regions of flow where the strong velocity gradients exist may cause inaccurate measurements, so care has to taken in analyzing the data obtained from such regions. Due to the strong rotation and curvature effects in centrifugal machines care must be taken to ensure that the particles follow the flow as closely as possible, either by choosing correct density and size of the particles or seeding concentration for given volumetric flow rates. Considerable relative slip between the particle and the local velocity vector can be found near the rotor hub as well as near highly cambered blade surfaces.

Flow visualization and flow measurement combining hot-wire methods (for measurements in the blade passage) with laser Doppler anemometry for different flow regions is the optimum solution. However LDV and smoke wire flow visualization technique will provide most of the information gathered during the experimental program. There are two specific reasons why quantitative information about the turbulent nature of the flow inside centrifugal fans is needed. First, using turbulence results, the correct turbulence generating grids are necessary to provide representative turbulence intensity and scale in the inlet flow and flow through the blade passage. This is essential since the centrifugal blowers operate at very high Reynolds number. Secondly, the reason for acquiring turbulence data is to enable more realistic application of turbulence models to centrifugal fan and blower CFD codes. In this context, Camp and Shin's [60] length scale measurements within a multistage axial compressor as well as the turbulence intensity measurements is a unique study, since earlier studies (see for example Evans [59] and Goestellow [61]) have concentrated mainly on the turbulence intensity and no information was acquired on the length scales. These two parameters are significant since the turbulence intensity expresses the "strength" of the turbulence while integral length scale assigns a spatial dimension to the turbulence structure, often called the average eddy size (see Camp and

Shin [60]).

A.3 Conclusions

From the literature survey on centrifugal fans it is evident that the relationship between various aerodynamic performance parameters and geometric fan parameters have been investigated for different fan configurations, however the squirrel-cage centrifugal fan has received the least amount of attention even though it is in high demand for low noise and high work capacity applications especially where there is a need for compactness. There are numerous areas within the fan system that have the potential for design modifications leading to higher fan performance and higher efficiencies. In addition to better aerodynamic performance, experimental investigation in conjunction with acoustic studies will lead to a better understanding of the sources of aerodynamic noise and their relationship with aerodynamic performance parameters, thus identifying potential areas of design modifications in the fan geometry leading to lower fan noise production. The experimental program should concentrate on the root causes of the specific flow structures that have been identified by previous research as well as any new phenomena related to the particular centrifugal blowers used in the automobile HVAC systems. Once the flow structures are identified on the large-scale blower and relevant design modifications are tested, they must be applied to the scaled blower to test if the blower rumble is eliminated due to the flow structure modifications. It is of paramount importance to test how these flow structure modifications (inherently related to the aerodynamic parameters) modify the blower noise; consequently acoustic tests have to be performed to verify whether flow structure modification reduces blower noise. The results of ([24,33,34,35,63]) clearly indicate that the flow at the fan inlet is highly distorted and leads to flow separation in the upper half of the impeller inlet shroud due to incorrect flow incidence at the blades.

This causes blade stall resulting in a lower fan performance and a decrease in fan efficiency. Thus the inlet flow to the squirrel-cage fan needs treatment, which will reduce if not eliminate the flow separation occurring on the inlet shroud and produce a more radially uniform inlet velocity profile for proper matching of the flow incidence and blade inlet angles. Improvement of the inlet flow can be achieved by various methods. First, the lip radius of the inlet cone can be increased, thereby reducing flow diffusion near the inlet wall before the flow enters the impeller. This will have several effects; the flow separation off the inlet cone side wall will be minimized, the flow will be able to turn from the axial direction to the purely radial direction with minimum losses and the flow will enter the blades with minimum shock losses, thus increasing fan performance. The inlet flow treatment will also increase the active region of the fan impeller, that is, a much smaller portion of the impeller will be stalled or the stall eliminated completely, resulting in a more uniformly distributed blade loading for a given duty. As a consequence it is possible that for an improved inlet velocity profile, the fan impeller width for the same number of blades can be reduced due to the more efficient use of the impeller blades for useful energy transfer to the fluid. The other possibility is to reduce the number of blades while maintaining the original width, but this approach is not well founded, since the blading used in typical squirrel-cage fans or blowers are based on two-dimensional flow, which occurs mostly due to the large number of blades used only in this type of fan. A lower number of blades will possibly reduce flow guidance and induce larger secondary flows thereby resulting in a more three-dimensional flow pattern as is evident from the literature on shorter width blades used in backward curved centrifugal fans, (see Cau et al. [36], Fowler [24]). It should be recognized that due to space constraints in automobile HVAC modules, only a small increase of the inlet radius of curvature of the blower might be possible, thus additional types of modifications are required. The other type of inlet modification that has been successfully employed is by Gessner [35], who used the edge

suction of the boundary layer at the inlet cone before the flow enters the impeller. Boundary layer suction techniques are well established in the aerodynamic field. For example boundary layer suction is employed on the aircraft wings to delay flow separation or induce flow reattachment after flow separation has occurred. This method is particularly useful for flows under adverse pressure gradients, such as occurring due to high surface profile curvature, as is occurring in the fan inlet cone. The suction flow can be induced due to pressure differentials existing in the manifold, since typical suction volume required are on order of 2 percent of volumetric flow through the fan. This type of modification has a high potential for practical application, since it is not complicated and is a non-intrusive method, which will not introduce any additional noise sources within the fan system. Another key fan component that has considerable potential for design modifications is the fan blading. From the literature survey, it is apparent that fan blading has received little attention, although some workers have indicated the need for improvements in blade design and further research in this area. There are two important issues in fan blade design that emerge from the work of different authors (see refs. [25,29,33,34,35,42,63]), they are the flow separation off the fan blades and the sensitivity of the leading edge of the typical thin circular arc blades used in standard squirrel-cage fans to flow incidence. The possibility of multiple solutions exists in alleviating the problem of flow separation in fan blades. One of the solutions pertains to modifications to the blade profile for delaying flow separation, thereby increasing the pressure rise characteristics within blade passage. On the blades itself, means of tripping the boundary layer can be tested if the boundary layer is laminar, upstream of the maximum camber location near the leading edge to induce early boundary layer transition from the laminar to the turbulent regime, thus increasing the ability of the boundary layer to sustain a higher adverse pressure gradient, thus delay separation. Also evident from the literature survey is that SCFC fans do not employ airfoil blading in contrast to BCC fans which have successfully

used airfoil blading with its superior performance compared to the thin circular arc blades. The effect of profile thickness and the applicability of airfoil blading in SCFC fans need to be tested experimentally. If airfoil blading (with profiles similar to highly cambered turbine blading but having a diffusing cascade for pressure rise purposes) is workable in the range of the required fan operation, then relevant improvements and modification in blade profile should be done on an empirical basis initially. As mentioned earlier, Fowler's [25] experiments show the advantages in using airfoil blading over thin circular arc blading in a BCC fan, however the workability of airfoil blading in SCFC fans remains indeterminate with the present status of research on this area.

The design of the scroll and cut-off geometry is fairly well established, however the design of the diffuser at the fan exit can be modified for improving downstream flow patterns as well as achieving some gain in pressure recovery at the fan exit. The modifications to the diffuser will be severely restricted due to the inflexibility in altering ductwork from the fan exit to the evaporator core and due to the lack of housing space. In any event, the scroll casing design needs to be improved to prevent excessive tangential (circumferential) pressure gradients. When the fan operates under rotating stall conditions the throughflow from the fan impeller has a non-uniform circumferential distribution, thereby inducing a significant tangential static pressure gradient along the scroll casing. This flow pattern is always observed under rotating stall conditions. With the present state of knowledge on rotating stall phenomena in centrifugal turbomachinery, it is not possible to identify the exact cause and effect relationships with the various geometric parameters of the fan design. Theoretical prediction of the onset of rotating stall and its suppression or control is beyond existing design methodologies. Therefore, a comprehensive study analyzing rotating stall is required. The program should first identify the causes of rotating stall and then develop and validate relevant design modifications for improving fan performance at flow rates significantly below design values or for high system resistances (that is,

operating in heater mode). Since the dynamics of the phenomena with respect to fan performance, noise and efficiency are not clearly understood an experimental study is required.

Results from the literature survey cannot be decisively extrapolated to an automobile HVAC system in order to identify whether blower rumble noise is associated with poor fan design or duct acoustics or a combination of both. The literature survey does raise several key questions. Does rotating stall occur in the blower of an automobile HVAC system? Is blower rumble noise associated with rotating stall of the fan impeller? These questions can be answered only by experimental analysis. If rotating stall is present, is its onset associated with the fan or the system geometry? If blower rumble noise is primarily system geometry (HVAC ducting design) dependant, then conventional design guidelines for HVAC module design need to be reexamined. If blower rumble noise is fan impeller dependant then the fan itself needs to be redesigned.

It is evident from the literature survey that rotating stall occurs at flow rates well below design, implying high system resistance (i.e. heater mode operation). This suggests that the influence of system resistance on the stall characteristics of the fan impeller may be an important variable indirectly related to blower rumble noise. By redesigning the heater core to have a larger flow area the backpressure on the blower system may be reduced and rotating stall eliminated. Experiment can verify if the reduction of the overall system resistance is sufficient to eliminate the blower rumble noise.

It is important to recognize that there are trade offs between noise reduction and cost benefits. A price must be identified that the customer is willing to pay for noise reduction. This added cost would identify those design modifications requiring development and validation that are also a solid business case.

Appendix B

Basic Review of Centrifugal Fan Aerodynamics

B.1 Euler's analysis for rotating fan blades

The analysis of the flow through the fan impeller itself can show the effects of the rotating fan blades on the fan aerodynamic characteristics, that is, the fan pressure rise and volume flow characteristics. Basic inviscid flow theory can be applied to a typical blade passage to demonstrate the essential features of the effect of the rotating fan blades (i.e., fan speed and fan blade inlet and exit angles) on the pressure rise/volume flow rate characteristics. The classical inviscid analysis of turbo machinery was first done by Euler (18), in particular the analysis was applied Turbines,(giving the famous "Euler Turbine Equation") but which can easily be applied to fans (or compressors) and pumps. Euler's steady inviscid analysis applied to rotodynamic machines suggests that the torque experienced by fluid mass due to the interaction of a the rotating blades can be established by using the principle of angular momentum under certain assumptions. The Euler turbine or pump theory is based on the following assumptions (Massey, Wilson):

1. The velocity vector at fan blade inlet is uniform between the blade passage (no circumferential variations are allowed) and constant along the span of the blades (no height variations).

2. All friction effects are neglected (inviscid flow), both at fan blade inlet and blade exit.

3. Finite blade thickness effects are neglected. This also implies that no flow deviations or "slip" is allowed at the blade trailing edge, that is, the flow perfectly follows the blade surface profile at blade inlet (leading edge and at the blade trailing edge).

4. The fluid enters the blade passage without any local separation or flow reversal , that is , a "shockless entry" occurs (according to a British turbomachinery vocabulary).

Notice that under the given assumptions the flow passage around the fan blades can be simplified to a single velocity vector approaching the inlet of the fan blade and a single velocity vector exiting the blade passage in the relative frame of reference. Thus by virtue of the fact that, the blades are rotating the absolute velocities can be determined by simple vector addition, both at the fan blade inlet and fan blade exit. The velocity triangles are shown for a forward curved centrifugal fan in Fig. 1. The velocity triangles also relate the flow angles and flow velocities to the blade setting angles and blade rotation speed in a very simple way.

It must be mentioned that such a simplified analysis only serves as a first approximation in fan design process, however, it is useful enough to relate the basic flow parameters to overall fan impeller geometric parameters, with the result of which, the overall fan impeller performance can be estimated.

The fan torque (neglecting friction effects) under the given flow assumptions can be determined using by utilizing Eq. 2.3.

$$T_{sh} = \int_{exit} (\vec{r} \times \vec{V}) \rho \vec{V} \cdot d\vec{S} - \int_{inlet} (\vec{r} \times \vec{V}) \rho \vec{V} \cdot d\vec{S} \tag{B.1}$$

After applying Eq. 2.3$ to the fluid through the blade passage of Fig. 1., under the stated assumptions,

$$T_{sh} = \int_{exit} (V_{t2} r_2) \rho \vec{V} \cdot d\vec{S} - \int_{inlet} (V_{t1} r_1) \rho \vec{V} \cdot d\vec{S} \tag{B.2}$$

Euler's theory assumes that both circumferentially and spanwise, and at both the fan blade inlet and fan blade exit locations. Notice that Eq. 3.01.1 is a fundamental relation for all types of turbomachinery [Massey], such as fans, pumps (or compressors) and turbines. The power requirements for fans (using Euler's theory) can be established utilizing Eq. 3.01.1.

$$K = T_{sh}\Omega = \int_{exit} (U_2 V_{t2}) \rho \vec{V} \cdot d\vec{S} - \int_{inlet} (U_1 V_{t1}) \rho \vec{V} \cdot d\vec{S} \tag{B.3}$$

$$K = T_{sh}\Omega = \rho Q (U_2 V_{t2} - U_1 V_{t1}) \tag{B.4}$$

Therefore the workdone per unit mass of the fluid is

$$\frac{K}{\rho Q} = (U_2 V_{t2} - U_1 V_{t1}) \tag{B.5}$$

notice that the pressure " head" (p/) can be expressed using Eq. 3.01.4

$$\frac{\Delta p}{\rho} = \frac{K}{\rho Q} = (U_2 V_{t2} - U_1 V_{t1}) \tag{B.6}$$

Therefore, the theoretical (Euler) pressure rise across the fan blade is obtained;

$$\Delta p_{th} = \rho (U_2 V_{t2} - U_1 V_{t1}) \tag{B.7}$$

Equation 3.01.6 shows the relationship between the total pressure rise, the relative flow velocities and fan blade velocities. In case there is no swirl component in the velocity at the inlet to the fan blades then the flow enters the blade passage at exactly the inlet blade setting angle, thus making $V_{t1} = 0$. Therefore zero swirl (radial entry) at fan blade inlet modifies the theoretical pressure rise, such that

$$\Delta p_{th} = \rho (U_2 V_{t2}) \tag{B.8}$$

and subsequently the theoretical shaft power input to the fan required becomes

$$K = \rho Q(U_2 V_{t2}) \tag{B.9}$$

It is interesting to note that the fan blades themselves cannot generate swirl (except in the case of highly viscous fluids). Flow swirl can be generated upstream of the fan through the certain devices such as, an inducer, inlet guide vanes, inlet ducting with sharp bend (which generate axial vorticity), louvers, etc...). The static ducting of the fan housing cannot generate bulk flow swirl, and thus cannot produce any torque on the fluid. In addition, Eq. 3.01.8 implies that the fan torque is independent of fan inlet radius.

If the fan blades are assumed to be thin, and have a blade span bs the flow rate Q, can be expressed as

$$Q = 2\pi r_2 b_{sp} V_{n2} \tag{B.10}$$

Where V_{n2} is the normal (or radial) relative velocity at the fan blade exit. Thus, the theoretical pressure rise across the centrifugal fan (Eq. 3.01.7) can be expressed as

$$\Delta p = \Omega r_2 (\Omega r_2 - \frac{Q}{2\pi r_2 b_{sp}} \cos \beta_2) \tag{B.11}$$

Therefor for a fan with fixed geometry and a given fan speed, fan pressure rise (Δp) is a linear function of volumetric flow rate, (Q). In addition, the fan (T_{sh}) torque or power (K) are also a linear function of volume flow rate. The prediction of the fan characteristics using the simplified theory, provides only a first approximation, to the actual fan characteristics. The actual flow through the fan blades is a highly 3-dimensional flow with regions of local flow separation and inter-blade flow stratification (due the "relative eddy" [Sheppard]), that is flow deviation due to viscous effects, turbulence, etc...). In addition, the actual flow is subject to system effects (inlet and exit boundary conditions (Wright, Bolton) that modify the velocity and pressure fields such that deviations from simple theory occur. Real viscous and

system effects make the fan characteristics nonlinear instead of the simple liner relationship predicted by inviscid streamline theory (Euler pump/turbine theory). The flow through centrifugal fans is generally a high Reynolds number phenomena. The flow losses that occur in the fan/scroll system, whether due to flow separation off the fan blades or the viscous losses in the fan scroll, or losses due to a sudden expansion in flow geometry can be generally modeled as function of flow rate squared. That is

$$\Delta p_{loss} \propto Q^2 \tag{B.12}$$

For example, suppose a fan with inlet ducting causes flow swirl, which subsequently causes a reduction on fan performance. In order to remove flow swirl, inlet guide vanes are attached upstream of the fan inlet orifice. Thus, the flow approaches the fan blades without any swirl (Vt1=0), so that the blade inlet angle is perfectly matched with relative flow velocity at inlet (radial entry). Note however, for each value of the blade inlet angle, there is only one shape of the inlet velocity diagram which gives ideal flow conditions, that is a "shockfree" entry. At off design fan operating conditions (non-optimal flow rate), the inlet velocity vector will be misaligned with the blade leading edge, and local flow separation becomes highly probable. Inlet flow angle/blade inlet angle misalignment is a well known phenomena in high speed compressors and hydraulic pumps (Zverdup, Bolton). In many industrial fans and turbines variable geometry inlet guide vanes are used for optimal control of the inlet flow. However in many industrial applications the IGV's become cost prohibitive and in certain specific environments, for example automobile HVAC modules, space constraints severely limit the possibility of installing upstream flow conditioning devices.

The general relationship between the theoretical pressure rise, flow velocities and blade velocities for a centrifugal fan

From geometry of the velocity triangles and blade angles, it can be shown [Massey], as in Fig. 1., that the workdone in terms of the relative velocities can be related to

the absolute velocities and blade angles. From the velocity triangle at fan blade inlet, it is shown that

$$V_{r1}^2 = U_1^2 + V_1^2 - 2U_1V_1\cos\alpha_1 = U_1^2 + V_1^2 - 2U_1V_{t1} \tag{B.13}$$

Similarly, from the velocity triangle at fan blade exit,

$$V_{r2}^2 = U_2^2 + V_2^2 - 2U_2V_2\cos\alpha_2 = U_2^2 + V_2^2 - 2U_2V_{t2} \tag{B.14}$$

But recognize that $U_iV_{ti} = \frac{1}{2}(U_i^2 + V_i^2 - V_{ri}^2)$, applies both at fan blade inlet and blade exit. Therefore the theoretical pressure rise across the fan blades can be expressed as:

$$\Delta p_{th} = \frac{\rho}{2}[\underbrace{(V_2^2 - V_1^2)}_{a} + \underbrace{(U_2^2 - U_1^2)}_{b} - \underbrace{(V_{r2}^2 - V_{r1}^2)}_{c}] \tag{B.15}$$

Where the term a shows the change in the absolute kinetic energy of the flow through the blades (these velocities are generally function of overall fan geometry upstream and downstream of the fan, in addition turbulence, local flow separation, etc...) can affect both, the absolute velocity's magnitude and direction. Term b denotes a source of a radial pressure gradient due to centrifugal forces. It is well known that for curved streamline flow, the integration of the inviscid Euler equation of motion normal to the streamline gives

$$\frac{\partial p}{\partial r} = \rho\frac{V^2}{R} = \rho\Omega^2 R \tag{B.16}$$

Equation 3.02.2 shows how a change in the tangential blade velocities at different radii can generate a pressure gradient. It is well known that in axial turbomachinery this term is generally zero for a particular radius, that is, there is no radial flow. The term c generates a pressure gradient mainly due to the change in the cross-sectional area of the blade passage from the blade leading edge to the blade trailing. The pressure gradient is positive (or adverse) for fans and pumps (or compressors), and negative in the case of turbines. In centrifugal fans, this pressure rise occurs mainly

due to flow deceleration from blade inlet to blade exit. The diffusion process is mainly a function of aerodynamic blade profile characteristics. For example, blade camber, maximum thickness location, blade thickness, leading edge radius and blade stagger to name a few [Lieblen, Turton, Goestellow]. In centrifugal fans (or pumps) the flow passage area increases from blade inlet to fan blade exit.

Eck (1971) applied elementary streamline theory (inviscid, incompressible 2-D flow), to centrifugal fans and demonstrated the effect of the important flow parameters on the performance of the fan impeller and the effects of certain important impeller geometric parameters on the pressure rise across the fan blades.

B.2 One-dimensional analysis of rotating fan blades: Derivation of the fan blade pressure coefficient

Simple one-dimensional analysis of the fan blades will use the nomenclature specified by White as pictured in Figure 3. The blade tip velocity $u = \omega r$, the velocity with respect to the moving blade is w, and the velocity with respect to a stationary frame of reference (i.e., the scroll) is V. The directional angle, α, corresponds to the velocity V in the stationary refrence frame. It is assumed that the directional angle for the velodity w in the moving frame of reference is parallel to the blade curvature and is named β. Velocities at the inside and outside radius of the fan blades are denoted with a subscript of 1 and 2, respectively. The radial (normal) component of velocity is indicated with the subscript n and the angular (tangential) component using the subscript t.

The angular momentum is used to relate the torque about the fan axis of rotation, T, required to induce a change in regular momentum across the blades.

$$T = \rho Q(\vec{r_2} \times \vec{V_2} - \vec{r_1} \times \vec{V_1}) = \rho Q(r_2 V_{t2} - r_1 V_{t1})\vec{k} \tag{B.17}$$

Consider an ideal case where the flow approaches the fan through a long straight pipe. The control volume is expanded upstream from the inlet of the fan blades to a position within the inlet pipe where the flow is uniform and irrotational. This location is identified using the subscript 0. The flux of angular momentum into the control volume is now zero since the velocity vector at this surface is parallel to the fan rotational axis. The resulting equation, if muliplied by ω, now defines the power required by the fan.

$$P_{fan} = \omega T = \omega \rho Q r_2 V_{t2} = \rho Q u_2 V_{t2} \tag{B.18}$$

Uding geometric identities, this equation is written in terms of the kinetic energy of the velocity components in the stationary and moving frames of reference.

$$P_{fan} = \rho Q[\frac{1}{2}(V_2^2 + u_2^2 - w_2^2)] \tag{B.19}$$

Dividing the fan power by the weight flow rate, $\rho g Q$, produces an expression for the head H_{fan} added to the fluid by the fan.

$$H_{fan} = \frac{P_{fan}}{\gamma Q} = \frac{1}{2g}[V_2^2 + u_2^2 - w_2^2] \tag{B.20}$$

This expression is used in the energy equation to describe the fan work done on the same control volume, assuming there are no frictional losses between the pipe inlet and fan outlet. Since the fluid is a gas, the effect of elevation difference can be ignored. The total head at the outlet of the fan is equal to the total head at the inlet plus the head added by the fan.

$$\frac{p_2}{\gamma} + \frac{V_2^2}{2g} = \frac{p_0}{\gamma} + \frac{V_0^2}{2g} + H_{fan} = \frac{p_0}{\gamma} + \frac{V_0^2}{2g} + \frac{1}{2g}[V_2^2 + u_2^2 - w_2^2] \tag{B.21}$$

The pressure rise due to the fan is solved for explicitly simply by rearranging the terms of the equation.

$$\frac{p_2 - p_0}{\gamma} = \frac{1}{2g}[V_2^2 + u_2^2 - w_2^2] \tag{B.22}$$

Using conservation of mass, the component of velocity in the moving frame of reference at the blade exit is expressed in terms of the volume flow rate, Q, blade height, b_2, diameter, D_2, and angle, β_2.

$$w_2 = \frac{w_{n2}}{\sin\beta_2} = \frac{Q}{\pi D_2 b_2 \sin\beta_2} \tag{B.23}$$

The velocity at the inlet is also expressed in terms of the volume flow rate and the pipe diameter.

$$V_0 = \frac{4Q}{\pi D_0^2} \tag{B.24}$$

The above two relations are substituted into the energy equation. The blade tip velocity, $u_2 = \frac{\omega D_2}{2}$, is expressed as a function of the fan speed, ω, and blade diameter in the energy equation.

$$\frac{p_2 - p_0}{\gamma} = \frac{1}{2g}[((\frac{4}{\pi D_0^2})^2 - \frac{1}{(\pi D_2 b_2 \sin\beta_2)^2})Q^2 + (\frac{\omega D_2}{2})^2] \tag{B.25}$$

The equation is made dimensionless by multiplying both sides by the gravitational acceleration, g, and dividing by the square of the product of the blade diameter and fan speed, $(\omega D_2)^2$.

$$\frac{p_2 - p_0}{\rho(\omega D_2)^2} = \frac{1}{2}[(\frac{1}{\pi^2}(\frac{2D_2}{D_0})^4 - \frac{1}{(\pi\sin\beta_2)^2}(\frac{D_2}{b_2})^2)(\frac{Q}{\omega D_2^3})^2 + \frac{1}{4}] \tag{B.26}$$

The terms involving pressure and flow rate are now dimensionless and are simply modified forms of the traditional pressure coefficient, ψ, and the flow rate coefficient, ϕ. In terms of the present nomenclature, ψ and ϕ can be expressed as follows:

$$\begin{aligned} \psi &= \frac{p_2 - p_0}{\rho(\omega D_2)^2} \\ \phi &= \frac{Q}{\omega D_2^3} \end{aligned}$$

Thus, using ψ and ϕ equation B.26 becomes

$$\psi = \frac{1}{2}[(\frac{1}{\pi^2}(\frac{2D_2}{D_0})^4 - \frac{1}{(\pi\sin\beta_2)^2}(\frac{D_2}{b_2})^2)\phi^2 + \frac{1}{4}] \tag{B.27}$$

B.3 Fan/system analysis using the energy equation

Energy considerations of the fan/motor system provide the required estimation of fan efficiency, fan power requirements (or torque characteristics). The correct estimation fan efficiency and power requirements subsequently provide the cost and feasibility for particular fan application, since various fan application environments constitute different system resistance (or fan loads). Also, the fan aerodynamic performance includes the fan torque characteristics, in addition to the fan pressure rise/volume characteristic, since the fan torque characterizes the power requirements as the system load changes across the fan. Whereas the pressure rise/volume flow coefficient characterizes energy transfer characteristics between the fan blades and fluid.

The appropriate integral relations for a fixed control volume across a fan [White(85)] is

$$\dot{Q} - \dot{W}_s - \dot{W}_v = \frac{\partial}{\partial t}\left(\oint_{cv} e\rho d\vartheta\right) + \oint_{cs}\left(e + \frac{p}{\rho}\right)\rho(\vec{V}\cdot\vec{n})dA \tag{B.28}$$

where

$$e = u + \frac{1}{2}V^2 + gz \tag{B.29}$$

Applying Eq. B.28 to the control volume across the fan, certain assumptions can be made, that are as follows:

1. There is no heat transfer into the c.v., thus $\dot{Q} = 0$

2. The potential energy changes are negligible, or gz=0

3. The flow is incompressible (constant density), = constant

4. The unsteady term in Eq. 2.21 is assumed to be negligible compared to the energy flux and power terms, since the flow is considered to be steady in the mean (flow is cyclical) [Massey (82)]

5..Ideal gas properties are assumed, with fluid properties being constant.

Using Eq. ref2.3)with the aforementioned assumptions, the equation reduces to

$$-\dot{W}_s - \dot{W}_v = \oint_{cs} \left(u + \frac{1}{2}V^2 + \frac{p}{\rho} \right) \rho(\vec{V} \cdot \vec{n}) dA \tag{B.30}$$

Eq. **??** can be rearranged into the following form

$$-\dot{W}_s = \oint_{cs} \left(\frac{1}{2}V^2 + \frac{p}{\rho} \right) \rho(\vec{V} \cdot \vec{n}) dA + \left\{ \dot{W}_v + \oint_{cs} u\rho(\vec{V} \cdot \vec{n}) dA \right\} \tag{B.31}$$

Where the last bracketed term in Eq. **??** represents lost work in the sense that this work cannot be used in the transformation of fan rotor energy into flow energy in the form of an increase of kinetic energy or pressure rise across the fan. In fact, the viscous dissipation part converts mechanical energy into heat (internal heating) and the change in internal energy constitutes an increase of fluid temperature leaving the c.v.

$$\dot{W}_{lost} = \left\{ \dot{W}_v + \oint_{cs} u\rho(\vec{V} \cdot \vec{n}) dA \right\} \tag{B.32}$$

Thus, a practical estimate of fan efficiency can be made by utilizing Eq. **??** For the case of a fan or pump the efficiency in general is given by

$$\eta_{fan} = energyout/energyin \tag{B.33}$$

With the aid of Eq. **??** the fan efficiency can be formed as

$$\eta_{fan} = \frac{-\dot{W}_s - \dot{W}_{lost}}{-\dot{W}_s} \tag{B.34}$$

Where

$$\dot{W}_s = \Omega_{shaft} T_{shaft} \tag{B.35}$$

By substitution from Equations 2.26, 2.10 and 2.6 one obtains the following for fan efficiency

$$\eta_{fan} = \frac{\oint_{cs} \left(\frac{1}{2}V^2 + \frac{p}{\rho} \right) \rho(\vec{V} \cdot \vec{n}) dA}{\Omega_{shaft} T_{shaft}} \tag{B.36}$$

Note that the dynamic pressure ($\frac{1}{2}\rho V^2$) and static pressure (p) are related via total (stagnation) pressure (PT), such that;

$$P_T = \frac{1}{2}\rho V^2 + p \tag{B.37}$$

Finally, Eq. 2.27 can be written as

$$\eta_{fan} = \frac{\int\int_{cs} P_T \vec{V} \cdot \vec{n} dA}{\Omega_{shaft} T_{shaft}} \tag{B.38}$$

It is interesting to note that the denominator of Eq. B.38 can be related to the velocity entering and exiting the fan rotor blades by virtue of the moment of momentum equation for a fixed (non-deforming) c.v. in the inertial frame of reference (i.e., one obtains the famous Euler's Turbine (or pump) equation for turbomachinery analysis). In Eq. B.38, if it is assumed for a single inlet and single outlet fan system, the velocity and pressure profiles across the control surfaces (usually taken as, far upstream and far downstream from the fan rotor/scroll combination) are uniform then Eq. B.38 can be simplified as follows

$$\eta_{fan} = \frac{(P_{T2} - P_{T1})Q}{\Omega_{shaft} T_{shaft}} \tag{B.39}$$

Notice the mass continuity equations was used thus introducing the volumetric flow rate Q into the equation. Thus for uniform flow conditions and incompressible flow, volume flow rate can be expressed as

$$Q = \iint \vec{V} \cdot \vec{n} dA \Rightarrow VA = cons\tan t \tag{B.40}$$

Equation B.39indicates that the fan produces both an increase in static pressure and a dynamic pressure increase (in the case f dynamic pressure difference is mainly due to the cross-sectional area differences between inlet duct and outlet duct.

B.3.1 Relationship of fan torque to the flow velocity at inlet and exit of fan blades

From mechanics, the principle of the moment of linear momentum on a particle about a reference point, can be used to develop a similar equation for fluid particles that are subjected to body force moments acting on a control volume and moments due to surface forces acting on a control surface. If the moments of the external forces and linear momentum are taken about a fixed point in an inertial frame or the center of mass, the principle of momentum of momentum (or angular momentum) for a c.v. [Allen and Ditsworth and Massey] may be written as

$$\sum \vec{M}_B + \sum \vec{M}_S = \int_{c.v.} \frac{\partial}{\partial t} \left[(\vec{r} \times \vec{V}) \rho \right] d\vartheta \div \oint_{c.s.} (\vec{r} \times \vec{V}) \rho \vec{V} \cdot d\vec{S} \qquad \text{(B.41)}$$

The application of Equation to a c.v. fixed to an inertial frame of reference around a fan rotor shows that under certain assumptions (given below), the torque on the fluid due to the fan shaft can be simply related to the flow velocities across the fan blades. The major assumptions for the fan c.s. are:

1. The unsteady term in the angular momentum equation vanishes for a periodically steady flow through the fan rotor.

2. The external moments due to body forces are zero, since the body-force vector is parallel to the moment axis. Thus only surface force moments are considered (i.e., rotating fan shaft).

3. . The moment produced by shear stresses at the hub and shroud sections of the fan are due to the portions of the fan rotor itself

4. Moments due to the normal stresses that act over sections of the c.s. at the inlet and exit of the fan blades are zero since these forces are either parallel to the moment axis or pass through this axis [Allen and Ditsworth].

Therefore, the angular momentum equation (Eq. 2.32) reduces to the following

simplified form

$$M_s = T_{shaft} = \oint_{c.s.} (\vec{r} \times \vec{V}) \rho \vec{V} \cdot d\vec{S} \tag{B.42}$$

Using the assumptions and c.s. selected for the fan and under uniform flow conditions (i.e., 2-dimensional velocity analysis) at fan blade inlet and exit, Eq. B.42 simplifies to

$$M_s = T_{shaft} = \oint_{c.s.} (\vec{r} \times \vec{V}) \rho \vec{V} \cdot d\vec{S} = \sum (\vec{r} \times \vec{V})_{exit} \dot{m}_{exit} - \sum (\vec{r} \times \vec{V})_{inlet} \dot{m}_{inlet} \tag{B.43}$$

Therefore, from Eq. B.43, the famous Euler's Turbine (or pump) torque equation results,

$$M_s = T_{shaft} = \rho Q (r_2 V_{2t} - r_1 V_{1t}) \vec{k} \tag{B.44}$$

Where V2t and V1t are the absolute tangential fluid velocities at fan blade exit and fan blade inlet respectively. Combining equations 2.35 and 2.26 one obtains an expression for fan shaft power

$$\dot{W}_s = \Omega_{shaft} T_{shaft} = \rho \Omega_{shaft} Q (r_2 V_{2t} - r_1 V_{1t}) \tag{B.45}$$

Note that if the continuity equation is applied to the fan blades then

$$Q = (A_p V_r)_{inlet} = (A_p V_r)_{exit} \Rightarrow 2\pi R_1 b V_{r1} = 2\pi R_2 b V_{r2}) \tag{B.46}$$

where b is blade span, so for thin blades Eq.B.46 reduces to

$$R_1 V_{r1} = R_2 V_{r2} \tag{B.47}$$

and since the blade velocity is given in terms of fan rotation speed

$$U(blade)_i = \Omega_{shaft} R_i \tag{B.48}$$

shaft power can be expressed as

$$\dot{W}_s = \Omega_{shaft} T_{shaft} = \rho Q (U_2 V_{2t} - U_1 V_{1t}) \tag{B.49}$$

Notice, that equation B.492.40 is an approximate result that neglects the viscous and bearing torques. Eq. B.49 can be modified to incorporate viscous effects by including a efficiency, resulting in

$$\dot{W}_s = \Omega_{shaft} T_{shaft} = (1/\eta)\rho Q(U_2 V_{2t} - U_1 V_{1t}) \tag{B.50}$$

The question of why is there a discrepancy in the representation of the fan Characteristic, whereas the fundamental theory supports the idea that the true fan performance curve should be based upon the total pressure rise across the fan and not just static pressure could be of importance. Common air-moving applications of centrifugal blowers in industry usually require, that the fan generates enough pressure to overcome system resistance at a particular volume discharge. In many applications the dynamic pressure contributions are lost to the atmosphere, thus lending ground to the argument against including dynamic pressure in both the evaluation of the fan performance curve and selection of the fan operating point, from which an appropriate fan selection is made. The contributions of the dynamic pressure generated by the fan are significant for low system resistances settings (low static pressure rise) since the fan acts more like a source of purely kinetic energy, i.e., a blower, thus its inclusion in the fan performance curve depending on the fan application can be advantageous.

Appendix C

Experimental verification of the performance of the AMCA/ASHRAE standard plenum chamber test facility (PLC)

C.1 Introduction

Fans are generally tested in accordance with requirements of AMCA Standard 210-74/85 [3], [45] and ASHRAE Standard 51-75/85. The AMCA Standard specifies the procedures and test setups to be used in testing several types of fans. Detailed information about two standard fan-testing methods are provided in Appendix **??**. In addition, individual industries have separately evolved their own internal techniques. In the course of the experiments described in subsequent chapters, it was observed from testing centrifugal fans under various configurations (e.g., different inlet and outlet boundary conditions) and utilizing several fan test methods, that different fan

performance characteristics were obtained for the same fan.

In order to test the validity of the fan testing procedure, several tests were conducted on two different AMCA recommended fan test facilities: a plenum chamber fan test facility, the PLC; and a straight outlet-duct fan test facility, the STD. Comparisons were made between the experimentally verified plenum chamber test facility and the standard outlet duct fan test facility method using identical upstream conditions. The study highlights the significance of fan exit boundary conditions (fan installation) on fan performance characteristics. Fan performance characterization is also discussed in relation to the method of measuring fan exit pressure and measurement accuracy.

C.2 Objectives

The main purpose of the experimental study was to check the accuracy of the wall static pressure measurements under two standard flow inlet conditions. The first is a laminar uniform flow profile. This uniform velocity was produced by an axisymmetric jet facility described in detail by Glauser [30]. It consisted of a blower, a diffuser, straight section with turbulence reduction screens and flow straightener, and finally an axisymmetric contraction nozzle (area ratio of 3:1) for accelerating the flow before the jet exit, as shown in Fig. C.1

The exit of the jet was connected to the Plenum with an 18-inch long, 4-inch diameter pipe. Static wall taps were placed at 16.5 inches from the jet exit inside the straight duct flush with the inside surface. The velocity profile at the exit of the jet duct was laminar and uniform. These flow characteristics imply that the streamlines at the exit are nearly straight. Thus to within the boundary layer approximation (i.e., the pressure drop across the wall boundary layer is assumed small), the wall static pressure (piezometric) at the jet exit is a true and accurate measure of the duct

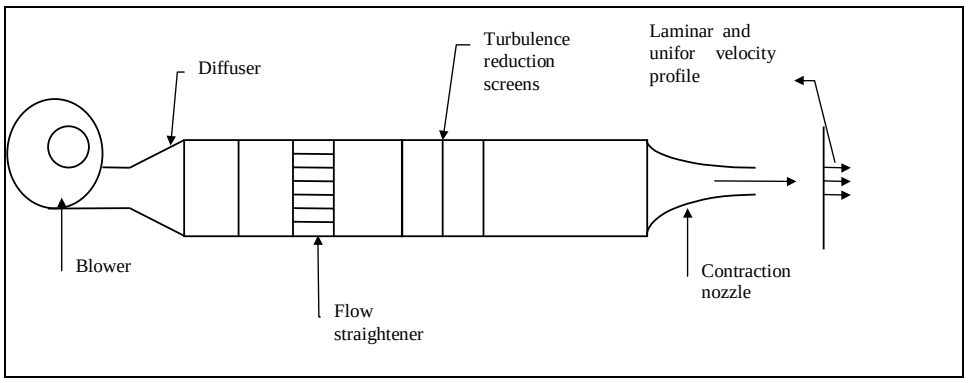

Figure C.1: Axisymmetric jet facility (a laminar flow source at inlet of Plenum chamber)

cross-sectional static pressure at the same exit location.

The second flow standard was a fully developed turbulent pipe flow profile. This was achieved by using an X-10 fan attached to the inlet of a long straight pipe, 4 inches in diameter and 90 inches in length. Four wall taps were placed around the circumference of the duct at distance of 0.038 m upstream of the duct exit as shown in Fig. C.2 . The measured duct exit static pressure (P_{bp}) was the average of the four wall static pressures at that location.

A third flow source was a turbulent and non-uniform flow from an actual HVAC fan (also an X-10 fan), connected directly to the plenum chamber as shown in Fig. C.3 . The duct was straight and rectangular, 0.15 m long with a cross-sectional area of 0.01 m^2. The wall pressure taps were located 0.18 m from the cut-off, as shown in Fig. C.3.

Another objective of the experimental investigation was to study the effects of the fan test rig geometry on the fan static pressure at the fan scroll outlet duct, P_{fs2}. Both AMCA/ASHRAE standard fan testing facilities were used; namely, the straight outlet duct (STD) and the plenum chamber (PLC) approaches. The same X-10 fan was used in the PLC tests as in the STD fan tests.

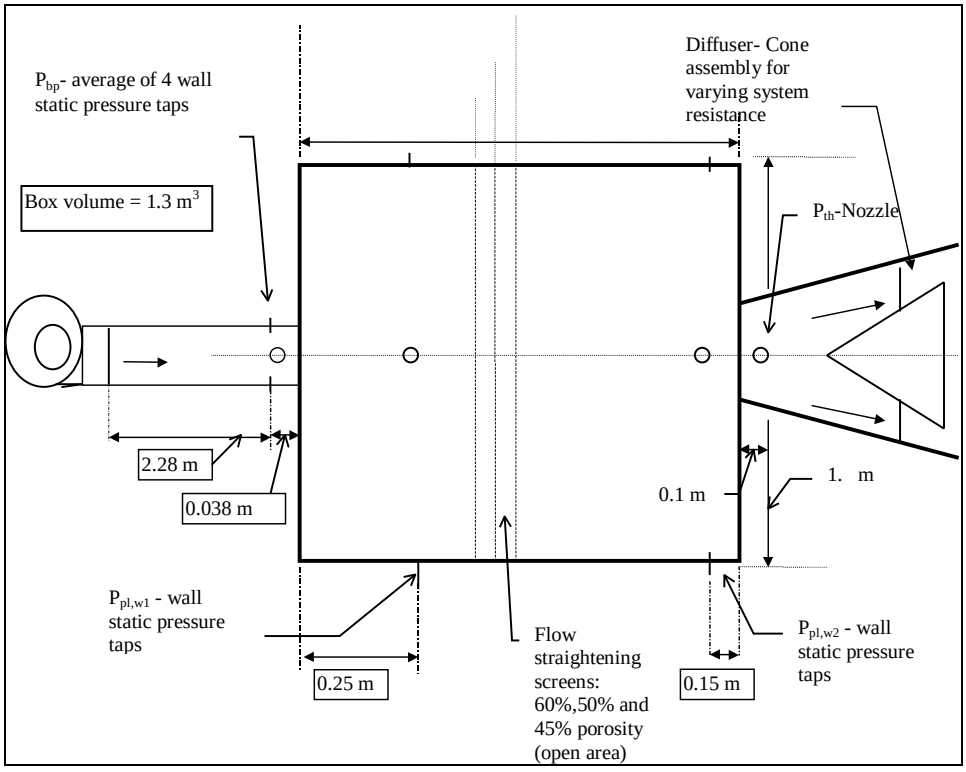

Figure C.2: X-10 fan with long exit duct (a turbulent flow source at inlet of Plenum chamber)

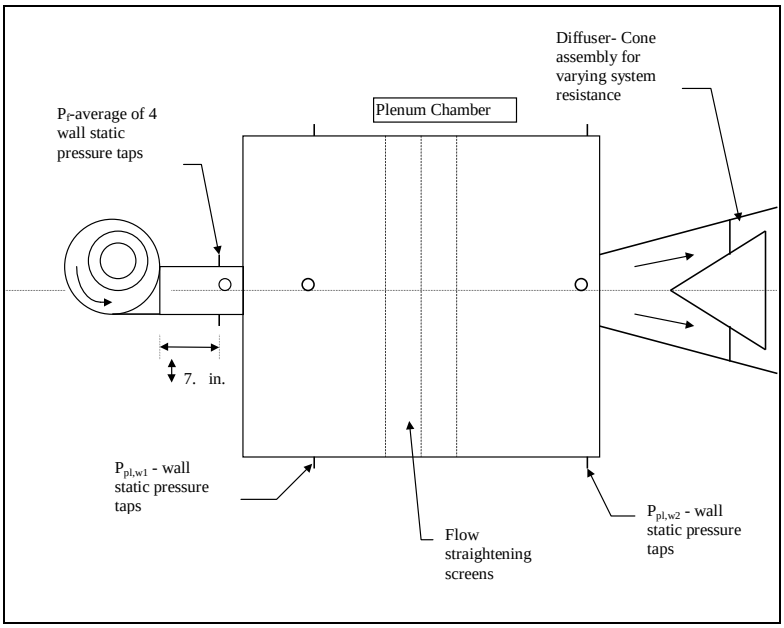

Figure C.3: X-10 fan connected directly to the Plenum chamber (a standard blower alone fan performance test)

C.3 Description of Test Facilities

C.3.1 Plenum chamber fan test facility

The plenum chamber test facility used for the present experimental study was the same one that was used in the study on HVAC fan scroll testing conducted by Taulbee Sonnenmeier and Knoll [63] at the University of Buffalo. The test facility consisted of a plenum chamber (designed and constructed in accordance with the AMCA Standards 210-74 and ASHRAE Standards 51-75 [45]), a Venturi nozzle for mass flow rate measurement, pressure transducers and plenum chamber wall pressure taps. The plenum chamber was used for measuring HVAC fan system exit static pressure (P_f). As shown in Fig. C.4 , the wall static pressure ($P_{pl,w1}$) was measured using taps around the four walls of the chamber upstream of the flow straightening screens. The ratio of the plenum chamber cross-sectional area to the plenum inlet area (or fan exit duct area) was 10:1. The flush mounted wall static pressure taps were located at such a location that the radial pressure gradient due to the inlet source flow inside the plenum chamber did not affect the wall static pressure measurements.

The static pressure difference measured just upstream of the flow nozzle inside the plenum ($P_{pl,w2}$) and the static pressure measured at the throat of the flow nozzle down stream of the plenum (P_{th}) are used to compute the volumetric flow rate (Q). The flow nozzle merges into a diffuser cone which returned the air to atmospheric conditions. The flow nozzle was designed and calibrated according to ASME/ASHRAE standards [63].

Three screens of various porosities, 60% 50% and 45% (open area), are placed at the locations shown in Fig. C.4 in the middle of the plenum. The role of the screens is to make the flow field more uniform, straighten the flow, and reduce the size of the large scale eddies before the flow enters the flow nozzle. The diffuser cone has a second solid cone mounted inside it that can be moved along the centerline of the

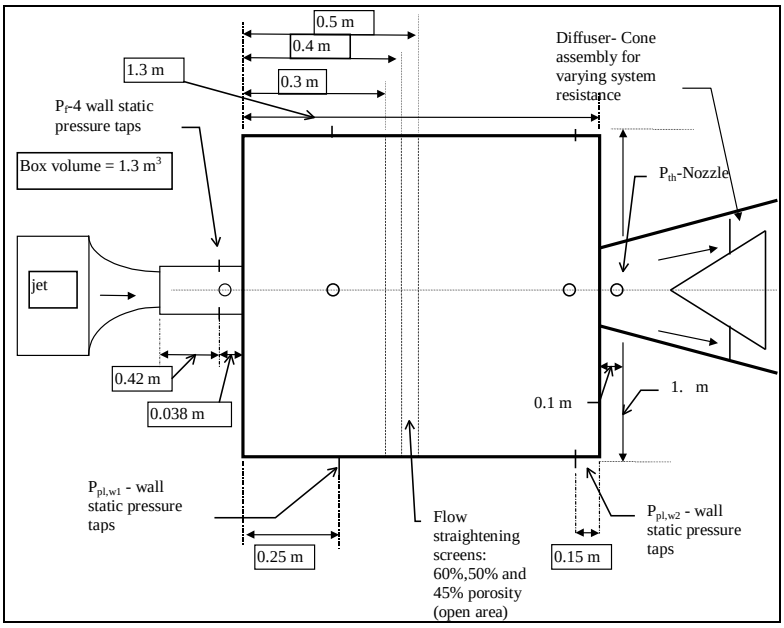

Figure C.4: Schematic drawing of the axisymmetric jet - Plenum chamber test facility

primary diffuser to vary the opening area and thus the resistance the test fan sees.

The motor power supply is variable. This, along with the variable resistance of the test chamber, allows for the generation of performance curves at either constant fan rotation rates or at a constant motor input voltage.

As detailed in the AMCA/ASHRAE fan testing standards, the total pressure rise generated by the centrifugal fan is determined by the pressure difference given by:

$$P_t = P_{t2} - P_{t1} \tag{C.1}$$

For the test geometry shown in Fig. C.3 with no fan inlet duct, P_{t1} is set to zero; thus the total pressure behind the fan is:

$$P_{t2} = P_{s7} + P_{d2} \tag{C.2}$$

This assumes no static pressure loss occurs between stations 2 and 7 (i.e., between fan scroll outlet and plenum chamber static pressure measurement locations). The dynamic pressure, P_{d2}, is given by:

$$P_{d2} = \frac{V_2^2}{1096}\rho_2 \tag{C.3}$$

where the velocity is expressed as:

$$V_2 = \frac{Q}{A_2}\frac{\rho}{\rho_2} \tag{C.4}$$

Combining these relations leads to an expression for the total pressure:

$$P_t = P_{pl1} + (\frac{\frac{Q}{A_2}\frac{\rho}{\rho_2}}{1096})^2\rho_2 \tag{C.5}$$

This represents the total pressure generated by the fan when tested against the variable resistance of the test chamber.

The performance of the fan is assessed by comparing the pressure rise given by Eq. C.5 to the flow generated by the fan. It should be recognized that in standard

HVAC engineering practice, the determination of the performance of the fan is based only on the static pressure, P_{pl1}. Thus it is assumed that the dynamic pressure is lost; and in practice it is, mostly in the diffuser.

In order to compare the performance of model and prototype test rigs under a range of system resistances, or alternatively, to compare the performance of two fans, a non-dimensional representation of pressure, volume flow rate and power can be used. The dimensional analysis approach given in Chapter 2 suggests plotting all the data in dimensionless form so that the complete fan performance characteristics are represented by a single characteristic curve. Basically dynamic and geometric similarity are maintained. Therefore, when the performance of a fan is assessed by using the model and prototype fan test rigs, the single fan performance characteristic curve can be used to identify similarities and differences in the performance of the two test rigs. A similar experimental study was conducted by Randall et al. [56]).

It is obvious that the actual performance of a given fan should not depend on the individual test rig. In other words, the same fan housed in a similar manner in different test rigs should give similar results. Thus, any differences in the measurement of the fan performance characteristic curve should be mainly due to measurement errors. Similarly, when the performance of two fans is assessed by using the same fan test rig, the non-dimensional fan performance characteristic curve generated by each fan can be used to identify similarities and differences in the performance of the two fans.

The pressure and volume flow coefficients that describe fan performance and allow for comparison between different fans were used in the forms as given in Eqs. 2.29 and 2.30. Performance maps can be (and were) generated over a range of the flow resistance: these consist of plots of pressure coefficient, ψ, versus the volume flow coefficient, ϕ.

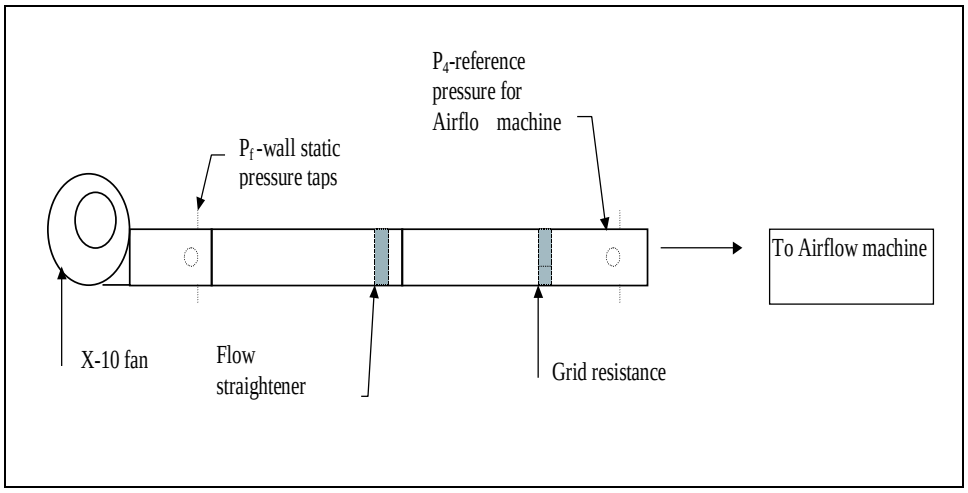

Figure C.5: X-10 fan airflow performance test facility (based on the AMCA fan test codes for Straight Outlet duct method

C.3.2 Straight Outlet Duct Fan Test Facility

The STD fan test rig is shown in Fig. C.5 . The details of STD approach are provided in detail in Appendix D (for more details see the AMCA Standard 51-74 fan test codes). An Airflow machine described later, was used to obtain both volume flow rate data and the static pressures from the STD fan test facility.

C.4 Experimental method

C.4.1 The PLC fan test method

The experimental setups described above were used to test the performance of the plenum chamber with a uniform airflow source under varying back-pressures (system resistance) conditions. The performance curves were generated by maintaining constant the fan speed of the blower that runs the axisymmetric jet, while varying the choke position at the plenum diffuser exit to set the system resistance (or back

pressure). The data recorded for each position of the choke is a test point on the resulting performance curve.

Testing included the measurement of the fan rotation speed, the static pressure at jet exit, P_j, the static pressure at the inlet of the chamber, P_{pl1}, and the pressure drop across the nozzle, Δp ($\Delta p = P_{pl2} - P_{th}$). The volume flow rate, Q[1], was determined from the pressure drop across the nozzle and local air properties. The static pressure at jet exit was measured by averaging the pressure from four flush wall taps around the straight circular duct, between the axisymmetric jet and the plenum (see Fig. C.4). The static pressure at jet exit was measured with a micro-manometer, whereas the plenum and nozzle static pressures were measured using pressure transducers. The fan rotation rate was determined with an accelerometer.

Fan performance curves were generated over the range of flow resistance, consisting of static pressure coefficient, ψ, versus volume flow coefficient, ϕ, based on both the jet static pressure, P_j, and plenum static pressure, P_{pl1}. These fan performance characteristic curves allow the comparison between the pressure coefficients based on the experimentally determined static pressures obtained from the fan/flow source and those from the plenum chamber.

Further, the plenum chamber was tested with both fully developed turbulent flow at plenum inlet (the case of the X-10 fan connected to the long pipe, Fig. C.2) and the non-uniform turbulent flow at plenum inlet (the case of the X-10 fan directly connected to the plenum, Fig. C.3). These tests were conducted with a constant fan motor input voltage (12 volts), and the angular velocity of the fan changed with

[1]The flow nozzle calibration curve was adopted from the work of Taulbee et al. [63], in the following form: $Q = 0.2358 + 335.34\sqrt{\Delta p}$ where Q is in [cfm] and Δp is [inches of H_2O]. Note that the conversion of voltage read by the pressure transducer into a pressure reading in terms of inches of water is included in the above flow rate formula.

varying system resistance. The performance curves for the cases of both fully developed turbulent (uniform) flow and non-uniform turbulent flow at the inlet of the plenum were generated in a similar manner to the ones obtained for the axisymmetric jet/plenum tests mentioned above.

C.4.2 The STD fan test method

The STD fan test facility was fitted with an X-10 fan/scroll and its performance characteristics were determined using both an Airflow machine for obtaining volume flow rate and using piezometric static pressure taps at the exit location of the fan scroll for static pressure rise information.

The Airflow machine housed ASME Standard flow nozzles of various sizes for mass flow rate measurement, a variable power supply, an auxiliary fan for extending the flow coefficient range, and pressure transducers for both absolute and differential pressure measurements from the fan test rig. The auxiliary fan can be used to adjust the static pressure at the exit of the flow duct in which measurements are being made. For example, it can simulate local atmospheric pressure conditions (similar to open atmosphere) at the exit of the flow measurement duct by adjusting its fan operating point.

The volume flow rate was evaluated from the mass flow rate measurements using the flow nozzles at the given temperature and barometric pressure. Note the Airflow machine also determines the local air density at the local air temperature. In like manner to the X-10 fan tests using the PLC method, the static pressure at the fan scroll exit duct was obtained by averaging the pressures obtained from the four wall taps at the fan scroll outlet, P_{fs2}. The actual fan was connected to a straight rectangular duct 0.015 m long with a cross-sectional area of 0.01 m^2. The wall pressure taps were located 0.018 m from the fan cut-off, as shown in Fig. C.5.

Since centrifugal fan performance is dependent on the operating load point, the

flow resistance was varied during the experiments to determine fan performance over a range of volume flow rates. This was achieved by using perforated metal grids of known porosity (i.e., total through flow area to total area) placed 10 exit duct diameters downstream of the fan impeller. The following grid porosities were used in the STD fan tests: 25%, 30%, 35%, 41% and 51%. Finally a test was also conducted with no grids (i.e., 100% porosity).

C.5 Discussion of results

C.5.1 Verification of the PLC fan test facility

Experimental results for the X-10 fan tests using the AMCA/ASHRAE plenum chamber fan testing method are shown in Fig. C.6. They show a variation in the fan performance curve based on wall static pressure measurements obtained at the fan scroll exit location compared to those in the plenum chamber. In order to verify the performance of the plenum chamber facility, the static pressure measurements in the plenum chamber were compared to the inlet static pressure obtained from standard flow sources at the inlet of the plenum. Note that the validity of the plenum chamber fan testing method *relies mainly upon the assumption that the static pressure at the fan scroll outlet duct plane is the same as the plenum chamber piezometric static pressure,* P_{pl1}.

The main objective of the experiment was to check whether the static pressure measured by the plenum chamber was in agreement with the jet exit piezometric (static) pressure. It is shown in Fig. C.7 that the plenum chamber static pressure (P_{pl1}) is in agreement (with an average relative error of 2.9 %) with the jet exit piezometric pressure (P_j) over the whole flow range tested ($0 < \mathrm{Q} < 350$ cfm). This result indicates that the AMCA designed plenum chamber static pressure is an accurate

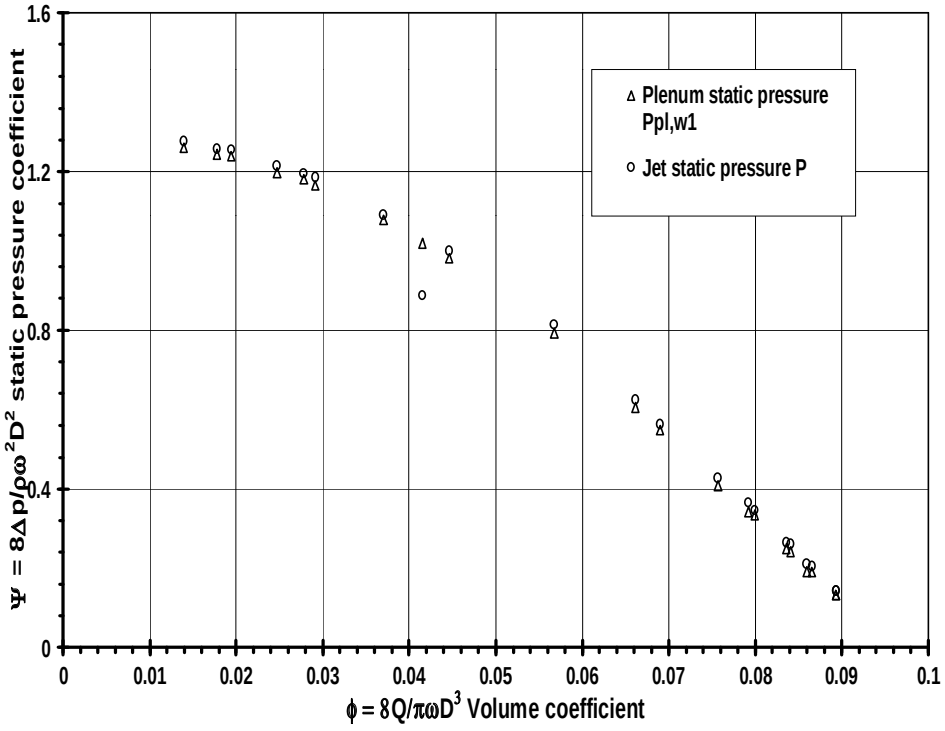

Figure C.6: X-10 fan performance using the AMCA Plenum chamber test method at 12 Volts

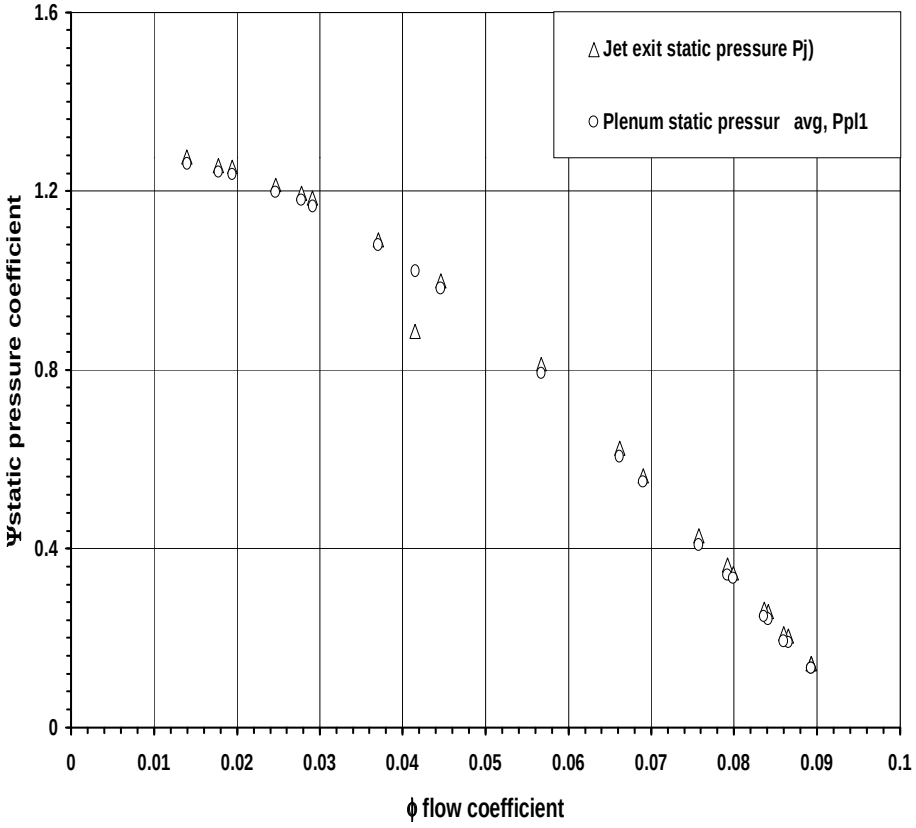

Figure C.7: Plenum chamber Static pressure validation test Results using the Axisymmetric jet laminar inlet flow source (supply blower fan speed was 2454 Rpm)

measure of the static pressure of a flow that is uniform and swirl-free.

An additional short study was conducted on the plenum chamber facility to check for any pressure differences across the flow straightener between P_{pl1} and P_{pl2}. There were no pressure differentials greater than 0.01 inches of H_2O found across the flow straightener. Thus, the screens do not cause any significant pressure loss, since the large volume of the plenum chamber acts as a flow stagnation box. The jet flow at the inlet of the plenum chamber behaves in such a manner that the static pressure at the jet centerline at the plenum inlet and the plenum wall static pressures are nearly the same.

For the case of a uniform and fully-developed turbulent inlet source flow to the plenum chamber, Fig. C.8 indicates that the static pressure measured at the exit end of the straight fan duct, denoted as P_{bp}, coincided with the static pressure (P_{pl1}) measured in the plenum chamber with an average relative error of 1.65 %. Both absolute and differential static pressure readings were made with pressure transducers and verified with a micro-manometer. It can be concluded from Fig. C.8 that the effects of a uniform turbulent flow on the static pressure measurements obtained with the plenum chamber are negligible. The results indicate that the plenum chamber static pressure, P_{pl1}, closely matches the straight duct exit static pressure, P_{bp}, with a maximum relative error of 3.0%.

In the case of an actual fan tested using the plenum chamber method, it is was observed that the fan exit averaged wall static pressure (P_f) was lower than the plenum chamber static pressure (P_{pl1}), especially at high volume coefficients. Fig. C.6 shows the variation of the static pressure measured with the plenum chamber (P_{pl1}) compared to the fan exit wall static pressure measurements (P_f). The difference between (P_{pl1}) and (P_f) increases with increasing volume flow coefficient (i.e., with increasing Reynolds number). Fig. C.9 indicates that the trend of the relative error between the X-10 fan exit static pressure and the plenum chamber static pressure is

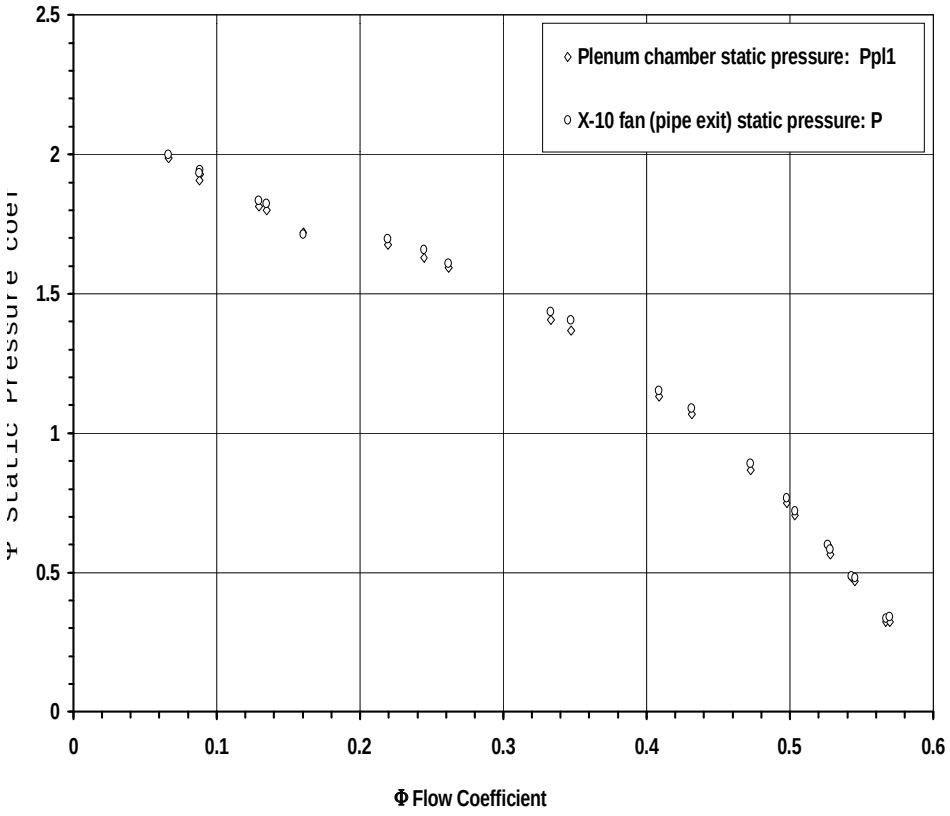

Figure C.8: Plenum chamber static pressure validation test results using the X-10 fan (with long circular exit duct) using a fully turbulent inlet flow source (at 12 Volts)

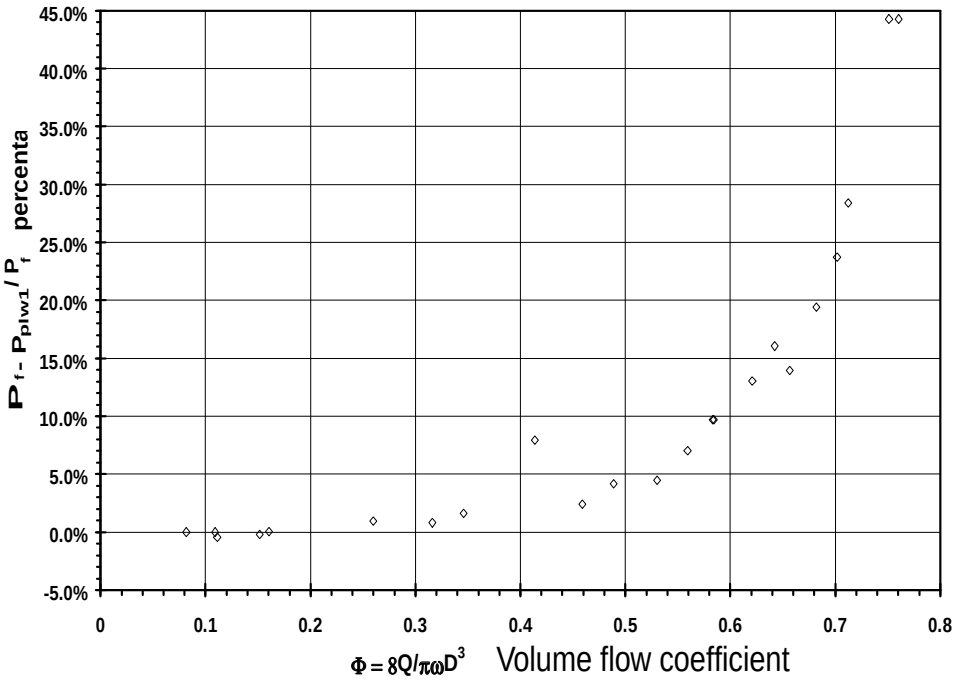

Figure C.9: Relative error between the X-10 fan exit static pressure (piezometric) and the Plenum chamber static pressure results for a constant voltage (12 V) test

nonlinear, with the average relative error of 11%. The reasons for this discrepancy are not yet clear.

In the case of the uniform turbulent inlet profile experiment (Fig. C.2), the static pressure loss ($P_f - P_{bp}$) between the fan exit location and the exit end of the straight fan duct was measured. The static pressure loss in the fan duct was plotted against the Reynolds number (based on pipe diameter)) as shown in Fig. C.10. The static pressure loss trend shown in Fig. C.10is consistent with the classical high Reynolds number pipe flow behavior (i.e., $\Delta p_{loss} \propto Q^2$).

C.5.2 Comparison of fan performance curves based on the STD and the PLC fan testing methods

In the case of the X-10 fan tested using the plenum chamber method, it was observed that the fan exit averaged wall static pressure (P_f) was lower than the plenum chamber static pressure (P_{pl1}), especially at high volume coefficients. Fig. C.6 shows the variation of the static pressure measured with the plenum chamber (P_{pl1}) compared to the fan exit wall static pressure measurements (P_f). In the case of the X-10 fan tested using the STD method, however, it is was observed from Fig. C.11, that the fan exit averaged wall static pressure (P_{fs2}) is consistent with the plenum chamber static pressure (P_{pl1}), across the whole range of the volume flow coefficient. Fig. C.11 also shows the variation of the static pressure measured with the plenum chamber, P_{pl1}, compared to the fan exit wall static pressure measurements: P_f from the PLC method, and P_{fs2} from the STD method. It can be observed from Fig. C.12 that the dynamic pressure coefficient obtained for the X-10 fan tests using both STD and PLC test facilities are similar, and follow the exact same trend. This implies that the flow rate measurement is consistent between the two fan test facilities.

System resistance curves (based on the fan exit static pressure and volume flow

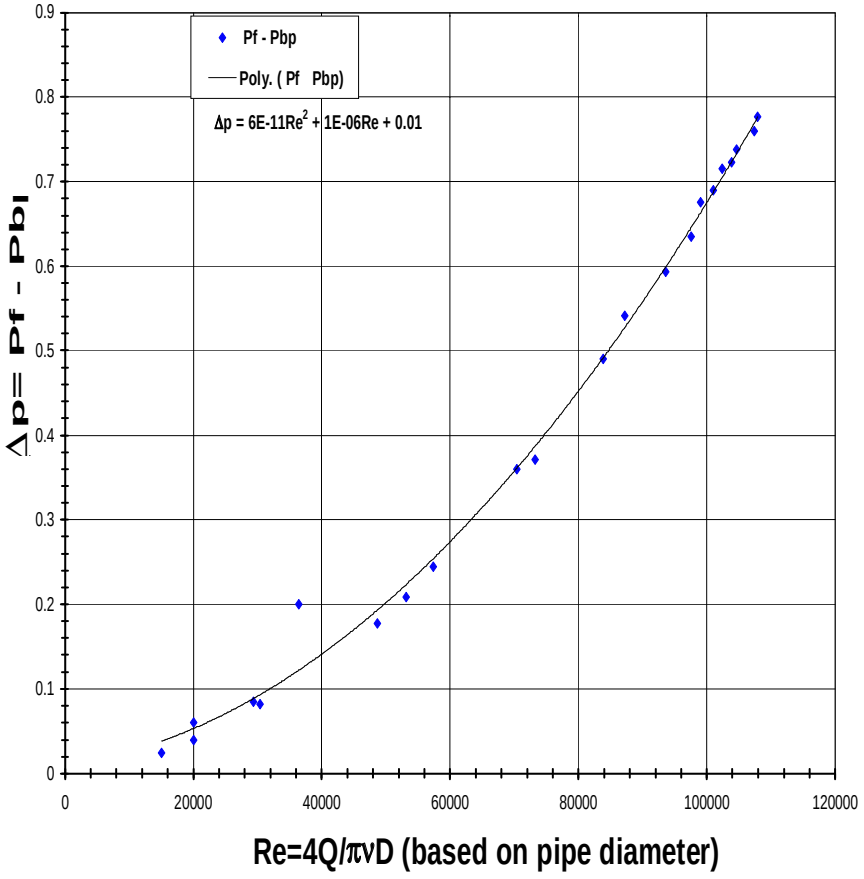

Figure C.10: Comparison of the X-10 fan exit static pressure to the static pressure at the exit of the long pipe upstream of Plenum chamber Plenum chamber versus pipe Reynolds number: the classical parabolic pressure loss curve for a circular pipe under turbulent flow

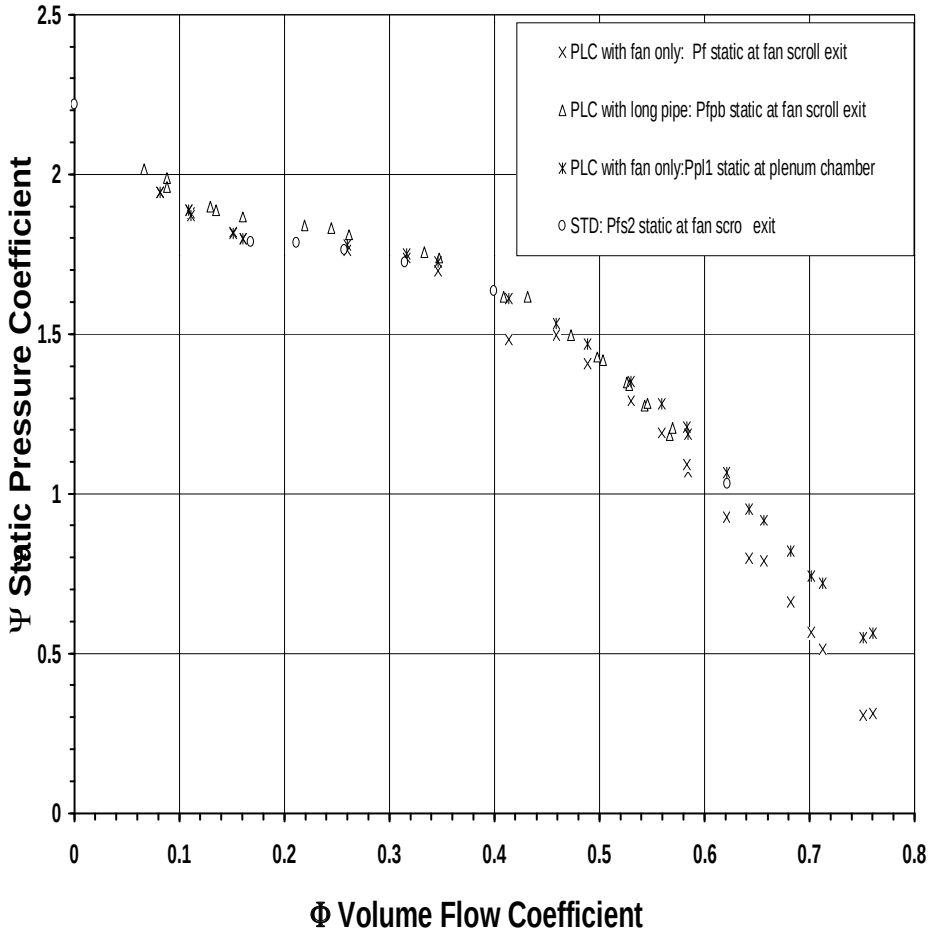

Figure C.11: Comparison of static pressures coefficients between: the X-10 fan alone scroll exit, X-10 fan (with long pipe) scroll exit, Plenum chamber, and the fan scroll exit (STD fan test method)

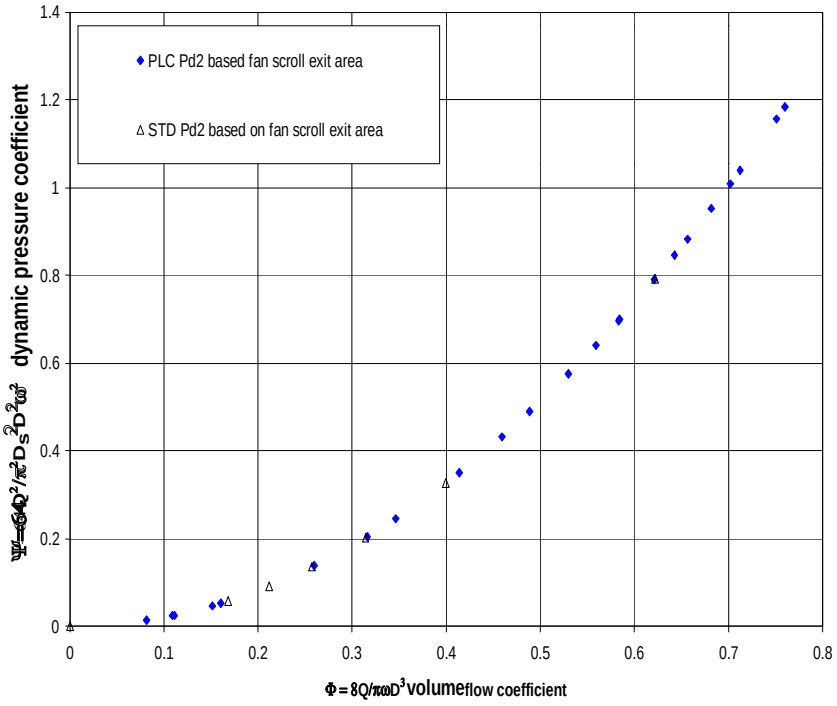

Figure C.12: Comparison of the X-10 fan exit dynamic pressure coefficient using both the Straight Outlet duct STD fan test method and the Plenum chamber (PLC)fan test- at 12 Volts. Note dynamic pressure results were calculated from volumetric flowrates measured in the two test facilities

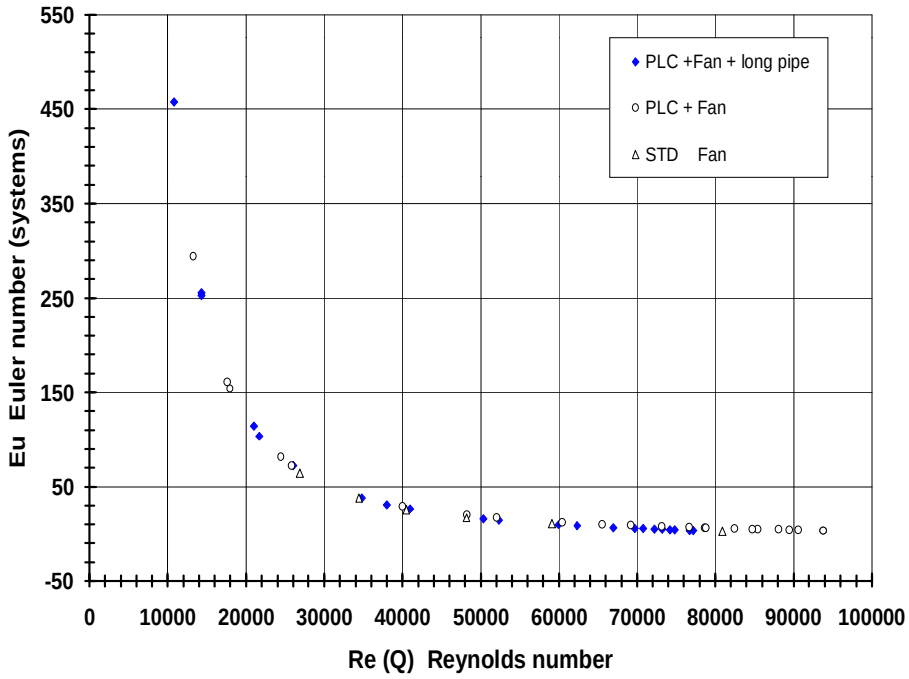

Figure C.13: Non-Dimensional plot of Euler (Eu) number versus Reynolds number (Re-based on volumetric flowrate) for the X-10 fan using the: STD, PLC, and long pipe with the PLC fan test methods

rate through the PLC and STD fan test facilities), are shown in Fig. C.13. It can be observed from the system curves that both the curves overlap for most of the flow coefficient range. Note that much higher resistance values can be achieved with the PLC facility, as is clearly evident from the system curves. A similar trend in system curves indicates Euler number similarity, which is essential for comparing fan performance between two different test facilities.

An important conclusion can be drawn from the fact there is consistency in fan static pressure measurements (Fig. C.11) between the STD and PLC methods. This clearly indicates that the location for piezometric static pressure measurement at the fan outlet duct (in the STD approach) is indeed an appropriate location for purposes of fan performance measurement. This static pressure measurement approach presents

an alternative to the one recommended by the AMCA/ASHRAE fan test codes.

Another important observation of this comparative fan test study is the fact that there is a discrepancy between the fan exit static pressure (from a fan without any additional system components) compared to the static pressure measured by the plenum chamber. As seen from the X-10 fan/pipe (PLC) and X-10 STD fan tests (both with additional ducting) there is complete consistency, however, between the fan exit static pressure of the same fan with additional system components and the static pressure measured by the plenum chamber.

In light of all the fan test results based on the different fan test configurations, it seems reasonable to suggest that the addition of system components to the fan that increase flow (system) resistance (e.g., due to extra ducting) causes a modification to the fan exit velocity profile which makes it more uniform, thus resulting in more consistent static pressure measurements between fan exit and plenum. In contrast, the isolated fan, demonstrates a highly skewed and non-uniform flow at the fan exit, which subsequently leads to inconsistent static pressure measurements between the fan exit and the plenum chamber.

For the case of a uniform velocity profile at the inlet to the AMCA/ASHRAE Standard plenum chamber test facility, the piezometric static pressure measurements (based on wall taps) gave an accurate prediction of the centerline static pressure of the incoming flow. It is plausible, however, that both non-uniformity and skewness of the inlet velocity profile can generate radial static pressure gradients inside the plenum which bias the static pressure measurements. There is no direct evidence to prove this hypothesis, but there is considerable indirect evidence from the results of all the various fan test configurations.

The only other plausible cause responsible for the inconsistency between static pressure measurements from the isolated fan (case of a non-uniform velocity profile)

and the plenum chamber, could be due to the errors in the static pressure measurements at the fan scroll outlet itself. In that case, the plenum chamber would still be accurately predicting the actual centerline static pressure at the fan scroll exit duct. On the other hand, in the case of the fan itself, the averaged static pressure measurements at the fan scroll wall do not accurately represent the centerline static pressure at the fan exit duct. Some reasons for the inconsistency between fan scroll wall tap static pressures and fan scroll exit duct centerline static pressures are the presence of local unsteady pressure gradients and flow curvature effects occurring at the junction of the fan scroll exit duct and plenum chamber. It is probable that the characteristics of the local flow phenomena at the fan scroll exit duct change with type of exit duct geometry. For example, in the STD fan test facility the presence of the long straight duct provides a much smoother transition than the sudden expansion in the plenum chamber test facility. In view of this, it is recommended that further tests be conducted using the plenum chamber fan test facility to verify the effects of exit boundary conditions on the accuracy of the fan scroll exit static pressure measurements.

In summary, the evaluations of HVAC fan exit static pressure for uniform flow fields using the plenum chamber technique show it to be an accurate measurement method for measuring HVAC fan performance. Present experimental results, based on flows both from a laminar flow source and a fully developed turbulent flow source, indicate that the plenum chamber wall static pressure technique produce similar results and agree within 3% of the inlet duct static pressure. The question of whether high flow swirl and non-uniform flow affect the plenum measurements of the static pressure at fan exit still remains unanswered, as evidenced by measurements taken with an actual HVAC fan. Based on the results obtained from the STD and PLC fan testing methods, it is highly recommended that isolated fans (with no system components) should not be tested using the plenum chamber method, but instead

the STD method should be adopted for accurate fan performance results. For the case of fans with additional system components, the plenum chamber method is more accurate and more practical than the STD method.

Appendix D

Evaluation of fan testing methodologies and characterization of fan performance

The evaluation of centrifugal fan aerodynamic performance can be conducted using different testing methods. The ACMA/ASHRAE Standards for fan testing recommends two basic methods for testing fan performance. The first method of fan testing is based on the straight duct approach (STD), and the second method of fan testing is based on the Plenum chamber approach (PLC). In studying methods of the fan performance evaluation, there were three main objectives. First, the performance of the Plenum chamber test facility (PLC) was verified, using a known uniform source flow. For this purpose a systematic series of fan tests were conducted using different source flow conditions at the inlet of the Plenum chamber. Second, the two methods of fan testing were compared to verify the results. To make these comparisons more meaningful, a new measurement location for fan outlet static pressure was proposed on the fan scroll exit duct. Lastly, a consideration which is generally overlooked in studying fans, that is, the effect of system components on fan performance and the

question of what is the most appropriate method of testing fans and /or fan system under the recommended fan test codes. This was considered important since it was hypothesized that the evaluation of the performance of a fan (i.e., impeller and scroll) without any additional system components, such as; diffusers, evaporators and inlet/outlet ducts, compared to a fan system combination, can show differences based on both the choice of the static pressure measurement location and on the type of fan test method adopted. In order to test this hypothesis, a fan, without any additional components was tested using both the STD and PLC approaches based on the static pressure right at the exit of the fan scroll duct. The method of evaluating fans without system components could differ compared to the method required for evaluating a fan with system components, due to certain differences in the measurement technique and or the influence of boundary conditions on the accuracy of the fan test method itself. Another question is what are the fan/system interaction effects on the fan impeller performance. Put in another way, what are the effects of the downstream boundary conditions on the performance of the fan impeller. These are difficult questions to answer all at once, however, this study throws some light on the effects of the various different downstream conditions on the overall fan performance. It should be pointed out that most CFD calculations are based on isolated fan impeller performance, that is, blade to blade performance, whereas the real scenario is not only different but also much more complicated.

D.1 Standard fan testing techniques

Fans are generally tested in accordance with requirements of AMCA standard 210-74/85 and ASHRAE Standard 51-75/85. The ASHRAE Standard specifies the procedures and test setups to be used in testing the various types of fans and other air-moving devices.

A common method of fan testing for developing the characteristics of a fan is as follows: The fan is operated from zero flow (shut off) conditions to nearly free delivery conditions (maximum flow or minimum system resistance). This procedure allows the determination of the fan performance over the full range, (although the full range is usually not used for most applications). At the shut-off (or maximum resistance) setting, the flow duct either at inlet or exit is completely blocked: at the free delivery conditions, the resistance is set to zero by removing flow restrictions, downstream of the fan impeller. The complete fan characteristic is obtained by using various flow restrictions in the downstream duct to impose different system resistances (or system load) on the fan. The AMCA/ASHRAE fan test standards suggest eight points (pressure/volume) on the fan curve are sufficient as a good representation of the true fan characteristic. The fan test codes also recommend Pitot tube surveys inside the exit duct downstream of the fan (in the straight duct fan test procedure (see Fig.C5)) to determine the volumetric flowrate and measure total and static pressures at constant fan speed. Other possible experimental test setups are also suggested by the fan test codes, for example, the Plenum chamber technique (PLC) both with and without an auxiliary fan (see Fig. C2). Each method should produce the same fan performance curve for the fan if the methods are to be consistent. In the STD approach (Fig.C5), the fan exit static and dynamic pressures are not directly measured at the fan exit location (location 2), but are estimated from the downstream static and dynamic pressures (location3) and corrected for the total pressure loss between the locations 2 and 3. The total pressure losses, due to pipe ducting and flow straightener are estimated from a flow model based on the classical high Reynolds number pipe flow model.

A fan test procedure that uses downstream circular ducting must have a sufficient length (8.5 to 10 exit duct diameters) before flow rate or pressure information can be obtained. It is thought, that since the long duct smoothes out the flow, along with,

the flow straightener (which partially removes flow swirl), this gives more uniform flow conditions at the downstream measurement stations.

D.2 Fan pressure measurements

The fan test codes do not recommend the measurement of the fan exit static and dynamic pressures directly at the fan exit location, but suggest that the measured pressures at the downstream locations be corrected back to the fan outlet conditions (see Fig.C5). The fan pressure rise formulations that the code uses for the Outlet Duct Setup (AMCA standard 210-74 & ASHRAE Standard 51-75) are as follows:

(The assumptions used are: fully developed turbulent flow, no swirl, symmetrical velocity profiles, etc...)

$$P_{t2} = P_{s3} + P_{d3} + f(\frac{L_{23}}{D_{h3}} + \frac{L_{efc}}{D_{h3}})P_{d3} \tag{D.1}$$

Again notice in Eq. D.1 no direct measurements of pressure or velocity are made at the fan exit location (2). All measurements are to done at the downstream location (3). The last part of Eq. D.1 is the loss of total pressure between the fan exit location (2) and the pressure measurement station (3). The friction factor, f, is a function of both pipe Reynolds number (Re_D) and pipe roughness factor (ϵ/D), which can be determined from the Moody chart for pipe flows. In the case of the outlet duct setup method of fan testing, the fan pressure rise is given by the following equations:

Fan total pressure rise:

$$\Delta P_{tfan} = P_{t2} - P_{t1} \tag{D.2}$$

Where usually $P_{t1} = 0$, for a fan without any inlet duct.

Fan static pressure rise:

$$\Delta P_{sfan} = P_{s2} - P_{s1} \tag{D.3}$$

Also, for a fan without inlet ducting; $P_{s1} = P_{atm}$. The total static and static pressures are related via the dynamic pressure, as follows

$$P_t = P_s + P_d \tag{D.4}$$

Where the dynamic pressure, Pd, is defined as

$$P_d = \frac{1}{2}\rho U^2 \tag{D.5}$$

Therefore the fan total pressure rise (Eq. D.1), can be rewritten as

$$\Delta P_{tfan} = P_{s2} + \frac{1}{2}\rho_2 U_2^2 \tag{D.6}$$

(with no inlet ducting)

$$\Delta P_{tfan} = P_{s2} - P_{s1} + \frac{1}{2}(\rho_2 U_2^2 - \rho_1 U_1^2) \tag{D.7}$$

(With inlet ducting)

For the case of constant density flow across the fan, Eq. D.7 can be expressed as

$$\Delta P_{tfan} = P_{s2} - P_{s1} + \frac{1}{2}\rho(U_2^2 - U_1^2) \tag{D.8}$$

It is important to recognize that pressure rise given by equation Eq. **??** occurs for the case when the fan impeller/fan scroll/fan ducting act in combination, and does not represent the pressure rise generated purely by the fan blades. The fan scroll (usually shaped as a logarithmic spiral volute) partially transforms the high degree of flow kinetic energy (i.e., high dynamic pressure) generated by the fan blades into a static pressure head towards the exit of the fan scroll. If the fan inlet and/or the fan scroll outlet ducting diameters are different compared to the fan inlet orifice the dynamic pressures at the fan inlet and the fan outlet would vary according to the following expression;

$$\frac{P_{d1}}{P_{di}} = (\frac{\rho_1}{\rho_i})(\frac{U_1}{U_i})^2 \tag{D.9}$$

Using the continuity of mass relationship (UA = constant) between the inlet duct location (i) and the fan orifice location (1) in Fig.C5, Eq. D.9 becomes

$$\frac{P_{d1}}{P_{di}} = (\frac{\rho_i}{\rho_1})(\frac{A_i}{A_1})^2 \tag{D.10}$$

Similarly, for the fan exit location (2) and the downstream duct location (e), the dynamic pressure ratio can be expressed as

$$\frac{P_{d2}}{P_{de}} = (\frac{\rho_e}{\rho_2})(\frac{A_e}{A_2})^2 \tag{D.11}$$

The dynamic pressure can either be measured directly, just upstream or just downstream of the fan inlet or the fan outlet respectively, or, can be measured at the far upstream and far downstream location and subsequently corrected for any change in duct diameter using the Eqs. and D.11 The average dynamic pressure at a given duct location can also be easily derived from the volume flow rate, especially in the case of incompressible (constant density) flow. The dynamic pressure can be expressed in terms of the flowrate (for a constant density flow) as follows:

$$P_{d2} = (\rho_2)(\frac{Q}{A_2})^2 \tag{D.12}$$

One way to measure the fan inlet and fan outlet static pressures in the near vicinity of the fan impeller, (for example, within, two duct diameters) is by using piezometric static ring or multiple wall static pressure taps around the duct, which provides measurement of static pressures. Dynamic pressures can be obtained with velocity surveys both at the inlet and outlet ducts. With both the static and the dynamic pressures, the total pressure information at both the fan inlet and fan outlet can be obtained, thus leading to the evaluation of fan performance.

The second method of fan testing, PLC, uses the principle of stagnation; flow, that is, the flow from the fan outlet enters a large volume chamber (Plenum) where it rapidly diffuses and stagnates, which subsequently allows the accurate prediction of the average static pressure at the exit duct of the fan system. The Plenum chamber itself is designed according to ACMA/ASHRAE Standards for fan testing.

Appendix E

Design and fabrication of the LSB fan test facility

E.1 The Large Scale Blower (LSB) Test Facility

A three times size, optically transparent Plexiglas model of a centrifugal fan, scroll and inlet were manufactured to the original prototype dimensions. This model was geometrically identical to the prototype, allowing similarity to be maintained through the fan scaling laws described above. Relevant dimensions are provided in Table 5.3. The inlet and outlet geometries of the model fan were not modelled exactly as the inlet and outlet geometries of the prototype fan system because of both ease of manufacturing and the need to provide simple geometries for CFD code validation. It is important to recognize that the large-scale blower facility was built primarily to test the centrifugal fan *without* all the auxiliary system components, such as inlet ducting and exit diffuser-evaporator combinations. A simple fan model was chosen instead of the whole fan system in order to provide a benchmark test for CFD code validation.

Fig.1 shows a schematic diagram of the apparatus used for the present experiment.

It consisted of a modified automotive HVAC squirrel cage fan driven by a D.C. motor coupled to a speed controller. The forward curved squirrel cage blower was made of resin material and built using the SLA technique. The model casing of the fan has front and back panels made out of Plexiglas sheets, which are grooved to accept a flexible Plexiglas sheet that formed the logarithmic spiral wall of the casing. The cross-section of the casing was rectangular, and continued past the fan throat section, making the fan exit geometry rectangular similar to the original prototype. The fan discharged into a rectangular duct 18 in. long. A 13.25 in. diameter circular duct with rounded lip was fitted to the fan's inlet opening. The LSB fan test facility design was based on AMCA design specifications in order to meet the AMCA fan testing code.

The reason for installing a circular duct at the fan inlet is to ensure parallel flow immediately before the inlet -scroll junction, thus allowing easy measurements of inlet and volume flow rates. A circular inlet duct used for the fan inlet simplifies the fan inlet model geometry input to CFD codes. Table 3 lists the inlet boundary condition as illustrated in Fig. 2. The locations of the boundary conditions required for the CFD code are shown in Fig. 3. The outlet fan duct has rectangular cross-section and constitutes an extension of the fan scroll volute. The diffuser at the exit of the prototype fan was not included in the large-scale model blower in order to provide a simple fan exit boundary conditions for CFD code validation. The straight rectangular fan exit duct is also simple to model in a CFD code, where as the prototype diffuser has a very complicated non-symmetrical three-dimensional geometry. The clearance gap between the top shroud of the fan impeller and the fan inlet duct was not modelled exactly to prototype geometry, but most other clearances were modelled maintaining geometric similarity.

The reasons for the difference in inlet geometry were mainly due to manufacturing; i.e., it is difficult to manufacture a highly curved circular inlet lip from lexan or

Plexiglas, although it can done, for the second generation fan model. However there were some compromises made the inlet duct design. A simple circular duct was used without any flow conditioning or proper inlet bell mouth. The fan inlet duct was directly installed into the front of the scroll at the fan orifice. This was mainly done in order to obtain preliminary inlet data, both with the LDA and obtain fan performance data with the same configuration, in order to characterize the inlet boundary condition in the case of simple inlet geometry for CFD analysis. The model fan inlet duct protrudes into the fan scroll by an inch, as shown in Fig.5.2, in contrast with the short round lip at the inlet of the prototype scroll. Also, it should be pointed out that, the fan blade roughness was much higher for the (SLA) model in comparison to the original prototype. These slight geometric differences may have some effect on the flow through the fan, but it is anticipated that most of these will be viscous-dominated flow phenomena which may have insignificant effect on the fan performance at high Reynolds number (based on blade chord).

The inlet flow is one of the major candidates for blower rumble noise and thus this region needs to be investigated thoroughly. The fan literature survey (Sardar [1], see Appendix 1) indicated that the fan inlet geometry can have a significant effect on fan performance. To study the effects of the differences between model and prototype, it was decided that a second fan model should be built with the exact inlet and outlet fan geometry. This model of the model (LSB) was called the "Mini-LSB", and it was a 1/3-scale model of the LSB fan. It was used for verifying the generalized fan similarity (scaling) laws as described in chapter 7.

E.1.1 HVAC fan (prototype fan) geometry

Centrifugal blowers (or fans) are air-moving devices commonly used to generate air-flow in automotive HVAC systems. A typical automotive HVAC system (i.e., the

prototype HVAC module) consists of a fan impeller run by a motor housed in a stationary volute (scroll) casing, that is connected to the downstream evaporator and heater cores by a diffuser, as shown in Fig 5.1. In typical automotive HVAC applications, forward curved centrifugal fans (fan blades are curved in the direction of rotation) are commonly used because of their small size and their lower operating fan speeds at the same load in comparison to backward curved centrifugal fans.

E.1.2 Fan / scroll geometry (Figs. 5.2 and 5.3)

A forward curved centrifugal fan impeller is made of a hub with a back-plate, top shroud and many fan blades (typically 37-60). The basic size and shape of the fan impeller is defined by its outer blade diameter and the blade span (height). Blade profiles are defined by blade inlet and outlet angles, blade camber, blade thickness, aspect ratio (span to chord ratio), blade taper and blade twist. Circular arced blades are the most common blade shapes used in FC fans due to cheap manufacturing costs and simple construction. (See lit review & HT rep for further details). The LSB fan impeller (Fig. ?) was built through the SLA technique. It had 37 blades straight blades of three-inch chord. Fan exit diameter was 16.5 inch with a top of the blades connected via a thin shroud.

E.1.3 Fan transition and exit duct design

The AMCA fan test codes recommend that volume flow rate should be determined from measurements made in a circular duct, whereas the LSB fan has a rectangular cross-section. Therefore, it was decided to build a transition duct for connecting the fan exit duct to the circular measurement duct. The transition duct was designed and fabricated according to AMCA Standards [PTC-11]. The rectangle to square aluminum transition duct was 2D long and turned out to be a converging duct.

Fan scroll exit duct cross-sectional area was approximately 147 sq in. while the downstream circular duct cross-sectional area was approximately 137 sq in. The axes of the fan exit duct and the transition duct coincided.

E.1.4 Flow conditioner

A flow straightener was designed and fabricated according to AMCA Standards. The flow straightener was placed about 3.5D (exit duct diameters) downstream of the transition duct, as recommended by AMCA Standards. It was of 0.44D in length, 0.005D in thickness and had a 1.0 in. diameter (0.076D) aluminum circular pipes as the basic flow straightener channel design instead of the square (0.075D) channel design suggested by the AMCA Standards. The circular pipe was chosen approximates the effect of the square channel, in such a way that the pressure drop was for a given flow rate remained constant. The differences between the AMCA recommended flow straightener and the one used are thought to be small.

E.1.5 System resistance (back pressure)

Since centrifugal fan performance is dependent on its operating load point (flow (system) resistance), the flow resistance was varied during the experiments to determine fan performance over a range of flow resistances. This was achieved by using perforated metal grids, of known porosity (i.e., total through flow area to total solid grid area) placed downstream (10 exit duct diameters)of the fan impeller. The following grid sizes were used in the LSB fan tests: 25%, 30%, 35%, 41% and 51%. Finally a test was also conducted with no grids (i.e. 100% open).

E.1.6 Fan drive system

The fan is powered by a 0.5 h.p. d.c. motor (constant torque) with a variable speed drive.

Appendix F

Definitions of cross-spectrum and power spectrum

Consider two signals A(t) and B(t) measured at arbitrary locations in space. The Fourier Transform for the two signals are denoted as and are given by...

$$\hat{A}(f) = \int_{\infty}^{\infty} A(t) e^{i2\pi f t} dt \qquad \text{(F.1)}$$

and

$$\hat{B}(f) = \int_{\infty}^{\infty} B(t) e^{i2\pi f t} dt \qquad \text{(F.2)}$$

The Power spectrums are estimated as...

$$S_{AA}(f) = \hat{A}(f)\hat{A}^{\circ}(f) = |\hat{A}(f)|^2 \qquad \text{(F.3)}$$

$$S_{BB}(f)=\hat{B}(f)\hat{B}^{\circ}(f) = |\hat{B}(f)|^2 \qquad \text{(F.4)}$$

where ^{o} denotes the complex conjugate of the Fourier transform. This leads to the estimate of the Cross-spectrum (or sometimes known as cross-spectral density) $S_{AB}(f)$, defined as...

$$S_{AB}(f) = \hat{A}(f)\hat{B}^{\circ}(f) \qquad \text{(F.5)}$$

The cross-spectral density (cross-spectrum) between two random signals provides a fundamental measure of the degree of linear correlation between the random signals in the frequency domain. Where as the Coherence function is a real, normalized (by the magnitudes of the power spectrum of the two random signals) measure of the degree of linear relation between a pair of random signals in the frequency domain.

Appendix G

The Preparation and Application of a Shear Thickening Dye

G.1 Preparation of the shear thickening dye

A new flow tracer was used for flow visualization. Its major properties useful as a dye tracer are shear thickening and high extensional-viscosity which have the advantage of resisting breakup in turbulent and complex separated flow. This new dye was developed and first used in external aerodynamic applications by Hoyt and Sellin ([**??**]). A typical recipe shown used in the development that produced the results in the HVAC fan tests was:

2% C16 TASal 500 ml

$\frac{1}{2}$ % PEO 150 ml

Tap water 1000ml

White paint 3 ml

The 2% C16 TASal solution was made from equal weights of cetytrimethylammonium bromide and sodium salicylate. This surfactant solution has the attribute

of shear thickening (Hoyt and Sellin). The PEO is poly(ethylene oxide), (commercial name Polyox WSR-301 (available from Union Carbide), and is well known as an effective drag-reducing additive as well as a water-treatment coagulant. The responsiveness to flow conditions can be adjusted by varying the concentration of the critical components (C16 TASal and PEO). Hoyt and Sellin used 250 ml PEO in 1 liter of water, where as in the present flow tests 150 ml was sufficient. This new dye is non-toxic and biodegradable, although care must be taken when drag or torque measurements are to be made, since this dye is a visco-elactic fluid it will over time cause the water to develop non-Newtonian characteristics, so that test water must be changed when prolonged testing is to be done. In the present case 120 ml of the dye will contaminate 350 gallons of water. Note that the visibility of the water usually will deteriorate sooner than water's flow characteristics.